Controlling Structure Across Length Scales with Directed Assembly of Colloidal Nanoparticles

by

Paul A. Gabrys

B.S. Chemical Engineering, University of Rochester (2015)

Submitted to the Department of Materials Science and Engineering
in Partial Fulfillment of the Requirements for the Degree of
Doctor of Philosophy
at the
MASSACHUSETTS INSTITUTE OF TECHNOLOGY
May 2020

Signature of Author …………………………………………………………………………...
Department of Materials Science and Engineering
April 22, 2020

Certified by …………………………………………………………………………...
Robert J. Macfarlane
Assistant Professor of Materials Science
Thesis Supervisor

Accepted by ………………………………………………………………………….
Frances M. Ross
Professor of Materials Science and Engineering
Chair, Departmental Committee on Graduate Studies

Controlling Structure Across Length Scales with Directed Assembly of Colloidal Nanoparticles

by

Paul A. Gabrys

Submitted to the Department of Materials Science and Engineering
on April 22, 2020 in partial fulfillment of the
requirements for the degree of
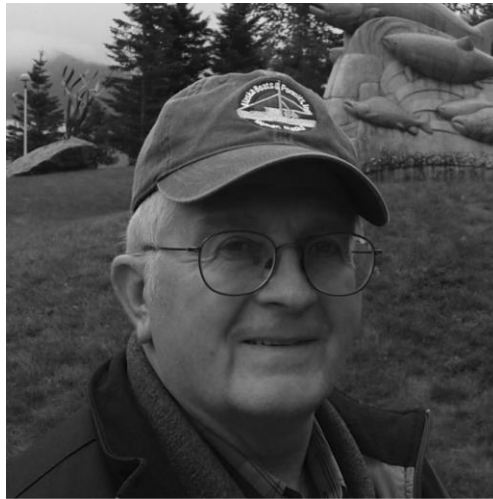Doctor of Philosophy in Materials Science and Engineering

ABSTRACT

One of the promises of nanotechnology is the ability to create a bulk, designer material with its structure programmed at each length scale using deterministic control over the placement of each nanoscale component. Self-assembled nanoparticle colloids, particularly those directed by sequence-specific DNA hybridizations, have emerged as a promising building block for producing these designer materials from nanoparticles that arrange themselves into precise symmetries through mechanisms analogous to atomic crystallization. However, DNA-directed colloids and other self-assembled nanoparticle systems still struggle to realize the goal of arbitrary structure control at length scales larger than a few microns due to the complexity of forces impacting different scales simultaneously. Utilizing existing atomic analogues for inspiration, this work extends the structure-defining nature of these programmable building blocks by imposing lithographic boundary conditions and devising processing techniques resembling those of atomic thin films and powders. Crystallization at an interface is explored, and preferential grain growth from a substrate is demonstrated to control large scale crystal texture. Full crystal orientation control is achieved by using standard nano-fabrication techniques to construct a lithographically-defined template for epitaxial growth that can define arbitrary macroscale shapes over millimeters. The resulting crystallization platform exhibits remarkable resiliency to lattice mismatch due to the 'soft' nature of the DNA ligands binding nanoparticles together. The understanding garnered from the DNA-grafted nanoparticle as a model system is extended to a colloid synthesized from a more scalable and robust directing polymer, polystyrene. The unique advantages of this new building block enable the fabrication of truly bulk, 3D materials with arbitrary macroscale shape on the centimeter scale *via* sintering and post-processing of nanoparticle-based crystallites. The results of this work are nanoparticle-based materials with dictated structure from the nanoscale (crystallographic unit cell), through the microscale (crystallite size and orientation), to the macroscale (lithographically defined shape).

Thesis Supervisor: Robert J. Macfarlane
Title: Assistant Professor of Materials Science and Engineering

To Dad
For teaching me to never give up

1955-2019

Acknowledgements

Table of Contents

Chapter 1. Programmable Atom Equivalents: Atomic Crystallization as a Framework for Synthesizing Nanoparticle Superlattices **43**

Chapter 2. Controlling Crystal Texture in Programmable Atom Equivalent Thin Films

Chapter 3. Epitaxy: Programmable Atom Equivalents *versus* Atoms 91

Chapter 4. Lattice Mismatch in Crystalline Nanoparticle Thin Films...........106

Chapter 5. Nanoparticle Composite Materials with Programmed Nanoscale, Microscale, and Macroscale Structure

List of Schemes

List of Figures

20

22

24

26

27

29

30

31

33

35

36

List of Tables

NANO · MICRO

small

Self-Assembly

In article number 1805424, Robert J. Macfarlane and co-workers highlight the characteristics of DNA-grafted nanoparticles as "Programmable Atom Equivalents" that enable controlled assembly behaviors analogous to atomic phenomena, which allow for rational material design well beyond what can be achieved with other crystallization techniques.

WILEY-VCH

Chapter 1. Programmable Atom Equivalents: Atomic Crystallization as a Framework for Synthesizing Nanoparticle Superlattices

CHAPTER ABSTRACT

Decades of research efforts into atomic crystallization phenomenon have led to comprehensive understanding of the pathways through which atoms form different crystal structures. With the onset of nanotechnology, methods that use colloidal nanoparticles (NPs) as nanoscale "artificial atoms" to generate hierarchically ordered materials are being developed as an alternative strategy for materials synthesis. However, the assembly mechanisms of NP-based crystals are not always as well-understood as their atomic counterparts. The creation of a tunable nanoscale synthon whose assembly can be explained using the context of extensively examined atomic crystallization would therefore provide significant advancement in nanomaterials synthesis. DNA-grafted NPs have emerged as a strong candidate for such a "programmable atom equivalent" (PAE), because the predictable nature of DNA base-pairing allows for complex yet easily controlled assembly. This chapter highlights the characteristics of these PAEs that enable controlled assembly behaviors analogous to atomic phenomena, which allows for rational material design well beyond what can be achieved with other crystallization techniques.

43
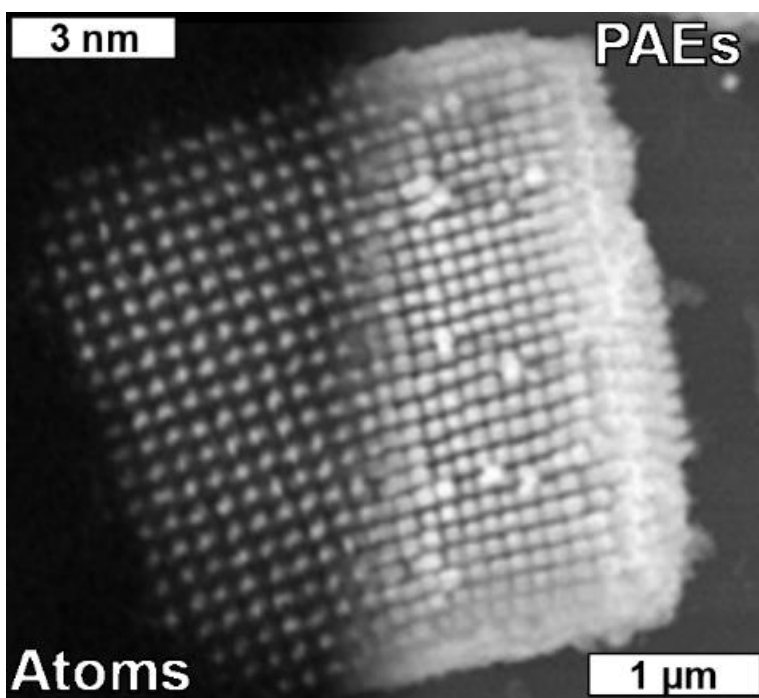
1.1. Introduction

The field of materials synthesis has historically been dominated by the development of new methods to control material structure that use atoms as building blocks and crystallization as a driving force for the formation of higher levels of ordering.[1,2] The diversity of the resulting materials is derived from a periodic table that is filled with a multitude of different atoms with different chemical identities, sizes, and bonding behaviors.[3–5] The kinetic and thermodynamic organization of atoms into these complex materials is well-studied, and therefore known to follow rational and (in simple cases) predictable pathways towards crystalline architectures.[6–9] As materials science and chemistry have expanded in recent decades to include the development of nanotechnology as a driving principle for materials discovery, new building blocks based on nanoparticles (NPs) have emerged as a means to further control the complexity of material structures across a wide range of size regimes.[10–13] However, the assembly of these nanomaterial synthons can be governed by many different chemical and physical forces,[14–20] and this increased level of complexity in NP assemblies is not nearly as well-understood or examined as the atomic crystals that came before them. Therefore, atomic crystallization behavior would be an ideal template upon which to model a framework to understand and program NP-based superlattices and bulk materials. The development of a set of nanoscale "atoms" that can be rationally directed into ordered assemblies with well-defined, hierarchical structures on length scales orders of magnitude larger than the individual building blocks would constitute a major step forward in the field of materials science. While multiple means of controlling NP assembly have been developed, correlating NP assembly behaviors to known atomic crystallization phenomena would require nanoscale "atoms" with several key design features that would allow for rational control over their formation into larger structures. NP building blocks that have well-defined compositions, sizes, shapes, and predictable binding interactions that dictate their local coordination environment would allow for complete control over material structure at the nanometer and larger scales. Moreover, if the assembly process truly mimicked atomic crystallization, it would allow for rational exploration of crystallization behaviors that are often difficult to study, like defect structures, surface faceting, or kinetic mechanisms of crystal growth.

While multiple types of ligands have been grafted to NP surfaces to control their assembly,[16,18–21] this chapter will posit that the most programmable means of dictating NP superlattice formation is the development of DNA-grafted NPs as "programmable atom equivalents" (PAEs). Specifically, we will outline the history of PAE crystallization, focusing on how the use of nucleobase pairing between surface-grafted oligonucleotides has developed from a simple means of aggregating NPs to a now completely controllable process for synthesizing complex hierarchical structures. These PAE building blocks follow crystallization phenomena that are remarkably similar to those exhibited by atoms, but the predicable and synthetically manipulatable DNA base-pairing interactions allow their assembly to be controlled in a means that is entirely impossible for atomic systems (Figure 1.1). As a result, the moniker of "programmable atom equivalent" is incredibly apt for this nanomaterial building block; we will demonstrate both how they have developed into a powerful materials synthon and highlight key areas of investigation that promise exciting discoveries in the fields of both chemistry and materials science.
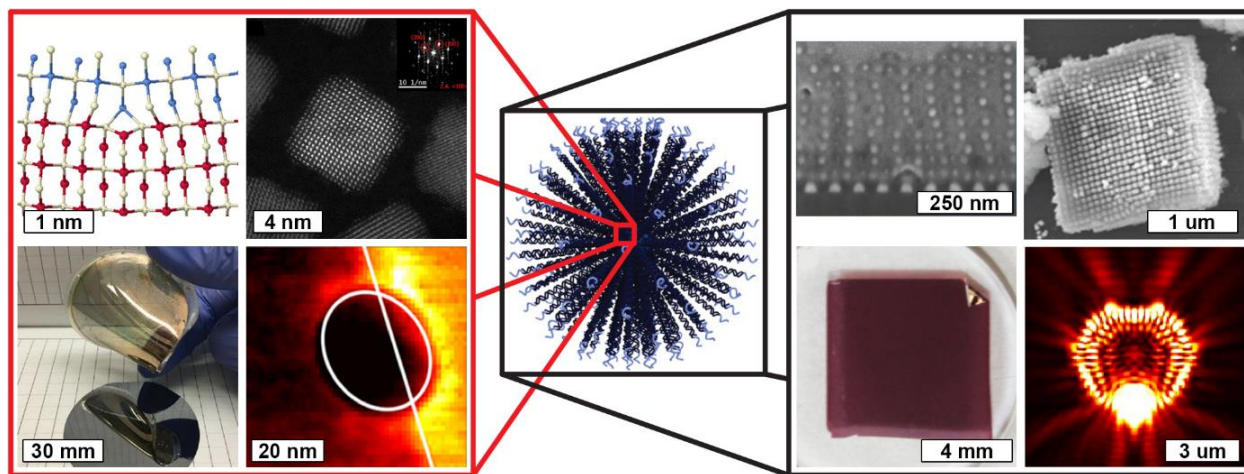
Figure 1.1: DNA-grafted nanoparticles as "programmable atom equivalents" utilize atomic crystallization phenomena as a framework to build nanoparticle superlattices at larger length scales. Adapted with permission.[22–29] Copyright 2016, 2018, American Chemical Society (ACS). Copyright 2015, John Wiley and Sons. Copyright 2017, The American Association for the Advancement of Science (AAAS). Copyright 2008 and 2015, IOP Publishing. Copyright 2013, Springer Nature. Copyright 2017, National Academy of Sciences (NAS).

1.1.1. "Atom-Like" Behavior in Colloidal Crystals

The concept of utilizing NPs to mimic atoms is not unprecedented, as the term "artificial atom" has been used to describe colloidal assembly systems for many years.[30] Early discoveries found that colloidal particles would undergo "solid-liquid-gas" phase transitions based on changes in NP concentration and relative interaction strengths between NPs, where the different phases were defined by the relative mobility and ordering parameters of the colloids.[31–33] More recently, "artificial atoms" with directional binding akin to molecular valency have been explored via the creation of "patchy particles" that express multiple types of ligands at different points across their surfaces or possess particle cores with specific polyhedral or anisotropic shapes.[34–38] However, all of these classic examples of "atom-like" behavior in colloids are limited to analogies in narrow circumstances. In particular, they do not always crystallize into materials with long range order or often provide just a singular example of crystallization that is not generally applicable to the formation of multiple different structures. The predominant methods to assemble these particle-based periodic structures are *via* evaporation or sedimentation of ~100-1000 nm colloids.[14,39] During this process, spherical particles close pack together due to solvent exclusion and maximization of entropy, generally yielding face-centered cubic (fcc) structures, as this structure represents the densest arrangement of hard spheres.[13,40]

Driven by the desire to harness the powerful driving force of crystallization in creating different periodic structures beyond just fcc lattices, significant research has been devoted to creating ordered superstructures (superlattices) of colloidal NPs with several different coordination environments. The technique of slow-drying a solution of colloids onto a substrate has proven particularly effective in producing several different crystal forms, at least in 2D NP thin films. To achieve this, uniform NPs (dispersity typically less than 5%) must be synthesized such that they will close-pack together into space filling arrangements.[41] Using the slow-drying method, both molecule- and macromolecule-grafted NPs have been shown to yield a large breadth of different crystal structures from dried mixtures of one,[17] two,[16,42] or even three NP components.[43] Complex arrangements like quasi-crystalline superlattices have been achieved with this method as well.[44] These crystalline symmetries have even been shown to be achieved with multiple NP compositions,[42,45] broadening the programmability of these NPs as "artificial atoms." Nevertheless, while NPs of various compositions, sizes, and shapes can be used in various

mixtures,[41] the final coordination environment cannot be directly programmed into the building block using this methodology. In other words, the structures that are achieved are inherently linked to the identities of the NPs being assembled and cannot be purposefully manipulated to yield a different crystalline arrangement without changing the NP size, shape, etc. The achieved crystalline phases have been retroactively explained to a remarkable level of certainty, though typically based on arguments of space-filling and maximization of ligand entropy.[46] Other systems using charged colloidal NPs and ionic attraction have been developed to harness explicit enthalpic attractive forces to govern interparticle interactions,[15,18,47] but these motifs require that only very short interparticle distances be used, meaning that the achievable arrangements are similarly restricted by the identity of the underlying NP. While effective at mimicking specific atomic behaviors, these "artificial atom" systems do not have the level of programmability required from a building block that could truly take advantage of atomic crystallization behavior and harness it to control structure.

1.1.2. Moving Beyond "Artificial Atoms"

For the purposes of this chapter, we would set the definition that the difference between a nanoscale "artificial atom" and a truly "programmable atom equivalent" is that a *programmable* building block must be modular, meaning that the moiety controlling the interparticle interactions must be entirely separate from the underlying NP identity (size, shape, composition). In other words, the synthesized building block must yield a direct output (i.e. crystalline unit cell) from a specific and intentionally designed input (i.e. programmed interparticle interaction). "Artificial atoms" (Section 1.1.1) have proven very successful in *correlating* specific aspects of the building block design to resulting crystalline architectures, enabling significant insight into colloidal crystallization behaviors and the synthesis of many unique materials. However, none of these motifs allow for the independent *manipulation* of NP coordination environments without adjusting variables such as NP size and shape. The above examples do demonstrate that self-assembly of colloidal NPs can remove some aspects of the NP's identity, particularly composition, from their coordination characteristics, but a higher degree of programmability is required to truly predict, control, and tune crystal formation. Ultimately, a building block that could rationally control

particle assembly in such a manner would not be considered simply an "artificial atom" but a fully programmable atom equivalent.

The use of DNA as a directing force for NP assembly was originally conceived and demonstrated over twenty years ago.[20,48] As a ligand, DNA can be synthesized with molecular purity and with unparalleled precision in monomer sequence. Mirkin *et al.* originally demonstrated that a DNA-grafted NP could be used to rationally design nanomaterials and precisely program crystalline NP superlattices,[20] as the DNA corona would dictate specified binding interactions to determine which NPs would form bonds with one another.[a] In the subsequent decades, this modular, tunable building block design has indeed become a powerful synthon in nanomaterials synthesis and has been used to assemble multiple different crystalline architectures, earning it the title Programmable Atom Equivalent (PAE). To fully understand the PAE's potential as a materials building block, we will first discuss their design features that allow PAEs to crystallize in a predictable manner that bears many analogies to atomic crystallization.

1.2. The Characteristics of a "Programmable Atom Equivalent" (PAE)

1.2.1. Discrete Nanoscale Arrangement of Oriented DNA Provides Multivalency

In the broadest sense, a PAE is defined as a particle of any shape and composition densely functionalized with a monolayer of synthetic oligonucleotides of designated base-pair sequence (Figure 1.2A). The first examples of such particles demonstrated that the addition of "linkers" could selectively program NP aggregation into clusters[48] or aggregates with no long range order.[20] The original design used two non-complementary single-stranded DNA (ssDNA) anchors on gold NPs (AuNPs) such that they would only undergo selective aggregation upon the addition of "linker" strands designed to duplex to the strands anchored on the NPs (Figure 1.2B).[20] AuNPs were used in these initial studies because gold-thiol chemistry can be used to easily and readily attach a large number of oligonucleotides to each NP. Additionally, AuNPs possess a

---

[a] A separate DNA-NP construct was concurrently developed by Alivisatos et al.[48] with a limited number of DNA strands per particle. This type of building block typically yields discrete clusters of particles that are more readily analogized to individual "molecules". While several interesting studies have arisen from this initial design, this work will not focus on these types of building blocks for the sake of brevity.

surface plasmon resonance that is sensitive to its local environment, meaning that aggregation is easily monitored by UV-Vis Spectroscopy.[49] The earliest work done on these materials was to maximize their colloidal stability by increasing the DNA loading and strength of the DNA-Au attachment chemistry. Using fluorophore-labeled linkers, the surface coverage of DNA on the AuNP surface could be quantified,[50,51] and modifications to the oligonucleotide sequence or the chemical structure of the oligos (e.g. incorporation of polyethylene oxide spacer groups[52]) were investigated as a means of controlling the grafting density at the particle surface.[53] Importantly, DNA loading was found to be dependent on steric hindrance between grafting strands,[54] and a key innovation to increase loading density was therefore to slowly shield the negatively charged DNA backbone with the addition of sodium chloride during the functionalization process (salt aging).[52] This ultimately enabled a maximum grafting density of 56 pmol/cm^2, which has been demonstrated to be critical in the use of PAEs for materials synthesis by enhancing the degree of multivalency between bonded PAEs.

Although an early goal for PAEs was to be able to use them to programmably build highly ordered nanostructures, the complexity of this new building block made this goal challenging, requiring a significant amount of investigation into the properties and behavior of PAEs as a function of their particle and oligonucleotide designs. As a result, early studies involving PAEs exploited their ability to selectively bind to DNA for sensing[55–58] and biomedical applications.[59–61] It was discovered early on that the arrangement of multiple oligonucleotides in a brush architecture around a nanoscale scaffold imparted higher binding constants,[62] greater discrimination against nucleotide mismatch,[63,64] and even enhanced cell uptake[65] and biocompatibility.[66,67] Due to these new properties that arise as a function of nanoscale geometry and multivalent binding behavior, the DNA-grafted particles were coined "Spherical Nucleic Acids"[68] to highlight the unique and important effects imparted by arranging a dense monolayer of oligonucleotides around a nanoscale core.
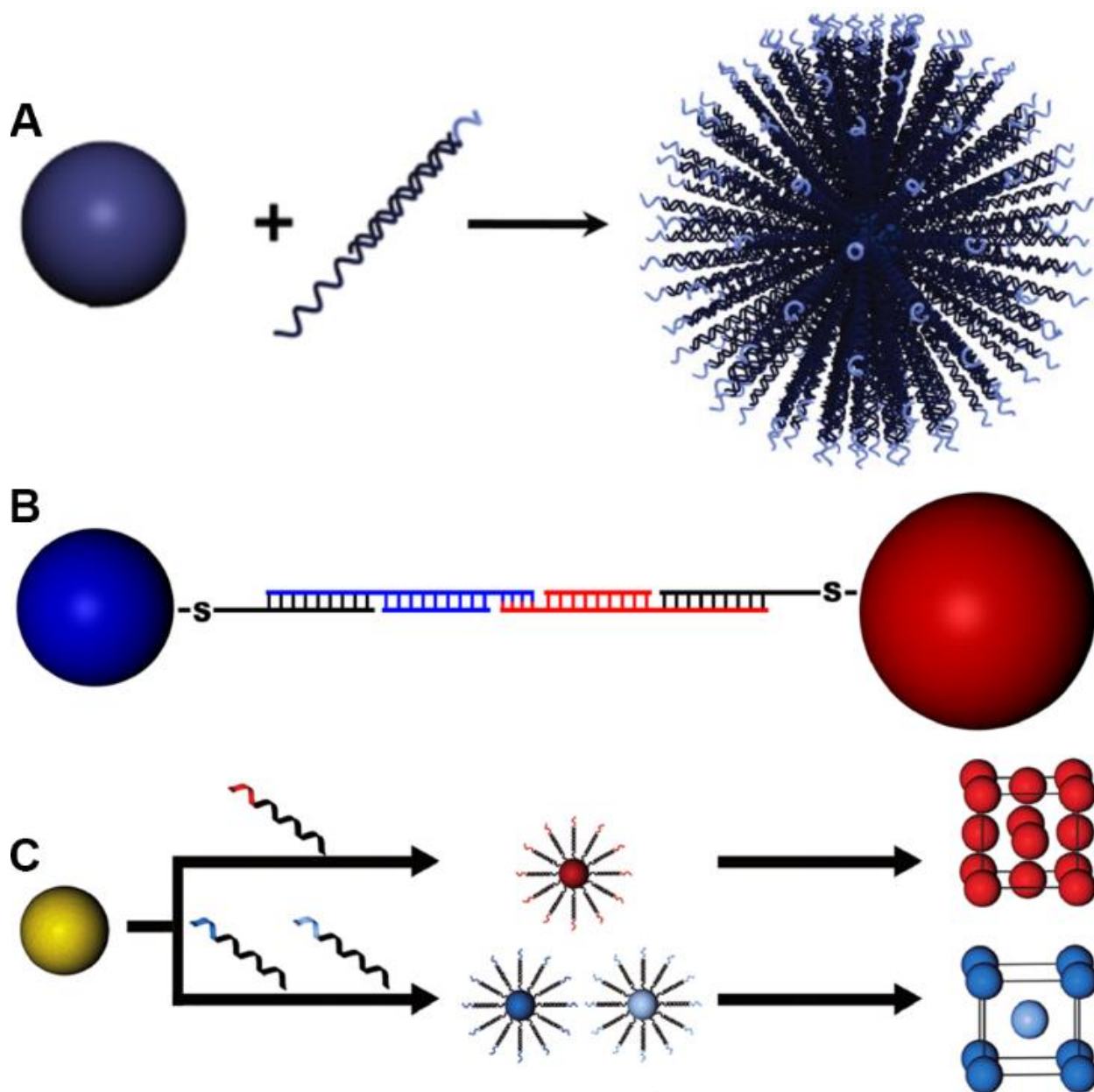
Figure 1.2: The characteristics of a DNA-grafted nanoparticle that allow it to be defined as a "programmable atom equivalent" are as follows: (A) a densely functionalized core that results in multivalency, (B) a "sticky end" motif that provides specific binding interactions between complementary particles, and (C) a programmable crystalline unit cell that is based on maximizing complementary contact. Adapted with permission.[69,70] Copyright 2011, AAAS. Copyright 2013, John Wiley and Sons.

A key feature of all PAEs is that the DNA duplex structures can be disrupted at elevated temperatures, and the particles can therefore be reversibly assembled and disassembled by thermal cycling.[20] Initially, it was observed that overall PAE aggregate sizes grew over time even under static temperatures; this was attributed to an "Ostwald ripening-like" process.[71] Similarly, an investigation of melting transition (T_m) sharpness revealed a dependence of T_m on aggregate size.[72] From these data, it was hypothesized that PAEs on the surface of aggregates must be in flux due to having fewer binding interactions than those in the bulk. This concept of PAE cooperativity was further corroborated by data revealing that an increased density of "sticky ends" linking the particles to one another (through higher surface loading or geometric factors like NP curvature) resulted in an increased and sharpened T_m[62] and could be capitalized upon to selectively aggregate PAEs of different sizes.[73] The collective nature of PAE binding, where not one but many DNA hybridization interactions exist between two PAEs, allows these building blocks to rearrange and densify when the temperature approaches T_m as observed in both Monte Carlo simulations[74] and experiment,[75] ultimately proving incredibly important in enabling the crystallization of PAEs.

1.2.2. Cooperativity of DNA "Sticky Ends" Enables Crystallization

The first decade of research into PAE assembly focused primarily on structures with well-defined interparticle interactions but was unable to generate materials with anything more than short range order defined by a constant interparticle distance.[76] In the late 2000s, a common intellectual breakthrough occurred independently in several research groups that enabled the formation of NP superlattices with long-range order.[77–79] The key discovery was that the ability to thermally anneal PAE aggregates into crystalline materials was inhibited by the strength of the individual DNA hybridizations holding them together. When the strength of each thermally-reversible binding interaction is reduced (e.g. shortening the ssDNA "sticky end" at the end of each grafted oligonucleotide from 12 to as little as 4 bases[78]), the rate of sticky end duplex dissociation increases by several orders of magnitude. However, because of the dense monolayer of oligonucleotides on the surface of the particles, the high local concentration of sticky ends results in equally rapid reassociation.[80] As a result, the individual connections between PAEs using these short sticky ends are in a constant state of flux, enabling particles to more rapidly

reorganize within an aggregate without fully dissociating from one another. This increased mobility enables the PAEs to reach the enthalpically-driven thermodynamic state that maximizes the overall number of DNA connections (i.e. maximizes the number of complementary nearest neighbor particles) which is typically a periodic, close-packed crystalline arrangement.[78] The first PAE crystals comprised either a unary system (using PAEs with self-complementary sticky ends) or a binary system (using two sets of equal size PAEs with different but complementary sticky ends) and formed either fcc or body-centered cubic (bcc) crystals, respectively (Figure 1.2C).[78,79] The fcc lattices were hypothesized to be stable due to the fact that each particle possesses the maximum number of nearest neighbors (and thus the maximum number of DNA connections to adjacent particles). While PAEs in a bcc lattice do not maximize the total number of nearest neighbors, each particle in this binary system does possess the maximum number of complementary nearest neighbors to which they can actually form a DNA bond. While several different DNA design motifs have been shown to successfully crystallize PAEs[77–79,81] (some with slightly different design rules governing their behavior[82]), all rely on the common intellectual principal of maximizing multivalent DNA interactions.

Following this initial breakthrough, a flood of new research began in understanding the basic principles that governed the assembly of crystalline PAE structures, and it was quickly discovered that many of the assembly behaviors closely matched atomic crystallization phenomena that had already been explored. Ultimately, a set of design rules was laid out in 2011 that explained PAE crystallization behavior in a manner similar to Pauling's rules for ionic solids,[6] and a simple "complementary contact model" (CCM) was established to semi-quantitatively explain the stability of different PAE lattice phases.[69] However, unlike Pauling's rules, the CCM developed for PAEs used simple geometric rules to predict the arrangement of particles that maximized favorable enthalpic interactions between DNA strands on complementary particles. As a result, the CCM can actually be used to predict and even program the crystalline lattice favored by a given set of PAEs, yielding a broad phase space of different, experimentally-achievable crystallographic symmetries beyond fcc and bcc.[69] While subsequent investigations have shown that the conformational entropy of the DNA ligands and more complicated aspects of DNA hybridization are required to fully explain all aspects of PAE superlattice formation, their assembly behavior remains highly predictable and controlled, resulting in an attractive crystallization technique for

chemists and materials scientists. The numerous similarities to atomic crystallization and ability to precisely dictate NP superlattice structure ultimately led to the development of the term "programmable atom equivalent" (PAE) to describe these building blocks.[70]

1.3. Versatility in the PAE Construct[b]

1.3.1. Modularity of the Nanoparticle Core

One of the major advantages provided by programming NP assembly with DNA is the ability to completely separate the chemical composition of the NP core from the lattice structure that is generated, enabling significant chemical diversity to the materials synthesis process. To date, PAEs have been experimentally synthesized, functionalized, and crystallized with cores of various metals, oxides, polymers, and even biological nano-structures (Figure 1.3). Gold,[20,79,83,84] silver,[85] and silver/gold core-shell[86] NPs are most commonly used, both because their plasmon resonances allow for simple monitoring of assembly, and thiol chemistry enables simple functionalization of particles with a dense DNA monolayer. NPs with luminescent properties (cadmium selenide,[84,87–89] cadmium telluride,[84] and zinc sulfide[83,84] quantum dots), magnetic properties (iron oxide[83,84,90]), and catalytic properties (palladium[84] and platinum[83]) have all also been demonstrated. The breadth of available PAE core sizes has increased with the DNA functionalization of other oxide cores (silica[91,92] and titania[92]) and polymer spheres (poly(styrene) (PS),[77,92–95] poly(methyl methacrylate) (PMMA),[92] and 3-(trimethoxysilyl)propyl methacrylate (TPM)[92]). Even metal-organic-frameworks (MOFs)[96] have been shown as a suitable PAE core material. Intriguingly, "hollow" NPs that lack a solid core have been synthesized using a cross-linking strategy that creates a thin polymer shell around a AuNP core by using gold-catalyzed polymerization of alkynes.[97] Subsequently, the Au can be dissolved out of this structure without disrupting the overall size, shape, or binding capability of the DNA corona, making a "3D spacer" that connects PAEs into a lattice. These hollow particles are a key example of a design

---

[b] The text and figures in Section 1.3 represent the highlights of achievable NP core identities (size, shape, and composition) and PAE crystallographic symmetries. While the list of examples is intended to be extensive, given the diverse breadth of research utilizing these building blocks, the cases mentioned may not be comprehensive.

parameter that would not be achievable in either atomic systems or close-packed colloidal lattices, thereby enabling the synthesis of non-close packed crystallographic symmetries (Section 1.3.3) and truly demonstrating the tailorability, diversity, and control afforded by DNA-programmed assembly.
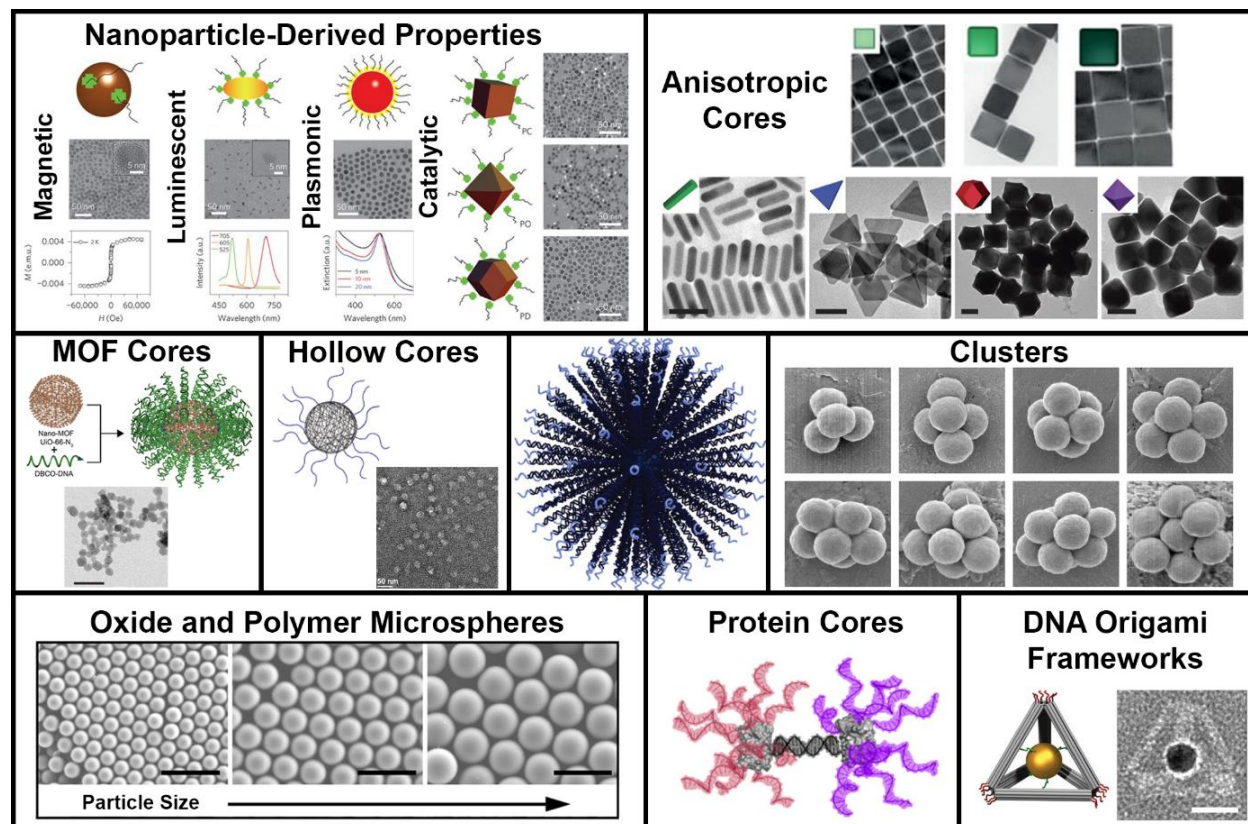
Figure 1.3: A modular nanoparticle core provides "programmable atom equivalents" with a breadth of compositions, sizes, and shapes (directional binding) yielding a wide array of different properties and characteristics. Adapted with permission.[84,92,96–102] Copyright 2010, 2011, 2013, and 2015, Springer Nature. Copyright 2014, 2015, and 2018, ACS. Copyright 2003 and 2016, AAAS.

PAEs have been synthesized on both the nanoscale (2 nm to 1,000 nm)[52,95,103] and microscale[104–106] with the same basic DNA design, and all follow the same design rules as particles in the ~10-50 nm core size regime[69,107] (Figure 1.3). The key rule that governs the crystallization of different PAE sizes is that the overall hydrodynamic radius of the PAE determines its binding behavior, not the core size alone.[78] However, at the nanoscale, the accessible size regimes are energetically limited to a "zone of crystallization" based on DNA length to NP diameter ratio.[107] Conversely, in PAEs constructed from particles at larger length

scales (e.g. ~1-3 µm), the DNA strands are often significantly shorter than the particle diameter, meaning that the particle size ultimately dictates the range of accessible lattice parameters.[104]

A majority of the NP cores in demonstrated PAEs are spherical and isotropically functionalized with DNA, as these highly symmetric constructs are easier to synthesize. However, in an effort to add more complexity to the PAE core and mirror the ability of atoms to adopt directional binding as a function of valency, several different strategies of PAE construction have been developed. First, while early work in PAE synthesis revealed multiple routes to either patchy[34] or asymmetrically functionalized particles,[108] the particles synthesized with these methods have not yet been demonstrated to form ordered crystals, and breaking the symmetry of spherical building blocks remains a challenge. Nevertheless, by functionalizing specific sites on pseudo-spherical proteins with DNA, PAEs were synthesized with tunable and precise bond distributions where both the number and direction of DNA linkages were controlled.[101,109–111] Such constructs have been demonstrated to produce arrangements that are unachievable with isotropically functionalized spheres.[101,110] It is even possible to functionalize different sites on the same protein with orthogonal DNA sticky ends, thereby yielding Janus-type PAEs that assemble into 1D crystalline chains,[111] or complex layered crystalline structures of PAEs that alternate in NP core identity (composition or size)[101] (Section 1.3.3). A second strategy to impart directional interactions between spherical particles involves trapping NPs within or at the vertices of anisotropic DNA origami constructs.[102,112,113] The 3D shapes of these structures dictate both the valency and possible binding directions of the overall construct, meaning that the shape of the contained spherical particle is separated from the factors that dictate lattice symmetry. This method enabled a non-close-packed diamond-type NP superlattice[102] and was later expounded upon using various DNA frameworks to achieve a breadth of crystalline symmetries.[112]

A separate strategy to control valency and directional binding in PAEs relies on isotropically functionalizing a non-spherical NP, such that the shaped core acts as scaffold whose local geometry enforces direction on the DNA binding groups.[114] This method is particularly promising given the wide array of synthetic protocols able to produce anisotropic NPs.[115–119] It was demonstrated that anisotropic NPs with flat faces tend to favor arrangements in which these flat faces are aligned parallel with one another in order to maximize DNA hybridization interactions, a concept understood as shape complementarity.[99] This anisotropic directing force

55

drives self-complementary plate-like NPs to form 1D chains, rods to form 2D hexagonal lamellae, cubes to from 3D simple cubic (sc) lattices, etc.[98,99,120] Shape complementarity has also been extended to include binary co-crystals of different shapes, generating crystallographic arrangements that would not be possible with other NP crystallization schemes.[99,121,122] PAEs have also recently capitalized on a synthesis method that produces clusters of spherical PS particles with well-defined arrangements.[100] Given their high stability, the clusters can then be DNA-functionalized and used as a PAE core with complex shape. This strategy not only enables PAE "reactions" between two clusters akin to molecular reactions but also is shown to produce unique crystalline symmetries[95] enabled by the shape of the cluster.[c]

1.3.2. Programming Dynamic Assemblies *via* Controlled DNA Binding

DNA was originally conceptualized as the ideal binding moiety for a PAE due to its high information content and predictable nucleobase interactions. Indeed, DNA has proven its programmability through tunable complementarity, length, binding strength, flexibility, and even dynamic manipulability. Given the molecular purity of oligonucleotide synthesis and the high persistence length of double-stranded DNA (dsDNA), the lattice parameter of a PAE crystal can be linearly controlled based on the number of base pairs that constitute a PAE-PAE bond.[123] The binding strength between PAEs is mediated by DNA sticky end sequence, number of linkers added to a PAE, and the solution's salt concentration; thus, each of these variables can be used to tune the temperature at which crystallization occurs.[80] Bond strength can even be post-synthetically increased through the use of ruthenium coordination complexes,[124] ethidium bromide,[125] or silver ion intercalators.[126] While dsDNA is relatively stiff, the flexibility of DNA strands between PAEs can be independently tuned by incorporating ssDNA bases or polyethylene glycol "flexors" to effect crystallization ability and quality[127] or alter the entropy penalty associated with PAE bond formation, which can result in alterations to PAE superlattice structure.[128]

To a great extent, the DNA corona of a PAE dictates its binding characteristics in a manner analogous to how electron orbital shape and energy dictates atomic bond formation.[1,5,6,129] The

---

[c] While a plethora of core compositions, shapes, and sizes have been demonstrated, not all compositions are currently accessible in all size regimes or in all possible NP shapes.

characteristics of the DNA corona (complementarity,[78] directionality,[99] etc.) yield consistent crystallographic symmetries in PAEs similar to orbitals dictating the final arrangement of atoms within the unit cell. One of the foremost analogies between PAEs and atoms is that both exhibit a well-defined equilibrium bond length based on a balance of repulsion and attraction (Figure 1.4). The interatomic distance between two atoms is often modeled by a Lennard-Jones potential[5,130,131] where there is an energetic minimum at a specific spacing balanced by the repulsive force of overlapping electron orbitals and the attractive force of atomic binding. Similarly, it has been shown both experimentally and through computational modeling that the interparticle spacing of binding PAEs reach an equilibrium length due to a balance of the electrostatic repulsive force between negatively charged DNA coronae and the enthalpic attractive force of maximizing DNA hybridizations.[132] Both forces can thus be modified through changing salt concentration (electrostatic shielding)[132,133] and changing sticky end binding strength, respectively.
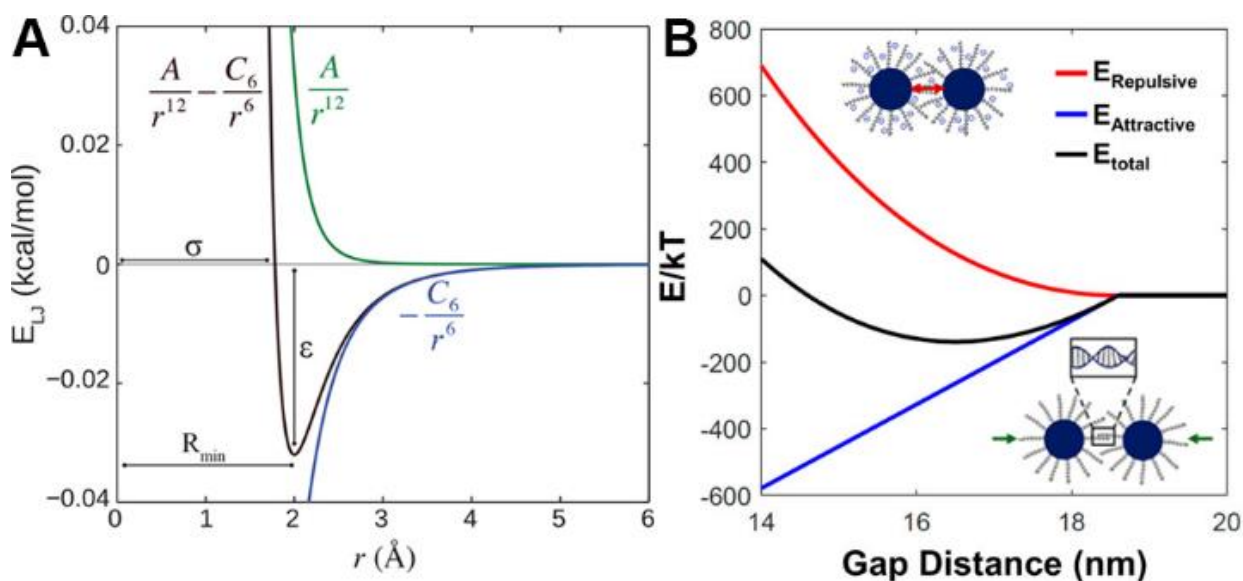
Figure 1.4: Both (A) atoms and (B) "programmable atom equivalents" analogously exhibit well-defined energy potentials based on interparticle distance, resulting in equilibrium bond lengths. Adapted with permission.[131,132] Copyright 2017, ACS.

Further investigation concerning DNA's behavior in different solution environments allows for dynamic manipulation of the DNA corona and thereby the PAE lattice. Adjusting from a phosphate buffered saline solution to ethanol causes reversible, dynamic changes in lattice parameter due to adjustments in the local dielectric constant and thus interparticle repulsion.[134]

Additionally, the addition of free water-soluble polymer to the solution causes lattices with significant regions of unpaired (and thus more flexible) ssDNA in their linkers to compress due to an increased osmotic pressure.[135] The incorporation of "i-motif" sections into the DNA linker strands allows for the PAE lattices to be adjusted as a function of solution pH, as i-motifs exhibit condensed structures at low pH and extended conformations at high pH.[136] Unfortunately, these adjustments are often small in magnitude given that the stability of a DNA double helix is restricted to a small set of solution conditions and fairly radical changes in solvent environment tend to destabilize dsDNA.[137–139]

However, the programmability of DNA base-pair sequences can induce more dramatic manipulation of PAE lattices by tailoring which bases along a DNA linker hybridize with one another. Specifically, the inclusion of DNA "hairpin" structures in the linker sections of PAEs was initially shown to reversibly and precisely toggle the lattice parameter of PAE lattices upon addition of DNA sequences to open and close the hairpin.[140,141] This motif was further developed to enable toggling between "activated" and "deactivated" states, thereby affecting both the number and nucleobase sequence of the sticky ends expressed on each particle. As a result, particle stoichiometry within a lattice, the ratio of the number of linkers contained on each PAE in a binary structure, and which PAEs were able to form bonds with one another could be reversibly altered, enabling the ability to dynamically toggle a lattice between different crystallographic symmetries.[142] It is worth noting that, although each different state of a hairpin-containing PAE mimics atomic crystallization behavior in the manners discussed here, the ability to switch this binding behavior independently of elemental composition is not possible in atomic systems. While the programmability and complexity of DNA structure allows for an individual particle to exist in multiple forms that possess distinct binding behavior, there is no way to "transmute" an individual atom to change its inherent bonding characteristics without changing its electronic structure. As a result, these hairpin-containing particles are a key example of how PAEs are more than simple nanoscale artificial atoms.

1.3.3. Programming Local Coordination within a PAE Lattice

As a result of the elucidation of the PAE crystallization design rules[107] and the development of PAEs of various shapes, sizes, and binding directionality (Section 1.3.1), a vast

library of lattice symmetries has been realized for PAE crystals (Figure 1.5).[d] While the first unit cells that were synthesized formed relatively simple fcc and bcc symmetries, the engineering of superlattice crystallographic arrangements has since broadened to include binary structures isostructural to cesium chloride (CsCl), aluminum diboride (AlB_2), chromium silicide (Cr_3Si), and an AB_6 structure that has no atomic analogue but is isostructural to the alkali-fullerene complex Cs_6C_{60}.[69,104] Importantly, mirroring binary mixtures of atoms, an entire binary phase diagram was elucidated where PAEs of differing relative sizes and amounts of linkers were found to maximize the DNA hybridization between nearest complementary neighbors and determine the energetically most stable unit cell.[69] These initial phase maps have since been refined using theoretical modeling[143,144] and extended to include stoichiometric phase behavior.[69,145] Unachievable in binary atomic unit cells, the "hollow" PAEs (Section 1.3.1) enabled the selective omission of one constituent, effectively creating sc lattices from bcc, graphite-type (omit A) or simple hexagonal (omit B) structures from AlB_2, and bcc (omit B) or 'lattice X' (omit A) – a crystallographic unit cell unique to only this system – from AB_6 symmetries.[97]

More complex functionalization of PAEs with both two different sets of linkers (one with self-complementary sticky ends and the other with sticky ends complementary to a second PAE) was shown to enable both sc and sodium chloride (NaCl) unit cells.[69] This same strategy of using multiple and orthogonally programmable DNA binding interactions was later used to create ternary lattices. This method involved first assembling a binary "parent" lattice using one set of complementary DNA sticky end interactions and later infiltrating this lattice with a third type of PAE capable of weakly binding to both parent PAEs, precisely designed so that it filled in the interstitial holes of the parent structure.[146] These ternary systems resulted in perovskite-type ABC_3 unit cells, as well as several unit cells without known atomic analogues (ABC_{12}, A_2B_3, AB_4), making these lattices the first NP-based crystal structures that were rationally designed *prior* to synthesis.

---

[d] The crystallographic symmetry of a PAE lattice is defined by only the identity and relative placement of the NP cores, as opposed to the full hydrodynamic radius of the PAE.
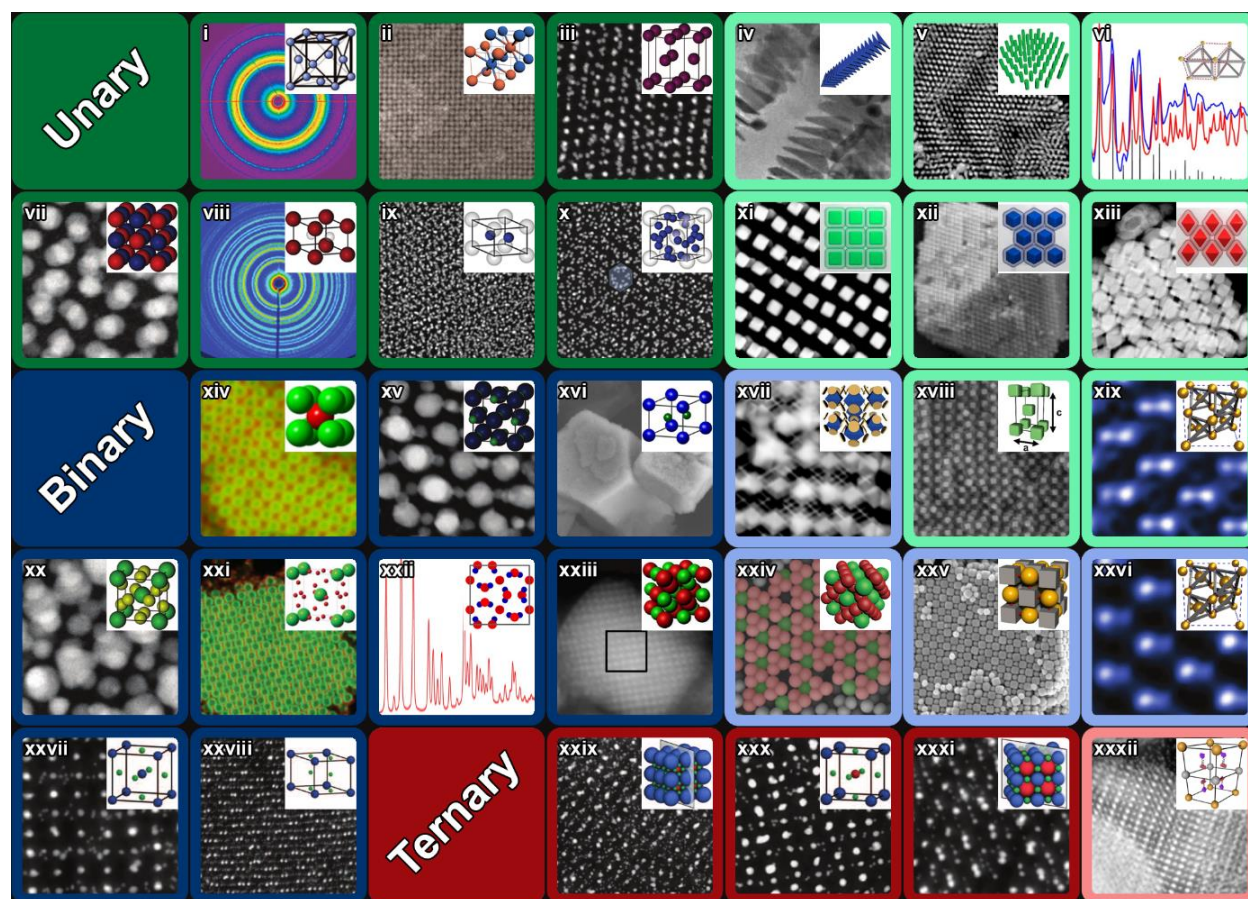
Figure 1.5: Specific and programmable binding, dictated by the DNA coronae, enables numerous crystallographic unit cell symmetries for "programmable atom equivalents," including (i) face-centered cubic (fcc), (ii) body-centered cubic (bcc), (iii) hexagonal close-packed (hcp), (iv) 1D chains, (v) 2D lamella, (vi) simple hexagonal, (vii) simple cubic (sc), (viii) simple hexagonal, (ix) graphite-type, (x) lattice X, (xi) sc, (xii) fcc, (xiii) bcc, (xiv) CsCl, (xv) NaCl, (xvi) AlB_2, (xvii) complex fcc cocrystals involving multiple particle shapes, (xviii) body-centered tetragonal (bct), (xix) diamond, (xx) Cr_3Si, (xxi) Cs_6C_{60}, (xxii) Th_3P_4, (xxiii) NaTl, (xxiv) $MgCu_2$, (xxv) NaCl, (xxvi) zinc blende, (xxvii) A_2B_3, (xxviii) AB_4, (xxix) ABC_{12}, (xxx) ABC_3 face-type perovskite, (xxxi) ABC_3 edge-type perovskite, and (xxxii) layered simple hexagonal. Unary lattices (one nanoparticle core type) are denoted in green, binary (two core types) in blue, and ternary (three core types) in red. Dark colors (left) signify lattices created using isotropic nanoparticle cores, light colors (right) signify lattices synthesized from nanoparticles with derived directional binding. Adapted with permission.[27,69,78,79,92,95,97–99,101–104,112,121–123,146–149] Copyright 2008, 2010, 2011, 2015, 2016, 2017, and 2018, Springer Nature. Copyright 2011, 2013, and 2016, AAAS. Copyright 2008, 2015, 2016, 2017, and 2018, ACS. Copyright 2016, NAS.

While the predominant driving force that dictated the thermodynamically favorable lattice structure for a given set of PAEs was initially discovered to be almost entirely an enthalpic maximization of DNA binding, it was later found that entropic effects could be increased with

flexible DNA linkers, thereby inducing self-complementary PAEs to form a bcc lattice even though this structure represents a lower packing density than the prior fcc structures that had been obtained in unary systems.[128] Making the core-core interactions appreciable in scale, one study found the binary phase isostructural to sodium-thallium (NaTl).[103] Additionally, it was discovered that higher energy unit cells could be synthesized in a kinetically trapped state under the correct conditions (e.g. hexagonal close packed (hcp) lattices form as a kinetic structure for PAEs whose thermodynamically preferred phase is fcc).[69] Another unique phase, isostructural with thorium phosphide (Th_3P_4), was isolated by changing the binding motif to one with increased "bond order" (achieved by using branching DNA strands where each linker terminated in multiple sticky ends).[149] Finally, the PAEs with programmed valency and directional binding as a result of anisotropic core shape or surface functionalization (Section 1.3.1) have exhibited several unique lattice arrangements not currently realized in PAEs with isotropic binding, namely 1D and 2D crystals,[98,111,113,120] body-centered tetragonal (bct) unit cells,[112,122] layered structures,[101] the Laves phase isostructural to dicopper magnesium ($MgCu_2$),[95] and even diamond symmetry.[102] As these more complex phases indicate, further experimental and theoretical investigations are required to garner a full understanding of the multiple different forces that are important in dictating PAE assembly. This chapter proposes the following perspective to serve as inspiration for future exploration of the DNA-grafted NP field: approaching PAE crystallization through the lens of atomic crystallization can offer insight and explanation to much of the complexity within colloidal NP crystallization.

1.4. Directly Analogizing Colloidal PAE Assembly to Atomic Crystallization

The major advantages of the PAE system in producing NP superlattices are the diversity of structures that can be synthesized and the programmability that allows for researchers to specifically dictate the lattice parameters and symmetries of the material being made. Importantly, this programmability stems from not only the predictability of DNA hybridization but also from the fact that the crystallization of PAEs can be readily explained using the wealth of knowledge that has been developed from studying atomic crystals. In contrast to early work using colloids as "artificial atoms" (Section 1.1), the formation of PAE crystals mediated by DNA binding uses localized concentrations of sticky ends that can be analogized to atomic binding *via* localized

electron orbitals. This results in lattice formation that follows fundamentally similar nucleation and growth dynamics as observed in atomic systems, as well as classical atomic materials science principals such as surface faceting, defect structures, and epitaxial deposition.

Many of these analogies were discovered by using atomic crystallization behavior as inspiration for hypotheses to investigate new PAE behavior, and the conclusions found in those studies were often explained by viewing them through the lens of known atomic behavior. However, unlike atoms whose binding characteristics are innately tied their atomic identity, modular PAEs can independently adjust individual variables to further investigate the observed phenomena in a way that is unachievable in atomic crystals, enabling more complex structure-property relationships to be developed (Section 6.4).

1.4.1. Nucleation and Growth Dynamics of PAE Lattices

Due to the similarities in binding behavior between atoms and PAEs, their crystallization dynamics are expected to follow analogous behaviors. Indeed, the "melting" temperature (T_m) of PAEs is several degrees higher than the "crystallization" temperature, as measured by UV-Vis spectroscopy.[150] This is due to a phenomena called undercooling, a form of super saturation commonly observed in atomic metals and even water.[1,151,152] There is a zone of temperatures below T_m where the driving force for nucleation is so low that crystals do not form in appreciable amounts; within this region, the free PAEs are metastable. Interestingly, the metastable zone width in the PAE system was found to be dependent on the valency of the PAE used.[150] The higher number of nearest neighbors the particle could support, the higher the energy barrier for nucleation, and therefore, the higher degree of undercooling required to induce nucleation. This is an example of a variable trait that cannot be independently studied in atomic systems where the valency of the atom is inherently tied to its identity.[5] Thus, the effect of nearest neighbor number on nucleation barrier in atomic crystals cannot be investigated without changing the constituent components and thereby introducing more variables into the nucleation behavior but, conversely, can be studied with PAEs.

A more thorough investigation of PAEs' crystallization behavior has been done with *in situ* structural analysis of crystallite size and quality during nucleation and growth. These studies demonstrated that PAEs display classic nucleation and growth behavior that has been

comprehensively explained for atomic solids, where small clusters form, reorganize into crystalline nuclei of a critical stable radius, then grow in domain size as a function of solution temperature.[153] However, these dynamics can be easily tuned by adjusting PAE characteristics (sticky end sequence, number of linkers, and salt concentration)[80] whereas atoms' behaviors are generally dictated by the valencies and bond strengths inherent to their element. Based on optical observations, it has been hypothesized that PAE crystal formation from an initial amorphous aggregate follows an "Ostwald ripening" behavior common to atomic crystallites where atoms migrate from small crystals to large crystals due to a size-dependent difference in melting temperature.[71] Molecular dynamics simulations, however, have shown behavior more akin to oriented attachment/rearrangement,[154] indicating the potential for further investigation into this complex behavior (Section 6.1).

PAE crystallization has also been experimentally shown to exhibit more complex crystallization phenomena, such as the classic time-temperature-transformation (TTT) behavior of atomic materials. TTT diagrams have a distinctive C-shape as a function of the undercooling temperature where a maximum rate of crystallization occurs at a specific temperature due to a balance of nucleation (faster at low temperatures due to larger undercooling and energetic driving force) and growth speeds (faster at high temperatures due to more thermal energy).[1] This behavior was characterized first in nanoscale PAEs using *in situ* small angle X-ray (SAXS) measurements[80] and later directly observed and mapped through optical, *in situ* imaging of micron-sized PAEs (Figure 1.6A).[104]

When a batch of PAEs is slowly cooled such that nucleation and growth occurs under equilibrium conditions, the crystallites adopt thermodynamic Wulff constructions with a controlled and predictable habit (overall faceted shape).[155] Behaving exactly like atomic crystals, the resultant shape is dominated by the slowest growing planes of the lattice, resulting in a Wulff polyhedron whose shape is characteristic to the crystallographic unit cell and planar energies.[1,156] Single PAE crystallites displaying faceting consistent with the Wulff construction have been observed for the bcc, CsCl,[155] and AlB_2[148] symmetries and for several anisotropic PAE systems[27] (Figure 1.6B). The nearly perfect crystallites only exhibited minor defects of "adatoms," ledges, kinks, and terraces on the planar faces,[148,155] which are also commonly observed in growing atomic crystals. Finding inspiration from chemical engineering studies in

63

existing crystal processing techniques used to sharpen size distributions of grown atomic crystals, recent work in the batch crystallization of PAE crystallites selectively removed those beyond a critical size with gravity to halt their growth and increase single-crystal size uniformity.[157] The process utilized a "batch crystallizer" solution of free PAEs placed above an immiscible, more dense liquid that would not allow free PAEs to disperse within it. Once crystals nucleated and grew to a critical size, gravitational forces were enough to sediment the PAE crystallites into the liquid without free particles, arresting their growth. Each of the investigations discussed in this section demonstrate that the strongest parallels between atoms and PAEs exist in this area of crystallization dynamics, allowing researchers to efficiently and effectively implement and apply the strategies used in atomic systems to control aspects of PAE crystallite size, shape, faceting, etc.
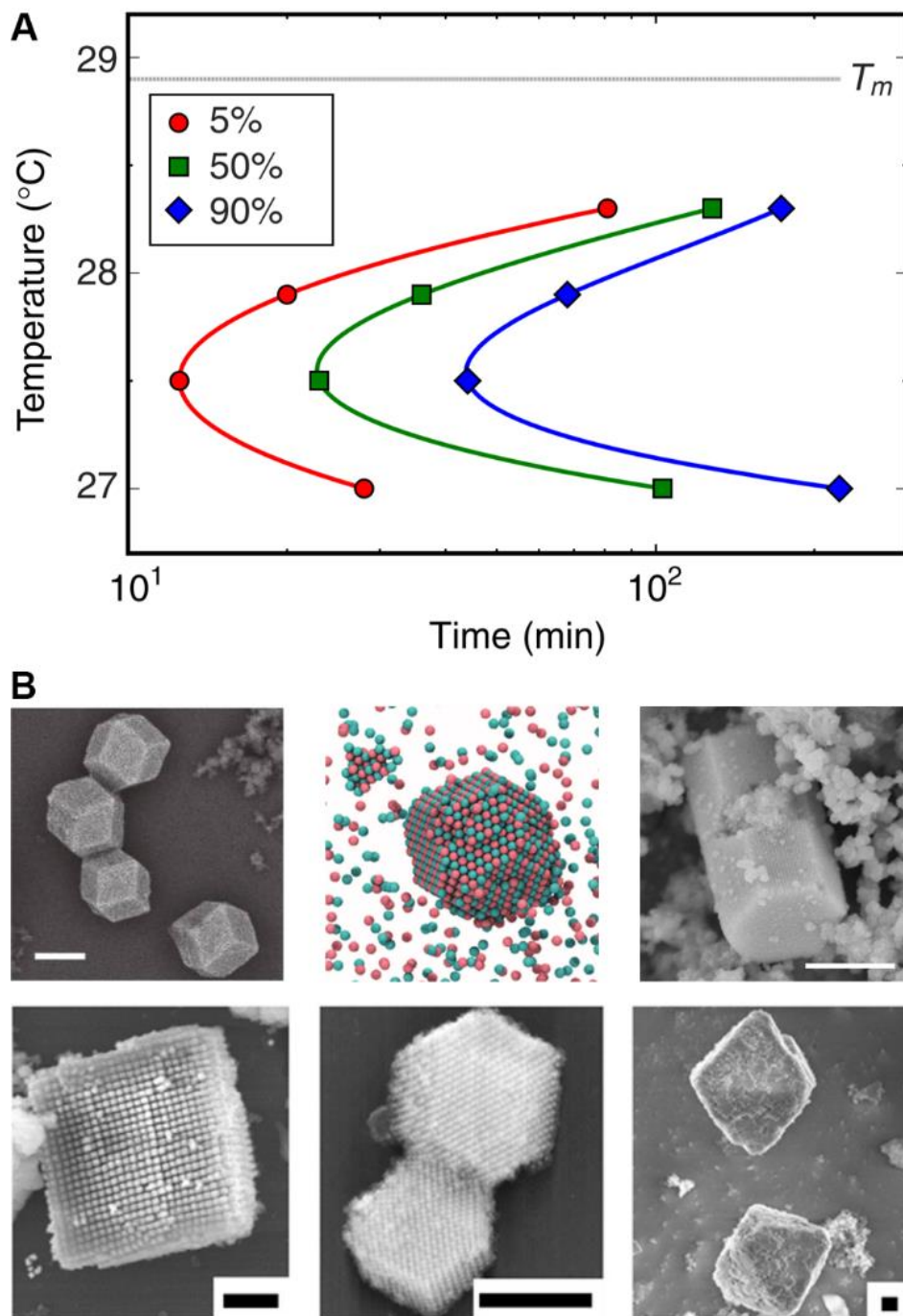
Figure 1.6: Atomic nucleation and growth behavior is mimicked by "programmable atom equivalents," resulting in (A) Time-Temperature-Transformation curves, and (B) well-defined crystallite habits based on the Wulff construction. All scale bars are 1 µm. Adapted with permission.[27,104,148,155,157] Copyright 2013, 2015, and 2018, Springer Nature. Copyright 2016 and 2018, ACS.

1.4.2. Interactions at Interfaces and Epitaxy

Behavior at a substrate surface represents an active area of research in both atomic and PAE systems due to the unique properties that arise from interfacial interactions, as well as potential applications that thin film materials enable.[24,28] In this regard, a number of studies have explored the thermodynamics and kinetics of PAE adsorption to a functionalized surface. For example, when PAE attachment onto a surface was restricted to lithographically defined gold "landing pads," adsorption that satisfies the assumptions of the atomic Langmuir model was observed.[158] Further restricting the free motion of PAEs by forcing movement through PMMA wells to reach interfacial attachment sites, PAEs kinetically followed Fick's classical law of diffusion (akin to atoms or molecules diffusing through pores)[159] and were organized into complex architectures through this strategy of template-confinement.[160] The interfacial binding strength and surface mobility of substrate-bound PAEs were found to be dependent on both PAE design features (e.g. sticky end length)[161] and substrate design features (e.g. areal DNA density)[162] with degrees of programmability difficult to attain in atomic adsorption. However, these studies were primarily limited to individual PAEs, small clusters, or monolayers.

Ultimately, the first example of bulk PAE crystallization at a surface used a method analogous to atomic layer deposition, where PAE thin films were synthesized using layer-by-layer deposition of complementary PAEs onto a flat DNA-functionalized substrate.[163] This proof-of-concept work demonstrated that the orientation of the thin film grains could be predictably controlled by the functionalization of the substrate with either one or both types of complementary sticky ends (Figure 1.7A). This preferential alignment of PAE orientation is directly mirrored in atomic thin films where grains of certain alignments relative to the substrate are energetically stabilized by it and thus dominate in the thermodynamic product.[164,165] In cases where this stabilization is extremely favorable, the depositing material will adopt the crystallographic arrangement and even lattice parameter of the substrate material in a process known as epitaxy.[166]
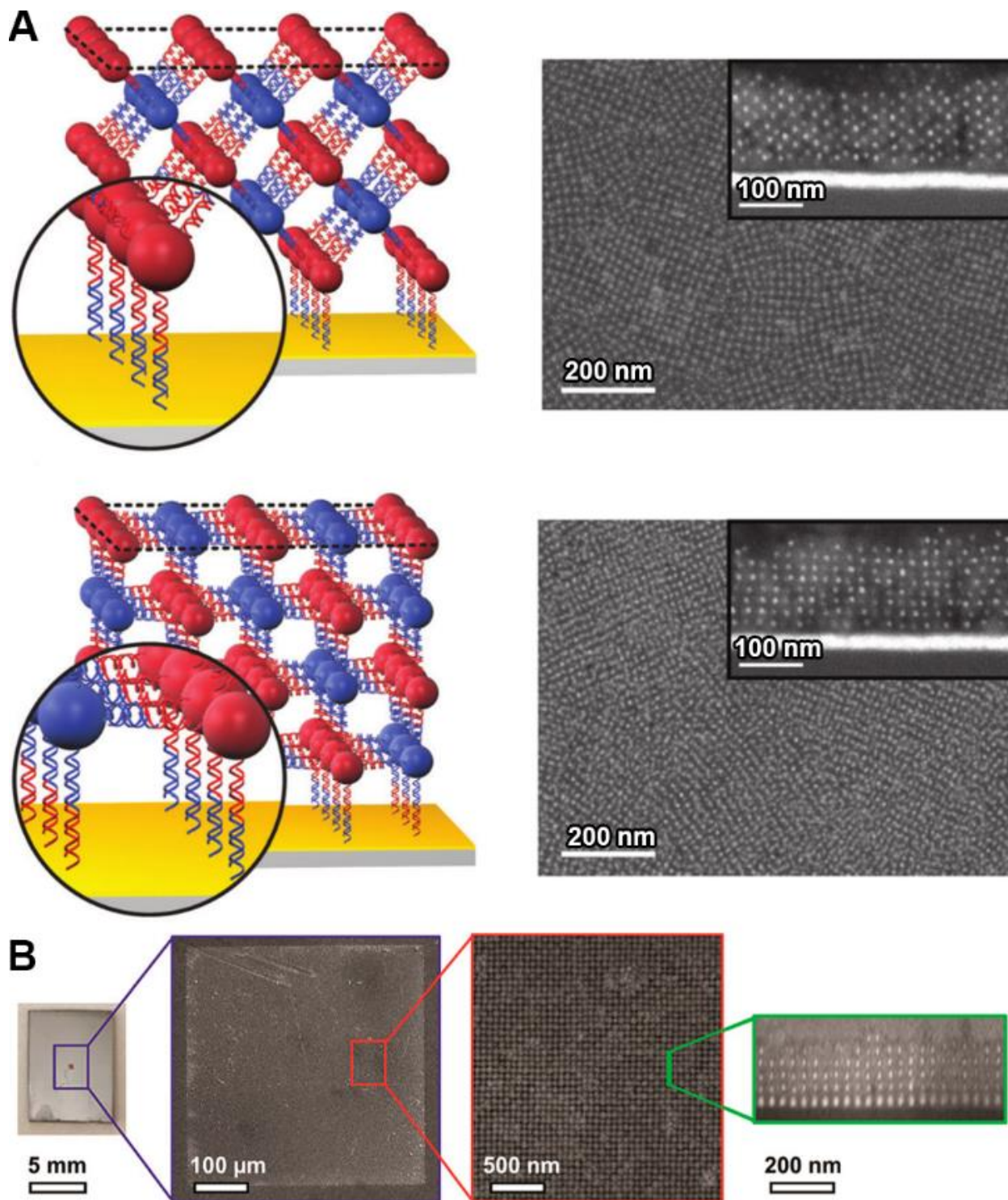
Figure 1.7: "Programmable atom equivalents" mimic atomic behavior at interfaces enabling (A) thin film crystallization and preferential grain alignment and (B) epitaxial growth. Adapted with permission.[147,163] Copyright 2013, John Wiley and Sons. Copyright 2017, ACS.

Recent advances have built upon the early work that used unpatterned surfaces by developing a platform that mimics the process of atomic epitaxy at the nanoscale with PAEs. Epitaxial deposition was demonstrated by first using lithographic patterning to produce a template of nanodots, where the shape of the nanodots was consistent with the size and shape of the deposited PAEs' NP cores, and the arrangement of the nanodots mimicked a particular crystallographic plane of the PAE lattice.[167] Following DNA functionalization of the nanodots and subsequent deposition of complementary PAEs, a layer of PAEs formed that matched the underlying patterned plane. By tailoring the structure of the lithographically defined patterning, monolayers were epitaxially grown to match the {100}, {110}, and {111} crystal planes of a bcc superlattice.[167] Later work demonstrated that subsequent rounds of deposition enabled the synthesis of a multilayer, millimeter-sized single-crystal (Figure 1.7B).[147] This proxy platform was then used to investigate the alleviation of strain due to lattice mismatch in the PAE thin films by patterning nanodots with periodicities inconsistent with the equilibrium, bulk PAE lattice parameter.[26] PAEs exhibited similar strain alleviation mechanisms as are hypothesized to occur in atomic systems,[22] including elastic relaxation and defect formation (vacancies and misfit dislocations).[26] This work also highlights a conceptual advance in controlling PAE microscale structure through combining top-down lithographic templating and bottom-up PAE self-assembly. With such a template, the overall shape of the crystallite is dictated by a set of arbitrary boundary conditions, and its size is theoretically unlimited beyond the conditions that limit the size of the pattern that can be lithographically fabricated.[147]

1.5. Conclusion

This chapter highlights the development and impacts of the "programmable atom equivalent" building block constructed from DNA-grafted NPs. Specifically, how these unique colloids mirror atomic behavior can be used as the framework of an effective strategy for the rational synthesis of hierarchical materials. DNA is arguably the most programmable directing ligand available for NP self-assembly methods due to its precise and tunable Watson-Crick base-pair hybridization. Thus, the architecture of a PAE that expresses a discrete nanoscale orientation of DNA "sticky ends" enables multivalent, cooperative binding behavior that can be used to generate crystalline arrangements of NPs that maximize DNA hybridization interactions.

Importantly, the programmability and versatility in the binding capabilities of the PAE construct is derived independently from its modular core (size, shape, and composition), allowing for this synthon to be used to synthesize multiple different materials using a single assembly strategy. Moreover, because PAEs mirror many aspects of atomic binding behavior, the principles that have been extensively examined by chemists and materials scientists can be used to explain PAE crystallization, further enhancing their use in a programmable manner. Nevertheless, while a significant amount of research has been done to begin the process of fully drawing a correlation between PAE assembly and atomic crystallization, to fully understand and utilize the PAE platform further investigation into the assembly kinetics, arbitrary control over the size and shape of the crystallites, and creation of spatial variance is required. Such research will enable both the synthesis of designer materials, as well as the use of PAEs as an atomic proxy system where behaviors that are difficult to directly observe at angstrom length scales can be more easily characterized at the nanoscale. A full understanding of the assembly process of PAEs based on the framework described in this thesis will therefore enable a new era of materials synthesis demonstrating that the "programmable atom equivalent" moniker is indeed an appropriate label for these unique nanoscale building blocks.

Chapter 2. Controlling Crystal Texture in Programmable Atom Equivalent Thin Films

CHAPTER ABSTRACT

DNA is a powerful tool in the directed assembly of nanoparticle based superlattice materials, as the predictable nature of Watson-Crick base pairing allows DNA-grafted particles to be programmably assembled into unit cells that arise from the complete control of nanoparticle coordination environment within the lattice. However, while the local environment around each nanoparticle within a superlattice can be precisely dictated, the same level of control over aspects of crystallite structure at the meso- or macro-scale (*e.g.* lattice orientation) remains challenging. This study investigates the pathway through which DNA-functionalized nanoparticles bound to a DNA-functionalized substrate reorganize upon annealing to synthesize superlattice thin films with restricted orientation. Preferential alignment with the substrate occurs due to the energetic stabilization of specific lattice planes at the substrate interface, which drives the aligned grains to nucleate more readily and grow through absorption of surrounding grains. Crystal orientation during lattice reorganization is shown to be affected by film thickness, lattice symmetry, DNA sequence, and particle design. Importantly, judicious control over these factors allows for rational manipulation over crystalline texture in bulk films. Additionally, it is shown that this level of control enables a reduction in nanoscale symmetry of preferentially aligned crystallites bound to an interface through anisotropic thermal compression upon cooling. Ultimately, this investigation highlights the remarkable interplays between nanoscale building blocks and mesoscale orientation, and expands the structure-defining capabilities of DNA-grafted nanoparticles.
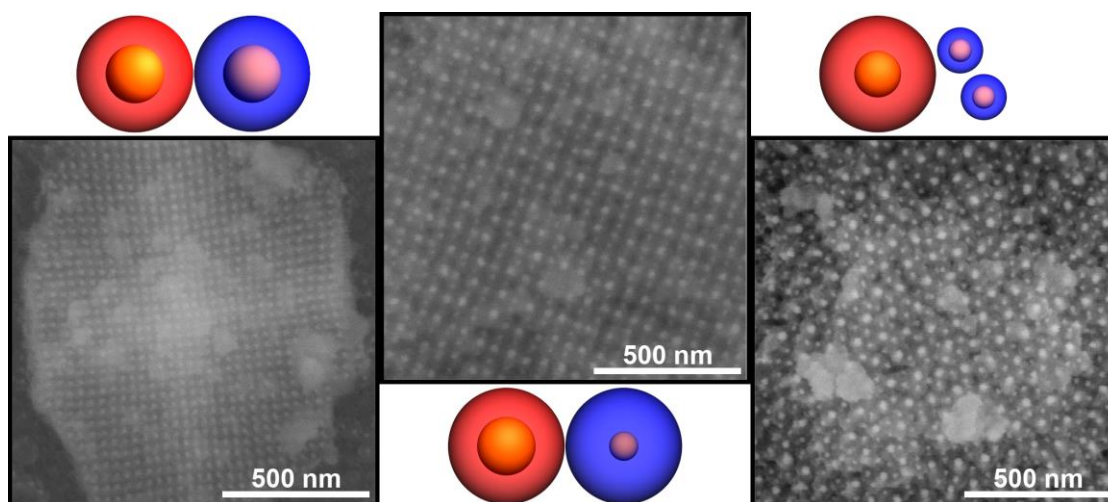
2.1. Introduction

DNA-directed nanoparticle (NP) assembly is a promising tool for materials synthesis, as the multitude of accessible particle sizes,[104,107] shapes,[95,98,121] and compositions[83,84,92] that can be made provide a large toolbox of material components,[168] and the programmability of DNA base pairing affords precise control over interparticle interactions.[69,79,112,142] A series of design rules has even been established that correlates NP and DNA design to the resulting favored crystallographic symmetry and lattice parameters.[69,104,107] Moreover, the assembly behavior of these building blocks in many ways mimics atomic and molecular crystallization, meaning that these "programmable atom equivalents" (PAEs) can draw on a wealth of established chemistry knowledge to both tailor and explain their assembly behavior.[70,104,153,168,169] As a result, PAE assembly has an incredible level of control over the coordination environment of each particle within a lattice. The next challenge for this materials synthesis technique is therefore developing methods to control aspects of material structure at length scales beyond just the crystallographic unit cell, such as crystallite size, shape, and orientation. Initial investigations into precise thermal annealing procedures have produced single-crystal structures with well-defined surface facets,[148,155] and lithographic patterning has been used to direct PAE superlattice shape using templated deposition.[147] However, these methods are typically limited to small-scale structures, and additional research is still required to make lattices with complete control over lattice macroscopic geometry. For example, there is still only a limited understanding of how to control crystal texture (orientation of crystal grains) within a bulk PAE material. In multiple proposed applications of PAE-based materials,[168,170–172] lattice orientation is a crucial determinant of structure-property relationships, and thus it is important to develop an understanding of how texture in bulk PAE superlattices arises during the crystallization process.

Nevertheless, manipulating lattice texture poses a challenging task, as fixing the orientation of a crystallite by definition necessitates controlling the overall meso- and macroscopic symmetry of the NP superlattice, resulting in a more anisotropic system. A common, and often the simplest, method of reducing the symmetry of both atomic and colloidal crystals is the introduction of an interface.[14,16,24,39,147,161,163,164,166] In atomic systems, interfaces have the ability to energetically stabilize specific crystalline orientations relative to the surface plane, causing aligned grains to nucleate and grow more readily and dominate the final structure.[164,165,173] This results in a

preferential orientation for the crystals, effectively locking one degree of rotational freedom. However, the surface energies in atomic crystals are intrinsic to the elemental composition of the crystal and substrate and thus cannot be arbitrarily modulated.[166] In contrast, the interaction potential of a PAE lattice with a DNA-functionalized substrate can use the tailorability of DNA binding to precisely program the binding specificity, functionality, and coverage of deposited PAEs,[161,163] and changes in the resulting thin film microstructure can be directly observed using various *in situ* techniques.[174,175] A preliminary study in PAE thin film growth demonstrated a simple example of DNA's programmability, where a body-centered cubic (bcc) lattice was grown with either the {001} or {011} planes parallel to the surface as a function of which DNA strands were used to bind PAEs to the substrate.[163]

While this prior result showed potential for using a substrate to control crystal growth, only one of the multiple accessible PAE superlattice crystallographic symmetries was examined. Moreover, only the thermodynamic end structure was investigated, and the rearrangement pathway to forming these crystals remains a mystery, despite the fact that this control is critical to understanding the influence of an interface on crystal formation. Significant questions therefore remain in terms of how different aspects of PAE design (*e.g.* particle size, DNA length), lattice crystal structure (*e.g.* crystallographic symmetry), and processing pathway (*e.g.* particle deposition order in a binary system) affect the crystal structure and texture at various stages of growth. The work presented here explores this unknown PAE design space where the implications of reorganization at a tailorable interface can be investigated and ultimately controlled. Specifically, we examined the *in situ* pathway of rearrangement that results in preferentially aligned thin films. Additionally, we explored the effects of reduced symmetry in PAE crystallization beyond just the introduction of an interface, specifically by altering unit cell crystallographic symmetry and using binary systems of PAEs with different interparticle and surface binding affinities. Finally, the asymmetric thermal expansion and contraction behavior exhibited by substrate-bound crystallites as a function of this ability to control crystal texture was examined, demonstrating the notable ability to dynamically alter the symmetry of a crystalline lattice when it is locked to an interface. The results presented here provide significant insight into the energetic interplay between nano- and meso-scale structural control of self-assembled NPs and broaden the ability to dictate material structure across several length scales.

2.2. Results and Discussion

PAE superlattice thin films were assembled using established synthesis protocols (see Section A.1 for full procedure).[59,163] Briefly, gold NPs were densely functionalized with oligonucleotides that each contained a short, unhybridized "sticky end." PAEs were functionalized with one of two complementary sticky ends, such that when the two complementary sets of particles were mixed together, sticky end hybridization between particles caused the PAEs to aggregate (Table A.1 and Table A.3). It has been shown that these PAEs can be thermally annealed near their melting temperature (T_m, the temperature at which assembled PAEs dissociate, see Section A.3.2), inducing their rearrangement into a crystalline lattice where the number of complementary nearest neighbors is maximized.[69,80,104] Gold-coated silicon wafers were functionalized with one set of oligonucleotide sticky ends and subsequently incubated in a solution of the complementary PAEs, resulting in the deposition of an amorphous monolayer (Scheme 2.1A and Figure A.2). Incubating the monolayer-coated substrate in a solution containing complementary particles resulted in a second layer of NPs binding to the first; this process was repeated step-wise to generate films of the desired thicknesses. It is important to note that, because these depositions were performed at ~23 ℃ (well below their T_m), the resulting films were kinetically trapped, yielding amorphous lattices containing no long-range ordering.

Once these amorphous films were deposited, their rearrangement into ordered superlattices was examined *in situ* by placing them in a temperature-controlled, solvent filled chamber in the path of a synchrotron x-ray beam, yielding high precision structural data (Section A.2.1). Small angle x-ray scattering (SAXS) patterns were subsequently collected as a function of annealing time and temperature (Scheme 2.1B and Figure A.3). In nearly all cases, the SAXS data revealed a complete transformation from amorphous (as-deposited) to fully crystalline within minutes when annealed near T_m. Importantly, the thin films were placed with the substrate normal to the x-ray beam direction such that any orientational alignment parallel to the superlattice-substrate interface was observed and characterized. Lattice alignment results in the suppression of specific scattering peaks, and the identities of the suppressed peaks are dictated by lattice orientation (Section A.4.2), which enables characterization of overall lattice texture. Finally, after the thin films reached equilibrium (determined by time-stable SAXS pattern), the samples were embedded in silica[176]

for visual characterization with scanning electron microscopy (SEM) (Section A.2.2). Additionally, some thin films were annealed for shorter amounts of time, quickly quenched, embedded, and imaged to observe changes in morphology throughout the annealing process.
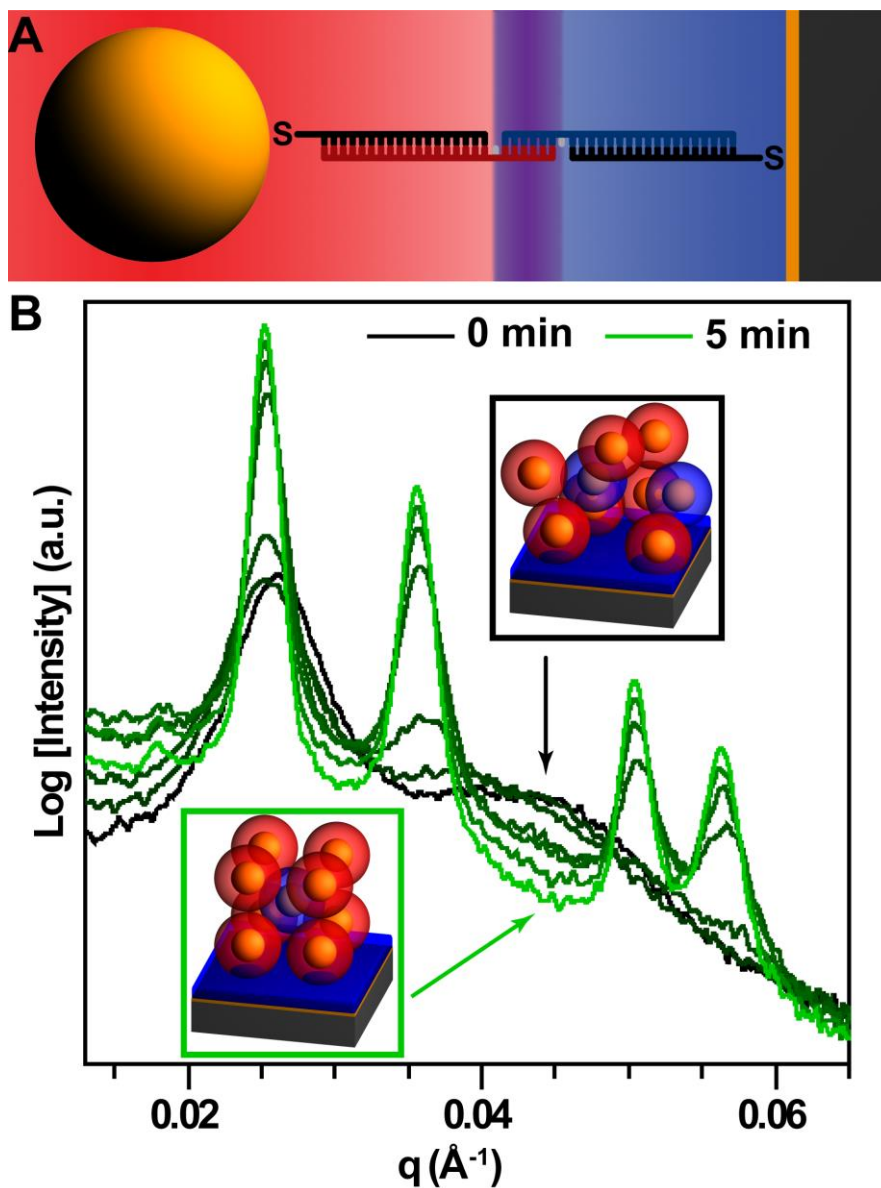
Scheme 2.1: Observing the PAE Thin Film Rearrangement Process. A) The DNA binding scheme utilizes complementary "sticky ends" to control binding. B) Time-resolved structural rearrangement of the thin film is determined through the SAXS pattern transforming from an amorphous structure (black curve and top inset) to an oriented, crystalline structure (green curve and bottom inset) upon annealing.

2.2.1. Morphological Evolution of Lattice Orientation During Crystallization

While the PAE rearrangement pathway is well understood for 3D superlattices in solution,[80] introducing an interface imposes an anisotropic constraint on crystal reorganization, meaning that PAEs may exhibit different kinetics of reorganization at the substrate interface compared to the bulk material. To examine this hypothesis, two sets of structurally identical PAEs were synthesized containing identical NP core sizes and DNA lengths, but complementary sticky end sequences (Table A.3). Previous work has shown that this type of binary PAE system rearranges into a bcc superlattice upon annealing, as this structure maximizes the total number of DNA connections between particles (Figure A.5 and Figure A.6).[69,107,163]

Initially, substrates were functionalized with only one type of sticky end (Table A.2) before depositing the PAEs, meaning that only one of the sets of PAEs in this binary system would be able to favorably bind to the substrate. Thus, after rearrangement, the {001} planes would be expected to align parallel to the interface, as the {001} arrangement is the densest-packed plane containing PAEs of only a single sticky end type. Indeed, post-rearrangement, a 5-layer thin film of PAEs was dominated by crystalline domains with the {001} planes parallel to the substrate (Scheme 2.1B), as evidenced by the suppression of the (211) scattering peak (Table A.8); this superlattice orientation noted by the SAXS data was confirmed by real-space SEM imaging (Figure A.17). This observed alignment was consistent with previously reported thermodynamic structures when depositions were done at elevated temperatures.[163]

Intriguingly, however, this 2D rearrangement process (Video S1)[177] did not follow the same pathway as the previously characterized rearrangement in 3D aggregates. Due to the presence of the substrate interface, the processes of crystal nucleation, grain growth, and melting all occurred at different rates for different crystal orientations. The percentage of grains that are {001} aligned within the thin film were quantified by comparing the relative intensity of the (211) scattering peak to the others, where an order parameter value of 1 indicated full alignment with {001} and an order parameter of 0 indicated no favored orientations (Equation A.10). This analysis clearly showed that the stabilizing impact of the substrate on {001} orientations strengthened with decreasing film thickness (Figure 2.1A, Figure A.8, Figure A.9, and Figure A.10). Tracking the order parameter throughout the rearrangement process elucidated the kinetic pathway of arriving at this preferential alignment (Figure 2.1B and Figure A.11). In PAE films with fewer than 10

76

layers, where the critical nucleus size was hypothesized to be on the order of the film thickness, aligned grains at the interface were energetically stabilized to such a degree that unaligned grains were never observed (Video S1).[177] However, above this critical thickness, grains of all orientations nucleated at the top surface of the thin film and began to grow toward the substrate (Section A.6.2). Grains in contact with the DNA-coated gold surface with the preferred {001} grain aligned parallel to the substrate were thermodynamically more stable due to the larger number of DNA connections between the (001) plane of the bcc lattices and the substrate. Thus, their net growth quickly outpaced that of the unaligned grains (Videos S2, S3, and S4).[177] In fact, given enough thermal energy, the aligned grains absorbed neighboring grains of other misaligned orientations (Figure 2.1C and D, Figure A.12, Figure A.13, and Video S5[177]). The introduction of an interface greatly stabilizes grains with preferentially aligned orientations, creating a significant difference in energies between these thermodynamically preferred grains and neighboring ones that are not aligned with substrate. Therefore, the result is a strong driving force for grain coarsening in this 2D system not previously observed in 3D systems devoid of substrate interfacial energies.
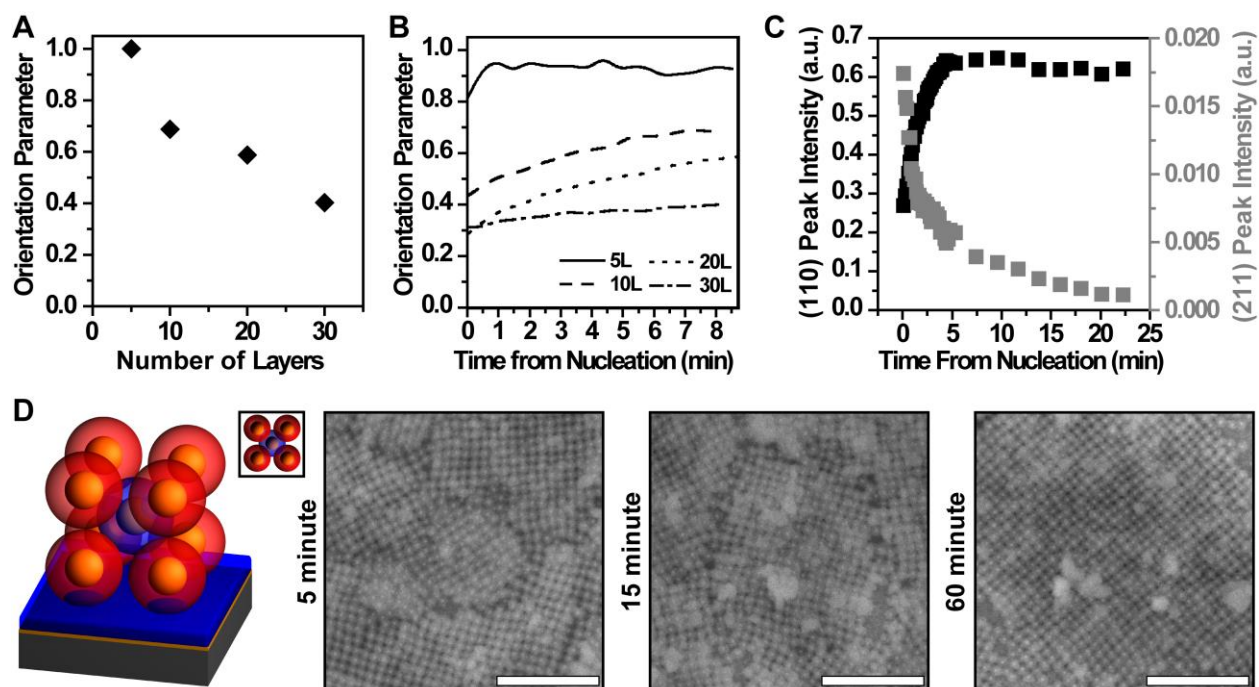
Figure 2.1: Morphological evolution of PAE thin films with "preferred alignment." A) Decreasing orientation parameter as a function of layer number reveals waning effects of interface as thickness of film increases and a critical film thickness of 5-10 layers for preferential alignment. B) Differing kinetics to final structure for films of 5, 10, 20, and 30 layer thicknesses (5L, 10L, 20L, and 30L) are observed based on different evolutions of the orientation parameter over time. C) Non-aligned grains (integrated intensity of (211) SAXS peak: grey points, right axes) are selectively eliminated over aligned grains (integrated intensity of (110) SAXS peak: black points, left axes) at higher temperatures. D) Schematic of an aligned unit cell (inset: top-down) and SEM micrographs of 5 layer films showing increasing aligned grain size over time (left to right: 5, 15, and 60 minutes). Scale bars are 500 nm.

2.2.2. Introducing Non-equivalent Substrate Binding Strength *via* Alterations to Lattice Symmetry

Prior work has shown that PAEs with identical hydrodynamic radii exhibited the same preferred thermodynamic crystal structure when assembled.[69] However, the use of two different NP core sizes alters the symmetry of the resulting unit cell, meaning that sets of complementary PAEs with identical hydrodynamic radii but different nanoparticle core sizes produce a cesium chloride-type (CsCl-type) lattice (Figure 2.2A, Figure A.5, Figure A.6, and Table A.3). Because the particle positions, number of nearest neighbors, and overall DNA connectivity were the same for these bcc and CsCl lattices, it was not surprising that CsCl thin films exhibited the same {001} alignment to the substrate as the previous bcc lattices (Figure 2.2B, Figure A.18, Figure A.23, Figure A.24, Figure A.25, Figure A.26, Table A.9, and Video S6[177]). While the absolute binding strength of PAEs attached to a complementary DNA-functionalized surface may vary as a function of particle diameter (due to the different number of DNA strands attached to PAEs with different NP core sizes, Equation A.3), the {001} planes of the CsCl lattice should always represent the densest packed arrangement of particles that can form a DNA connection to substrates functionalized with only one type of DNA linker.
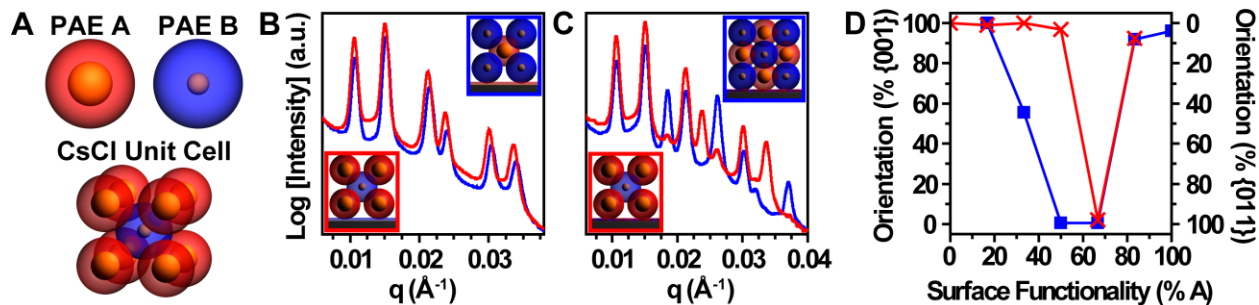
Figure 2.2: Effects of reducing unit cell symmetry to investigate non-equivalent substrate binding strengths. A) Schematic representation of A (red) vs B (blue) PAEs resulting in a CsCl unit cell structure. Final SAXS patterns of the reorganized CsCl thin films are (B) independent of deposition order (red, A first; blue, B first) when the substrates are functionalized with 100% B or 100% A DNA sticky ends, but are (C) order dependent when functionalized with 50% A, 50% B. Insets: representative cross-sections of each corresponding thin film lattice structure. D) The overall percentage of grains aligned with either {001} (left axis) or {011} (right axis) oriented to the substrate differ as a function of surface functionalization ratio of A to B DNA sticky ends.

Conversely, it was previously demonstrated that a bi-functionalized substrate with both sticky end types present at the interface would allow both PAE types to bind to the surface, thereby

generating bcc lattices with the denser {011} orientation parallel to the substrate (Figure A.15, Figure A.16, and Figure A.17).[163] Since {011} is also the closest packed plane in CsCl, a bifunctionalized substrate may also be predicted to yield {011} preferential alignment for CsCl lattices. However, because the binding strength of the different PAEs in a CsCl lattice are not equivalent, the deposition order of PAEs in this binary system had significant impact on the final texture of the superlattices. When amorphous films were deposited and the PAE with the smaller NP core (PAE B) was deposited first, the expected {011} orientation was observed after thermal annealing (Figure 2.2C, blue, and Video S8[177]). However, when amorphous films were deposited and the PAE with the larger NP core (PAE A) was deposited first, the lattices still exhibited the {001} preferential alignment observed in the monofunctionalized substrates after annealing (Figure 2.2C, red, and Video S7[177]).

       This result confirms that the two, non-identical sets of PAEs in these CsCl lattices interact differently with the interface and drive the thin film reorganization towards different end products. Because each layer of PAEs was deposited sequentially, the initial amorphous film should only have one type of particle at the interface—the PAE type that was used in the first round of deposition. The {011} plane would therefore only be expected to form if the second particle type being deposited were able to displace some of the initial monolayer of the opposite type of PAE. The differing interfacial rearrangement behavior for A and B particles was hypothesized to be caused by a stark difference in the sticky end density of the two PAE types in the CsCl structure.[107] Since the DNA on PAE B must be longer to match the overall radius of the PAE A, it will splay out to a greater degree at the PAE periphery, making the density of binding groups less than half that of the PAEs with a larger core (0.010 sticky ends per nm^2 *vs.* 0.024 sticky ends per nm^2, Equation A.3 and Table A.4). A lower sticky end density resulted in PAE B binding more weakly to the substrate and thus they should have increased mobility during crystal annealing compared to PAE A.[161,174] Altering the assembly behavior of PAEs with different substrate affinities therefore necessitated altering the surface chemistry of the substrate to control the relative binding strengths of the two PAE types. To examine this hypothesis, several substrates were functionalized with a breadth of surface functionalities ranging from 100% A sticky ends to 100% B sticky ends (Table A.2). It was previously shown in bcc lattices that as the surface functionalization was modulated from 100:0 to 50:50 mixtures of complementary ligands, the thin

films formed grains that were {001}- and {011}-aligned, respectively, with a mixture of the two orientations at intermediate ligand mixtures (Figure A.15, Figure A.16, and Figure A.17).[163] In contrast, the CsCl system explored here displayed distinctly different distributions of {001} and {011} alignment based on the nanoparticle deposition order (Figure 2.2D, Figure A.23, Figure A.24, Figure A.25, Figure A.26, Equation A.11, Equation A.12, and Equation A.13).

Specifically, when the low-sticky-end-density PAE B was deposited first, it was more readily displaced, resulting in a fairly symmetric distribution of orientations as a function of surface functionality. Conversely, when the strongly-bound PAE A was deposited first, the final structure only contained {011} aligned lattices when the relative density of A-complementary sticky ends was approximately half the density of B-complementary sticky ends. In other words, the increased sticky end density on PAE A resulted in an increased affinity to the substrate, meaning that it could only be displaced when the number of sticky ends at the interface to which PAE A could bind was radically reduced. Therefore, in this lower symmetry CsCl system, the deposition order of the non-equivalent PAE A and B had a strong impact on the overall lattice texture, and lattice alignment could be tuned by controlling the relative PAE-substrate binding potentials.

2.2.3. Introducing Variations in Stoichiometry *via* Utilizing a Hexagonal Unit Cell

The programmability of the PAE building block allows the superlattice unit cell symmetry to be tailored to lower symmetry arrangements than the cubic bcc or CsCl type lattices, including a lattice with a hexagonal unit cell that is isostructural with aluminum diboride (AlB_2).[69,104] In this hexagonal lattice, the PAEs have both different numbers of DNA strands attached to their surfaces, as well as different overall hydrodynamic radii (Figure 2.3A and Table A.3). As a result, the two particles in an AlB_2 lattice have different coordination environments, relative binding strengths to the substrate, and number of particles per unit cell. Moreover, the hexagonal unit cell is less symmetric than the cubic unit cells examined above, with an overall unit cell c/a ratio that is typically ~0.7 - 0.85.[69] It could therefore be expected that the reorganization of an AlB_2-type lattice at a surface would show even stronger anisotropy in its crystallization compared with the cubic lattices examined previously.
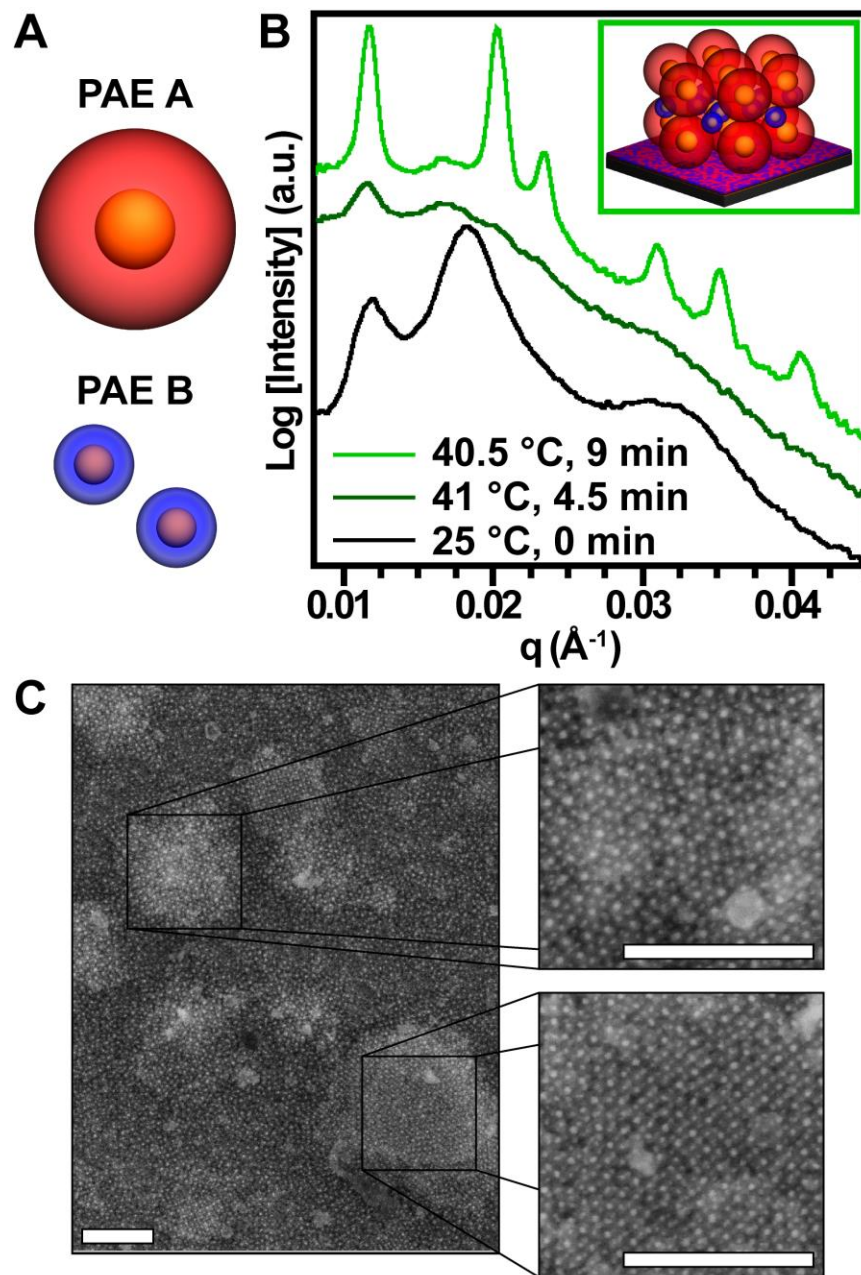
Figure 2.3: Effects of local stoichiometry and PAEs of different hydrodynamic sizes. A) Schematic representation of PAEs capable of creating a hexagonal, AlB_2 lattice. B) These PAEs exhibit a distinctive 'fluidic' (dark green curve) state characterized by very little presence of structural peaks in SAXS during their reorganization to AlB_2 grains with {001} alignment parallel to the substrate. C) As evidenced by the SEM micrographs, upon cooling, the thin film crystallizes into distinct grains of hexagonal, AlB_2 {001} aligned grains (top right) and cubic, CsCl {011} aligned grains (bottom right) surrounded by glassy regions. All scale bars are 500 nm.

In the case of a mono-functionalized surface, the PAE lattice was hypothesized to preferentially align with the hexagonal close-packed {001} plane parallel to the interface, given that it is the most densely-packed single-particle-type plane in the unit cell; this alignment was indeed observed using SAXS (Figure 2.3B, Figure A.27, Figure A.29, and Table A.10). In fact, the SAXS data indicated that {001}-oriented AlB_2 grains were exclusively observed in the thin films, even when the surface was functionalized with DNA linkers complementary to both types of particles (Figure A.29), irrespective of particle deposition order. This result was likely due to both the increased binding strength of the larger PAE, as well as the fact that the hexagonal close-packed arrangement of larger PAEs (PAE A) in the {001} plane represented a significantly denser packing than any other potential lattice plane, even when considering the possibility of both particles binding to the substrate.

Interestingly, despite their significant differences in PAE design, the precursor structures to CsCl and AlB_2 lattices were strikingly similar prior to thermal annealing (Figure A.5, Figure A.6, Figure A.22, and Figure A.28). However, the reorganization process for this AlB_2 PAE system exhibited several notable differences to the previous bcc and CsCl systems. In both the bcc and CsCl cases, the broad peaks corresponding to the initial short-range ordering were observed to gradually sharpen into the long-range ordered, crystalline peaks without significant alteration to the peak positions (Scheme 2.1B, Videos S1 and S6[177]), and reorganization was induced at temperatures relatively low compared to T_m (Table A.5). This indicated that the particle coordination environment in the initial, short-range ordered structures was similar enough to the final long-range ordered bcc or CsCl lattices that particles could easily rearrange into the thermodynamically preferred crystal state.[153] Conversely, in the AlB_2 cases, nearly all the short-range order was lost before crystalline, long-range order appeared (*i.e.* the broad amorphous peaks disappeared nearly completely before sharp crystalline peaks arose) (Figure 2.3B, Figure A.36, and Video S9[177]), and the AlB_2 reorganization into crystalline order only occurred in a very narrow temperature window immediately below T_m (Table A.5). Moreover, during this reorganization process, the macroscopic thin film appeared "molten" by visual inspection, as the mass of PAEs at the surface slowly flowed down a vertically aligned substrate under the influence of gravity, without fully breaking up the lattice and releasing large quantities of PAEs into solution. Together, these observations implied that the local ordering of PAEs in the initial amorphous

sample was significantly different than the AlB_2 lattice and required greater amounts of reorganization to achieve an ordered state. Thus, AlB_2 reorganization was more challenging compared to bcc or CsCl systems, explaining the narrow thermal window in which crystallization was observed. At temperatures immediately below the lattice T_m, PAEs were able to crystallize because in the initial stages of reorganization they were essentially behaving as a viscous fluid where individual particles were only weakly tethered to their neighbors. This fluidic state allowed for significantly increased PAE mobility, enabling the large amount of restructuring needed to form the AlB_2 lattices.

Although only AlB_2 lattices with the {001} planes parallel to the substrate were observed at the end of the annealing process, when the films were subsequently cooled to room temperature, a new SAXS peak clearly arose at a new scattering angle that did not correlate to an AlB_2 structure (Figure A.35 and Figure A.36). However, this peak was consistent with the {110} peak for a CsCl crystal of 53nm lattice parameter, which would be the expected lattice spacing for a CsCl lattice made with these PAEs (Figure A.37). Morphological inspection of the reorganized thin films using SEM confirmed an unanticipated combination of {001}-aligned AlB_2 crystalline regions, as well as both {011}-oriented CsCl crystals and large disordered regions (Figure 2.3C, Figure A.30, Figure A.31, Figure A.32, Figure A.33, and Figure A.34). It is important to note that the PAE design used here was close to the phase boundary for CsCl and AlB_2 lattices.[69,145] The ability for a binary PAE design that exists near a phase boundary to simultaneously exhibit two stable crystallographic symmetries has been demonstrated previously in non-surface-bound PAE crystallites by changing the relative stoichiometric ratios between the A and B particles.[69,142,145] As the ratio neared 1:1, CsCl was favored, while AlB_2 was favored as the relative amount of B PAEs was increased. This was previously explained as a result of the energetic penalties of vacancies in the AlB_2 lattice making the CsCl lattice more favored when using close to a 1:1 ratio of A- and B-type PAEs. Thus, the presence of these CsCl and amorphous regions that were only observed after cooling the system can be explained as a function of local differences in particle stoichiometry induced by the reorganization process.

Given the nature of layer-by-layer PAE deposition, there was no inherent control over the stoichiometric ratio between A and B PAEs in the initial amorphous films. SAXS data of these initial structures can be used to confirm that the A and B particle types existed in a 1:0.96 ratio

84

(Figure A.38 and Figure A.39), not the ideal 1:2 ratio for an AlB_2 structure. Therefore, in order to form an AlB_2 lattice, localized exclusion of the excess A-type PAEs was required to achieve the ideal 1:2 stoichiometric ratio. This PAE positional reorganization was significantly enhanced in a molten, fluidic state, resulting in the localized accumulation or depletion of PAE types. Once the superlattice is cooled, regions of the substrate that are near a 1:1 ratio began to form CsCl-type lattices. As a result, while the {001} oriented AlB_2 lattice was the thermodynamically preferred state for these thin films, the inherent non-uniform stoichiometry of the final structure meant that different symmetries were stabilized in localized regions on the surface. The ability of the surface to stabilize the less-thermodynamically stable {011} CsCl lattices can be enhanced as a function of which DNA linker strands were attached to the substrate. Specifically, bi-functionalized substrates were observed to contain a higher prevalence of CsCl regions than mono-functionalized ones. This observation was consistent with the hypothesis that such a surface energetically stabilized the more densely packed {011}-plane of CsCl as opposed to any bi-particle plane in AlB_2, further making CsCl symmetries more thermodynamically accessible when limited amounts of B-type PAEs were present. Finally, even with the same particle designs, the AlB_2 and CsCl arrangements would be expected to have different unit cell energies[69,145] and thus slightly different crystallization temperatures, accounting for the observation that CsCl only crystallized in this system upon cooling. Overall, the AlB_2 system further expounds upon the concept that asymmetry in PAE design can dictate the millimeter scale crystal texture of an entire thin film of PAE crystallites.

2.2.4. Asymmetric Thermal Contraction of Surface-Bound PAE Crystallites

Previous work on solution-dispersed PAE superlattices has demonstrated that PAE crystallites exhibited temperature-dependent lattice parameters, with larger interparticle distances at higher temperatures. The soft, deformable DNA corona around each PAE swelled and contracted as a function of solution temperature, leading to up to 10% shrinkage in unit cell dimensions for certain PAE designs when cooling from ~45 to ~22 °C.[107] When PAEs were not bound to a substrate, this lattice contraction was isotropic, as the spherical PAEs decreased in diameter uniformly due to their highly symmetric shape and the ability of all DNA strands to expand or condense equally. However, the introduction of a boundary condition like a DNA-

functionalized surface changes these interactions, as the DNA strands tethered to the substrate are significantly less mobile, and contraction of the lattice parameters for the plane of particles bound to the substrate would require a significant number of PAE-substrate DNA connections to be broken.[161,174] This reduced mobility of the first layer of PAEs bound to a substrate would be predicted to prevent (or at least limit) lattice compression in the directions parallel to the DNA-functionalized surface, meaning that the contraction of the DNA brush around each PAE would generate a significant amount of strain that could only be alleviated by expansion or contraction in the direction perpendicular to the surface.

To test this hypothesis, a bcc thin film with all crystallites {001} oriented was cooled from its rearrangement temperature (48.5°C) to room temperature (25°C) over several minutes while monitoring the SAXS pattern (Figure 2.4A and Table A.8). Strikingly, this SAXS pattern showed no change in either the positions or quality of the peaks during cooling. While the lack of change in observed PAE superlattice structure could indicate that there is no change in the interparticle spacing of the superlattice, previous work[26,174] suggested that it would be unlikely that the PAEs would store ~10% strain within the crystal without some disruption of crystal structure. However, since the x-ray beam used to scan these samples was perpendicular to the substrate, the SAXS pattern was only reflective of structure in the planes parallel to the interface. In other words, every peak that has any l-character (*e.g.* the (211) peak) was suppressed. Therefore, it was possible that the ~10% strain in this system was alleviated by breaking lattice symmetry and compressing the lattice *only* in the direction perpendicular to the substrate. Because none of the peaks observed in superlattices with the {001} orientation parallel to the surface (*e.g.* (110), (200), (220), *etc.*) have any l-character, any expansion or contraction that occurred strictly normal to the substrate would be unobservable. However, these SAXS data did confirm that the in-plane lattice parameters of these crystallites remained unchanged during cooling, indicating that the introduction of a boundary condition *via* the DNA-functionalized surface did indeed pin the bottom layer of the PAE superlattice in place when cooling for these samples.
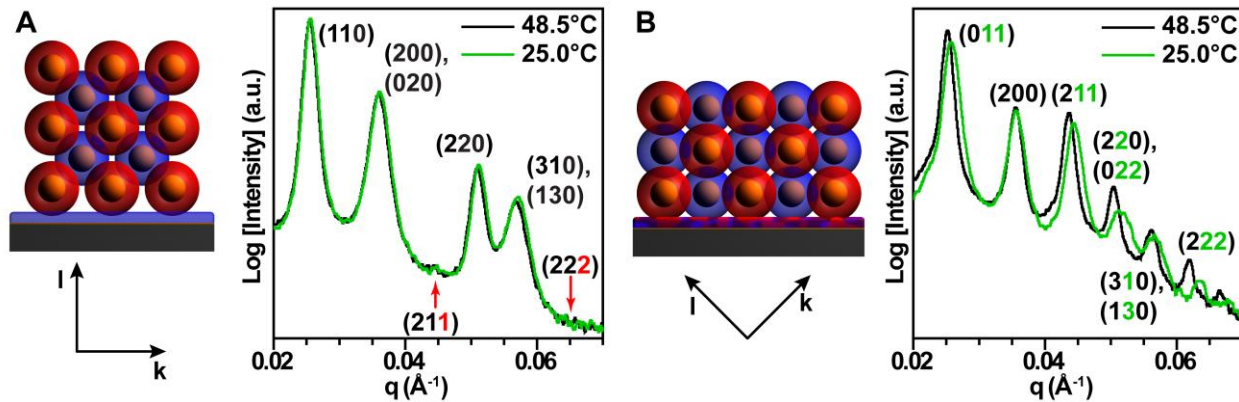
Figure 2.4: Schematic representations of (A) {001}-oriented and (B) {011}-oriented bcc crystals bound to a substrate with defined h, k, and l directions and correspondingly indexed SAXS patterns reveal asymmetric shrinkage upon cooling. (A) Peaks with l-character (red index numbers) are suppressed because the l direction is parallel to the x-ray beam direction. (B) Peaks with k- and/or l-character (green index numbers) shift or broaden dependent upon the amount of k- and l-character in its constituent peak(s) because the compression occurs in the combined k and l direction.

To further explore the hypothesized anisotropic compression, a bi-functionalized interface that enforces a {011} orientation was used. Aligning the PAE lattices in this orientation meant that any changes in the direction perpendicular to the substrate were now a combination of the l and k crystal directions, while only the h-direction remained in-plane. Monitoring substrate-bound {011}-oriented crystallites during cooling yielded a SAXS pattern that was altered with temperature (Figure 2.4B and Table A.8). Every peak with k- and/or l-character shifted in the expected *q*-direction with temperature-driven compression, while the (200) peak that has only h-character remained constant. This further corroborates the notion that the interface held the PAEs in the lattice direction parallel to the substrate stable, driving the crystallites to asymmetrically densify in the other lattice planes when the temperature was lowered, thereby breaking lattice symmetry to create a tetragonal unit cell shape in the {001}-oriented case and a monoclinic shape in the {011} case.[26] The morphological results of this phenomena can be directly observed in the SEM micrographs of the final thin film structure (Figure A.17). Importantly, this finding highlights that the interface remains an important (and anisotropic) driving force not just during reorganization, but during all processing of the PAE crystallites while they are still bound to the substrate. This anisotropic compression phenomena warrants deeper exploration in the future.

2.3. Conclusion

The work presented herein reveals the powerful influence the introduction of an interface can have on PAE superlattices. A substrate, based on its functionalization, will energetically stabilize some crystal orientations over others, allowing them to nucleate and grow more readily and result in a mesoscale structure containing a preferred crystal texture. Additionally, in binary systems where each PAE has differing interfacial binding affinities, the entire mesoscale orientation can be controlled as a function of processing conditions. Finally, substrate-bound PAE crystallites will exhibit unusual, asymmetric behavior due to the anisotropic directing force an interface provides. Ultimately, better understanding how orientation control is programmable through interfacial interactions and how nanoscale and mesoscale structure are interconnected in these systems moves the field one step toward realizing total structural control across many length scales with colloidal materials.

2.4. Methods and Experimental

Detailed descriptions of the methods can be found in the Supporting Information (Appendix A); a brief discussion is provided here for reference.

2.4.1. Synthesis and Fabrication of PAE Thin Films

Gold NPs were synthesized using an established seeded growth protocol where $HAuCl_4:3H_2O$ was rapidly added to a boiling solution of trisodium citrate dihydrate (Section A.1.1). NPs were characterized using a JEOL 2010 Advanced High Performance TEM and ImageJ. Oligonucleotides (Table A.1) were either purchased from Integrated DNA Technologies or synthesized using standard manufacturer protocols and reagents from Glen Research on a Mermade 48 DNA synthesizer (BioAutomation) (Section A.1.2). If synthesized, oligonucleotides were characterized by MALDI-TOS-MS. PAEs were synthesized by functionalizing Gold NPs with a dense shell of thiol-modified "anchor strand" DNA using gold-sulfur chemistry and salt aging and purifying using centrifugation (Section A.1.3). "Linker strands" of DNA were then hybridized to the anchor strands to yield the PAE construct, whose concentration was then determined by UV-Visible Spectroscopy.

Using standard fabrication techniques at the Materials Technology Laboratory at MIT, silicon wafers had 2 nm chromium then 8 nm gold deposited on them using an AJA eBeam

evaporator (Section A.1.4). Functionalization of the substrate with DNA was performed in a similar fashion as attaching DNA to the gold NPs. Finally, layer-by-layer deposition was done by successive incubation (1 hour, 25 °C, 1,000 rpm on an Eppendorf Thermomixer) of the functionalized substrate in alternating 10 nM binary PAE solutions for the desired number of layers (Section A.1.5).

2.4.2. Instrumentation and Data Collection

In-situ SAXS data collection was done at the 12ID-B station at the Advanced Photon Source at Argonne National Laboratory (14keV x-rays) (Section A.2.1). Scattered radiation was detected using a Pilatus 2M detector, calibrated with a silver behenate standard, and radially averaged for analysis. Samples were placed in a vertical, temperature-controlled, solvent-filled chamber such that the thin film was perpendicular to the x-ray beam direction. Samples were ramped to their bulk melting temperature and held, sampling every 30 seconds (moving down the substrate to avoid beam damage) until the SAXS pattern stabilized.

After embedding the thin films in silica using a sol-gel process requiring the addition of *N*-(trimethoxysilyl)-propyl-*N,N,N*-trimethylammonium chloride followed by triethoxysilane, SEM micrographs were collected on the solid state films using a Zeiss SEM (Section A.2.2). Cross-section micrographs were imaged following focused ion beam milling on a Helios Nanolab 600. Characterization of the bulk behavior of each PAE system (Table A.3) was conducted in the Center for Materials Science and Engineering at MIT. Bulk melting temperature of PAE aggregates was determined by monitoring the absorbance at 520 nm during a slow temperature ramp on a Cary 5000 UV-Visible Spectrometer (Section A.3.2). Bulk crystallography of the PAE systems was determined through SAXS of free, slow-cooled (Techne Prime Thermal Cycler) crystallites on a SAXSLab system.

Chapter 3. Epitaxy: Programmable Atom Equivalents *versus* Atoms

CHAPTER ABSTRACT

The programmability of DNA makes it an attractive structure-directing ligand for the assembly of nanoparticle (NP) superlattices in a manner that mimics many aspects of atomic crystallization. However, the synthesis of multilayer single crystals of defined size remains a challenge. Though previous studies considered lattice mismatch as the major limiting factor for multilayer assembly, thin film growth depends on many interlinked variables. Here, a more comprehensive approach is taken to study fundamental elements, such as the growth temperature and the thermodynamics of interfacial energetics, to achieve epitaxial growth of nanoparticle thin films. Both surface morphology and internal thin film structure are examined to provide an understanding of particle attachment and reorganization during growth. Under equilibrium conditions, single crystalline, multilayer thin films can be synthesized over 500×500 µm^2 areas on lithographically patterned templates, whereas deposition under kinetic conditions leads to the rapid growth of glassy films. Importantly, these superlattices follow the same patterns of crystal growth demonstrated in atomic thin film deposition, allowing these processes to be understood in the context of well-studied atomic epitaxy, and enabling a nanoscale model to study fundamental crystallization processes. Through understanding the role of epitaxy as a driving force for nanoparticle assembly, we are able to realize 3D architectures of arbitrary domain geometry and size.
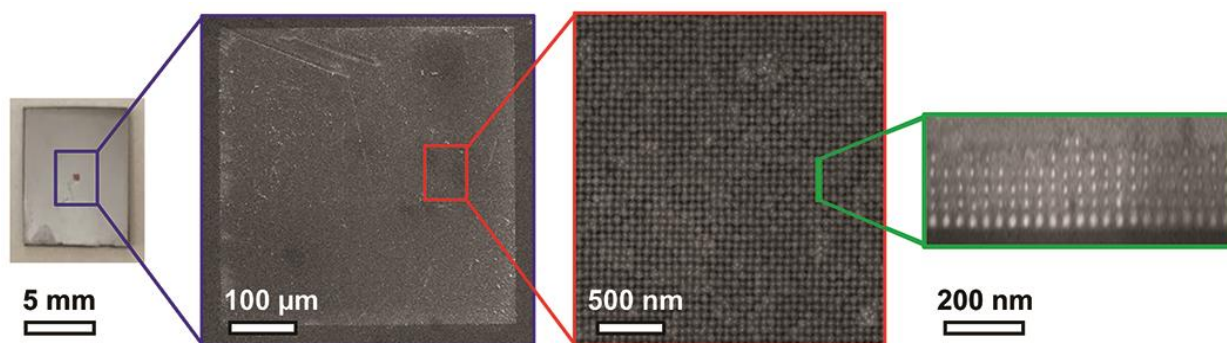
3.1. Introduction

The epitaxial deposition of thin films has been key to the semiconductor industry in its efforts to control material properties as a function of crystal structure. The transfer of order and orientation from a substrate to a deposited crystal is dependent upon many interlinked variables (*e.g.* interfacial chemical potential, crystal lattice parameters, defect stability) that vary as a function of both atomic composition and deposition protocol.[166,178,179] As a result, significant effort has been expended to fully understand atomic epitaxy, leading to a wealth of information about thin film crystallization behavior. For nanoscale systems, many strategies have also been developed to assemble nanomaterials into thin films;[16,180–183] however, these methods often lack the ability to precisely control the overall 3D structure of the resulting crystals (*e.g.* size, shape, and orientation).

Recent developments in NP assembly have shown that NPs functionalized with a dense monolayer of oligonucleotides can form ordered superlattice structures with programmable lattice parameters and crystallographic symmetries, and these building blocks exhibit many crystallization behaviors similar to those observed in atomic systems.[69,78,99] These "programmable atom equivalents" (PAEs), therefore hold promise for tailoring material structure at the nanoscale in a precise and controllable manner. In the context of PAE thin films, assembly on unpatterned surfaces has been demonstrated to produce rough, polycrystalline films with lack of long-range order or alignment.[163] Assembly of nanoparticles on patterned substrates has also been attempted, but was limited to only monolayers of single crystalline thin films, as the combination of both NP-substrate and NP-NP binding events significantly increases the complexity of multilayer epitaxial crystal formation.[16,167,184] In order to fully control thin film morphology in PAE superlattices, these complexities must be better understood *via* investigations into the thermodynamics of lattice growth as a function of different variables. The fundamental information gained from these comprehensive studies provides the opportunity to not only develop superlattice morphologies with complex 3D structures, but also has the potential to provide insight into the process of atomic thin film epitaxy.

Like atomic systems, there are many design parameters that can affect multilayer epitaxy, such as factors inherent to the deposition protocol (*e.g.* thermal annealing temperature) and factors

dictated by PAE design (*e.g.* DNA hybridization strength).[69,80,163] However, unlike atomic epitaxy where only the deposition protocol can be modulated, parameters related to the individual PAE building blocks can be precisely controlled as a function of DNA,[69,78,163] particle,[83–85,185] or substrate pattern design.[167] Fully understanding how PAE epitaxy can be manipulated as a function of these variables will potentially yield single-crystal superlattices with controlled 3D geometries, allowing for the realization of materials possessing desired optical,[71,186,187] electronic,[188] and magnetic responses.[45] Here, we report a stepwise method for synthesizing large epitaxial thin films of PAEs up to 10 layers thick and 500 µm wide and show that the corresponding growth process mimics atomic thin film epitaxy, allowing us to study epitaxy as a driving force for building a nanomaterial as it evolves from a 2D monolayer to a 3D crystal lattice.

Scheme 3.1: Layer-by-layer assembly of PAE superlattice thin films on a DNA-functionalized template.

3.2. Results and Discussion

Epitaxial growth of NP superlattices was realized by depositing PAEs layer-by-layer onto lithographically defined substrates designed to resemble a continuous (100) plane of a body-centered cubic (bcc) lattice (Scheme 3.1). Using standard electron-beam lithography (EBL) techniques, 500 µm × 500 µm arrays of gold posts were synthesized on a silicon wafer, such that post diameters and post-to-post distances were comparable to the PAE NP core diameters and the lattice parameter of the superlattice. These posts were functionalized with DNA and hybridized with complementary DNA linkers that presented a single-stranded recognition region to which PAEs could bind. Stepwise thin film growth was done *via* successive immersion of the template into suspensions of PAEs displaying a single-stranded recognition region complementary to that of the previous layer. They were then embedded in silica and characterized by synchrotron-based small-angle X-ray scattering (SAXS, Figure 3.1 middle row) and grazing incidence small-angle

93

X-ray scattering (GISAXS, Figure B.4) to determine overall degree of epitaxy.[189] Lattices were also examined by scanning electron microscopy (SEM, Figure 3.1 top row), which allowed for real-space imaging of superlattice surface morphology; focused ion beam milling was used to etch selected sections of the silica-embedded lattices, allowing for SEM characterization of internal structure (FIB-SEM, Figure 3.1 bottom row).
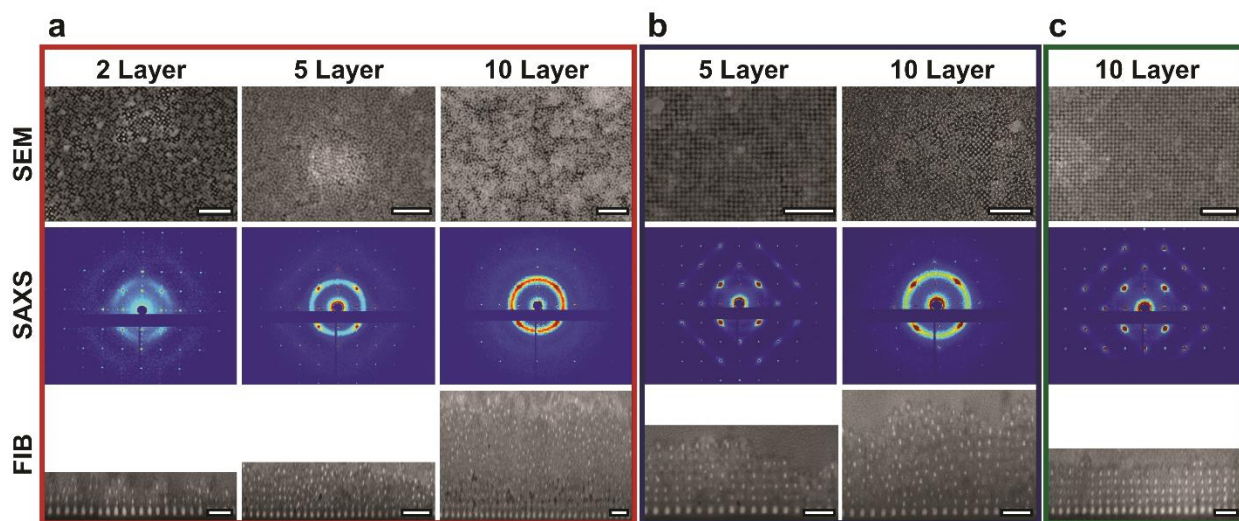
Figure 3.1: SEM, SAXS, and FIB-SEM characterization of DNA-NP thin films. a) 2, 5, and 10-layer DNA-NP thin films assembled at 25 °C exhibit kinetic roughening and non-epitaxial growth beyond 4 layers of deposited PAEs. b) 5 and 10-layer DNA-NP thin films assembled at 25 °C and thermally annealed after the full deposition process demonstrate enhanced ordering, but only the 5-layer sample is fully epitaxial since only PAEs that are close to the initial 4 epitaxial layers experience sufficient driving force to align with the patterned template. c) A 10-layer DNA-NP thin film where each layer is assembled at an elevated temperature; this process produces smooth, crystalline thin films fully epitaxial with the patterned substrate. Scale bars for SEM and FIB-SEM are 500 nm and 200 nm, respectively.

3.2.1. Far-From-Equilibrium Deposition

We first investigated the deposition of particles onto templated substrates *via* far-from-equilibrium conditions (*i.e.* low growth temperature) to understand the effectiveness of the EBL-patterned template itself as a driving force for multilayer epitaxy. When compared to atomic systems, this low temperature deposition is analogous to chemical bath deposition, where atoms rapidly precipitate from solution, resulting in disordered materials.[190] Here, when conducting templated PAE deposition at 25 °C, initial layers conform epitaxially to the substrate, but subsequent layers transition to a kinetically roughened, glass-like state (Figure 3.1a). This can be

observed in the SAXS data, where a sample with 2 deposited layers shows diffraction spots (corresponding to aligned, single crystal bcc lattices), while 5 and 10-layer films exhibit diffuse scattering, corresponding to disordered PAE aggregates. The relative degree of epitaxy (X_A) at each layer was determined by comparing the SAXS intensity of the spots from the (110) peak of the epitaxial PAEs and the intensity of the diffuse ring (Figure B.1), where an X_A value of 1 indicates complete epitaxy of the PAEs; the value of X_A decays from 0.99 to 0.88 after 5 layers, and to 0.65 at 10 layers (Figure 3.2a). This was corroborated by the FIB-SEM cross-sectional images, which showed that the first few layers of all samples are indeed epitaxial, up to a critical layer number of ~4, with PAEs above the critical layer adopting a kinetic, glassy state (Figure 3.1a bottom row and Figure B.2). This is a morphological transition commonly observed in atomic thin films, which exhibit temperature-dependent surface roughening when the adsorption rate is faster than the reorganization rate.[179] Similarly, PAEs adsorbed at low temperature are stuck in kinetic traps, leading to an accumulation of defects in the film, which increases the surface area available for the subsequent NPs to bind. This results in amorphous, rough films; the root-mean-squared roughness (R_{RMS}) increases by 140% from 2 to 10-layer deposited films (Table B.2). The rapid, nonlinear increase in height, as measured by the mean z-distance of top-most nanoparticles from the substrate, is further indication of non-equilibrium growth (Figure 3.2b). These data clearly show that the EBL template does serve as a strong driving force for epitaxy, but this driving force rapidly decays with increasing layer number when lattices are assembled at non-equilibrium conditions.
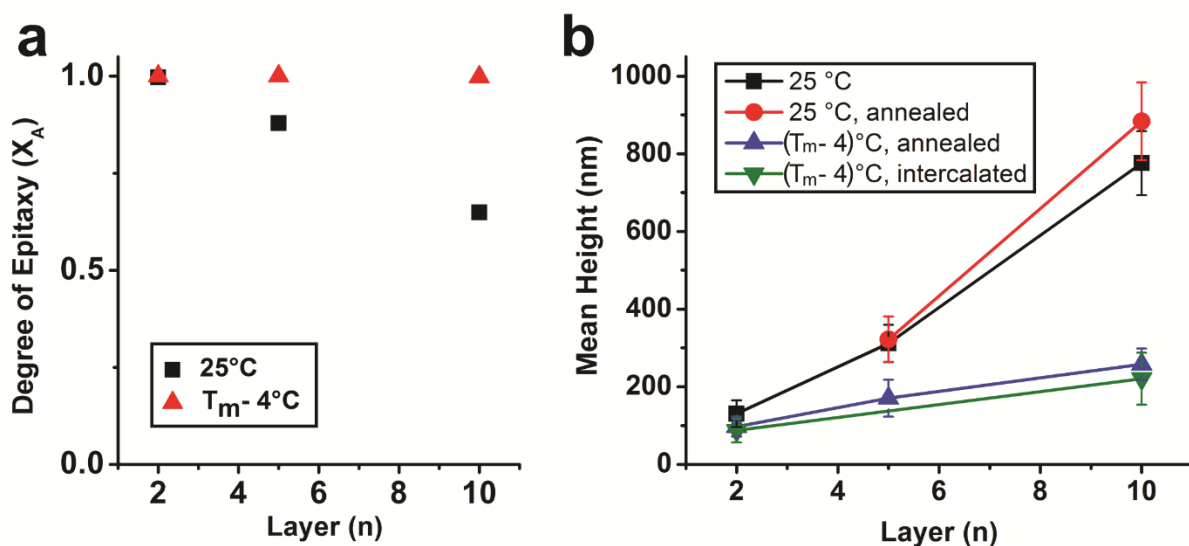
Figure 3.2: Quantitative characterization of films shows that depositing PAEs at near-equilibrium conditions induces a) higher degree of epitaxy (as determined by SAXS) and b) more controlled growth and a smoother film morphology (as determined from FIB-SEM).

3.2.2. Thermal Annealing of Epitaxial Thin Films

It is possible to reorganize thin films into more thermodynamically preferred configurations by adding thermal energy. This is done frequently in atomic systems to turn disordered or polycrystalline thin films (*e.g.* from sputter coating) into a film with a single crystal orientation. This annealing process was mirrored in the PAE system by first depositing 5 and 10 layers at 25 °C and then heating the sample slightly below the film's melting temperature (T_m, the temperature at which the superlattice dissociates). Interestingly, in the process of determining the films' T_m, it was observed that they exhibit thickness-dependent melting point depression, analogous to atomic thin film systems (Figure B.3). The thermal stability of the film, measured by monitoring lattice decomposition using SAXS, showed a concomitant increase with thickness, due to the decreasing surface-to-volume ratio, as described by Lindemann's criterion and the Gibbs-Thomson relationship. Upon annealing the samples at (T_m–2) °C, the 5-layer film became crystalline and epitaxial while retaining the same height and R_{RMS} (Table B.2). On the other hand, the 10-layer sample became crystalline, but not epitaxial (Figure 3.1b). This is most likely due to the fact that the previously observed critical layer thickness for epitaxy is ~4, indicating that, in the 5-layer sample, only the top-most layers of nanoparticles were disordered. The differences in

epitaxy for these two samples mirror previous findings for non-epitaxial PAE systems, in which post-assembly annealing is capable of inducing crystallization, but grain boundaries are difficult to remove once formed.[80]

3.2.3. Near-Equilibrium Deposition

The greatest degree of ordering in thin films can be achieved when the entire deposition process occurs under near-equilibrium conditions. To achieve this in atomic systems, molecular beam epitaxy is performed at high temperatures where deposition and desorption occur at equivalent rates, allowing each adatom to find its thermodynamic position in the monolayer before the next layer is introduced. To achieve this effect in the PAE system, each layer was deposited at an optimized growth temperature, $(T_m–4)$ °C. With this method, nearly perfect Frank-van der Merwe (layer-by-layer) growth was observed, with films remaining epitaxial ($X_A = 0.99$) far beyond the critical layer thickness of room temperature growth (Figure 3.1c and Figure 3.2a). Film cross-sections examined with FIB-SEM show smooth surfaces with an absence of kinetic roughening; the R_{RMS} of the 10-layer film is 51% less than that of the equivalent film assembled at 25 °C (Table B.2). Film height increases linearly with deposition layer, indicating that deposition occurred under equilibrium conditions (Figure 3.2b). Both GISAXS and SAXS confirmed that the film is well-ordered over a large area and nearly completely epitaxial with the patterned template (Figure 3.1c middle row and Figure B.4). Notably, a loss of radial broadening in the SAXS pattern, corroborated by FIB-SEM, indicates that as the film grows from 2 to 5 layers, the stability of the PAE network increases to such a point that the particles become locked within a single domain. The appearance of thin lines of diffuse scattering between the peaks originates from the vibrational motion of the particles (Figure B.5 and Figure B.6). This equilibrium growth condition was therefore able to create a crystalline film of well-defined and arbitrary crystal habit that is epitaxial over a domain of 500 µm (Figure 3.3 and Figure B.7).
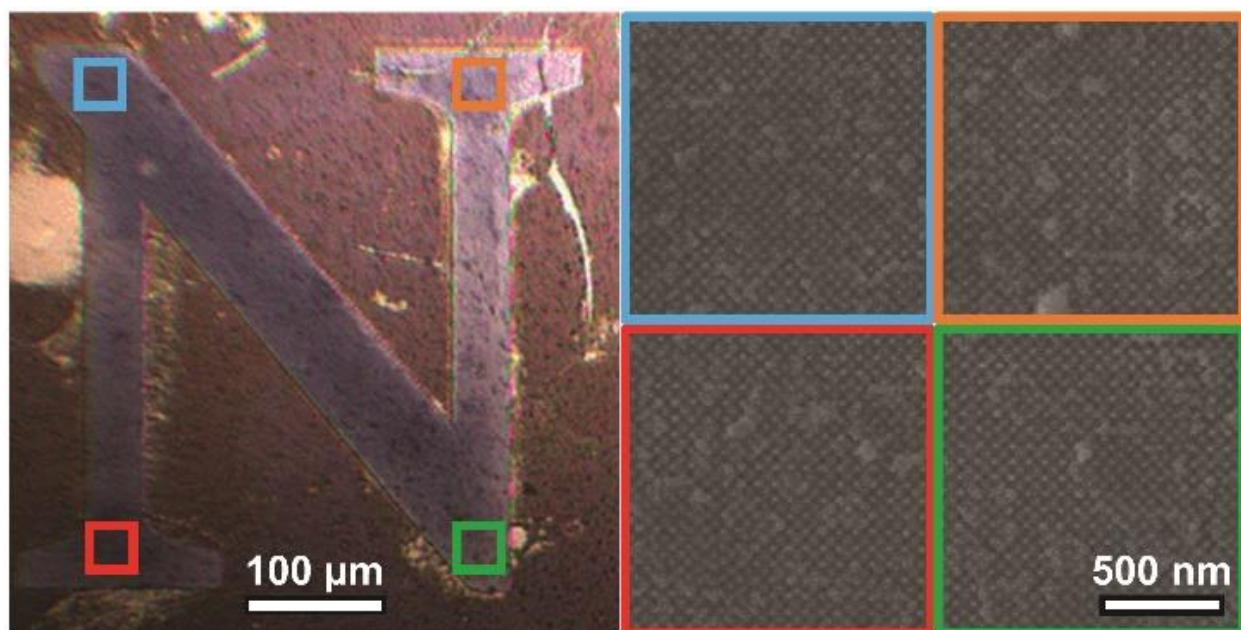
Figure 3.3: Optical image of DNA-functionalized nanoparticle thin film grown from a template exhibiting an arbitrary geometry. SEM images show that the thin film possesses the same crystallographic orientation across the entire structure.

Finally, an interesting aspect of this PAE system that does not have an atomic analogue is the ability to tune interfacial potential. In atomic crystals, chemical potentials between adatoms and the substrate are influenced by atomic identity and crystallographic symmetry. However, in PAEs, the chemical potential between NPs and the substrate can be tuned by adjusting DNA bond strength; we have recently demonstrated that this can be accomplished after assembly using DNA intercalators.[124,125] Here, these intercalators can be used to "staple" each PAE layer after deposition and annealing, thereby increasing their binding strength and preventing reorganization during subsequent cycles of growth. When this stapling method was employed, 10-layer thin films exhibited similarly high epitaxy ($X_A = 0.99$) but 66% higher R_{RMS} than the non-intercalated counterpart, which can be attributed to defect immobilization by the intercalators (Table B.2, Figure B.2, and Figure B.8). These data and the observed thickness-dependent melting point depression indicate that thermal annealing after each round of deposition induces reorganization not only in the top-most layer of PAEs, but also in sub-surface layers. This reorganization is critical for achieving perfect epitaxy, indicating the importance of being able to precisely modulate PAE binding strength during deposition.

98

3.3. Conclusion

In this work, we have determined that DNA-mediated nanoparticle crystallization follows similar thin film growth processes that are observed in atomic thin films, but importantly PAEs offer a set of parameters distinct from atomic systems that can be independently tuned to control crystallization outcome. Unlike atomic systems, the epitaxy can be controlled lithographically and through the choice of oligonucleotide bonding elements. These observations allow one to grow precisely defined crystalline nanoparticle architectures of arbitrary shape and size over thousands of μm^2. Future studies will be able to take advantage of the tunable nature of the bonding interactions between the PAEs and the substrate to investigate how different parameters (DNA sequence, grafting density of DNA on PAEs) affect the epitaxial deposition process, laying the ground work for making functional device architectures from crystalline nanoparticle networks.

3.4. Methods and Experimental

3.4.1. DNA Functionalization of Gold Nanoparticles

DNA functionalization on gold nanoparticles (20 nm diameter from Ted Pella) was done using previously described methods.[69,124] The 3' propyl-mercaptan protecting group of the thiolated DNA (Table B.1) was cleaved with 100 mM dithiolthreitol (Sigma Aldrich) for 1 hour, followed by desalting on a NAP5 size exclusion column (GE Healthcare). The deprotected DNA was combined with colloidal gold nanoparticles in a ratio of 6 nmole of DNA per 1 mL of gold colloid. After a 30-minute incubation, 1 wt% sodium dodecyl sulfate was added to bring the solution concentration to 0.01 %. 5 M NaCl was added stepwise, followed by 10 seconds of sonication after each salt addition, until the final concentration of 0.5 M NaCl was achieved. The solution was then allowed to incubate in a shaker overnight to maximize the DNA loading (140 rpm, 37 °C). Unbound DNA and excess salt were removed by 4 successive rounds of centrifugation and resuspension in nanopure water using a 100 kDa filter centrifuge tube (Millipore) on a swinging bucket centrifuge (2500 rpm, 5 minutes). After the last round of centrifugation, the DNA-NPs were concentrated down to the total volume of 500 μL. The concentrations of resulting AuNPs were determined using absorbance measured on a Cary 5000 UV-Vis-NIR spectrophotometer (Agilent) and known extinction coefficients from Ted Pella.

3.4.2. Substrate Preparation and Functionalization

3.4.2.1. Patterned Template Synthesis

Si wafers with native oxide (<100>, B doped, 10Ω•cm (Silicon Quest International)) were cleaned (2-minute acetone rinse, 2-minute methanol rinse, drying under nitrogen) and baked for 2 minutes at 180 °C. PMMA resist (495-A4) was spun onto the wafers (3500 rpm for 60 seconds) and post-baked (5 minutes at 180 °C). Once cooled, 950-A2 PMMA resist was spun coat onto the coated wafers at 3500 rpm for 1 minute to create a bilayer and post-baked (5 minutes at 180 °C). EBL was used to write the desired pattern with an optimized beam current (500 pA to 700 pA) and dose range (640 to 15000 uC/cm^2). The substrates were developed in cold MIBK:IPA in a 1:3 ratio for 60 seconds, briefly rinsed in IPA, and dried under nitrogen. The posts were then deposited using an electron-beam evaporator: 3 nm of Cr at a rate of 0.5 Å/sec followed by 30 nm of Au at a rate of 1 Å/sec. Wafers were then diced into pieces with one pattern per chip. Liftoff was done in heated (100-150 °C) PG Remover (Microchem); the chips were then rinsed (acetone followed by IPA) and finally dried under nitrogen.

3.4.2.2. Silanization of Patterned Templates

A hydrophobic hexamethyldisilazane (HMDS, Sigma-Aldrich) coating was employed to prevent non-specific adsorption of DNA-NPs to the silicon chip, so that DNA-NP assembly occurred only on the DNA-functionalized Au posts of the template. This is a widely used vapor coating technique where the Si of HMDS reacts to form a strong bond with the oxidized silicon, creating a hydrophobic surface. Substrates were pre-baked in a Vulcan 3-550 Burnout Furnace for 1 hour at 150-200 °C to remove adsorbed water molecules. Silanization was performed by incubating the pre-baked substrates in a sealed, dry chamber with a small open beaker containing 5 mL of HMDS and 5 mL of anhydrous hexane (Sigma-Aldrich) for 24 hours. After 24 hours, the substrates were rinsed and sonicated in water or ethanol for a few seconds.

3.4.2.3. Unpatterned Substrate Preparation

Unpatterned substrates were prepared by depositing a 2 nm Cr adhesion layer followed by 8 nm of Au on Si wafers using a PVD 75 E-beam evaporator (Kurt J. Lesker) at a base pressure of 5×10^{-8} Torr. Cr and Au were evaporated at the rates of 0.3 Å/sec and 0.5 Å/sec, respectively.

These conditions yielded a smooth Au film, which is crucial for the crystalline DNA-NP thin film growth.

3.4.2.4. Substrate DNA Functionalization

DNA functionalization of the patterned substrates were done by incubating each substrate in 2 mL Eppendorf Tubes (Fisher Scientific) containing 5 µM HS-A DNA solution diluted in Buffer A (0.5 M NaCl, 10 mM phosphate buffered saline (PBS)) overnight. The propyl-mercaptan protecting group on the thiolated DNA was cleaved prior to the functionalization, as described above. The substrates were then washed 3 times in Buffer A with vigorous agitation to remove unbound DNA and then hybridized with "linker" sequences (Table B.1). "Linkers" consist of one complementary section that hybridizes to the thiolated DNA sequence, two double-stranded "duplexed" regions, and a short single-stranded sticky end. To prepare the duplexed linker stocks (100 µM), "duplexer" strands were added to Linker A and Linker B in a 2:1 molar ratio in 0.5 M NaCl. The linkers were heated up to 70 °C for 5 minutes and cooled down to room temperature over 4 hours to achieve full hybridization. Duplexed linker stock solutions of 100 µM concentration were made fresh every few weeks. Complementary linker (Linker A) was hybridized to the DNA-functionalized substrate by incubating substrates in 0.5 µM duplexed Linker A solution at 0.5 M NaCl at 35 °C for 4 hours. Prior to layer-by-layer growth of DNA-NPs, the substrates were rinsed 5 times in Buffer A.

3.4.3. Layer-by-Layer DNA-Nanoparticle Superlattice Thin Film Assembly

3.4.3.1. Determining the Thin Film Annealing Temperature

To find the appropriate annealing temperature for the DNA-NP thin films, it is first necessary to determine the T_m of DNA-NP aggregates. Although the thermal melting and desorption behaviors are slightly different for solution-phase aggregates *versus* thin films, the T_m DNA-NP aggregates can be used as a quick way to inform thin film assembly and annealing temperature. Nanoparticle superlattice aggregates were prepared by mixing 0.5 pmole of DNA-functionalized 20 nm AuNPs (HS-A and HS-B) and 400 equivalents per particle of each duplexed linker in a final concentration of 0.5M NaCl at room temperature. Assembly was mediated by the complementary pendant "sticky ends" displayed on the linkers. After allowing the sample to aggregate over 5-10 min, the thermal melting behavior was monitored using a Cary 5000 UV-Vis-

NIR spectrophotometer. The extinction of the solution was monitored at 520 and 260 nm while the solution was heated from 25 °C to 60 °C at a ramp rate of 0.25 °C/min and T_m is calculated from the point of inflection of the melting curve. Typically, reorganization and crystallization can be achieved by annealing a thin film superlattice at 2 °C below $T_{m, aggregate}$ for 15 min. This is experimentally determined by confirming the crystallinity of annealed DNA-NP thin films grown on unpatterned substrates using SEM (Figure B.9).

3.4.3.2. DNA-NP Superlattice Thin Film Assembly

"A" and "B" type DNA-NP assembly solutions were made by hybridizing each type of NP with its corresponding linker DNA (duplexed as described above) at 400 linkers per NP and incubated at 35 °C for 5 minutes. The NPs were subsequently diluted to 1 nM concentration (0.5 M NaCl, 10 mM PBS) and used for 5 layers of PAE assembly. DNA-NP superlattices were grown from the patterned substrates in a layer-by-layer fashion using four different growth conditions: **1.** low temperature growth, **2.** low temperature growth followed by annealing step, **3.** elevated temperature growth, and **4.** same condition as **3** with an intercalation step after each annealing step. Intercalator solution was prepared by diluting [Ru(dipyrido[3,2-a:2',3'-c]phenazine)(4,4'-dimethyl-2,2'-bipyridine)$_2$](Cl)$_2$ in 10 mM PBS buffer. This compound was synthesized according to previously reported methods.[191] For further details on the individual growth conditions, see Table B.3. Layer-by-layer assembly was accomplished in the following way. Substrates functionalized with "A" type DNA were incubated in a suspension of "B" type DNA-NPs for 4 hours. Then, the substrates were washed 5 times in Buffer A and immersed in "A" type DNA functionalized AuNP for 4 hours. This constituted two layers of DNA-NPs. For the annealing step, the substrate was incubated in Buffer A at an elevated temperature for 15 minutes. This process was repeated until the desired number of layers was achieved. After reaching the desired layer numbers, the samples were stored in Buffer A at 25 °C.

3.4.4. Silica Embedding

In order to transfer liquid-phase thin film superlattices to solid-state for characterization by SEM and GISAXS while preserving the structure, samples were embedded in silica using a sol-gel process.[192] First, 3 µL of *N*-trimethoxysilylpropyl-*N*, *N*, *N*-trimethylammonium chloride (TMSPA, Gelest, 50% in methanol) was added to the thin film superlattices in 1 mL of Buffer A

and left to fully associate with the DNA bonds within the superlattices for 30 minutes on an Eppendorf Thermomixer R (1400 rpm, 25 °C). Then, 5 µL of triethoxysilane (Sigma Aldrich) was added and the sample was shaken for another 30 minutes before taken out. The samples were rinsed with running water, sonicated for a few seconds, and blown dry with N_2. In the case of unsuccessful silica embedding, NPs will dissociate during the rinsing step. In order to prevent such failure, it is crucial to use dry, relatively fresh silane solutions (stored in a desiccator).

3.4.5. Small Angle X-Ray Scattering

All SAXS and GISAXS experiments were conducted at the 12ID-B station at the Advanced Photon Source (APS) at Argonne National Laboratory. The samples were probed using 14 keV (0.8856 Å) X-rays and the sample-to-detector distance was calibrated with a silver behenate standard. The beam was collimated using two sets of slits and a pinhole was used. The beam size was ~ 200 µm × 50 µm. Scattered radiation was detected using Pilatus 2M detector.

3.4.5.1. SAXS Experimental Conditions

Unembedded samples were probed using a vertical sample holder made from two cover slips that allowed a buffered environment to be maintained around the sample to preserve DNA hybridization. Embedded samples were mounted on a horizontal sample holder allowing for movement in the in-plane direction (normal to the beam). Sector averaging of diffraction patterns was used to determine degree of epitaxy (Figure B.1).

3.4.5.2. Grazing Incidence SAXS

Embedded samples were aligned to the beam on a sample positioning stage in the x (parallel to the beam), y, z (normal to the substrate), theta (rotation around the y-axis), and phi (rotation around the x-axis) directions. The center of rotation and tilt of the sample was aligned with that of the stage. Data was collected at incident angles of 0.1°. After alignment of the sample, scans were taken at several chi angles (rotation around the z-axis). In depth information about GISAXS analysis is available from Senesi *et al.*,[163] and Li *et al.*[189] GISAXS scattering patterns of 5 and 10 layer films (Figure B.4) were indexed to bcc crystals with (100) orientation corresponding to space group I4/mmm (#139).

3.4.6. Focused Ion Beam-Scanning Electron Microscopy

After embedding samples in silica, a representative cross-section SEM image of each sample was obtained on a Helios Nanolab 600 Dual Beam Focused Ion Beam Milling System with a 52° relative difference between ion and electron beam. Scheme B.1 shows the cross section bcc crystallographic orientations obtained by FIB-SEM. After depositing a layer of titanium over the area of interest, a 15 µm × 1 µm area, aligned lengthwise with the (100) followed by the (110) plane of the superlattice, was milled with a 93 pA (30 kV) ion beam. Each cross-section was imaged with an 86 pA (5 kV) electron beam using the in-lens detector on the SEM, without using software's tilt correction. Post-image collection, SEM images of the cross-sections were lengthened in the y-direction by the appropriate factor to account for the tilt. Data analysis on cross-sections was done for entire 15 µm cross-section; the larger image was subsequently cropped to a representative section and included in the figures for qualitative reference. Degree of epitaxy was determined using Photoshop and Matlab to track the positions of internal PAEs relative to the positions of the templated posts (Figure B.2 and Figure B.5).

3.4.6.1. RMS Roughness and Mean Thickness Calculation

To calculate the thin film thickness and surface root mean square (RMS) roughness, the 15 µm cross-section of (100) plane images were cropped into one image, where the posts met the substrate and the top-most PAEs were marked using Photoshop. Mean thickness was measured from the substrate surface to the center of the top-most PAE core and averaged over the entire cross section (Table B.2). Since FIB-SEM images were taken at an angle, the images were adjusted for the tilt using Matlab prior to data processing. RMS roughness was calculated in its standard fashion: $R\_RMS = \sqrt{(sum(y\_i^2)/N)}$, where N is the number of the PAEs on the thin film surface and y_i = height-mean_height.

Chapter 4. Lattice Mismatch in Crystalline Nanoparticle Thin Films

CHAPTER ABSTRACT

For atomic thin films, lattice mismatch during heteroepitaxy leads to an accumulation of strain energy, generally causing the films to irreversibly deform and generate defects. In contrast, more elastically malleable building blocks should be better able to accommodate this mismatch and the resulting strain. Herein, that hypothesis is tested by utilizing DNA-modified nanoparticles as "soft," programmable atom equivalents to grow a heteroepitaxial colloidal thin film. Calculations of interaction potentials, small angle X-ray scattering data, and electron microscopy images show that the oligomer corona surrounding a particle core can deform and rearrange to store elastic strain up to ±7.7% lattice mismatch, substantially exceeding the ±1% mismatch tolerated by atomic thin films. Importantly, these DNA-coated particles dissipate strain both elastically through a gradual and coherent relaxation/broadening of the mismatched lattice parameter and plastically (irreversibly) through the formation of dislocations or vacancies. These data also suggest that the DNA cannot be extended as readily as compressed, and thus the thin films exhibit distinctly different relaxation behavior in the positive and negative lattice mismatch regimes. These observations provide a more general understanding of how utilizing rigid building blocks coated with soft compressible polymeric materials can be used to control nano- and micro-structure.
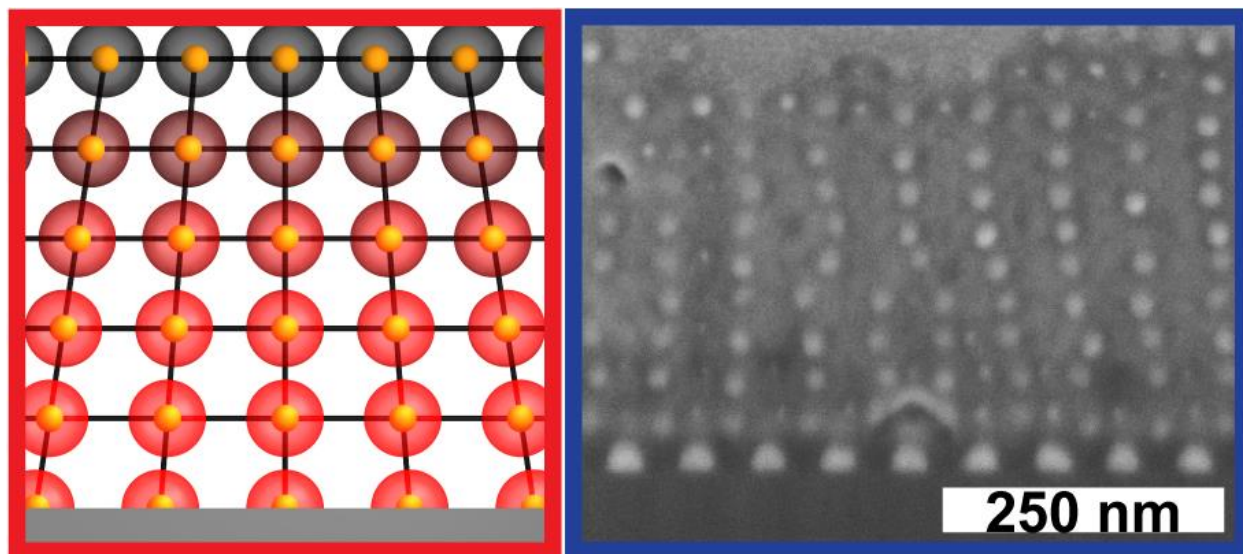
4.1. Introduction

Heteroepitaxy is the process of depositing a thin film of one material atop a dissimilar material while maintaining the crystallinity of each composition. However, when the two lattice parameters are misaligned, significant strain is generated in the deposited crystals. In cases where there is minimal strain, the lattices form a coherent interface with a continuous crystallographic alignment. Unfortunately, in atomic thin films, only heteroepitaxial processes with a low lattice mismatch (max ±1%) tend to be coherent, and strain is instead generally alleviated by the formation of defects within the deposited crystal.[1,166,193,194] Since atoms behave like and are often modeled as hard spheres, engineering this crystal interface requires significant modulation of lattice composition (*e.g.* introducing dopant atoms to adjust lattice parameter). As a result, material composition must often be compromised in order to prevent the formation of undesirable defects.[193] However, if a more elastically malleable building block was used, the equilibrium thin film crystal structures would be more accommodating of strain from lattice mismatch as a function of film thickness.[14,181]

While it is not possible to adjust an individual atom's "softness," programmable atom equivalents (PAEs) generated from rigid nanoparticles (NPs) and soft, highly tunable DNA ligand shells can be chemically adjusted in a deliberate and rational manner.[20,78,79,123,127] Indeed, such PAEs can be assembled into ordered, crystalline structures in a manner that is analogous to atomic crystallization.[69,153,155] We have previously shown that PAEs and lithographically defined templates can be used to grow single-crystalline thin films in an epitaxial manner.[147,167] In principle, this enables the study of epitaxy using building blocks that are more tunable than atoms. In this work, we extend this motif to the concept of heteroepitaxy by inducing controlled lattice mismatch between substrate and PAEs. While significant research effort has been devoted to investigating atomic heteroepitaxy,[166] PAEs have not been fully explored in this context yet. Understanding how strain is alleviated in these thin films is key to improving control over nano- and micro-scale structure in NP-based crystalline materials. This understanding could enable the fabrication of more complex nano-devices, particularly those requiring variations in NP composition with different lattice constants within the lattice.

4.2. Modeled Strain Energy Accumulation in Heteroepitaxial PAE Thin Films

In heteroepitaxial systems with lattice mismatch, elastic strain energy accumulates within the deposited thin film with the addition of each layer.[166,194] In atomic systems, all strain energy must be stored within the atomic bonds themselves, raising the overall potential energy of each individual building block. An oversimplified model can describe crystalline lattices as masses (atoms) connected by springs in each of the lattice directions. Each spring has an equilibrium length corresponding to an ideal interatomic spacing based on the energetics of binding and a spring constant that opposes deviation.[195–197] Similarly, PAEs exhibit a well-defined, equilibrium interparticle distance that balances favorable DNA hybridization between neighbors with unfavorable steric repulsion between DNA coronae.[69,79,132,198] To an extent, PAEs can store elastic energy in different modes such as compression, extension, bending, and rearrangement of the DNA bonds between each set of neighboring PAEs, suggesting that they are significantly "softer" building blocks than atoms.[122,127,199] Given the numerous modes of elastic energy storage available to soft matter, we hypothesize that the PAE thin films will more readily accommodate any deviation due to lattice mismatch.

To explore the energetic stability of a heteroepitaxial PAE thin film, a mathematical model based on mean field approximation[132] was used to calculate theoretical PAE interaction potential energies (Figure 4.1). These calculations used a PAE design consisting of 20 nm spherical gold NPs functionalized with one of two oligonucleotide sequences bound to linker strands with complementary "sticky ends" (Figure C.1). This binary system was assembled into body-centered cubic (bcc) crystals with an equilibrium lattice parameter of 65 nm. The foundation for this model is based on the assumptions that (i) all DNA sticky ends within the region of overlap between complementary PAEs are hybridized (Equation C.1), and (ii) the PAEs are assembled into a rigid lattice with well-defined x,y-spacing (*i.e.* dissipation of strain energy was not considered). Previous studies show that the main thermodynamic contributor to lattice stability is the balance between attraction from DNA hybridization (Equation C.2) and interparticle repulsion due to excluded volume interactions between the DNA brushes (Equation C.3 and Equation C.4).[62,144,200,201] A "bulk" energy was first calculated by modeling a free-standing PAE film of a given thickness at the equilibrium lattice parameter. This is the energy associated with an unstrained lattice without

the additional stability arising from being bound to a substrate. In the presence of a heterogeneous interface for the thin film cases, an interfacial energy term was included in the model (Section C.1.3).
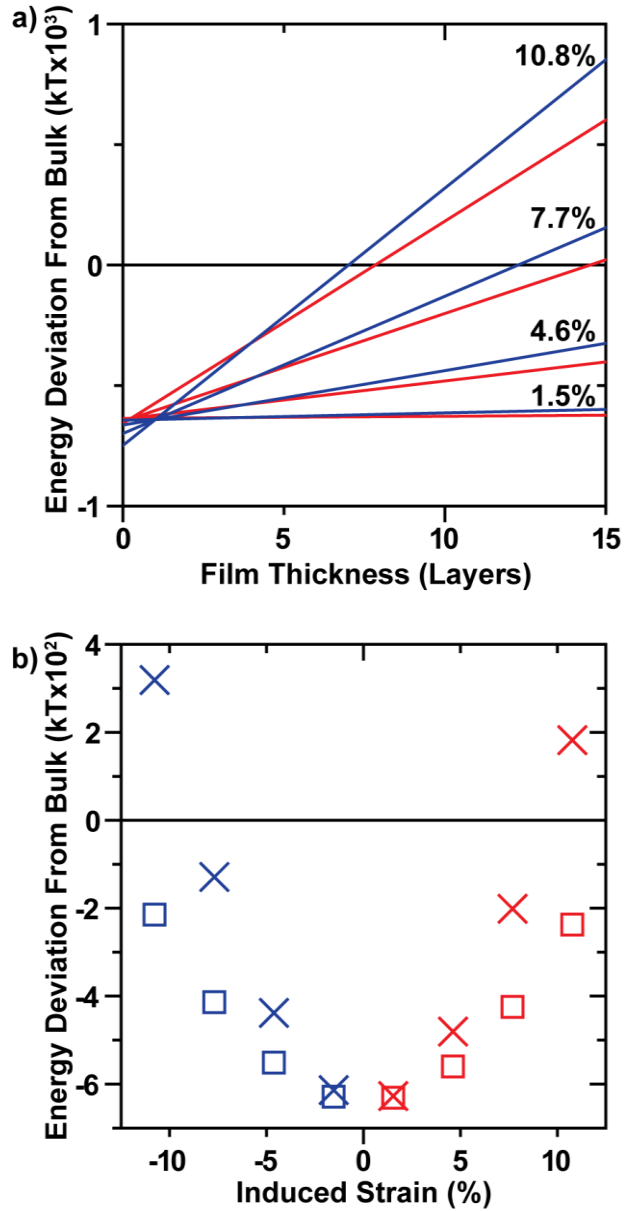
Figure 4.1: Modeled PAE thin films are energetically stable up to roughly ±9% lattice mismatch at 10 layers. Calculated PAE thin film potential energies relative to bulk a) as a function of film thickness and b) as a function of induced strain. In all figures, blue data correspond to negative lattice mismatch, red data to positive lattice mismatch; squares correspond to 5 layer samples, "X"s to 10 layers. Black lines correspond to "ideal" values.

The impact of lattice mismatch on PAE thin film energy was investigated by calculating the potential energy of coherently assembled PAE thin films subjected to various amounts of lattice mismatch strain (Figure 4.1). The lattice energy calculations, compared to their bulk analogues, demonstrate that the soft DNA shell allows the assembled thin films to withstand a significant amount of strain. However, strain energy accumulates with each layer of the film and eventually destabilizes the overall structure to the point that the film is energetically less stable than the bulk state (Figure 4.1a). This also implies that at greater lattice mismatch the energy barrier for coherent, heteroepitaxial growth will be prohibitively high, resulting in incoherent growth. The model reveals that 10 layer films beyond roughly ±9% strain are less stable than their bulk analogue (Figure 4.1b). Thus, for the PAE design studied here, 10 layer thin films are predicted to only exhibit epitaxial alignment when the heterogeneous interface induces less than ±9% strain. Beyond this regime, the analytical model predicts that the accumulated strain energy will make thin film growth energetically unstable, favoring the formation of defects or dewetted amorphous (bulk) structures.

4.3. Methods and Experimental

To investigate these hypotheses experimentally, PAEs consistent with the modeled design (DNA functionalized 20 nm gold NPs that can arrange in a bcc lattice with a 65 nm lattice parameter upon annealing) were synthesized following literature protocols[59,69] (Section C.2, Table C.1, Figure C.2, Figure C.3, Equation C.5, and Equation C.6). Arrays of gold dots commensurate in size with the PAEs were deposited on a silicon wafer in a pattern mimicking the (001) plane of the targeted bcc superlattice using electron beam lithography (Section C.3.1). Once the dots were functionalized with one of the DNA strands and linkers (Table C.1 and Section C.3.2), PAEs functionalized with the complementary sequence could bind and form a monolayer on the patterned array (Figure C.4). Previous studies have shown that the PAEs bind to the dot array in the position that maximizes the number of DNA linkages.[147,167] In this case, the particle was driven to sit in the center of four dots, epitaxially continuing the patterned crystal plane (*i.e.* the formation of the (002) plane). This process was continued in a layer-by-layer fashion to assemble multiple layers on each template (Table C.3). To study the phenomenon of heteroepitaxy and the impact of lattice mismatch, arrays were fabricated with different lattice parameters than

the ideal bulk PAE superlattice (up to ±10.8% lattice mismatch, Table C.2 and Scheme 4.1). The thin films were embedded in silica following established protocols[176] (Section C.4.2) and the structure of each was determined by synchrotron-based transmission small angle X-ray scattering (SAXS), as well as focused ion beam (FIB) cross-sectioning followed by scanning electron microscopy (SEM).
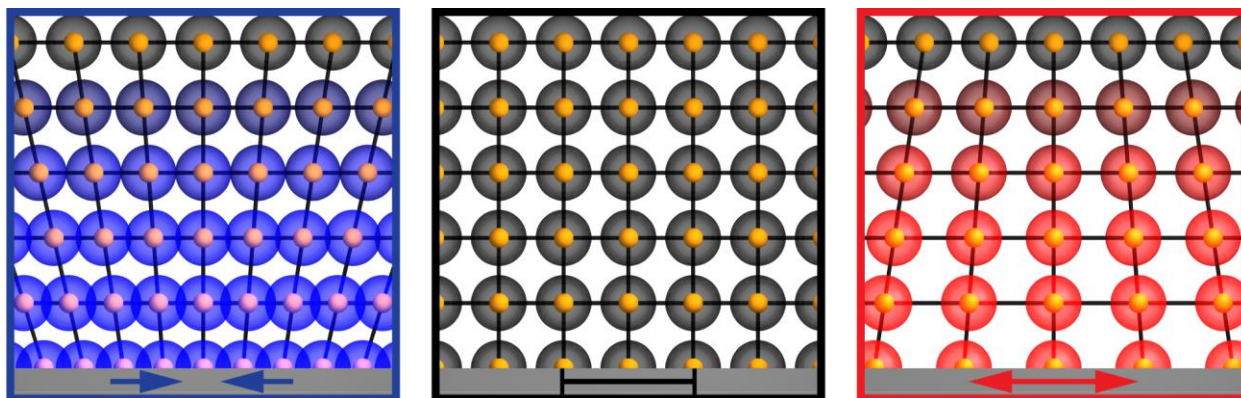
Scheme 4.1: Representation of the layer-by-layer PAE epitaxy platform and heteroepitaxial PAE thin films under negative (left) and positive (right) lattice mismatch (compressive and tensile strain, respectively) with coherent interfaces elastically relieving strain. Cross-section of the (001) plane is shown.

4.4. Results and Discussion

4.4.1. Degree of Epitaxy as Function of Lattice Mismatch

First, SAXS was used to determine the degree of crystallinity and epitaxy. Since the incident X-ray beam was normal to the substrate for these measurements, the resulting SAXS data shown in Figure 4.2 are 2D projections of the x,y-plane positions in reciprocal space. Each SAXS pattern shows a high degree of single-crystalline ordering consistent with the patterned bcc (001) plane (Figure 4.2a). Full 2D images (Figure C.6) and 1D circular averaging (Figure C.7) for samples consisting of either 5 or 10 layers are available in Appendix C. In these data, epitaxially aligned PAEs contribute to the intensity of the reciprocal space lattice positions. Any deviation in alignment results in a broadening of each diffraction spot. Regions of non-epitaxial PAEs within the thin film add to the intensity of a diffuse ring encircling the beam center. Therefore, we can define an order parameter (Equation C.8) by comparing the integrated SAXS intensity of a diffraction spot to the relative integrated intensity of the diffuse ring over the same q-range (Figure 4.2b). Consistent with both the hypotheses and the calculations of interaction potentials, all

samples exhibit a reasonably high degree of order (intensity at the diffraction spot 2.5 times greater than the integrated intensity of the corresponding diffuse ring), even the cases of $\pm10.8\%$ lattice mismatch. Within $\pm7.7\%$, the thin films exhibit near perfect ordering, matching the analytical model. This is in stark comparison to atomic thin film heteroepitaxy, which rarely remains epitaxial and coherent above $\pm1\%$ lattice mismatch.[166] SAXS also confirms that the interparticle distance between PAEs in the thin film (calculated from the $q_{(110)}$ position, Equation C.9) conform to the induced mismatch (Figure 4.2c). Finally, additional confirmation of the epitaxial alignment was achieved with SEM (Figure C.5) and atomic force microscopy (Figure C.11) of the thin films, which both show a transition from an aligned and ordered surface into an amorphous layer beyond $\pm7.7\%$ mismatch.
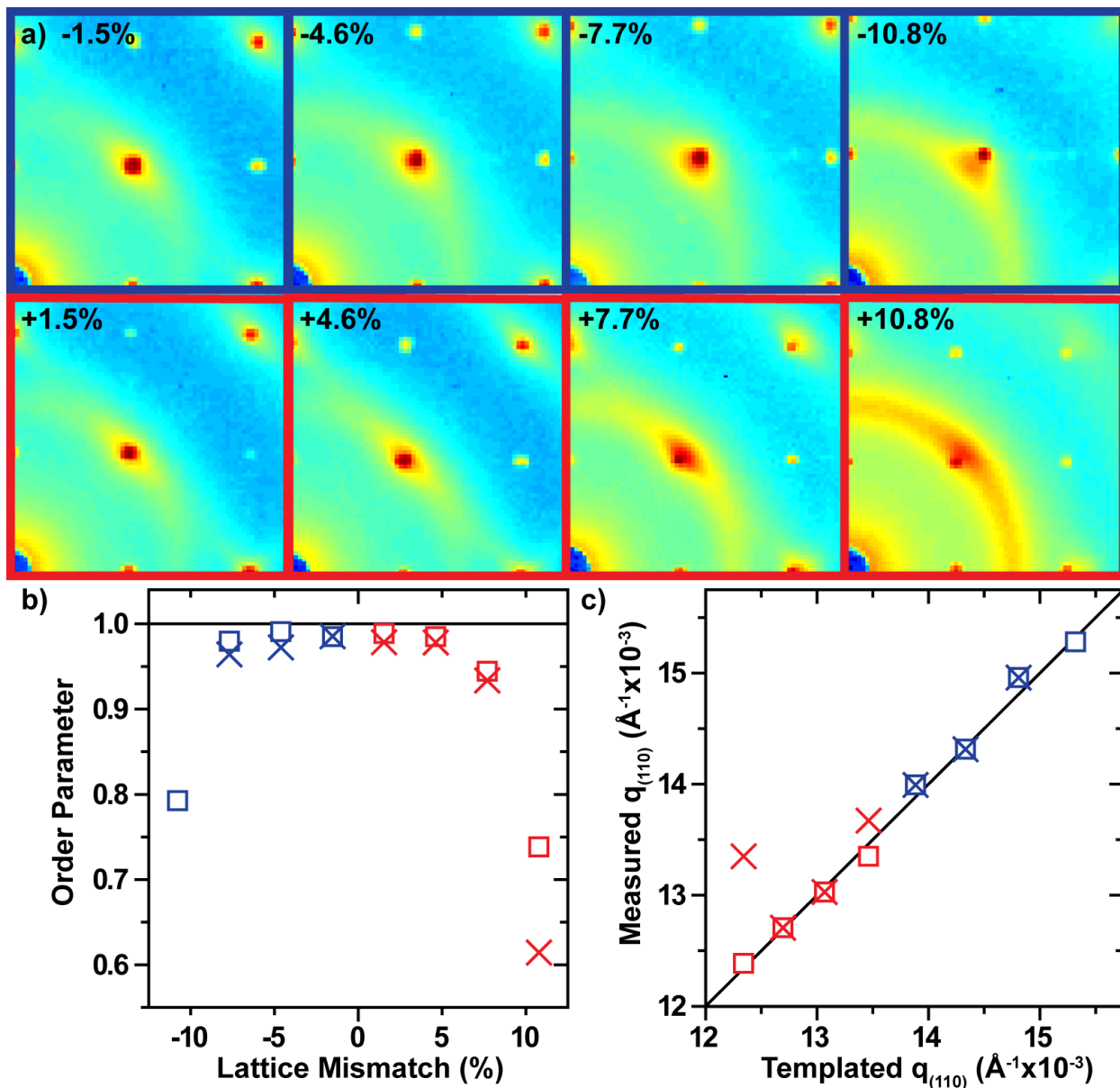
Figure 4.2: PAE thin films maintain coherency with the patterned crystallography up to ±7.7% lattice mismatch. a) 2D transmission SAXS data centered on the (110) reciprocal spot – 10 layer sample for all shown except -10.8% (5 layer) shown, b) order parameter – calculated by comparing the integrated intensity of the (110) spot to the intensity of the amorphous ring – as a function of lattice mismatch, and c) the maximum $q_{(110)}$ value from the measured SAXS data compared to the templated $q_{(110)}$ position.

4.4.2. Elastic Relaxation of Lattice Parameter

The strong parallels between the modeled and experimental results indicate that a majority of the accumulated strain energy in this "soft" heteroepitaxy system is likely stored within the DNA shell. However, broadening of the diffraction spots (which increases with larger values of lattice mismatch) is indicative of deviation of PAEs from ideal lattice positions and suggests that some of the strain energy is being dissipated throughout the thin film structure. In general, a material can alleviate strain energy in two ways: elastically or plastically. Elastic alleviation is strain removal that is done without breaking any bonds between individual building blocks, while plastic deformation requires the breaking of individual bonds and generally manifests in the form of defects.[1] Heteroepitaxial thin films (atomic or PAE-based) that can dissipate strain elastically largely do so through a gradual change of the interparticle distances in lattice planes further from the heterogeneous interface (Scheme 4.1). In other words, lattice planes further from the mismatched interface will have interparticle distances closer to the ideal. Atoms in a crystalline lattice have relatively rigid and directional atomic orbitals resulting in a sharp and deep energy well as a function of position. Therefore, atoms incur significant energetic penalties for deviating too readily from an ideal lattice position. At high lattice mismatch, the strain energy present in the bond between two atoms outweighs the energy cost of breaking that nearest neighbor bond, driving the atoms to rearrange their equilibrium structure and form defects like misfit dislocations or lattice vacancies.[1] The mechanisms of alleviating the strain from lattice mismatch available to heteroepitaxial PAE thin films can be deduced from their resulting, equilibrium structure. In contrast with atoms, spherical PAEs are isotropic and have omni-directional binding. Additionally, the flexibility of the DNA corona allows for a wider range of achievable binding distances at a lower energy cost.[127] Therefore, these "soft" building blocks are hypothesized to more readily allow for elastic alleviation of strain.

Indeed, the SAXS data clearly reveal an elastic mode of strain relief (Figure 4.3). Intensities at larger scattering angles (larger q values) correspond to smaller real space distances, and vice versa. By averaging radially along *only* the 45° angle, trends in the average interparticle distance can be observed (Figure 4.3a and Figure C.8). In all mismatch cases, the (110) peak intensity is strongest where matched with the template position and exhibits a tail that leans toward the bulk, ideal interparticle spacing. Plotting the (110) peak maxima and their respective rightward and

leftward peak widths at half max (Equation C.10 and Equation C.11), the data demonstrate that when the thin films are compressed under negative lattice mismatch, the PAEs relax toward larger spacing and vice versa (Figure 4.3b). While this conclusion may be intuitive for soft matter in general, it highlights the behavior unique to a "soft" building block in the construction of crystalline materials.
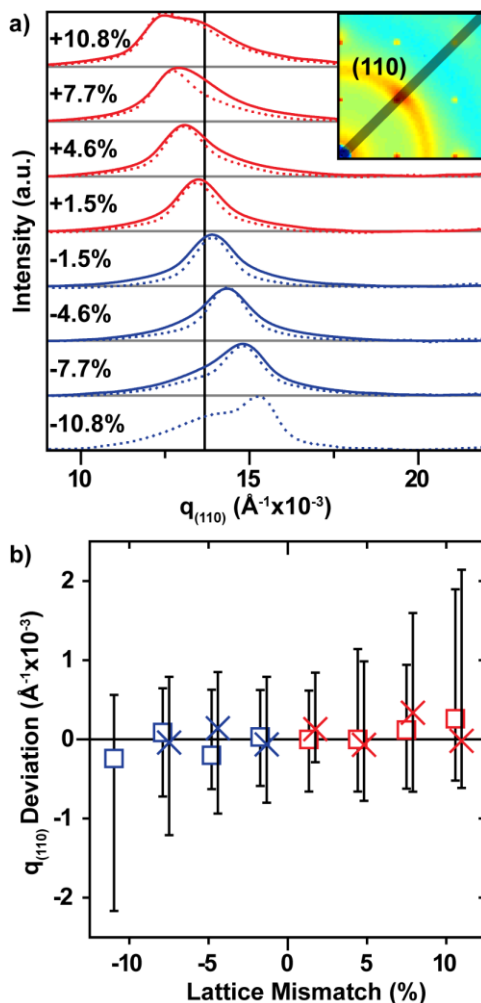
Figure 4.3: PAE thin films alleviate strain energy elastically in the *x,y*-plane through gradual retraction/expansion of interparticle distance toward the bulk value. a) 1D radial line averages of the SAXS data along the close-packed direction with the "ideal" bulk phase (110) peak position noted for reference. Dotted lines are 5 layer films and solid lines are 10 layers. Inset: representative schematic of direction and width of radial line cuts. b) Plot of max (110) peak positions relative to the template and the peak width at half max of each line cut in the high-*q* (small interparticle distance) and low-*q* (large interparticle distance) directions displayed as error bars.

4.4.3. Plastic Deformation of PAE Lattices

While strain energy in these PAE systems is alleviated predominantly in an elastic manner by stretching or compressing soft DNA shells, plastic deformation would be expected to occur when the accumulated strain energy in the collective DNA "bond" between two particles exceeds the energy penalty associated with breaking that bond (*i.e.* the DNA ligand shell is too stretched or compressed for the DNA sticky end duplexes to remain in the hybridized state). Given the high grafting density of oligomers on the surface of the PAEs (which results in a crowded environment for the DNA strands)[52,54] and the fact that the DNA bonds consist almost entirely of duplexed DNA, we hypothesize that the DNA corona surrounding an individual particle will display different physical characteristics under compressive and tensile lattice mismatch. Specifically, under negative mismatch, the volume available to a PAE in the lattice is reduced, generally confining it to its local lattice position. However, under positive mismatch, the free accessible volume of each lattice site is increased, providing a larger space for each PAE to occupy. Thus, PAEs under positive lattice mismatch have higher degrees of translational freedom (variation around ideal lattice sites) than films of a corresponding compressive mismatch. According to the analytical model in this work, an increased interparticle distance reduces the overlap region between complementary particles, leading to fewer DNA sticky end hybridization events and a higher overall energy. Therefore, the maximum number of DNA hybridization events may occur when the particle is shifted away from the lattice site, a behavior that is not considered in the model. By releasing entirely from one neighbor (breaking the "bond" between the two PAEs) and shifting toward its other complementary nearest neighbors, each PAE in a larger-than-ideal unit cell could increase its overall DNA hybridization, resulting in a lower equilibrium, lattice energy.

This type of random, plastic deviation results in azimuthal, instead of radial, broadening of SAXS diffraction spots as the PAEs within the film transition from precise locations to more random, amorphous ones. After taking broad azimuthal cuts (from q-values of 0.0093 to 0.0183 Å^{-1}) that encompass the entirety of the (110) diffraction spot in each sample, the 1D averaged intensities were plotted as a function of angle (Figure C.9); the relative breadth of these peaks (Equation C.12:) was then plotted to determine the degree of translational freedom for each sample (Figure 4.4a). As hypothesized, the tensile samples have a much higher degree of translational freedom. To corroborate this conclusion from the SAXS data, the 10 layer thin films were cross-

sectioned *via* FIB milling and imaged with SEM. Each cross-section was aligned with the (001) plane of the thin film to readily observe any deviation in the PAE positions. The significant difference between translational freedom in the negative *versus* positive mismatch cases is visually apparent by observing the (001) planes moving in the *z*-direction in the representative FIB cross-sections comparing the +7.7% lattice mismatch sample to the -7.7% sample (Figure 4.4b). Similar to atomic materials under tensile strain,[1] the PAE films under positive lattice mismatch show signs of "micro-tears" (gaps) where void space within the structure is a result of PAEs locally breaking bonds in the same direction. The fact that these gaps are not observed in the negative mismatch samples indicates that the PAEs' "soft" coronae can be compressed with the addition of strain but not as readily stretched. This is consistent with prior experimental results on the mechanical properties of single DNA strands.[202–206] This non-reciprocal difference gives rise to the different physical characteristics and amounts of plastic versus elastic deformation of the PAE lattices under positive and negative lattice mismatch.

The microscopy images (full 15 µm cross-sections of each 10 layer thin film)[26] corroborate the broad conclusions of the SAXS data; all thin films appear, in general, epitaxial with increasing frequency of defects as mismatch increases. These defects culminate in the formation of large "glassy" regions under extreme mismatch. Under positive lattice mismatch, the defects are commonly random deviations in the spacing between lattice planes (Figure 4.4b). Interestingly, the FIB cross sections, particularly for the negative lattice mismatch films, also show the presence of other plastic deformation mechanisms to alleviate strain that are commonly observed in atomic systems.[166,193] These include both dislocations and vacancies, which alleviate strain by breaking bonds between particles and changing the local crystal structure of the lattice (Figure C.10).
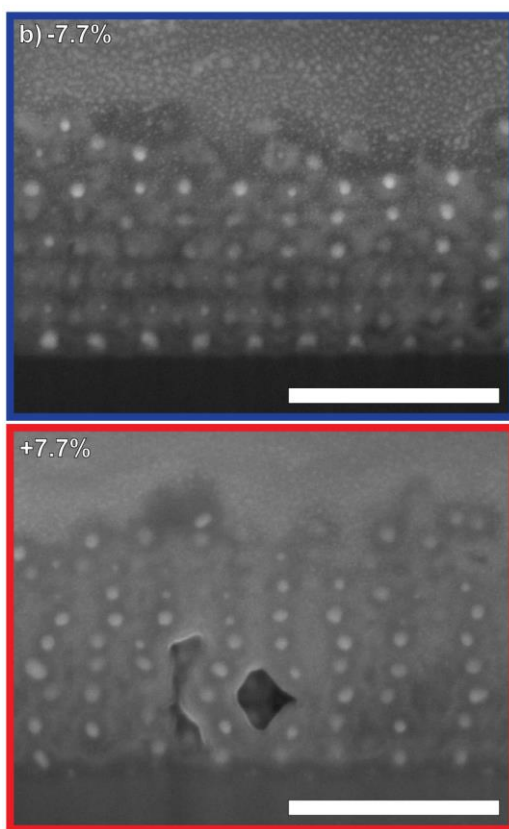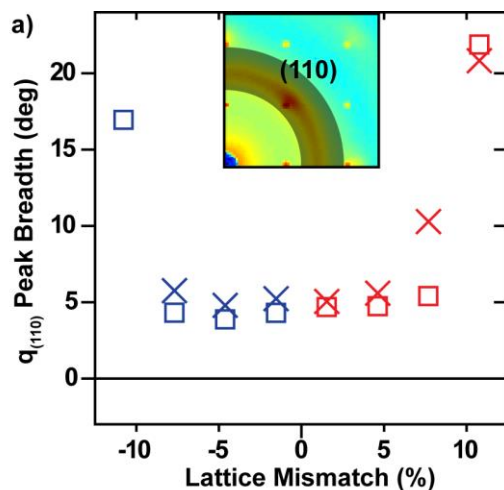
Figure 4.4: Plastic alleviation of strain in PAE thin films in the presence of high strain. a) Plot of relative breadth of the (110) SAXS peak in the azimuthal direction (corresponding to the degree of PAE translational freedom within the thin film) versus lattice mismatch. Inset: representative schematic of direction and width of azimuthal cuts. b) The higher frequency of random, lateral deviations in *x,y*-planes under high positive lattice mismatch was verified visually from the FIB cross-sections. Scale bars are 250 nm.

4.5. Conclusion

The conclusions presented here reveal the complexity of using PAEs as thin film building blocks. They exhibit remarkable strain tolerance based on their design, accommodating a lattice mismatch up to ±7.7% while maintaining coherency. Unlike atoms, PAEs are readily able to store the accumulated strain energy within the DNA bonds between particles and alleviate some of the strain elastically through a change in lattice parameter as a function of layer number. While the release of any strain in these PAE thin films is primarily elastic relaxation, these building blocks still undergo plastic defect formation. The observed misfit dislocations and vacancies are comparable to atomic thin films. In principle, these PAEs should be tunable to behave more like soft matter or more like hard sphere atoms depending on synthetic variation of the building block design and deposition parameters. "Soft" heteroepitaxy, while maintaining similarities to atomic heteroepitaxy, contains unique mechanistic differences that can greatly affect material synthesis. This effect might be even more prominent for crystals in solution, where macroscopic curvature could provide additional mechanisms for strain relief. In principle, the induced strain at the interface could be used to control the thickness of overgrown material atop a dissimilar material with different lattice parameter, *i.e.* in a core-shell structure. Ultimately, this study yields unparalleled control over nano- and micro-structure in NP-based systems. The platform investigated in this work can provide a toolkit for novel NP devices requiring improved control over interparticle distances, as well as provide a proxy system for the study of interface/thin film science at the boundaries of heteroepitaxial interfaces.

Chapter 5. Nanoparticle Composite Materials with Programmed Nanoscale, Microscale, and Macroscale Structure

Written in collaboration with Peter J. Santos, Leonardo Z. Zornberg, and Robert J. Macfarlane

CHAPTER ABSTRACT

One of the original promises of nanotechnology is simultaneous structure control across length scales. Bottom-up colloidal nanoparticle self-assembly has emerged as a programmable tool to determine precise nanoscale control over placement and arrangement of nano-building blocks. Utilizing strategies akin to crystallization of atoms, this control has been extended into the synthesis of microscale crystallites and thin films. However, no process currently exists to bring these nanoparticle-based materials into the level of macroscopic manipulation. Here, we utilize the lens of materials processing to view nanoparticle crystallites as a material capable of being manufactured into arbitrary, 3D shapes. Utilizing the advantages of the scalable, flexible, and robust colloidal building block, the Nanocomposite Tecton (NCT), we demonstrate a 'sintering' strategy to densify nano-ordered crystallites into bulk, composite materials which can further be pressed into a desired, macroscopic shape. Importantly, the material's nanoscale lattice parameter can be actuated with the solvent environment, and its microstructure (grain size and composition) is directly controlled by the size and composition of the processed NCT crystallites. Ultimately, the methodology described in this chapter constitutes a realization of nanotechnology's aim: an arbitrarily shaped, 3D macroscopic object with dictated microstructure, and precise nanoscopic crystalline arrangements of nanoparticles.
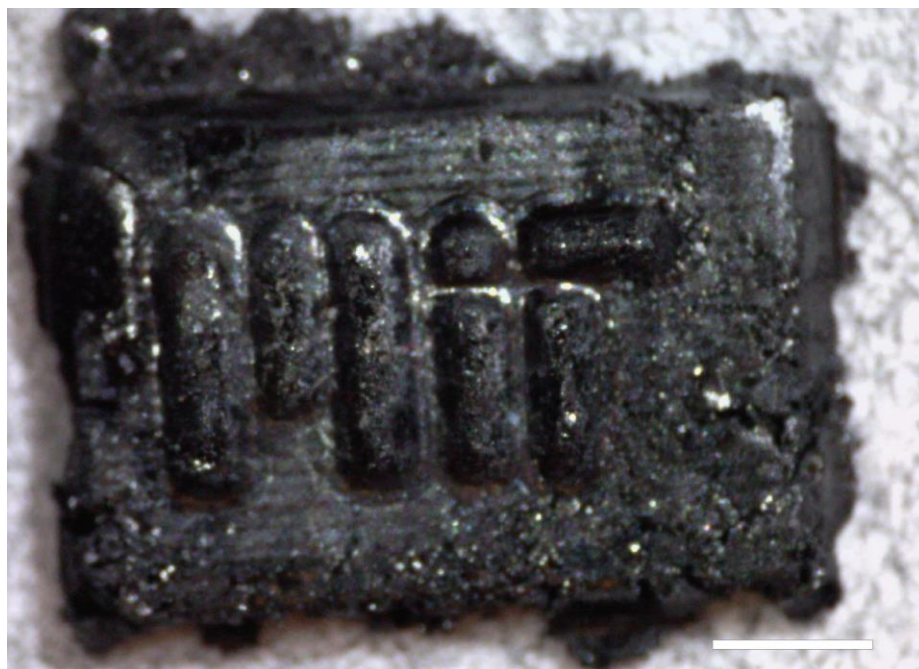
5.1. Introduction

One of the promises of nanotechnology is the ability to make designer materials with deterministic control over both composition and 3D spatial organization.[207–209] The self-assembly of nanoparticles[79,210–213] has emerged as a promising method for synthesizing these nanomaterials because they offer a vast array of materials fabrication components of varying sizes, shapes, and chemical compositions.[84,95,214,215] A significant accomplishment has been the formation of ordered superlattices of nanoparticles that resemble the crystalline lattices of atomic materials,[16,18,20,48,69,104,168,216–218] and even creating unnatural crystallographic symmetries by exploiting the broad design-space of the building blocks.[219–225] The resemblance of nanoparticle superlattices to atomic crystals has inspired the development of a number of processing methods for creating thin films[147,177,226] and single crystals of precisely arranged nanoparticles.[148,227–231] Although current efforts have therefore succeeded at creating materials with designed nano- and micrometer geometry, the fundamental promise of being able to build a bulk material with controlled structure across the length scales of atomic crystal structure, nanoscale size and organization, and ultimately material microstructure and macroscopic form, has been challenging to realize. Progress towards designed macroscopic nanomaterials has been impeded by the difficulty of producing bulk quantities of the building blocks, the slow processing of the nanoparticle components into assemblies, and the lack of a method for transforming micron sized crystallites and films with well-defined microstructures into a larger material. A major advancement would therefore be a single materials synthesis and processing route that could create free-standing, macroscopic materials of arbitrary three-dimensional shapes with precisely controlled nanoparticle positions across the entirety of the material composition.

Here, we address these challenges with a recently developed building block, the Nanocomposite Tecton (NCT),[21] and demonstrate its unique suitability for producing well-ordered macroscopic nanomaterials. We investigate the assembly of NCTs into ordered crystallites directed by a simple, enthalpically driven supramolecular interaction, allowing for precise and rapid control over microscale size and distribution. Finally, we extend the analogy between nanoparticles and atoms by devising a processing route akin to the sintering of nanocrystalline powders to fabricate an NCT-based polycrystalline, bulk monolith that can be post-processed

(dried and pressed) into large, arbitrarily shaped solids. In other words, we have devised a single materials synthesis and processing route for nanoparticle-based, bulk materials with designed structure at the atomic scale (supramolecular chemistry), nanoscale (crystalline unit cell), microscale (controlled grain size and composition), and macroscale (arbitrary shape) (Figure 5.1).
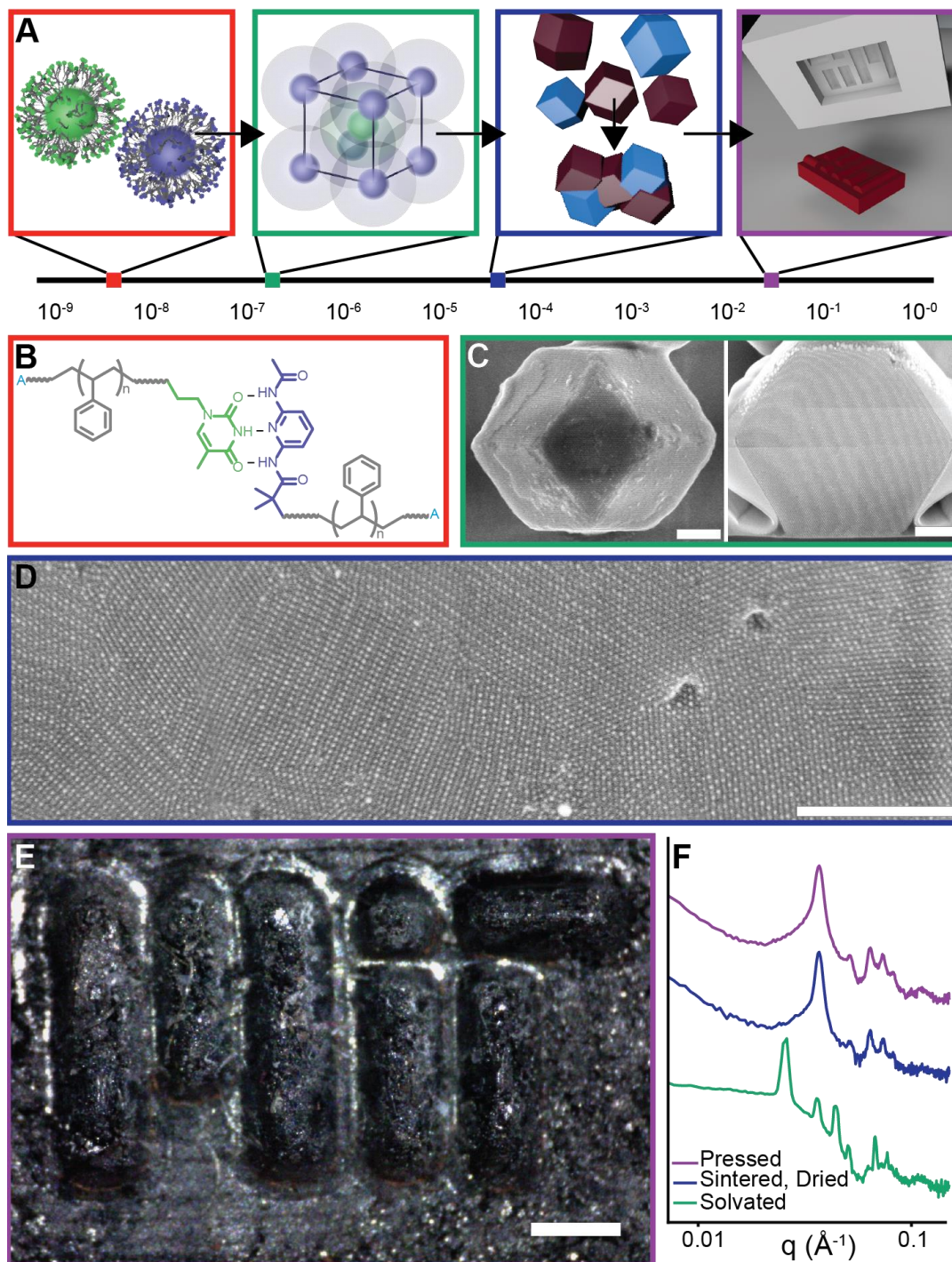
Figure 5.1: The Nanocomposite Tecton (NCT) design concept allows for structural control from the nanoscale to the macroscale. A. Supramolecular interactions drive the assembly of nanoparticles. Under appropriate conditions the NCTs will assemble into ordered superlattices, and form micron-sized crystallites. These crystallites can be sintered together to form a macroscopic solid material. The NCT solid can be mechanically pressed into an arbitrary shape. B. NCTs consist of a nanoparticle core coated with a polymer brush terminated in a supramolecular binding group. In this work, polystyrene was used as the polymer and diaminopyridine (DAP) and thymine (Thy) as a supramolecular binding pair. C. Scanning electron microscope (SEM) micrographs of the surface morphology (left) and cross-section (right) of a gold nanoparticle NCT (Au-NCT) crystallite that formed a Wulff polyhedra. Scale bar is 500 nm. D. SEM micrograph of the cross-section of a sintered Au-NCT solid. Scale bar is 500 nm. E. Iron Oxide nanoparticle NCTs mechanically shaped into the MIT school logo. Scale bar is 0.5 mm. F. Small angle X-ray scatting (SAXS) of the NCTs in part E while solvated in toluene (green), after being sintered and dried (blue), and after mechanical deformation (purple), demonstrating the body centered cubic (bcc) ordering is preserved throughout the process.

5.2. Results and Discussion

5.2.1. Nanoscale Structure Control: The Nanocomposite Tecton (NCT)

At the scale of the building block, each NCT consists of an inorganic nanoparticle core covered with a dense polymer brush, and each polymer chain is terminated in a supramolecular binding group (Figure 5.1B), which upon the mixing of complementarily functionalized NCTs, directs their assembly.[232] Previous work has shown that after a mild annealing process, NCTs self-assemble into well-ordered superlattices,[233] but no work has been done to either further modify nanoscale behavior or characterize their larger length-scale structure. NCTs are able to crystallize because they are near-equilibrium materials; as they are heated the supramolecular bonds that hold together the lattice are capable of rapidly breaking and reforming until the NCTs freely disperse into solution in a process characterized by a melting temperature (T_m).[234] Upon cooling the binary NCTs through T_m, the nanoparticles organize into body-centered cubic (bcc) crystallites (Figure 5.1C).

NCT crystallization occurs in good solvents for the polymer shell, meaning that the brush is in a swollen state. However, the configuration of polymer chains is highly dependent on their enthalpy of mixing with the solvent; introducing a non-solvent causes the polymer to adapt a coiled conformation due to the repulsive interaction energy.[235,236] Because the polymer brushes in NCTs are a dynamic material, it was hypothesized that the conformation of the polymer chains could be modified by the addition of a poor solvent, allowing for actuation of interparticle distance within

124

the crystalline lattice. To study control over polymer brush swelling with solvent, a model NCT system was developed using previously developed chemistries: 15.4 nm gold nanoparticle cores (AuNPs), ~14 kDa polystyrene polymer brushes, and a DAP-Thy hydrogen bonding supramolecular attachment chemistry scheme (Figure D.1 and Figure D.2). During assembly, the NCT system is dispersed in toluene, a good solvent for the polystyrene chains, and therefore the brush is in a fully swollen condition. Simple alkanes (*e.g.* n-hexane, n-octane, n-decane) can serve as non-solvents for polystyrene while not interfering with hydrogen bonding. When any of these non-solvents are added to the NCTs, the system robustly maintains its bcc crystallinity, but the interparticle spacing decreases in a continuous, monotonic fashion (Figure 5.2A and Figure D.4). Interestingly, the polymer brush collapse is reversible, as a lattice can be cycled from solvent to non-solvent and back again without any decrease in crystallinity as determined by SAXS (Figure D.5). This cycling represents a dramatic 40 percent linear compression and expansion of the lattice, changing the interparticle spacing from 38.2 nm in pure toluene to 22.9 nm in pure n-decane. Because this change in lattice parameter is dependent on the behavior of the polymer brush, it is possible to further control interparticle spacing by changing the length of the polymer brush used. For example, NCTs with a smaller 6 kDa polymer were found to create a lattice with a 19.5 nm interparticle spacing in the collapsed state, a notably short surface-to-surface distance of 4.1 nm (Figure D.6). Strikingly, polymer conformation can be controlled by solvent content with Angstrom-level precision as measured by small angle x-ray scattering (SAXS). The ability to modulate the distance between nanoparticles and therefore, create high inorganic fraction nanocomposites with NCTs, may have significant implications for materials that could engage in plasmonic or magnetic coupling. [134,237]

However, solvated NCTs are unsuitable for implementation as bulk materials, because, although their low barrier to rearrangement aids their ability to crystallize, it leaves them susceptible to destabilization upon exposure to adverse thermal or chemical stimuli. Simply evaporating the NCTs from their good solvent (toluene) destroys the ordering as the brush collapses (Figure D.3), indicating that the toluene is a key structural element of the lattice. Therefore, it is hypothesized that the solvent ceases to be a structural component once fully transitioned to the non-solvent, and can be subsequently dried without loss of crystallinity. Indeed, NCT lattices evaporated from n-decane demonstrate near identical ordering to the solvated state

(Figure 5.2A and Figure D.4). Unlike the existing strategies to transition enthalpy-driven colloidal crystals to the solid-state,[126,176,238] transitioning NCTs to a solid materials *via* this deswelling of the polymer brush is a promising and powerful technique as it requires no additional reagents that may affect the system, diminish its ordering, or modify its properties.
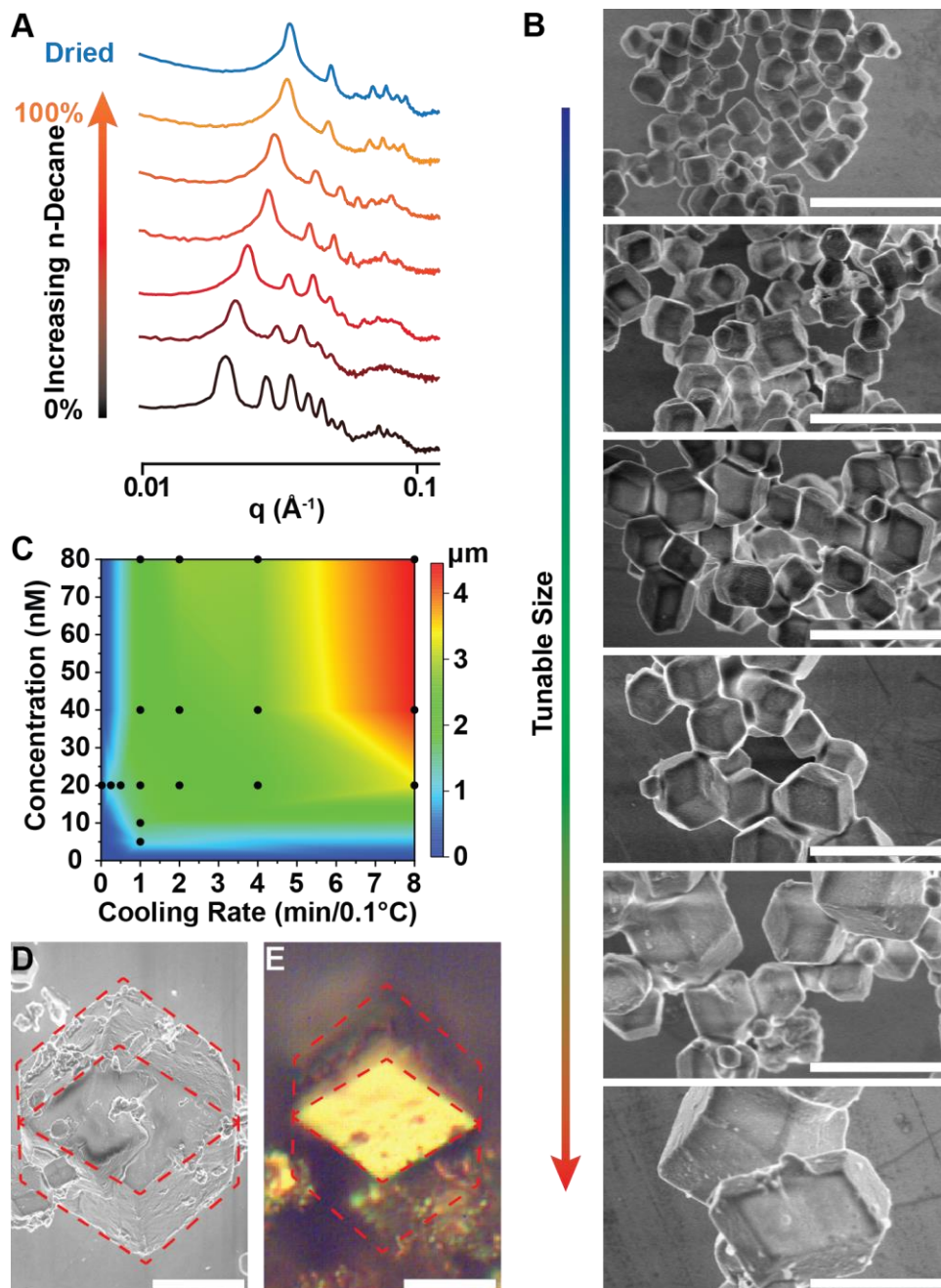
Figure 5.2: The formation of solid Wulff polyhedra from NCTs. A. During crystallization, NCTs are suspended in a solvent compatible with the polymer brush, such as toluene. However, because

the polymer brush is swollen, evaporating the solvent causes a loss of ordering and destroys the crystallites. Adding a non-solvent, in this case n-Decane cause the brush to de-swell, preserving ordering, as demonstrated by SAXS, and resulting in a significant (40%) contraction of the lattice parameter. B. During crystallization, the NCTs assemble into Wulff polyhedra. The size of the polyhedra can be tuned by modifying the concentration of NCTs and their cooling rate during crystallization. Scale bars are all 5 microns. C. The largest polyhedra form when a high concentration of NCTs and a slow cooling rate is used. Under optimal conditions, very large crystallites form, up to 30 microns in diameter. D. SEM and E. Optical image of large Wulff polyhedra. Scale bars are 10 microns.

5.2.2. Microscale Structure Control: Precise Crystallite Size Distribution

In addition to providing precise, actuatable control over nanoscale periodic spacing and expanding the accessible environments available to NCTs, the drying process allowed for imaging of NCT assemblies using scanning electron microscopy (SEM). NCTs slowly cooled (standard rate 1 minute per 0.1°C) through their melting transition yield crystallites with consistent, rhombic dodecahedron shapes (Figure 5.1C). The highly ordered nanostructure evident in the SAXS data (Figure 5.2A) is corroborated by SEM imaging of focused ion-beam (FIB) cross-sections, confirming the materials are highly crystalline throughout (Figure 5.1C) even after drying. A rhombic dodecahedron is the predicted Wulff polyhedra for bcc crystallites that forms because the surface is capped with the (110) closest-packed crystal planes and has been observed in other nanoparticle systems.

Other nanoparticle assembly strategies to produce Wulff polyhedra typically require either a slow solvent evaporation over hours to days[239] or a slow cooling through the melting transition with typical speeds of 10min/0.1°C.[155] In contrast, due to the lack of electrostatic repulsion between NCTs and their assembly through an enthalpy-mediated process the NCT system is capable of crystallizing very quickly; at the fastest rate that could be controllably measured and achieved (1s/0.1°C), NCTs still form highly ordered lattices (Figure D.7 and Figure D.8), and faceting can be clearly observed on crystallites cooled at 15s/0.1°C (Figure D.9).

The ability of NCTs to rapidly crystallize enables the use of cooling rate as a variable for controlling the resulting crystallite average size and distribution. In more traditional crystallization systems, crystallite size is positively correlated to slower cooling rate and lower precursor concentration, depending on the specific conditions of the system.[240] Consistent with this analogue, slower cooling rates in NCT crystallization were found to produce larger crystallite sizes

(Figure 5.2B), and as a result, the crystallite size can be reasonably well controlled with median characteristic lengths between ~500 nm and ~5 µm (Figure 5.2B&C, Figure D.8, Figure D.9, Figure D.10, Figure D.11, Figure D.12, Figure D.13, Figure D.14, and Figure D.25). Surprisingly, it was also observed that higher concentrations yielded larger crystallites, but with a larger distribution of sizes (Figure D.11, Figure D.15, Figure D.16, Figure D.17, Figure D.18, and Figure D.26). This is contrary to what is commonly observed in atomic systems, wherein higher precursor concentrations typically increase the total number of crystallites, thereby reducing the size of individual crystallites. To understand the dependence of crystallite size on concentration and cooling rate, a model was developed treating the cooling NCTs as aggregating clusters of nanoparticles (see Section D.5 for full details, Figure D.28 and Figure D.29). During cooling, these clusters collapse into an aggregate whose size is determined by the number of particles in a diffusion-limited volume as the system cools through the NCT melting window and crystallizes. Consequently, the model predicts that a slower cooling rate would increase the interaction volume, while a higher concentration would increase the total number of NCTs that would be present within the interaction volume, resulting in a larger aggregate. Furthermore, due to the stochastic nature of the aggregation process, increasing these two parameters would also be expected to broaden the distribution of crystallite sizes, and so the predicted trends of the model are consistent with the experimental data (Figure 5.2C, Figure D.30, and Figure D.31).

Utilizing the insights garnered from the model, combining the effects of a slow cooling rate and a high NCT concentration (Figure D.19, Figure D.20, Figure D.21, Figure D.22, Figure D.23, and Figure D.24), crystallites with a diameter > 30 microns when collapsed can be synthesized (Figure 5.2D and Figure D.27), equivalent to 50 microns when the polymer brush is extended. These large NCT crystallites have a diameter nearly 2.5 times the largest previously reported nanoparticle Wulff polyhedra, and contain approximately 10 times more particles.[169] As a result, the crystallites can be easily observed under an optical microscope (Figure 5.2E) and exhibit a highly reflective gold coloration, indicative of strong plasmonic coupling between the particles.

5.2.3. Macroscale Structure Control: 'Sintering' NCTs Crystallites

Even with this substantial increase in the size of individual, colloidal crystallites enabled by NCTs, the field still struggles to extend its reach to bulk, macroscopic materials. After their assembly, the NCTs are a powder of individual, micron sized crystallites with a negligible number of connections between crystallites. Turning to conventional metallic, ceramic, and polymeric materials where nanocrystalline powders are often sintered into macroscopic compacts for inspiration, it is hypothesized that an analogue to 'sintering' within the NCT system could be accomplished. In conventional materials, the application of heat and pressure allows for powder particles to plastically flow and deform in order to densify into a solid.[241–243] When the polymer brush of NCTs is swollen with toluene the system is near its melting transition (within 50°C), and so the dynamic supramolecular bonds of NCTs are hypothesized to be able to break and reform upon NCT crystallite deformation. Pressure was applied to NCT crystallites *via* centrifugation (20,000 RCF for 10 minutes), and, indeed, a monolithic solid was obtained after polymer brush collapse and drying (Figure D.34 and Figure D.35). SAXS confirms the NCTs maintain their crystalline ordering throughout this processing (Figure 5.1E), and SEM imaging of FIB cross-sections reveals the NCTs have been formed into a densified structure with grain boundary-like features (Figure 5.1D, Figure 5.3, Figure D.36, Figure D.37, and Figure D.38). Analysis of the microstructure is consistent with a sintering mechanism for compact formation: necking is evident near remaining void spaces and grains appear to have deformed form their original Wulff shape (Figure D.41 and Figure D.42).

Combining the control over microscale crystallite size distribution enabled by the understanding of crystallization dynamics with this macroscale processing method, it is hypothesized that a sintered NCT material would retain the size distribution of the initial crystallites in its final grain structure. To investigate this, NCT crystallites were prepared at different cooling rates as per Figure 5.2, so as to result in two distinct populations of crystallite sizes which were subsequently exposed to the abovementioned centrifugation compacting protocol (Figure 5.3A&B, Figure D.37, and Figure D.38). Indeed, SEM analysis reveals that the NCT bulk solids can be designed to have controllable grain sizes that track with the initial size distribution of crystallites (Figure 5.3C&D), indicating the ability to dictate microstructure along with nano-ordering and macro-shape. Furthermore, solids prepared from NCTs with larger size distributions

were also qualitatively observed to have an increase in void space, supportive of a sintering mechanism (Figure D.36 and Figure D.38).
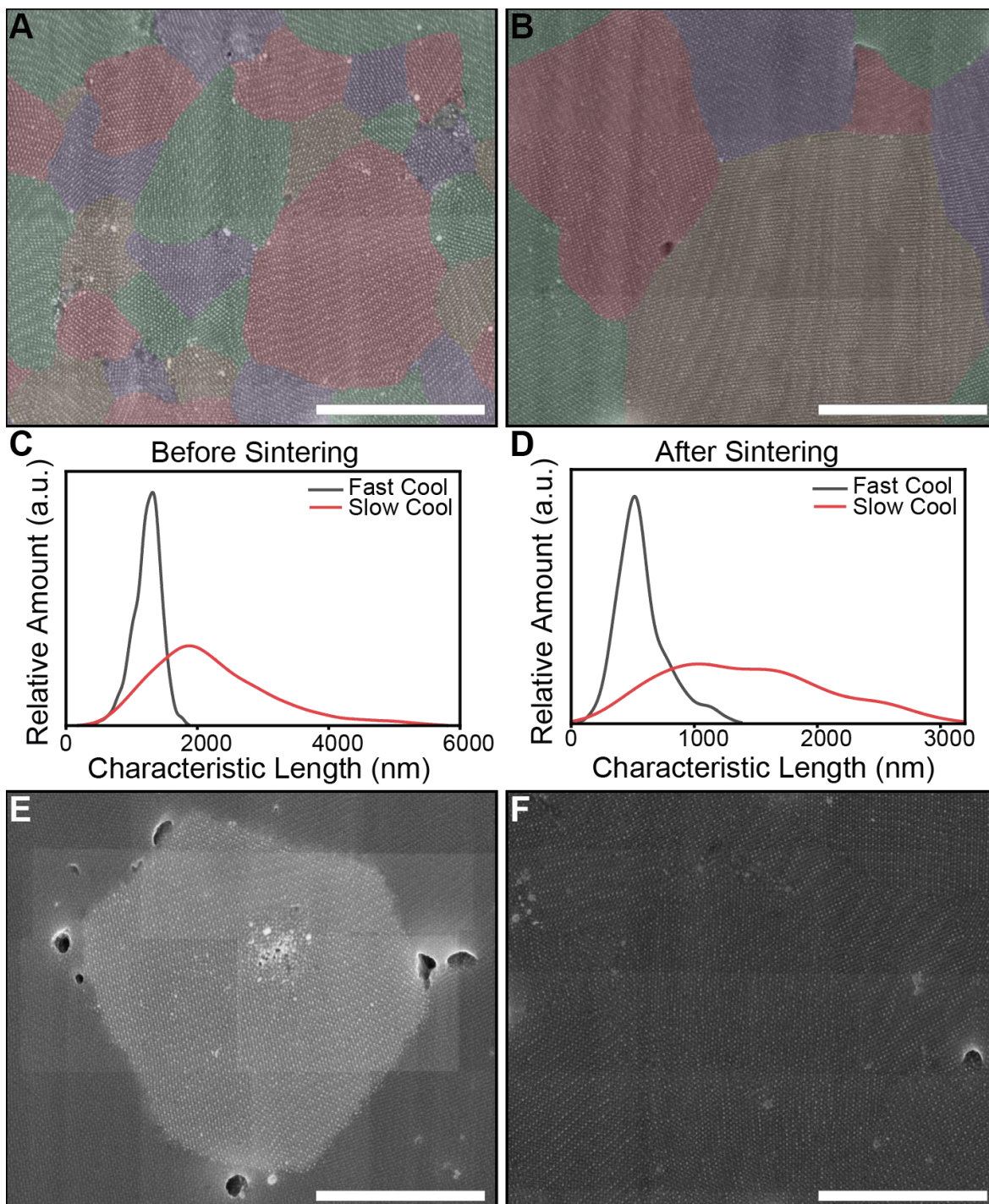
Figure 5.3: The NCT crystallites can be sintered into macroscopic solid materials. These solid NCTs are polycrystalline, with clearly identifiable grain boundaries in cross-sections. The size of

the grains in the polycrystalline solid is dependent on the characteristic sizes of the initial NCT crystallites. A. When a faster cooling rate is used, smaller crystallites form, and the resulting solid has smaller grains. B. Conversely, a slower cooling rate results in larger crystallites and bigger grains. The overall distribution of crystallite sizes before sintering (C) matches the distribution after sintering (D), though the average size decreases, hypothesized to be a result of deformation. E. The sintering method can be used to create materials of multiple compositions. Gold and iron oxide NCTs can be separately crystallized, and then blended together and sintered to create a heterogenous microstructure. F. Gold and iron oxide NCTs can also be assembled together to create a lattice with isostructural symmetry to CsCl where every alternating nanoparticle is gold or iron oxide, sintered into a solid with a homogeneous microstructure. Consequently, depending on the processing route, two materials of equivalent composition but dramatically different microstructure can be fabricated with NCTs.

The microstructure of NCT solids can be further programmed by changing the composition of the nanoparticle constituents. Previous work has demonstrated that NCTs can be synthesized with iron oxide nanoparticle cores (IO-NCTs), and the assembly process is largely unaffected by nanoparticle core identity (Figure D.33).[244] Therefore, sintered NCT solids were prepared using a mechanically blended combination of bcc IO-NCT crystallites and bcc Au-NCTs crystallites (Figure D.32 and Figure D.35). The result is a macroscopic material with control over the composition of microscopic grains (Figure 5.3D and Figure D.39). Notably, the Au and IO-NCTs remain phase segregated in this sample, suggesting a minimal degree of grain boundary diffusion occurs during the sintering process (Figure D.42).

To extend this compositional control to the nanoscale, NCT crystallites co-crystallized with Au and IO-NCTs to form superlattices isostructural with CsCl (Figure D.32 and Figure D.33) were produced and similarly sintered. The resulting macroscale, continuous material with well-defined, microscale grain size also demonstrates a tailored nanostructure where every-other nanoparticle consists of a different composition (Figure 5.3E and Figure D.40).

As IO-NCTs consist of iron oxide nanoparticles and polystyrene polymers, each synthesized at gram-scale quantities, it is possible to conveniently produce macroscopic materials from these building blocks and process them into arbitrary three-dimensional shapes. A sintered solid of IO-NCTs was prepared by the abovementioned centrifugation method (Figure D.43), and a mold was created by etching the MIT school logo into a bar of polyoxymethylene (Figure D.44). The solid was then pressed into the mold with 500 Newtons of force and removed to yield a freestanding block with the embossed logo and dimensions of 3.9 mm x 2.6 mm x 0.25 mm (Figure

131

5.1E, Figure D.45, and Figure D.47). SAXS confirms the NCTs remain ordered after processing (Figure 5.1F), and SEM imaging reveals the microstructure is preserved (Figure D.46).

5.3. Conclusion

Here, we have demonstrated a method for manufacturing bulk, solid materials from a nanoparticle-based building block that can be manipulated into arbitrary macroscopic shapes while maintaining nanoscale control over ordering. The observation of sintering and grain development makes the NCT system an excellent platform for future studies into the similarities between colloidal assemblies and atomic materials. Furthermore, NCTs may serve as analogues to atoms in conventional materials, but their larger size will enable their *in-situ* characterization during deformation to allow the visualization of defect formation. Finally, these hierarchically designed NCT solids offer a new opportunity for integrating nanoscale properties into macroscale materials to create advanced nanocomposites with unique plasmonic, magnetic, or mechanical properties.

Chapter 6. Future Areas of Investigation for Directed Assembly of Colloidal Nanoparticles

CHAPTER ABSTRACT

DNA, given its information-rich capacity in nucleobase sequence, has proven a highly programmable ligand to direct nanoparticle crystallization. Indeed, the organization behavior of DNA-grafted nanoparticles mimics atomic crystallization to such a degree, this building block has earned the moniker "Programmable Atom Equivalents" (PAEs). Atomic behaviors, systems, and processing methods continue to provide hypotheses and inspiration for further study into PAE assembly and for controlling structure of PAE-based materials. As more analogies to atomic behavior are developed, PAEs can become a key proxy system for examining complex atomic phenomena. The areas still underexplored in the field of PAEs and colloidal assembly are *in-situ*, real-space imaging of crystallization behavior and controlled, arbitrary habit of PAE crystallites. Given the precision accessible by the PAE building block, its behavior is the ideal model system for systematically studying and understanding complex, colloidal structure control. Ultimately, the insights garnered from PAEs can be universalized and extended into the other colloidal systems (*e.g.* Nanocomposite Tectons) to improve the structure-defining capacity of nanoparticle-based materials.
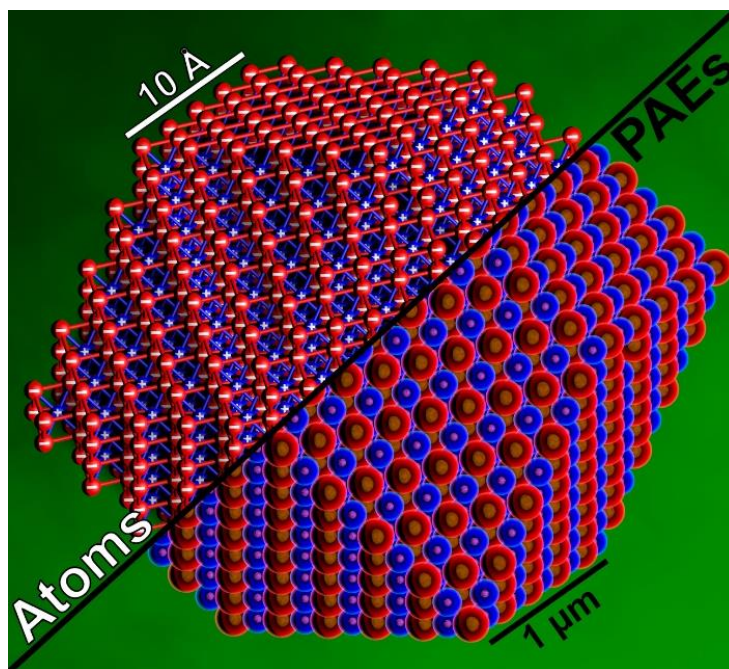
6.1. Using PAEs as a Proxy System to Study Atomic Crystallization

As more analogies between atomic crystallization and PAE crystallization are elucidated, the atomic scale continually provides concepts and knowledge that can be explored at the nanoscale using PAEs. In turn, PAEs could potentially provide a nanoscale platform through which specific crystallization behaviors that are challenging to directly study at the atomic scale could be investigated (Figure 6.1). This section will elucidate potential areas of investigation in which the programmability of DNA-coated NP assembly has not yet been fully realized as a means to understand basic crystallization phenomena, but in which there exists significant potential for scientific discovery.
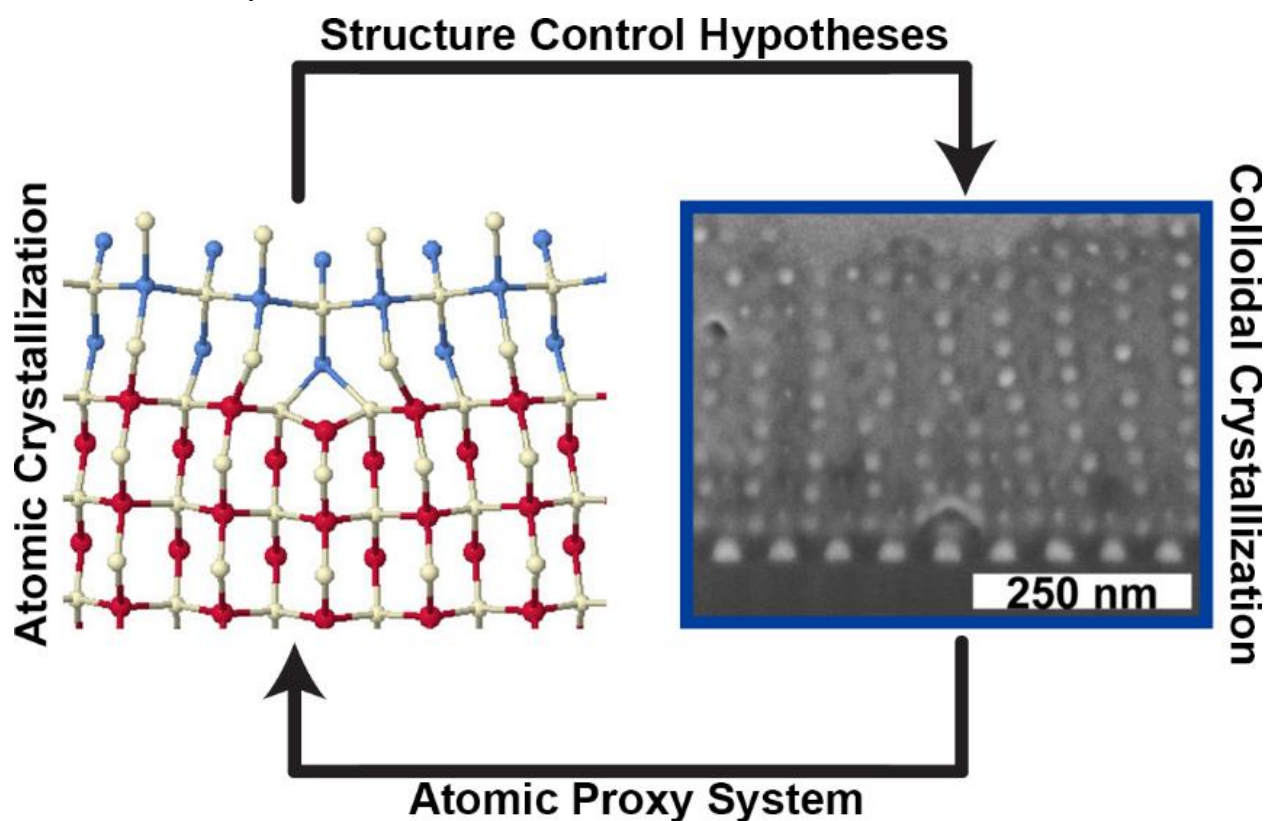
Figure 6.1: The strong structural analogies between atomic and "programmable atom equivalent" crystal formation allows for both atomic systems to provide hypothesis inspiration for colloidal crystallization and for "programmable atom equivalents" to be used as a proxy system for atomic crystallization. Adapted with permission.[22,26] Copyright 2008, IOP Publishing. Copyright 2018, ACS.

Historically, proxy systems have precedence in elucidating atomic behavior before direct analytical techniques are available. For instance, "bubble rafts" were used to observe grain

boundary formation,[245] providing the first experimental evidence for behavior such as plastic deformation *via* slip and impurity segregation at the grain boundary.[246,247] The main advantage of the bubble raft proxy system is that bubble rafts can be observed with the naked eye, while atomic scale resolution was only developed decades later.[23] On the same principle, PAEs as analogs for atomic systems can be readily imaged with micron scale or even nanoscale resolution, allowing for optical and electron microscopy techniques to monitor the crystallization processes with real-space imaging techniques.[104,248,249] Furthermore, the properties of a PAE (binding characteristics, size, relative softness, etc.) are precisely programmable and tunable (Section 1.3), whereas an atom's characteristics are dictated by its identity. Utilizing atoms as building blocks, it is difficult to independently adjust variables like size and binding strength without simultaneously changing characteristics such as binding direction or electronic properties.[129] Using PAEs as a proxy system could enable the independent investigation of the effects of specific variables on complex, atomic phenomena. One potential area of investigation is why certain systems undergo surface diffusion *via* atom exchange mechanisms as opposed to adatom hopping mechanisms.[250] Current theories include effects from tensile surface stresses, surface relaxation about the adatoms, or increased stability from surface-adatom interactions during coordinated exchange.[251] Using PAEs as a proxy system, in which the effects of each of these parameters may be isolated by separately programming adatom-surface, surface-surface, and surface-bulk interactions (Section 1.3.2), could provide more controlled empirical datasets relative to that provided by existing atomic systems and facilitate the development of a theoretical framework behind these distinct mechanisms. Already, the heteroepitaxial PAE template elucidated in Chapter 4 has proven promising in demonstrating key atomic thin film behaviors that could be more deeply explored. Namely, when PAEs are slow-cooled onto nandodot arrays with slight amounts of lattice mismatch, the near-equilibrium, thin film crystallization allows for the development of a faceted surface designed to alleviate bulk strain or eliminate high-energy facets at the cost of more surface area. This phenomenon is commonly known as the "faceting instability" in atomic thin films[166,252,253] and should be investigated more deeply in the PAE epitaxy platform.
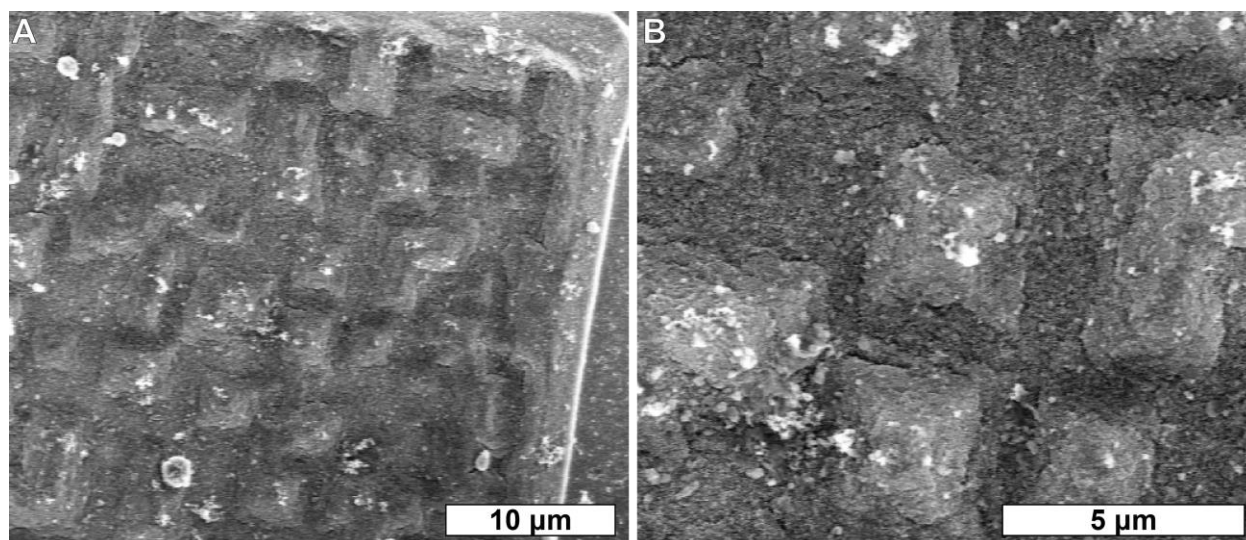
Figure 6.2: SEM micrographs of PAEs slow-cooled onto nanodot arrays with slight lattice mismatch, demonstrating single-crystal, thin film constructions that potentially exhibit a faceting instability.

The PAE building block provides a platform for structure control across many length scales, including the elemental composition of the NP cores, the nanoscale size and shape of the particle and DNA linkers (Section 1.3.1), the coordination environment of the particle within a crystallographic unit cell (Section 1.3.3), and potentially the lattice superstructure (crystallite habits, orientations, and defects) (Section 1.4). However, most of the potential and hypothesized applications of PAEs as a proxy system to study analogous atomic crystallization behaviors and as a unique materials synthon are just beginning to be realized. An ever-growing understanding of the PAE construct and its colloidal assembly behavior is necessary to develop both analogies to atomic behavior as well advance the field of colloidal interactions in general. Thus, this chapter encourages both experimental and theoretical research that facilitate in understanding the complexities of dictating structure in PAE assemblies, in particular the development of new analytical tools and imaging techniques.[248,249]

6.2. Development of New Tools and Techniques to Probe PAE Assembly

Major breakthroughs in materials design are often preceded by the invention of new diagnostic tools or instrumental measurement techniques, as these allow for exploration of previously unanswerable research questions. As understanding of the strengths and limitations of analogizing PAE assembly to atomic crystallization are elucidated, many of the hypotheses that

could be probed will require advancements in characterization tools to fully explore these comparisons. A key area of investigation for PAE crystallization is therefore the development of new tools and techniques that allow for complete understanding of PAE assembly behavior. For atomic systems, *in situ* imaging of chemical reactions has only been achieved using sophisticated non-contact atomic force microscopy with a single carbon monoxide molecule tip.[254] However, the PAE proxy system occurs at significantly different size, time, and energy scales that make PAE assembly potentially much easier to directly observe and characterize *in situ*.[104,255] If the studies into the complex factors that control PAE assembly continue to show strong correlation to atomic crystal formation (Section 1.4), it is reasonable to hypothesize that the direct observation of these phenomena could lead to generalizable insights into not just the thermodynamics of crystallization but also the pathways by which both colloidal and atomic crystals form. Nevertheless, the predominant method for monitoring nanoscale PAE assembly *in situ* still relies on reciprocal space techniques such as X-ray scattering. While SAXS has allowed for real-time examination of crystal formation in nanoscale PAEs,[153] this method is indirect and provides information solely about the bulk structure of the lattices being formed.[256] At larger length scales, micron-sized PAEs have been observed using optical microscopy, which has already afforded a wealth of information on material structure during the crystal growth process.[104] Nevertheless, these PAEs are typically only examined in pseudo-2D architectures that are significantly affected by gravitational forces, meaning that their behavior may not entirely mimic atomic crystal formation.

In principle, recent advances in solution phase electron microscopy[255] could be used to examine PAE assembly at the nanoscale—indeed, some examples of *in situ* imaging NP crystallization (using non-PAE architectures) have already been developed,[248,249] indicating that this method has significant potential for examining PAE behavior. The major challenge for such a technique is in producing an *in situ*, solution phase electron microscopy platform with the necessary resolution that uses non-damaging levels of radiation to the PAE construct. However, the establishment of such a technique would provide significant benefit for the use of PAEs as atomic proxy systems (Section 6.1), as it could allow for imaging of crystallization behaviors that would be challenging or impossible to observe in atomic crystals.

Importantly, development of these *in situ* techniques would further enable the ability to investigate atomic systems through a PAE proxy by taking advantage of the independently

programmable design handles to isolate the effects of each individual PAE characteristic. For example, while some techniques exist to image behavior such as defect diffusion or surface diffusion in atomic systems,[257–259] a PAE proxy system would allow for investigation into changing one parameter, such as bond energy, without altering any other properties like building block size or bond directions. Additionally, *in situ* microscopy would enable direct observation of phenomena like grain formation and grain growth mechanisms which have been hypothesized for atomic grains but prove incredibly difficult to track at the level of each individual atom.[173,260,261] Ultimately, such a technological advance would allow for the use of PAEs to investigate any number of crystallization mechanisms including TTT behavior in nanoscale PAEs, Ostwald ripening versus oriented reattachment of crystallites, defect formation, grain boundary diffusion, plastic deformation, and crystal growth both homogenously and heterogeneously at interfaces. Furthermore, this more advanced observation of PAE assembly would enable a deeper understanding to the complex combination of forces that contribute to colloidal behavior beyond those already analogized in the "atom equivalent" framework. We would note that, in the context of nanoscale PAEs, the direct imaging of crystal formation remains an underinvestigated area. Thus, while the strong analogies to atomic crystallization indicate that the projected benefit from such studies would be large, it remains to be seen exactly how much information gained from such systems can be directly generalized to atomic crystallization. We would therefore encourage the community to continue to develop characterization tools to achieve this goal.

6.3. Arbitrary Control over Superlattice Habit

In addition to a stronger understanding of the dynamics of individual building blocks, a second major goal for PAE superstructure control is the ability to arbitrarily control PAE crystallite habit (size and shape). Recently, single-crystal PAE architectures have been used as individual optical devices in geometrically sensitive applications, reliant on their well-defined, thermodynamic Wulff polyhedron structure.[29,262,263] Furthermore, theoretical work indicates that AuNP superlattices of precisely defined shapes exhibit unique optical responses.[264,265] However, the shape of the currently accessible Wulff crystals[27,148,155] is inherently dictated by the crystallographic symmetry of the corresponding unit cell and cannot be arbitrarily manipulated. If successful in dictating PAE crystallite size and shape, such a structure-defining strategy would

advance the understanding of colloidal crystallization and broaden the realm of applications available to NP-based crystallites.

In atomic systems, multiple mechanisms have been explored as a means of controlling crystal habit,[266] and many of these have yet to be examined in PAE superlattices, indicating a wide area of potential research opportunities. For example, limited tuning of superlattice shape could theoretically be achieved by nucleating crystals at a DNA-functionalized surface, possibly allowing for tunable Winterbottom constructions that effectively truncate the thermodynamically preferred Wulff polyhedra at specific lattice planes, taking advantage of DNA's programmability to tune substrate-PAE interactions.[267,268] Extending this strategy of imposing boundary conditions on PAE crystallite growth, the Summertop formalism (where nucleation and growth are restricted by multiple interfaces)[269] could also be investigated by assembling PAEs at surfaces with concave or convex shapes. Alternatively, just as metal NPs of varying shapes have been synthesized through the introduction of facet capping agents during nucleation and growth,[117,119,270,271] it may be possible to manipulate PAE superlattice crystal shape using nanoscale "capping" constructs. Each of these hypotheses to control PAE crystal habit utilizes an atomic mechanism as inspiration. However, none of the methods has been explored yet, and no analogous means of using these mechanisms to control PAE lattice habit has been developed to date.

In atomic systems, the synthesis of heterocrystals with disparate material properties allow for the fabrication of devices, such as transistors, enabled by junctions of semiconductors with different band structures (*e.g.* non-uniform composition or doping profiles).[194,272,273] Analogously, the development of crystals that possess a singular overall crystal structure but different PAE compositions at different points along the lattice would yield spatially variant properties within a PAE material, enabling the creation of highly complex NP-based devices if the variance is well-understood and programmable. It is important to note that such a structure could be achieved due to the fact that the packing of PAEs within a lattice is dictated by the overall hydrodynamic radius of the building blocks, and the identities of the NP cores can be tailored independently of this value (Section 1.3).[69] As a result, multiple different PAEs could, in principle, be used to form a single crystal structure, even if their NP cores were widely varied in size or elemental composition.[69,83,84,88,92,274]

Recently, preliminary work has been done to extend spatial control over PAEs at a surface by templating the deposition of PAE films using top-down lithography methods (Section 1.4.2). Strategies include using site-specific e-beam irradiation to damage a DNA-functionalized interface prior to deposition of a PAE monolayer resulting in NP size segregation,[162] depositing PAEs onto lithographically defined gold "landing pads" or into PMMA wells,[158–160] and epitaxial deposition on arbitrarily shaped arrays of gold nanodots.[26,147] For instance, extending the concepts of Chapter 3, preliminary steps to control PAE, single-crystal habit shape utilizing slow-cooled crystallization of PAEs on nanodot arrays (Figure 6.3). When crystallized on a square array, the resulting single-crystal, PAE crystallite conforms to the size and epitaxial orientation of the lithographic pattern. When the pattern is elongated in one direction, the resulting habit shape is similarly elongated. This preliminary evidence demonstrates that the epitaxial PAE template may be a suitable strategy to explore the effects of several varied and complex shapes on nanoparticle crystallization at an interface.
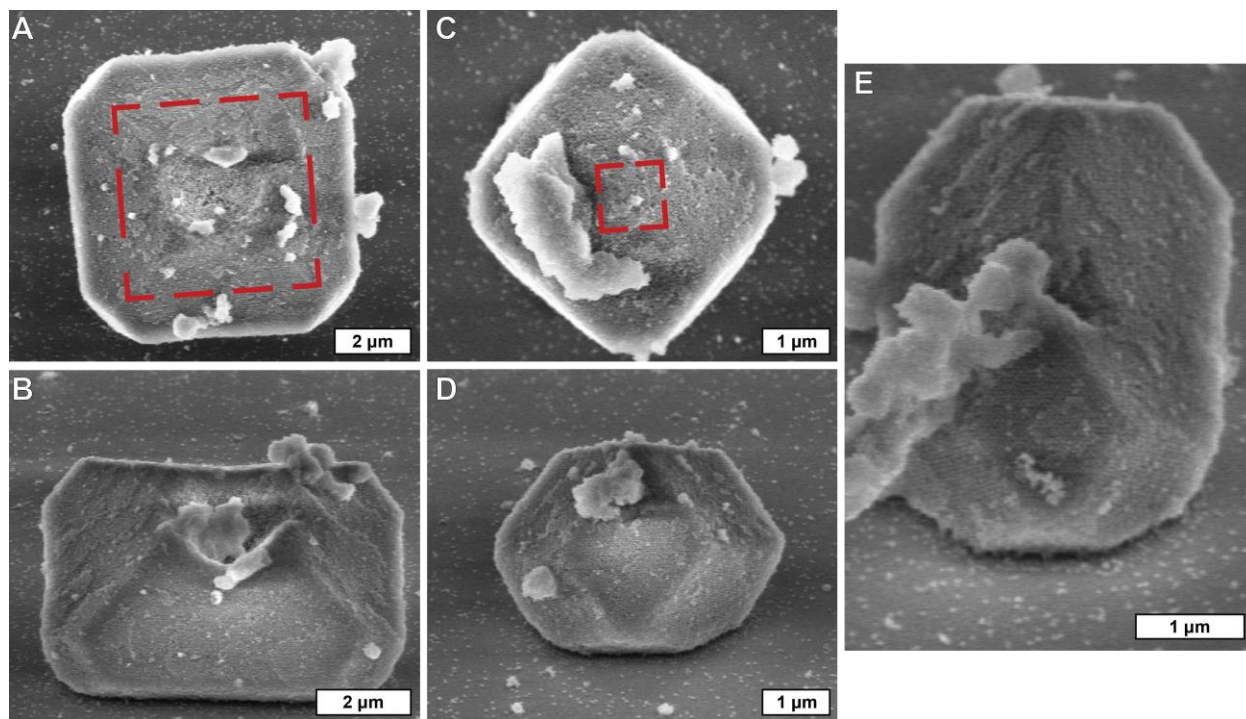
Figure 6.3: Top-down (A and C) and tilted (B, D, and E) SEM micrographs of PAEs slow-cooled onto epitaxially matched nanodot arrays demonstrating single-crystal constructions that conform to the lithographically defined array shape of a 5 µm square array (A and B), a 1 µm square array (C and D), and 1 µm x 5 µm rectangular array (E).

Future work may be done to investigate post-processing techniques to manipulate the PAE material after assembly. For example, DNA hairpins could be utilized to detach the resulting crystallites or thin films from a substrate to produce free-standing PAE structures of defined shape and size. Additionally, lithographic ablation could potentially be used to controllably remove sections of the PAE aggregate without altering or damaging the other regions of the superstructure. The development of such high fidelity, high precision lithographic techniques would enable the construction of nanomaterial devices from PAE materials, taking full advantage of the properties nanostructured architectures provide. It is important to note that much of this work is still at the stage of simply developing the prerequisite tool-set needed to make such complicated structures. Regardless, pairing the programmability of DNA-encoded assembly with sophisticated lithographic patterning techniques could potentially enable hierarchical structures with design features across multiple length scales; similar types of structures that have been fabricated *via* lithography alone have shown promise for developing materials with multiple unique physical properties.[275–278] The advantage of the PAE system would be to improve the resolution,[123] complexity,[69] or stimuli responsiveness[136,142] of such systems.

6.4. Expanding the Properties of Nanostructured Materials

In NP-based materials, properties are garnered through the collective properties of the constituent composite materials (*i.e.* PAE core composition, Section 1.3.1),[119,187,188] but, more importantly, emergent properties can arise from an ordered, nanoscale structure,[279] which PAEs are able to provide with exquisite programmability (Section 1.3.3). While many of the properties that will be discussed in this subsection have only been proposed and not yet realized, it is important to note that PAEs do indeed provide a unique platform for studying structure-property relationships. Thus, the key advantage of PAEs in developing new structures is not necessarily in providing access to materials for commercial or industrial applications but rather in better understanding how material organization across multiple length scales can be used to tune such physical and chemical characteristics. As specific examples, this subsection explores the impacts of structure on the optical, electrical, and mechanical properties of NP-based materials.

At the atomic scale, optical properties are dictated by interactions between photons and electrons in the material (Figure 6.4).[280,281] However, in "photonic" materials with periodic

structures at length scales comparable to the wavelength of visible light, diffraction from superlattice subunits can be used to design interference conditions to further manipulate light in the material.[280,282–284] A common example of this is a phenomenon known as "structural color," in which a band of light exhibits destructive interference within the material and is, therefore, reflected rather than transmitted. The result is a bulk material color not exhibited in a non-assembled or randomly positioned set of NP subunits.[285–287] Specifically, PAEs have demonstrated structural color due to index contrast between slip planes, causing reflection of specific wavelengths.[288] However, a thorough investigation into the effects of PAE design variables (e.g. lattice parameter, NP core shape, etc.) on the resulting color and further optical properties of NP assemblies still remains an underdeveloped area of research.

Electrical behavior in atomic systems is governed by electron-lattice interactions within the material,[25,289] but materials with coupled capacitive and inductive subunits can be used to design collective excitation behaviors (Figure 6.4).[290–292] Macro-scale antenna arrays have utilized these concepts to manipulate electromagnetic fields in exotic ways, such as the split-ring resonator arrays to generate negative refractive-index surfaces enabling stealth planes to remain undetected by radar.[290] By fabricating similar coupled structures at the much smaller nanoscale, it would be possible to extend this cloaking behavior into the visible.[293] However, conventional, top-down lithographic techniques capable of fabricating the nanoscale features required to manipulate wavelengths of light in the visible spectrum are impractical methods to generate large, 3D patterns.[294,295] This inherent tradeoff between resolution and bulk synthesis restricts these unique materials to either limited-size applications or the manipulation of low-frequency electromagnetic waves, such as radio waves. Conversely, PAEs offer a programmable, bottom-up synthesis approach to create and study 3D bulk materials with well-defined nanostructure, promising an expansion of light-manipulating applications for NP-based materials.
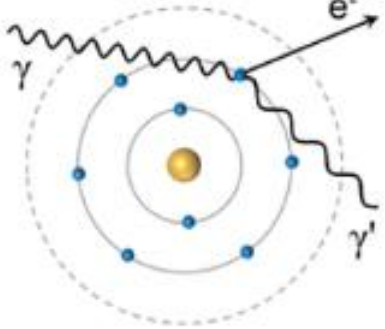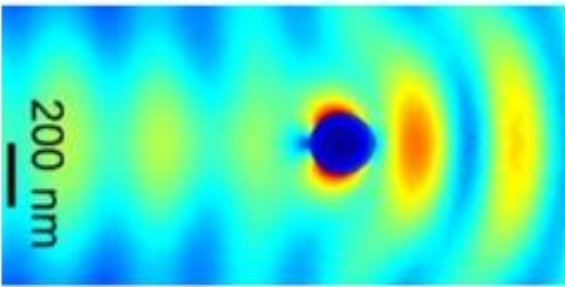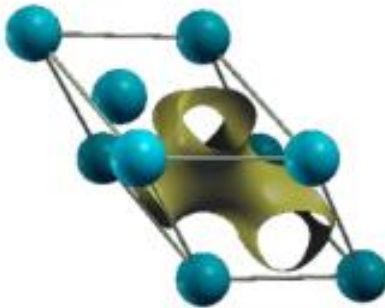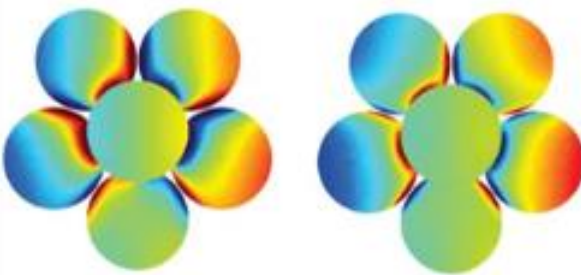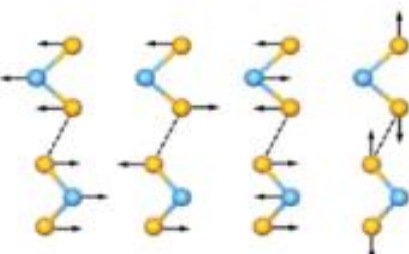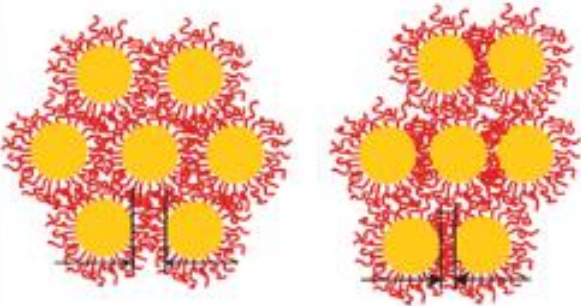
Figure 6.4: (Top) Optical, (middle) electrical, and (bottom) mechanical properties of materials can be manipulated at both the (left) atomic scale and (right) nanoscale, yielding different physical phenomena depending on the length scale of the ordering. Adapted with permission.[281,284,291,296,297] Copyright 2009, 2012, 2013, and 2018, Springer Nature. Copyright 2012, Elsevier. Courtesy of L Paulatto.

In atomic systems, phonons are responsible for the transport of sound and heat through a material due to atomic vibrations (Figure 6.4).[289,296] Previous work has demonstrated that NPs

144

embedded into a substrate can modify the behavior of these phonons by either modifying the interfacial behavior of the embedded matrix[298] or by causing phonons to scatter.[299] As with photonic and electronic structural properties, designing a PAE system with interfering mechanical modes, or coupled mechanical oscillations, could potentially allow for structural control over simple mechanical properties (*e.g.* propagation of heat and sound).[300] More sophisticated structures, such as auxetic composites at the macroscale,[301] have demonstrated exotic properties that are specifically enabled by collective behavior (*e.g.* negative Poisson ratio[302]). Because these behaviors are dictated solely as a function of the overall organization of structural features and not length scale, nanoscale equivalents are hypothesized to be achievable with PAEs due to their exquisite control over hierarchical organization; however, this would require further investigation into the mechanical behavior of PAE lattices, as well as techniques to probe PAE structural response to mechanical stimuli.

While the potential for PAE-based materials with exotic properties is enormous, many of these applications require NPs with specific elemental compositions. However, not all compositions, sizes, and shapes of NPs that can be synthesized have been demonstrated as templates for PAEs as yet (Section 1.3.1). The major challenge limiting the number of particle compositions that can be examined in PAE crystallization is that new attachment chemistries will be required to functionalize a dense monolayer of DNA on those materials. While there have been some attempts at creating a generalizable attachment chemistry for DNA to NPs of arbitrary composition,[83] this methodology has not been widely adopted due to the challenging synthetic protocol and limited yields. Additionally, the current crystallographic symmetries available to PAEs almost exclusively rely on isotropic particles, and different particle valencies are largely imparted by the use of different NP core shapes (Section 1.3.3);[98] this is in direct contrast to the atomic valencies that give rise to complicated and low symmetry lattices.[5,271] In theory, PAEs with greater control over the directions of their bonds could be realized with the development of anisotropically functionalized particles. Simulations reveal that such "patchy" PAEs with specific binding sites across their surfaces would have unique self-assembly behavior,[303] but the currently synthesizable patchy particles have yet to produce crystalline materials with long-range order.[34] However, if successful, anisotropic control over assembly could enable creation of exotic analogs to atomic symmetries including quasicrystals,[304] chiral lattices,[305] or high-entropy alloys.[306]

Research developments in chemistry will therefore be required to access the full programmable potential of the PAE building block.

In addition to limitations in accessible core compositions, one of the major inherent limitations in the utility of PAE-based materials synthesis is that DNA duplexes exhibit limited stability in different environments,[132,134,138,139] and thus, PAE lattices are not readily usable for many different devices or applications. Some techniques have been developed to increase the stability of the PAE system after assembly, such as incorporation of intercalating elements to increase the DNA binding strength[124,125] or selective nucleation of materials such as silica[192] or silver[126] in the vicinity of the PAE crystals, embedding them into stable states that can be removed from solution. Modifications to the DNA linkers (Section 1.3.2) enable further control of the material properties of the PAE system, such as the dynamic responsivity,[136] stability in varying environments,[134] Young's modulus,[192] or conductivity.[126] However, the physical and chemical limitations of DNA still inhibit transference of PAEs to a wide array of conditions.

As mentioned at the beginning of this section, the key advantage of PAEs is in the development of structure-property relationships that could later be explored in a more diverse set of building blocks that are not necessarily based on DNA-programmed assembly. As a result, much of the PAE work highlighted in this thesis provides a blueprint for such materials, allowing PAEs to serve as inspiration for future work and to aid the development of future building blocks. If a suitable replacement for DNA that possesses many of the characteristics that enable PAE assembly (programmable binding interactions, controlled length, *etc.*) were developed, much of the work elucidated in this thesis could be translated to a significantly greater range of material designs. An example would be to replace the DNA with different polymeric analogues, thereby enabling control as a function of both the NP core and the ligands that bind the particles into a lattice. Recently, the first example of such a broadly tunable NP structure has been developed, dubbed the "nanocomposite tecton" (NCT).[21] NP superlattice synthesis with NCTs has demonstrated that many of the concepts developed in the PAE system can apply to a generalized NP building block thus allowing the significant amount of information that has been outlined in this thesis to be translated to potentially a significantly wider array of materials. As a proof of concept, initial work on NCTs used poly(styrene) ligands rather than duplexed DNA, where a complementary hydrogen bonding motif at the ends of the poly(styrene) chains enabled multivalent binding interactions

between particles. Like the PAE system, the NCTs exhibit selective particle-particle bonding that allows for the assembly of superlattice structures with independently tunable particle size, interparticle spacing, and crystallographic symmetries. However, unlike the PAE system, NCTs use no expensive biological components and are stable in nonpolar solvents. This work to replace DNA with a wider range of materials greatly expands the design space of accessible material properties, including new mechanical, optical, thermal, or chemical properties.

Appendix A. Supporting Information for Controlling Texture in Programmable Atom Equivalent Thin Films (Chapter 2)

A.1. Synthesis and Fabrication

A.1.1. Gold Nanoparticle Synthesis

Gold nanoparticles (AuNPs) were synthesized from an established seeded growth protocol.[307] Briefly, a 500 mL solution of 2.2 mM trisodium citrate dihydrate was brought to a boil. 2 mL of 25 mM $HAuCl_4:3H_2O$ was rapidly injected to the solution under vigorous stirring. Within one minute the solution began to darken, and after 15 minutes it stabilized as a deep red color. After the initial injection to synthesize the seeds, the solution temperature was lowered to 90 °C and given 30 minutes to equilibrate. To garner NPs of larger size, further injections of 2 mL of 25 mM $HAuCl_4:3H_2O$ were performed, allowing the solution 30 minutes to equilibrate after each. The NPs were characterized by casting onto formvar coated TEM grids and imaging on a JEOL 2010 Advanced High Performance TEM. Image analysis on images with at least 250 NPs total was performed with ImageJ and used to calculate the mean particle diameter. Two different sizes of NPs were synthesized with average diameters of 12.5 nm (8% st. dev.) and 19.1 nm (9% st. dev.), nominally referred to as "small" and "large" NPs in this document.

A.1.2. DNA Sequences and Synthesis

The following oligonucleotides (Table A.1) were either purchased from Integrated DNA Technologies (IDT) or synthesized as described below.

Table A.1: DNA Sequences.

Sequence Name	Sequence (5'-3')
Anchor Strands	
Anchor Y-SH	TCA ACT ATT CCT ACC TAC (EG$_6$)$_2$-SH
Anchor X-SH	TCC ACT CAT ACT CAG CAA (EG$_6$)$_2$-SH
Linker Strands	
Linker Y-B	GTA GGT AGG AAT AGT TGA A TTCCTT
Linker X-A	TTG CTG AGT ATG AGT GGA A AAGGAA
Linker X-1d20-A	TTG CTG AGT ATG AGT GGA A TTT AGT CAC GAC GAG TCA TT A AAGGAA
Linker Y-2d20-B	GTA GGT AGG AAT AGT TGA A TTT AGT CAC GAC GAG TCA TT A TTT AGT CAC GAC GAG TCA TT A TTCCTT
Linker X-2d20-A	TTG CTG AGT ATG AGT GGA A TTT AGT CAC GAC GAG TCA TT A TTT AGT CAC GAC GAG TCA TT A AAGGAA
Duplexer Strand	
d20	AAT GAC TCG TCG TGA CTA AA

Synthesized oligonucleotides (thiolated anchor strands) were created on a Mermade 48 (MM48) DNA synthesizer (BioAutomation) using standard, manufacturer protocols and reagents purchased from Glen Research (Sterling, VA). All strands were synthesized from the 3' end to 5' end on controlled pore glass (CPG) beads. After synthesis, each 1 µmole column of DNA was cleaved from the CPG beads in 1 mL of a 1:1 mixture (by volume) of 30% ammonium hydroxide and 40% aqueous methylamine solution at 55 °C in a shaker set to 1400 rpm for 1 hour. After cleaving, the solution was evaporated with flowing air. The dried samples were resuspended in nanopure water and filtered through a 0.2 µm syringe filter to remove the CPG beads. Oligonucleotides were then purified using reverse-phase, high performance liquid chromatography (RP-HPLC) on a Phenomenex Jupiter C18 column (5 µm, 250x4.6 mm) and lyophilized. After purification, the DMT protecting groups on the oligonucleotides were removed by adding 2 mL of 20% (by volume) acetic acid solution in water for each 1 µmole synthesis column and allowed to set for 1 hour. This solution was then washed three times with ethyl acetate to separate and extract the purified, deprotected DNA strands. Strands were then aliquoted, lyophilized, and stored in a

freezer until needed. All synthesized strands were characterized by matrix-assisted laser desorption ionization time-of-flight mass spectrometry (MALDI-TOF-MS).
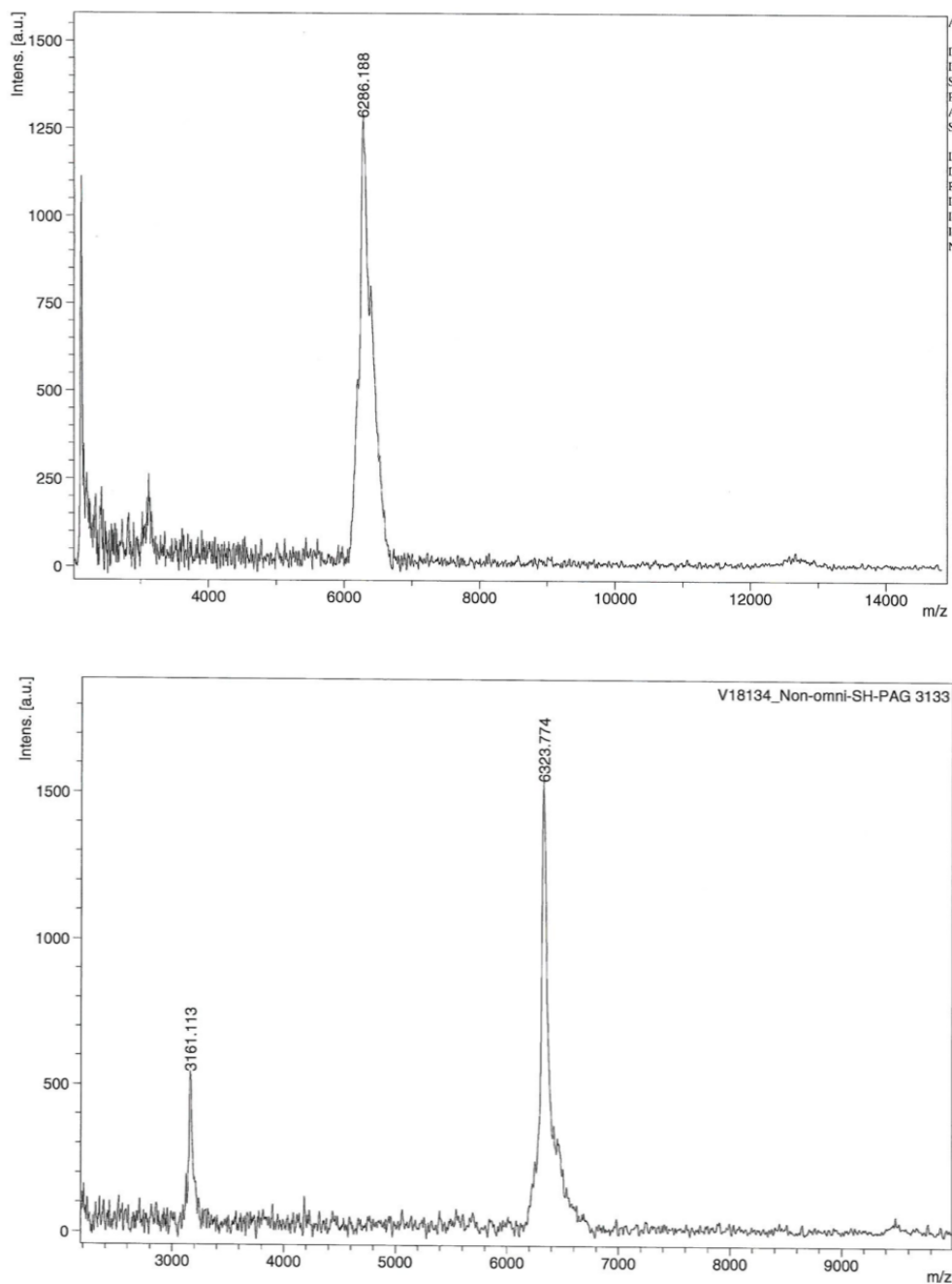
Figure A.1: MALDI-TOF-MS analysis of Anchor Y-SH (top) and Anchor X-SH (bottom) DNA strands showing high purity and accurate molecular weight.

A.1.3. "Programmable Atom Equivalent" (PAE) Synthesis
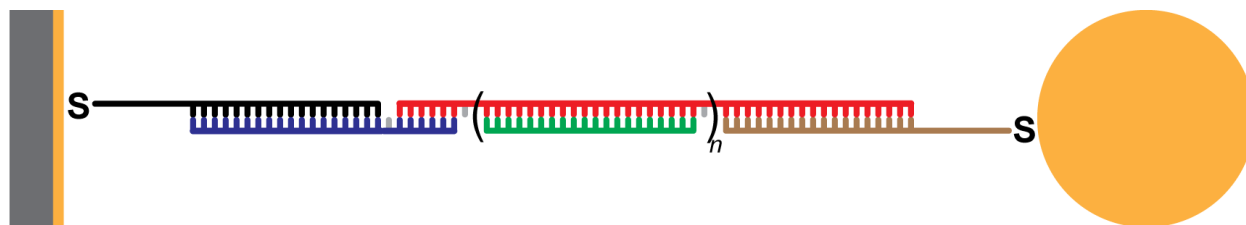
Figure A.2: Schematic representation of DNA design (consisting of modular sections) that allows PAEs to bind to other PAEs with the complementary sticky end and to bind to a functionalized substrate.

DNA "anchor strands" (denoted in black and brown in Figure A.2) are thiol-modified to allow for efficient functionalization to gold surfaces using Au-S chemistry. These strands consist of two six-unit ethylene glycol segments (denoted as $(EG_6)_2$) to increase the flexibility of the DNA chains and improve both grafting density and crystallization ability. The next 18 base sequence is unique and hybridizes only to the complementary "linker strand." In the naming scheme used in Table A.1, the terms X and Y are used to denote these two different 18 base recognition sequences and their complements on the linker strands. Using two, orthogonal anchor sequences ensures that the PAE types do not exchange linkers and thereby binding functionality.

DNA "linker strands" (denoted in blue and red in Figure A.2) contain the complementary, 18-base recognition sequence to hybridize to the anchors (X or Y). The linker strands may or may not contain 20-base "duplexer" region(s) designed to hybridize to an additional "duplexer" strand (green in Figure A.2) and add overall length to the DNA strand and thus increase the PAE's hydrodynamic radius. Table A.1's naming scheme uses "d20" to denote either the sequence of the "duplexer strand" or its complement present in the linker strand. The number preceding d20 in the linker names correspond to the number of these units present in the overall linker. Finally, and most importantly, the linkers conclude in a 6-base, single-stranded "sticky end" denoted as A or B in Scheme 2.1. (Note, a single, ultimately unpaired adenine base exists between each of the aforementioned sequence sections in the linker strands to add flexibility and improve crystallinity.[127]) These sticky ends will exist at the periphery of the DNA corona surrounding a NP or off the substrate and be able to bind to the complementary sticky end sequence (*i.e.* blue and red or A and B sticky ends are complementary). These binding events drive the aggregation

of complementary PAEs. Given their short length, these sticky end connections are constantly forming and breaking, especially when given increased thermal energy. However, many sticky end connections constitute a PAE-PAE bond, keeping the particles tethered below the "melting temperature" (Section 0). This allows the particles to "anneal" and rearrange when heated. The driving force for rearrangement is the maximization of sticky end connections which is accomplished in the densest packing of complementary particles which is generally crystalline arrangements. The particular geometric arrangement (crystal unit cell) that is favored is determined by the size ratio and linker ratio on the two PAE types.[69]

"Programmable Atom Equivalents" (PAEs) were synthesized by functionalizing the synthesized citrate capped AuNPs with a dense shell of one of the thiol-modified DNA ("anchor strands," Table A.1). The 3'-propylmercaptan protecting group of the thiol-modified DNA sequences was cleaved by treating the sequences with 100 mM dithiolthrietol for 1 hour. The strands were desalted using a size exclusion column (GE Healthcare) and then added to a solution of AuNPs (mixed at roughly 1 OD of DNA per 1 OD of AuNPs). After incubating for 1 hour, the solution was brought up to a concentration of 0.01% sodium dodecyl sulfate and 10 mM sodium phosphate. A salt aging process was used to increase the DNA loading by adding phosphate buffer saline (PBS) with 2 M sodium chloride stepwise over the course of several hours until a final concentration of 0.5 M NaCl was reached. After the final NaCl addition, the solutions were set overnight. Unbound DNA was removed by three rounds of centrifugation (13,000 rpm for 70 min for the small NPs and 12,000 rpm for 20 min for the large), removal of supernatant, and resuspension in nanopure water. The final resuspension was done in PBS with 0.5 M NaCl.

"Linker strands" were pre-hybridized by incubating with appropriate number of equivalents of the "duplexer strand" (d20) in 0.5 M NaCl PBS. Stock solutions of 100 μM duplexed linkers were incubated at 35 °C for 1 hour to ensure full hybridization and subsequently combined with the corresponding anchor-functionalized AuNPs (in either 80 or 160 equivalents per NP) to yield PAEs. All PAEs created in this project only contained one type of DNA linker. Generally, PAE stock solutions were kept at 200 nM of NPs until needed. In all cases, the concentrations of AuNPs and DNA were characterized using UV-Visible Spectroscopy, monitoring at 520 nm or 260 nm, respectively, and using extinction coefficients calculated by Ted Pella and IDT, respectively.

A.1.4. Substrate Fabrication and Functionalization

The substrates for PAE thin film deposition were fabricated using standard fabrication techniques at the Materials Technology Laboratory (MTL) at MIT. 150 mm P-Type Prime (100) silicon wafers with polished surfaces and resistivity 1-100 Ωcm were purchased from Wafernet. 2 nm of chromium (Cr) followed by 8 nm of gold (Au) were deposited on the wafer at a rate of 0.2 Å/sec in an AJA eBeam evaporator under vacuum (6 x 10^{-6} Torr). The thin layer of Cr was included to improve the adhesion of the Au thin film to the silicon surface. Au was chosen to enable use of the same thiol attachment chemistry used to functionalize DNA to the nanoparticles. Finally, in principal, any thickness of Au could be utilized for the fabrication of these surfaces as long as the surface was a continuous thin film; 8 nm was found to meet these specifications. The chip was then diced using a diesaw in 8x8 mm pieces.

DNA functionalization of the substrates was performed by incubating each substrate in a 5 µM "anchor strand" solution (Anchor Y-SH, Anchor X-SH, or a mixture) in buffer (0.5 M NaCl PBS) overnight, after the propylmercaptan protecting group of the thiol-modified DNA was cleaved (see Section A.1.3). To remove unbound DNA, the substrates were rinsed 3 times in nanopure water with vortexing. Linkers then were hybridized to the substrates by incubating the substrates in the appropriate 0.5 µM "linker strand" solution (Linker Y-B, Linker X-A, or a mixture) at 0.5 M NaCl at 35°C overnight. Unhybridized linkers were removed by rinsing the solution 5 times in buffer.

To garner substrates with differing relative amounts of binding functionality (i.e. different amounts of the complementary sticky ends), both the anchor strand solution and the linker strand solution described above contained varying amounts of Y vs X strands such that the overall DNA concentration remained constant. The relative amounts explored in this project are summarized in the following table.

Table A.2: Variable Sticky End Ratios.

% Linker Y-B	Amount Linker Y-B	Amount Linker X-A	% Linker X-A
0%	0/6	6/6	100%
16.67%	1/6	5/6	83.33%
33.33%	2/6	4/6	66.67%
50%	3/6	3/6	50%
66.67%	4/6	2/6	33.33%
83.33%	5/6	1/6	16.67%
100%	6/6	0/6	0%

A.1.5. Layer-by-Layer Deposition

The layer-by-layer deposition of amorphous PAE thin films was done rapidly at room temperature. A and B PAEs, appropriate to the system chosen (Section A.3.1), were diluted with PBS down to 10 nM. One functionalized substrate (or a pair of two identical substrates positioned back-to-back) was placed in 1 mL of one type of PAE and incubated for 1 hour in an Eppendorf Thermomixer held at 25 °C and 1,000 rpm to deposit the first layer. The substrate(s) was then removed, gently washed 8 times in PBS, and placed in the opposite PAE type for the second layer deposition. 2 µL of the 200 nM PAE stock was then added to the 1 mL of the first PAE type to "refresh" and return the solution to 10 nM. This process was repeated for the desired number of layers (5, 10, 20, or 30). In the bi-functionalized substrate cases, thin films with the first deposition layer being PAE A and films with PAE B as the first layer were both synthesized. However, in the mono-functionalized cases, incubation in the PAE type containing the same sticky end as the substrate resulted in no particle deposition, so only the complementary PAE type was deposited as the first layer.

A.2. Instrumentation and Data Collection

A.2.1. In-Situ Small Angle X-ray Scattering (SAXS) Data Collection

All SAXS scans conducted on PAE thin films required the x-ray flux of synchrotron radiation to penetrate the substrate; thus, the *in-situ* rearrangement SAXS experiments were conducted at the 12ID-B station at the Advanced Photon Source (APS) at Argonne National Laboratory. The samples were probed using 14keV X-rays and the system was calibrated with a

silver behenate standard. The beam was collimated using two sets of slits and a pinhole, resulting in a beam size that was ~ 400 µm wide by ~ 200 µm high. Scattered radiation was detected using a Pilatus 2M detector. 1D SAXS profiles of scattering intensity as a function of scattering vector q was obtained *via* radial averaging of the 2D scattering pattern. Where appropriate and applicable (*e.g.* scans taken at several different locations across the homogenous thin film surface), several identical 1D scans were averaged together to increase signal to noise and make the data more generalizable. Example 2D SAXS patterns of PAE thin films, corresponding to the 1D curves presented in Scheme 1B of the main text, are provided below for reference (Figure A.3). Notice, as a consequence of the polycrystalline nature of the thin films relative to the beam direction (Section A.4.2), the 2D SAXS patterns are radially symmetric. Hence, 1D radial averaging results in no loss of information. Therefore, for brevity and clarity, not every 2D SAXS pattern is included in this SI. Where 1D data is presented without its corresponding 2D pattern, the 2D SAXS was confirmed to be radially symmetric.
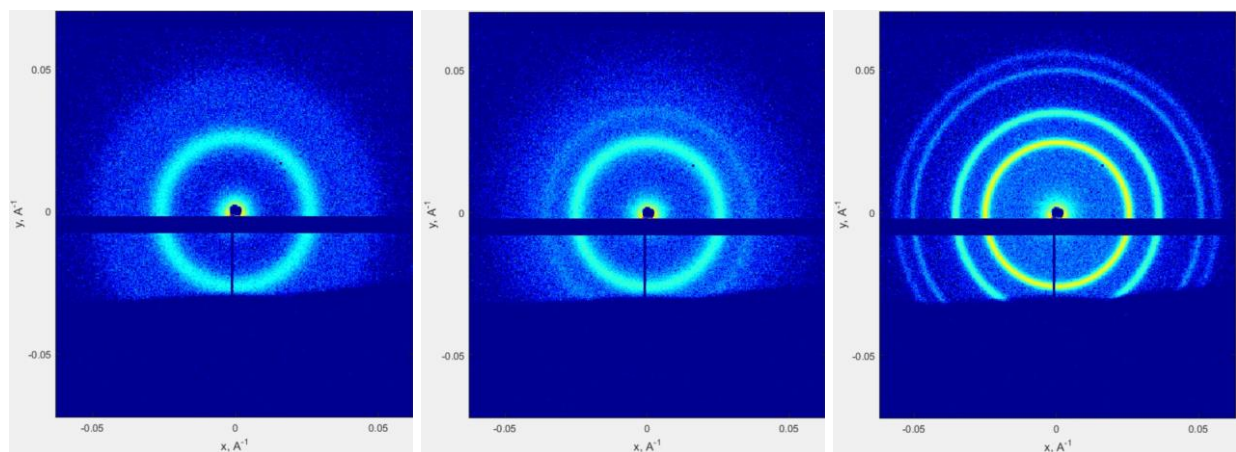
Figure A.3: Time-resolved structural rearrangement evidenced by the 2D SAXS data transforming from an amorphous structure (left, 0 min) with few broad and diffuse rings, through an intermediate state (center, 3 min), to an oriented, crystalline structure (right, 5 min) as evidenced by the presence of several, sharp rings.

The samples were probed using a vertical sample holder constructed from silicone rubber and two glass cover slips that allowed a buffered environment to be maintained and heated (by sample stage) around the sample to preserve DNA hybridization. Importantly, each substrate was

held perpendicular to the x-ray beam direction such that any changes in lattice alignment relative to the substrate plane could be observed (Section A.4.2).

Each *in-situ* annealing/rearrangement experiment was conducted using a temperature-controlled heating stage. The temperature was first set to 5 °C below the PAE system's melting temperature (T_m, Section 0), then ramped to T_m at a rate of 1 °C/min and held at T_m until the SAXS pattern stabilized. During the temperature ramp and hold, a SAXS scan was collected every 30 seconds. Due to damage caused by the x-ray beam, each subsequent scan was collected 250 µm below the previous scan. Prior to and following each rearrangement experiment, the thin film was characterized *via* SAXS at several locations across its surface and its structure was found to be homogenous across the substrate. Following data collection, the stage temperature was cooled quickly over a couple minutes to 25 °C. For some samples, during this cooling process, additional SAXS scans were collected every 30 seconds.

A.2.2. Electron Microscopy of Embedded Thin Films Data Collection

In order to transfer solution-phase PAE thin films to the solid state for characterization by electron microscopy, thin film samples were embedded in silica using a sol-gel process modified from the existing protocols.[176] First, 3 µL of *N*-(trimethoxysilyl)-propyl-*N,N,N*-trimethylammonium chloride (Gelest, 50% in methanol) was added to each substrate in 1 mL of 0.5 M NaCl PBS and left to encapsulate DNA bonds within the superlattices for 30 min on an Eppendorf thermomixer (1,400 rpm, 25°C). 5 µL of triethoxysilane (Sigma-Aldrich) was then added, and the samples were left on shaker for another 30 min before being rinsed with nanopure water 3 times under vigorous agitation. The samples were finally blown dry with compressed air. The embedded thin films were then imaged, top-down, with a Zeiss SEM. Since the substrate with the thin film was placed perpendicularly relative to the electron beam direction, the top surface of the thin film was imaged. This allowed for visualization of the crystalline PAE grains furthest from the substrate.

To image the cross-section of embedded PAE thin films, some samples were characterized on a Helios Nanolab 600 dual beam focused ion beam milling system with a 52° relative difference between the ion and electron beam. After a layer of titanium was deposited over the area of interest, a 15 µm × 1 µm area was milled with a 93 pA (30 kV) ion beam. Each cross-section was then

157

imaged with an 86 pA (5 kV) electron beam using the in-lens detector on the SEM without using the software's tilt correction. Post processing of the SEM micrographs can be done to adjust the *y*-axis to a scale that is representative of the real space length using Equation A.1.

Equation A.1:

$$y_{processed} = \frac{y_{raw}}{\cos(90° - 52°)} = \frac{y_{raw}}{\cos(38°)} = 1.269 \times y_{raw}$$

It is important to note that the titanium protection layer (10s of nm thick) is deposited to prevent the thin film's surface from being destroyed by the ion beam during milling. This deposition is conformal and visible in the cross-sectional SEM micrographs near the top of the images (Figure A.13, Figure A.20, and Figure A.21). Additionally, since this deposition is conducted through the electron irradiation of a gas containing titanium, the deposition penetrates into the lattice to some degree as opposed to simply lying atop it. In crystalline regions, channels of void space between PAEs exist through which the gas can flow and ultimately deposit. However, closer to the substrate surface (always observed near the bottom edge of the micrographs) where the gas has further to diffuse and within amorphous regions with trapped or convoluted void spaces where the gas has difficulty diffusing into, physical voids can be observed.

A.3. PAE Systems

A.3.1. PAE System Designs

For this manuscript, three binary model PAE systems were chosen to explore (bcc, CsCl, and AlB$_2$). Appropriate pairs of A and B PAE designs (specific hydrodynamic size ratios and linker ratios) to achieve these crystal structures were selected from literature precedent,[69] synthesized (Section A.1.3), and verified using SAXS (Section 0). Hydrodynamic size (r_{PAE}) of each PAE is determined based on the diameter of the NP core (d_{NP}) and the number of DNA bases between two NPs, assuming a constant rise per base-pair (bp) of 0.255 nm, each EG$_6$ group is ~ 5 bps, and n is the number of duplexer sections (Equation A.2).[69] The linker ratio refers to the number of linker DNA strands added to each NP (Section A.1.3).

Equation A.2:

$$r_{PAE} = \frac{d_{NP}}{2} + [(2*5bp) + 18bp + (n*21bp) + 4bp] * \frac{0.255nm}{bp}$$

Table A.3: PAE System Designs.

Crystal System	PAE A				PAE B				Size Ratio	Linker Ratio
	d_{NP}	Linker DNA	r_{PAE}	Linker Equiv.	d_{NP}	Linker DNA	r_{PAE}	Linker Equiv.		
bcc	12.5 nm	Linker X-A	14.41 nm	80	12.5 nm	Linker Y-B	14.41 nm	80	1.0	1.0
CsCl	19.1 nm	Linker X-1d20-A	23.065 nm	160	12.5 nm	Linker Y-2d20-B	25.12 nm	80	0.92	0.5
AlB$_2$	19.1 nm	Linker X-2d20-A	28.42 nm	80	12.5 nm	Linker Y-B	14.41 nm	80	0.51	1.0

Calculation of the "sticky end" density at the tip of the DNA corona on each PAE is achievable with geometry by assuming the DNA strands are homogenously distributed across the NP surface. Linker equivalent in the above table is equal to the number of sticky ends (n_{SE}) on each NP. Since the PAE construct forces each sticky end to exist at the periphery of the spherical DNA corona, the areal density can be determined through dividing n_{SE} by the surface area of a sphere with radius r_{PAE} (Equation A.3).

Equation A.3:

$$density_{SE} = \frac{n_{SE}}{4*\pi*r_{PAE}^2}$$

Table A.4: Calculated Sticky End Densities.

Crystal System	PAE Type	Density$_{SE}$ (#/nm^2)	Ratio
bcc	PAE A	0.031	1.00
	PAE B	0.031	
CsCl	PAE A	0.024	2.37
	PAE B	0.010	
AlB$_2$	PAE A	0.0079	0.26
	PAE B	0.0307	

A.3.2. Bulk Melting Temperature (T_m) Analysis

The homogenous (bulk) melting transition of PAE aggregates in solution was monitored with UV-Vis spectroscopy using established literature protocols.[62] For the bcc and CsCl systems, 5 µL of each PAE A and B at 200 nM was mixed together and allowed to aggregate; for the AlB_2 system, 3 µL of PAE A was mixed with 6 µL of PAE B (to match the unit cell stoichiometry). The mixture was then diluted to 1 mL with PBS and placed in a capped cuvette with a stir bar. Under continuous stirring and monitoring at 520 nm with a Cary 5000 UV-Vis, the solution was heated from 30°C to 60°C at a ramp rate of 0.25°C/min. The bulk phase melting temperature was taken to be the inflection point of the melt curve (Figure S4).
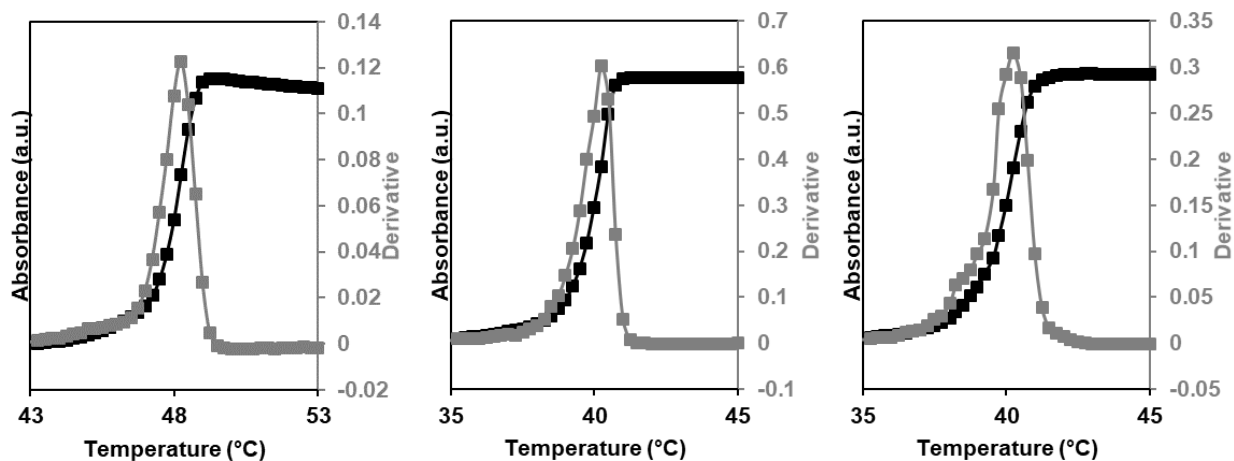
Figure A.4: Melting transition as monitored by UV-Vis absorbance at 520 nm and first derivative whose maximum denotes melting temperature for the PAE systems: (left) bcc, (middle) CsCl, and (right) AlB_2.

Table A.5: Melting Temperatures (T_m) of PAE Systems.

Crystal System	Melting Temperature
bcc	48.25 °C
CsCl	40.25 °C
AlB_2	40.25 °C

A.3.3. Bulk SAXS Data

Verification of the bulk crystallography for each of the PAE systems used in this manuscript was determined from transmission SAXS of slow-cooled PAE aggregates in solution.

For each system, PAE A and PAE B were mixed in the appropriate 1:1 or 1:2 stoichiometric ratio and allowed to aggregate. Some of these aggregates were transferred to a glass capillary (Charles Supper) and sealed with 5-minute epoxy (Home Depot). The rest of the aggregates were transferred to 0.5 mL Eppendorf PCR tubes and placed in a Techne Prime Thermal Cycler. They were heated to above their T_m (Section A.3.2) and slowly cooled over several days, allowing for the equilibrium crystal structure to be formed. These crystals were similarly transferred to capillaries and sealed.

SAXS measurements on both the amorphous aggregates and slow-cooled crystallites were performed at the Massachusetts Institute of Technology (MIT) Center for Materials Science and Engineering (CMSE) X-ray Diffraction Shared Experimental Facility on a SAXSLAB system. The Rigaku 002 microfocus X-ray source produced Cu Kα1 X-rays of wavelength 1.5409 Å; Osmic staggered parabolic multilayer optics focused the beam crossover at the second pinhole. Two sets of JJ X-ray jaw collimation slits set at 0.45 mm and 0.2 mm, respectively, were used to define the beam. The system was calibrated using silver behenate as a standard.

The capillary was placed horizontally in the sample chamber and pumped down to 0.08 mbar. The scattered radiation was detected with a Dectris Pilatus 300K detector set at a distance of 1,400 mm. The 1D SAXS data was obtained *via* radial averaging of the 2D scattering patterns (Figure A.5). These data were then transformed into profiles of scattering intensity as a function of scattering vector q (Figure A.6). The crystallography of each PAE target system was confirmed with comparison to previous work on PAEs[69] as well as through peak indexing (Section A.4.1).

PAE System	bcc	CsCl	AlB₂
Amorphous Aggregates			
Crystalline			
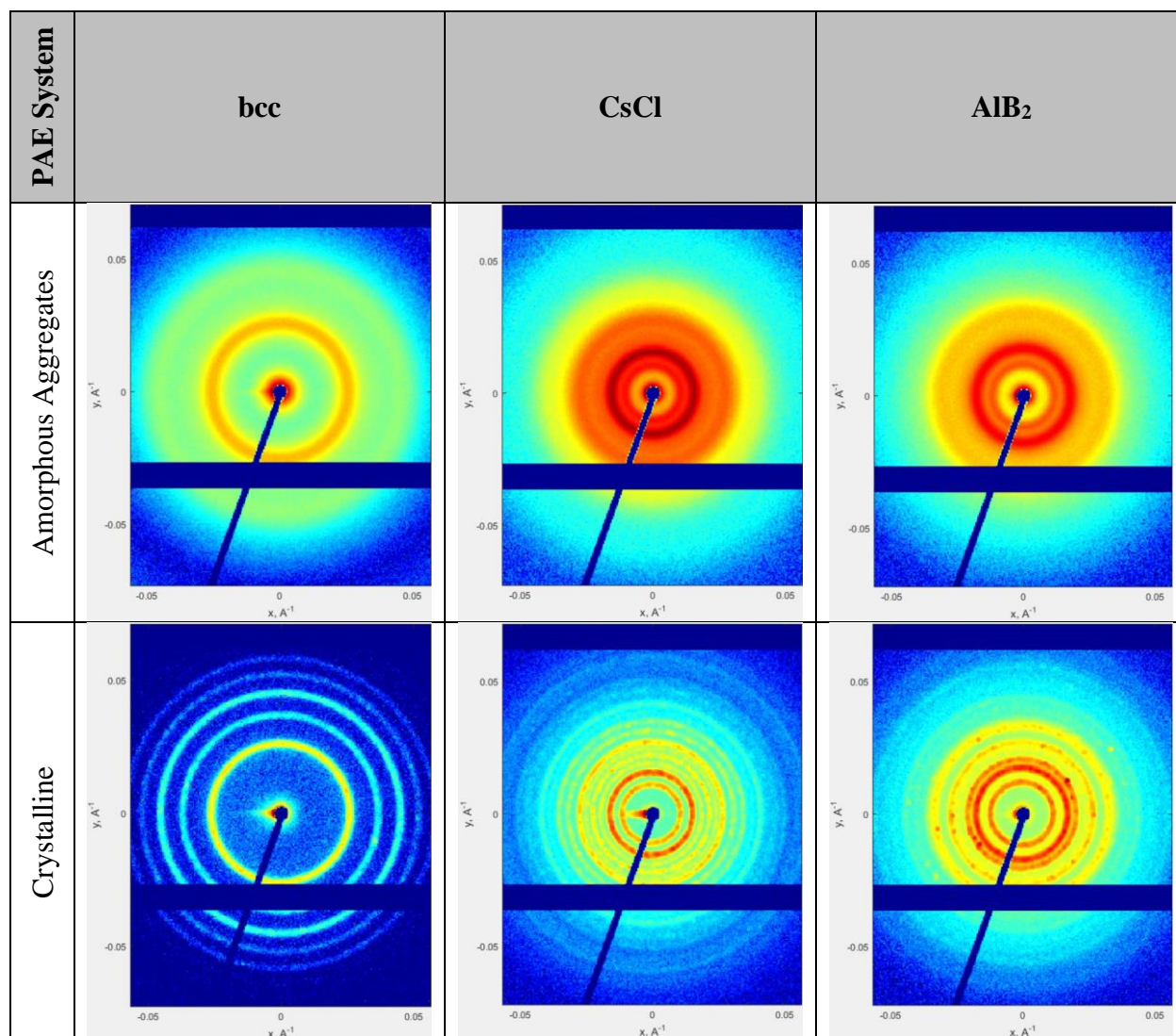
Figure A.5: 2D SAXS data for each PAE system in its bulk (aggregated in solution without the presence of a substrate) amorphous state prior to annealing (left) and its bulk, polycrystalline state after slow-cooling (right).
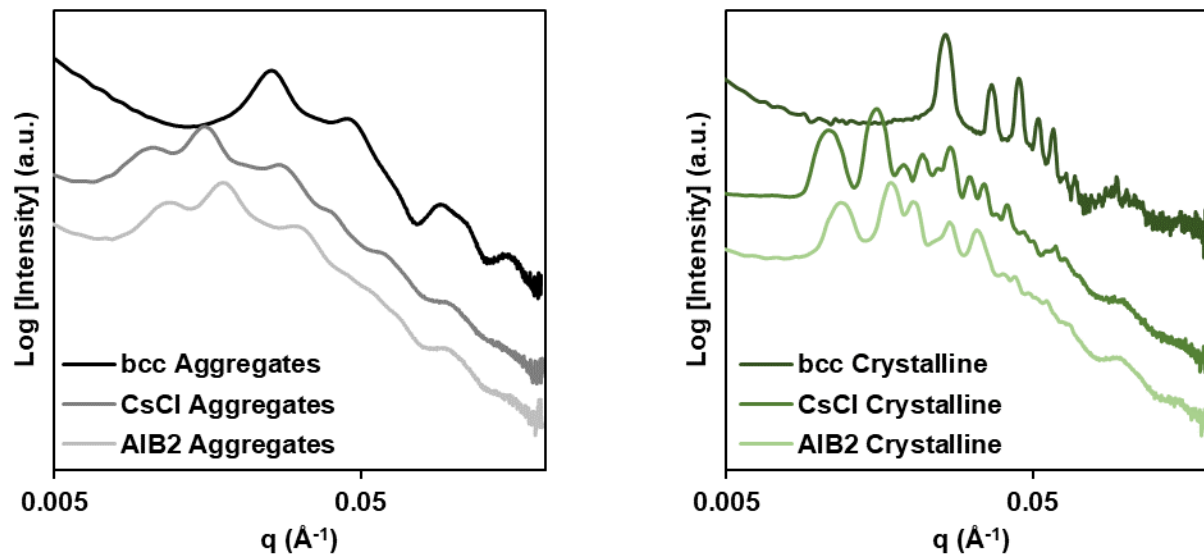
Figure A.6: 1D SAXS curves for each PAE system in its amorphous state prior to annealing (left) and its crystalline state after slow-cooling (right).

Note, some of the 2D SAXS patterns collected in this manner (within a capillary as opposed to on a substrate) contain an artifact known as "capillary scattering" that presents as a streak of high intensity just to the left of the beam center. Since this did not impact the positions or breadths of the 1D peaks, it was ignored in the analysis. Additionally, the slow-cooled PAE crystallites yield 2D SAXS rings containing several spots. This is indicative of several large, single-crystal crystallites present in the scanned sample, known to appear in slow-cooled PAEs.[155] Again, these did not alter the positions of the 1D peaks nor the relative intensity ratios, so did not impact the peak indexing analyses (determination of crystallographic symmetry, Section A.4.1) nor the determination of bulk, polycrystalline peak ratios (calculating order parameter, Section A.4.3).

A.4. SAXS Data Analysis

A.4.1. SAXS Peak Indexing

Determining the Miller indices of the 1D SAXS peaks was done using standard scattering principals[256,308] which have been applied to PAE crystal systems in the previous work.[69,163,189] This analysis is the same for both bulk, polycrystalline samples as well as crystalline PAE thin

films. First, for each PAE system, the real space unit cell lattice vectors ($\mathbf{a}_1$, $\mathbf{a}_2$, $\mathbf{a}_3$) were determined in x,y,z-space based on symmetry of the Bravais Lattice (Table A.6), such that every real space lattice point could be expressed with Equation A.4 (where x, y, and z are integers).

Equation A.4:

$$\boldsymbol{R}_{xyz} = x\boldsymbol{a}_1 + y\boldsymbol{a}_2 + z\boldsymbol{a}_3$$

Table A.6: Lattice Vectors.

Crystal System	$\mathbf{a}_1$	$\mathbf{a}_2$	$\mathbf{a}_3$
bcc/CsCl	(a, 0, 0)	(0, a, 0)	(0, 0, a)
AlB$_2$	(a, 0, 0)	(-a/2, (a*sqrt(3))/2, 0)	(0, 0, c)

In this table, a and c are lattice parameters that were adjusted later such that the index peak positions aligned with the observed 1D SAXS peak positions.

Next, reciprocal space lattice vectors ($\mathbf{b}_1$, $\mathbf{b}_2$, $\mathbf{b}_3$) were calculated based on the following equations.

Equation A.5:

$$\boldsymbol{b}_1 = 2\pi \frac{\boldsymbol{a}_2 \times \boldsymbol{a}_3}{\boldsymbol{a}_1 \cdot (\boldsymbol{a}_2 \times \boldsymbol{a}_3)}$$

Equation A.6:

$$\boldsymbol{b}_1 = 2\pi \frac{\boldsymbol{a}_2 \times \boldsymbol{a}_3}{\boldsymbol{a}_1 \cdot (\boldsymbol{a}_2 \times \boldsymbol{a}_3)}$$

Equation A.7:

$$\boldsymbol{b}_3 = 2\pi \frac{\boldsymbol{a}_1 \times \boldsymbol{a}_2}{\boldsymbol{a}_3 \cdot (\boldsymbol{a}_1 \times \boldsymbol{a}_2)}$$

This allowed for every reciprocal lattice point to be expressed in terms of h,k,l-space with Equation A.8.

Equation A.8:

$$\boldsymbol{G}_{hkl} = h\boldsymbol{b}_1 + k\boldsymbol{b}_2 + l\boldsymbol{b}_3$$

Next, specific hkl peaks that are forbidden based on unit cell symmetry (when I equals zero) were determined using Equation A.9. (F_i is proportional to scattering length density (SLD) of the ith NP of N total, which is proportional to the NP volume since all are the same material, which is related to the NP diameter – Table A.3. In this case, the DNA corona is assumed to be

164

negligible since its SLD is orders of magnitude lower than that of gold. Finally, r_i is the relative position of the ith NP in the unit cell in terms of the real space lattice vectors – Table A.7.)

Equation A.9:

$$I = \frac{1}{N} \left| \sum_{i=1}^{N} F_i * e^{-i*G_{hkl}*r_i} \right|^2$$

Table A.7: Positions and Sizes of NPs within unit cells.

Crystal System	NP Position (r)	NP Diameter (nm)
bcc	(0, 0, 0)	12.5
	(1/2, 1/2, 1/2)	12.5
CsCl	(0, 0, 0)	12.5
	(1/2, 1/2, 1/2)	19.1
AlB$_2$	(0, 0, 0)	19.1
	(1/3, 2/3, 1/2)	12.5
	(2/3, 1/3, 1/2)	12.5

For example, in the bcc case, Equation A.9 yields an intensity (I) of zero for (hkl) = (100), (010), (-100), etc. Furthering this analysis yields the classic selection rules for bcc crystals (all peaks where h+k+l = 2n+1 (i.e. odd) are forbidden). However, in the CsCl case, since the two particles types have different SLDs ($F_1 \neq F_2$), no peaks are forbidden due to symmetry. A similar analysis for AlB$_2$ was conducted. The q-value of each index is then equal to the magnitude of G_{hkl} and can be grouped together into families based on identical q-values.

A.4.2. Determining Lattice Orientation Alignment from Suppressed Peaks

The analysis in Section A.4.1 yields a 3D reciprocal space lattice with peaks at hkl points for each PAE system. Upon closer inspection, it can be seen that the reciprocal lattice of the bcc PAE system is an fcc lattice, the CsCl PAE system yields a simple cubic lattice, and AlB$_2$ yields a hexagonal lattice rotated 30° about the c axis. In scattering analysis, only those reciprocal space lattice points that intersect the Ewald sphere (a reciprocal space mathematical construct that, by definition, contains the (000) hkl point of the reciprocal lattice; such a sphere can be approximated as a plane in small angle scattering) will appear in the resulting scattering pattern.[189] Therefore, the orientation of the reciprocal space lattice will determine which index peaks appear in the collected data. The real space lattice and the reciprocal space lattice are directly correlated in terms

of orientation. As such, in the bulk, "powder" diffraction cases (Section A.3.3) where the SAXS instrument is sampling real space unit cells of all possible orientations, these reciprocal space lattice points are fully rotated in all three dimensions. Thus, all reciprocal lattice points are sampled and appear in the resulting SAXS data.

However, in the case of a thin film where one degree of rotational freedom is locked parallel to the substrate and the x-ray beam is normal to the substrate, the reciprocal lattice will only be rotated about this normal direction. In this restricted case, only the reciprocal points already on the plane of the Ewald sphere will be sampled and all points that are out-of-plane will not appear in the collected SAXS data.[189] For example, if the CsCl system were oriented with the (001) plane parallel to the substrate, the simple cubic reciprocal lattice would have the following hkl points in-plane with the Ewald sphere: ($\pm$1 0 0), (0 $\pm$1 0), ($\pm$1 $\pm$1 0), etc. However, (0 0 1) – the same q-value as {1 0 0} – and ($\pm$1 $\pm$1 $\pm$1) – having a unique q-value – occur out-of-plane and will not appear in the scattering data. In this simplest case, it can be noticed that any hkl point where $l \neq 0$ is suppressed. This is consistent with the findings reported in previous work.[163] While not as intuitive for more complex crystal symmetries or alignment orientations, the same basic principal can be applied for every case and used to identify the alignment of the thin film. The peaks expected to be suppressed for each PAE case and each orientation is summarized in the appropriate sections (bcc, Section A.5.1; CsCl, Section A.6.1; AlB$_2$, Section A.7.1).

A.4.3. Quantification of Orientation Parameter

Quantitative analyses of ordering were done for the bcc system (Figure 2.1A and B) and the CsCl system (Figure 2.2D). In the former, an orientation parameter was defined such that a thin film fully oriented with (001) plane parallel to the substrate would have a value of 1 and a thin film with no orientational alignment would have a value of 0. This was achieved through quantifying and comparing the integrated intensities of the first scattering peak – (110) – and the third scattering peak – (211) that are present in a bulk, polycrystalline sample (Section A.5.1). Using the analysis in Section A.4.2, it can be determined that the (211) peak is suppressed when the bcc thin film is oriented with the (001) plane parallel to the substrate (Section A.5.1). Thus, a "perfectly" aligned/oriented thin film would have zero (211) peak intensity. In samples where increasingly more grains were not aligned, the intensity of the (211) peak would be increasingly

higher until the ratio between the (110) and (211) peaks reached that of a bulk, polycrystalline sample; at this point, the orientation parameter should be zero.

Therefore, the following orientation parameter calculation was developed to match these specifications (Equation A.10). In each case, the (110) and (211) peaks first had their backgrounds interpolated and subtracted, followed by integration of the intensity (*I*). Since the area beneath a scattering peak is proportional to the number of NPs squared, the intensities were square rooted to better compare the number of NPs in an oriented versus unaligned state. The ratio of these integrated areas was then calculated and compared to the ratio present in a polycrystalline, bulk sample. Similar analyses (*i.e.* defining order parameters based on SAXS patterns) have been conducted for PAE thin films in previous works.[26,147]

Equation A.10:

$$Orienation\ Parameter = 1 - \frac{\sqrt{\dfrac{\int_{(211)\ Thin\ Film\ Peak} I}{\int_{(110)\ Thin\ Film\ Peak} I}}}{\sqrt{\dfrac{\int_{(211)\ Polycrystalline\ Peak} I}{\int_{(110)\ Polycrystalline\ Peak} I}}}$$

A more detailed discussion of the orientation parameter and the resulting results/conclusions for the bcc system on a mono-functionalized surface, namely concerning alignment as a function of layer number, can be found in the main text (Figure 2.1) and Section A.5.2. In principal, this orientation parameter calculation could be extended to the integrated intensity of any suppressed peak divided by the integrated intensity of any non-suppressed peak. Therefore, similar analyses can be done for the bcc systems on bi-functionalized substrates where the (011)-orientation is the "ordered" state and for the CsCl and AlB_2 systems. However, all these analyses yielded the same findings and conclusions as discussed by Figure 2.1 and the main text (*i.e.* the kinetic pathway of thin film rearrangement as a function of layer number, time, and temperature were similar for all PAE systems and substrate functionalizations). Therefore, for succinctness, the results of this analysis are only included for one case.

The latter quantitative analysis conducted in this manuscript assesses the relative amounts of two different orientations present in the same thin film sample (used in Figure 2.2D). This

analysis was conducted in a manner consistent with literature precedence.[163] For this case, the 1D SAXS intensity curves ($I(q)$) for the two extremes that contained only one type of orientation (100% (001) or 100% (011)) were averaged together and used as "ideal" cases. Then, for each curve to be analyzed, the 1D SAXS intensity was fit to a linear combination of the two ideal cases (*i.e.* in Equation A.11, x was varied between 0 and 100 until y was minimized). The resulting mixture of the two orientations was then reported and plotted (Figure A.39).

Equation A.11:

$$y = \left[I(q)_{Measured} - (x * I(q)_{Ideal\,(001)} + (100 - x) * I(q)_{Ideal\,(011)}) \right]^2$$

Equation A.12:

$$Orienation\,(\%\,\{001\}) = x$$

Equation A.13:

$$Orienation\,(\%\,\{011\}) = 100 - x$$

This analysis can similarly be conducted for the bcc system explored in this manuscript. However, that analysis was found to match previous literature results,[163] and so was excluded from this discussion for succinctness.

A.4.4. Calculation of Stoichiometry

The observed intensity of a 1D SAXS curve is a combination of the form factor, $P(q)$, which results from the shape of the constituent building blocks, the structure factor, $S(q)$, which results from the relative positions of those constituents to each other, and the background scattering, $B(q)$ (Equation A.14).[189,256,308]

Equation A.14:

$$I(q) = P(q) * S(q) + B(q)$$

The background scattering results from all the media (air, container, buffer, substrate, etc.) through which the x-ray beam passes. For each scan, the background can be simply subtracted from the observed intensity. In this manuscript, the background was measured experimentally by taking an x-ray SAXS scan of the exact setup (cover slip chamber, filled with PBS and a functionalized but bare substrate) simply without the presence of any PAEs.

For a superlattice system consisting of only one NP type (e.g. the bcc PAE system), the form factor can be experimentally approximated by taking a SAXS measurement of functionalized

PAEs that contain no linkers. These particles will be non-interacting (having no sticky ends to bind to one another) and thereby have no correlation in position (*i.e.* no structure factor). The resulting form factor curve will be unique to the size and shape of the NP constituent. This curve (following background subtraction) can then directly divide a background-corrected SAXS scan to yield the sample's structure factor.

For a two-component system (*e.g.* the AlB_2 PAE system which contains two differently sized NP cores), the overall "form factor" can be approximated as a linear combination of the two constituent's individual form factors (taken at the same concentration). The combination will be roughly equivalent to the relative amounts of the two particle types present in the superlattice or aggregate.[189] In this manner, the mixture's form factor can be approximated mathematically (Equation A.15).

Equation A.15:

$$P(q)_{Mixture} = x * P(q)_{PAE\ A} + (1 - x) * P(q)_{PAE\ B}$$

To improve the accuracy of this calculation, the individual form factor scans should be measured at the same concentration and have the appropriate background scattering subtracted. This calculated form factor of the mixture can then be compared to the measured SAXS data, varying x from 0 to 1 until the difference between the scans is minimized (residual minimization). Since the structure factor alone cannot be easily measured experimentally and divided from the overall intensity to isolate the form factor from the SAXS scan of the mixture (Equation A.14), this linear combination and residual analysis should be done in a q-range that does not include structure peaks (generally high q-values).

A.5. Additional bcc System Data

A.5.1. Indexing of Possible Orientation Alignments

Using the protocol outlined in Section A.4.1, the bcc system peaks were indexed for the bulk, polycrystalline sample (Section A.3.3) and confirmed to align well to a bcc lattice with a lattice parameter of 34.1 nm (Figure A.7). Additionally, following the analysis in Section A.4.2, the suppressed peaks were determined for thin film alignments with various proposed planes

parallel to the substrate (Table A.8). Note, that only alignments of {001} and {011} were observed in this manuscript data, other alignment possibilities are only tabulated for reference.
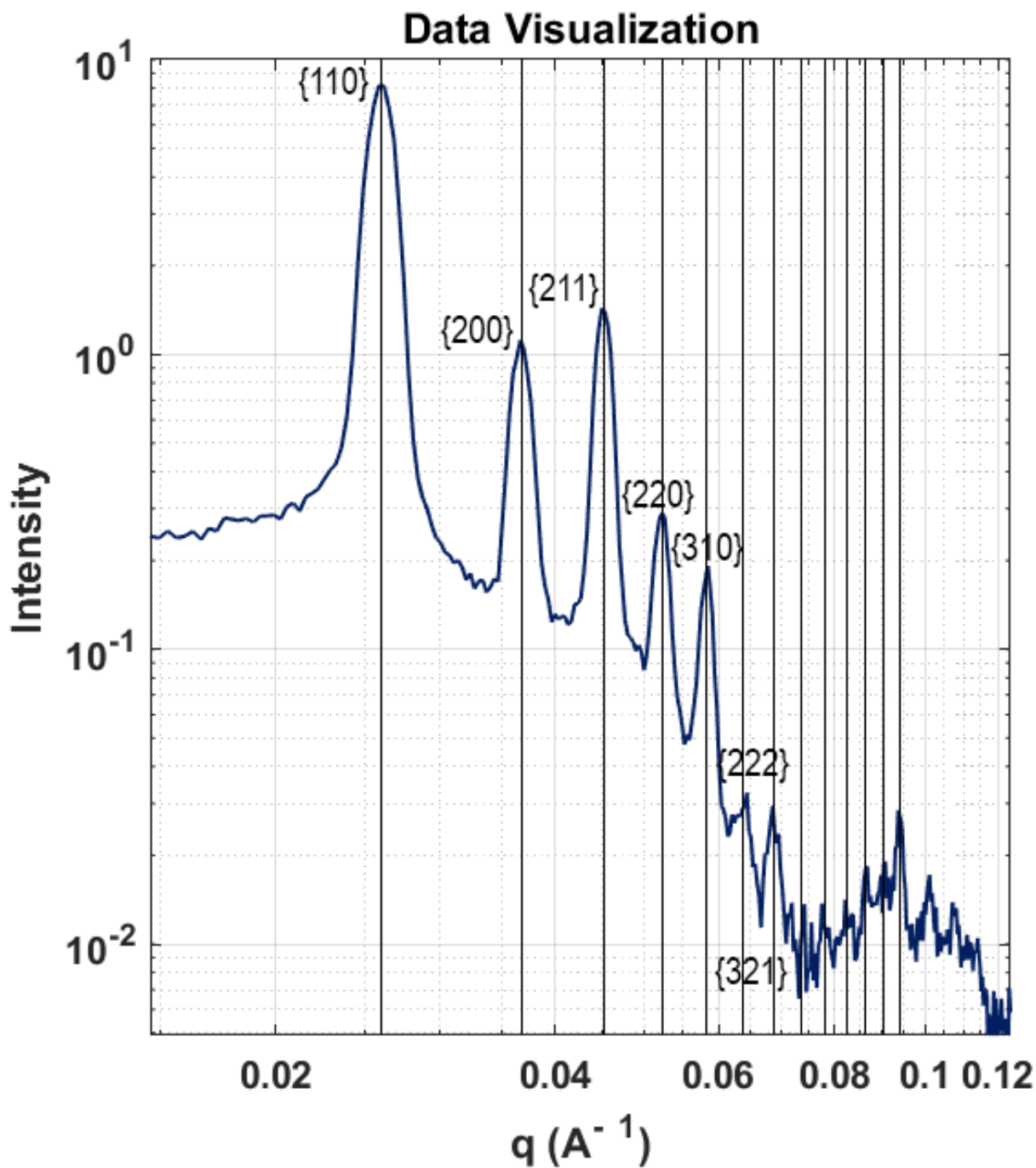
Figure A.7: Indexed 1D SAXS data for the bcc PAE system (bulk, polycrystalline data shown).

Table A.8: Indexed bcc (a = 34.1 nm) peak positions (q) and suppressed peaks for given alignments.

Indexed Planes Bulk	q	Indexed Planes Present {001}-Aligned	Indexed Planes Present {011}-Aligned	Indexed Planes Present {111}-Aligned
{110}	0.0261	(110), (1-10), (-110), (-1-10)	(01-1), (0-11)	(10-1), (01-1), (0-11), (-101), (1-10), (-110)
{200}	0.0369	(200), (020), (0-20), (-200)	(200), (-200)	Suppressed Entirely
{211}	0.0451	Suppressed Entirely	(21-1), (2-11), (-21-1), (-2-11)	(2-1-1), (11-2), (1-21), (-12-1), (-1-12), (-211)
{220}	0.0521	(220), (2-20), (-220), (-2-20)	(02-2), (0-22)	(20-2), (02-2), (0-22), (-202), (2-20), (-220)
{310}	0.0583	(310), (3-10), (130), (1-30), (-130), (-1-30), (-310), (-3-10)	Suppressed Entirely	Suppressed Entirely
{222}	0.0638	Suppressed Entirely	(22-2), (2-22), (-22-2), (-2-22)	Suppressed Entirely
{321}	0.0689	Suppressed Entirely	Suppressed Entirely	(3-1-2), (1-32), (-13-2), (-312), (3-2-1), (21-3), (2-31), (12-3), (-1-23), (-23-1), (-2-13), (-321)
{400}	0.0737	(400), (040), (0-40), (-400)	(400), (-400)	Suppressed Entirely
{330}, {411}	0.0782	(330), (3-30), (-330), (-3-30)	(41-1), (4-11), (03-3), (0-33), (-41-1), (-4-11)	(3-30), (-330), (30-3), (03-3), (0-33), (-303)
{420}	0.0824	(420), (4-20), (240), (2-40), (-240), (-2-40), (-420), (-4-20)	Suppressed Entirely	Suppressed Entirely
{332}	0.0864	Suppressed Entirely	(23-3), (2-33), (-23-3), (-2-33)	Suppressed Entirely
{422}	0.0903	Suppressed Entirely	(42-2), (4-22), (-42-2), (-4-22)	(4-2-2), (22-4), (2-42), (-24-2), (-2-24), (-422)
{431}, {510}	0.0940	(510), (5-10), (150), (1-50), (-150), (-1-50), (-510), (-5-10)	Suppressed Entirely	(31-4), (13-4), (-1-34), (-3-14), (4-1-3), (4-3-1), (3-41), (1-43), (-14-3), (-34-1), (-431), (-413)

A.5.2. Thin Film Texture as a Function of Layer Number

The main text, specifically in Figure 2.1A and B, explores the impact of increasing layer number on the prevalence of grains with a preferred alignment (as described by the orientation parameter –Section A.4.3). The SAXS patterns from which orientation parameter for Figure 2.1A are collected below (Figure A.8 and Figure A.9). It is important to note that the SAXS patterns appear different not because of a difference in degree of crystallinity (all patterns presented are from after each thin film has reached a fully crystalline equilibrium state), but rather due to a difference in the overall average orientations of the grains within the sample.

This data corresponds to bcc thin films having PAE A deposited first onto monofunctionalized substrates (100% A) and subsequently annealed at 48.5 °C until equilibrium was reached. From these data it is clear to see that the third scattering peak – (211) – is only observed beyond 5-layers and grows in relative intensity with increasing layer number. As stated in the main text, this can be summarized as "perfect" {001} alignment at 5L and a decreasing order parameter with more layers (Figure 2.1A). The stabilizing effect of the substrate on specific grain orientations only originates at the substrate surface, and its influence wanes further from the surface.
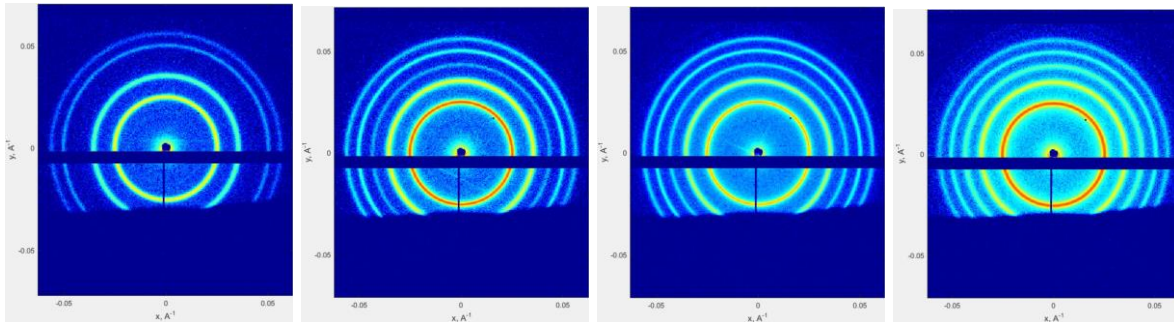
Figure A.8: 2D SAXS data for annealed bcc thin films of varying number of layers (from left to right, 5L, 10L, 20L, and 30L).
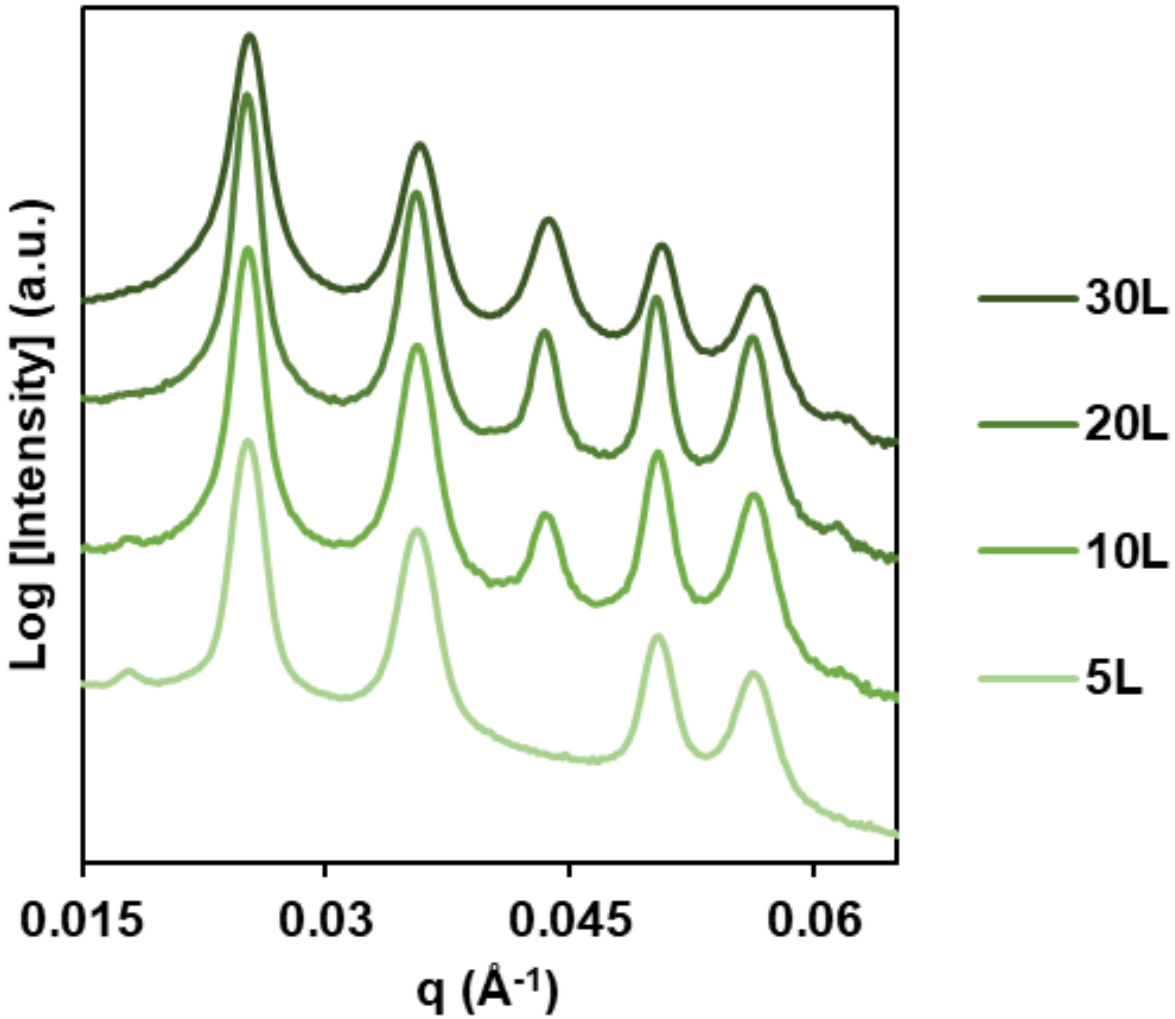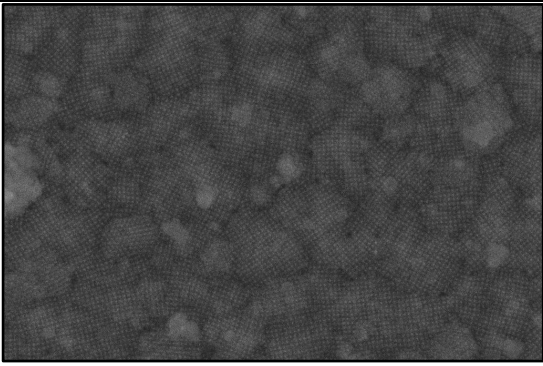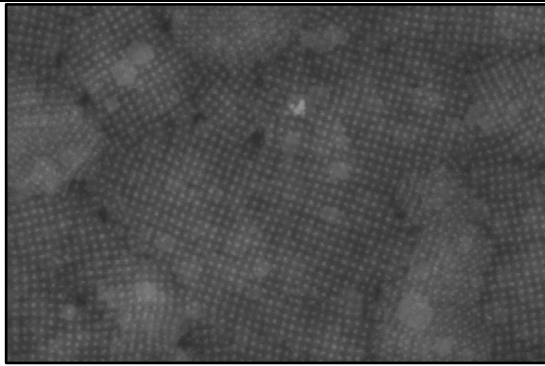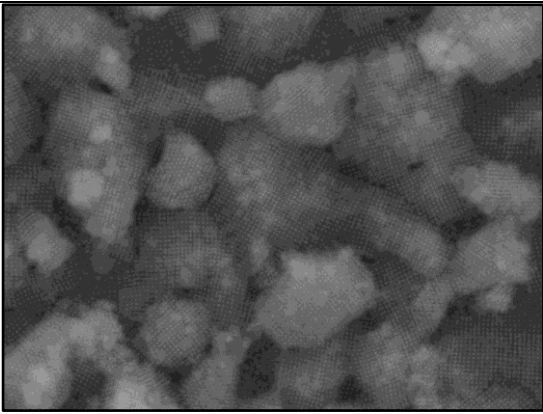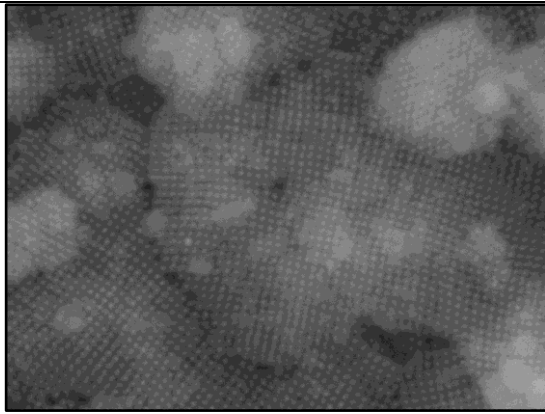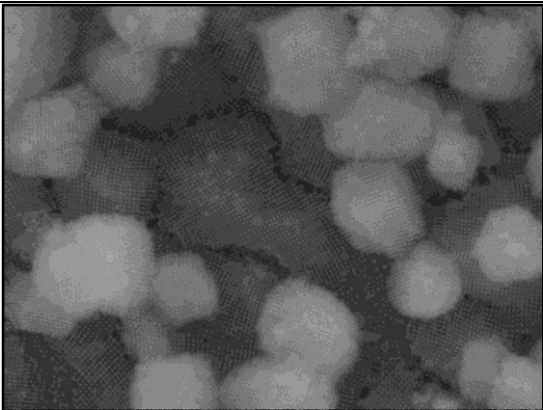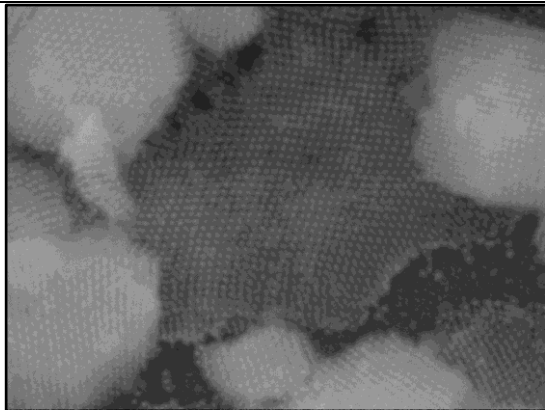
Figure A.9: 1D SAXS data for annealed bcc thin films of varying number of layers. The SAXS curves have been offset in intensity for clarity.

This conclusion is further corroborated by the visual observation of the morphologies of these thin films in the following SEM micrographs (Figure A.10). These data reveal that virtually all of the crystal grains in contact with the substrate are aligned {001}; this result is consistent with the hypothesis that PAEs are energetically driven to adopt an aligned configuration because it is lower in energy than other alignments. Conversely, the crystal grains that are not in contact with the substrate interface, lacking a directing force to align, are generally poly-crystalline in orientation. It is also worth noting that the average size of the aligned grains upon the substrate far exceeds the average size of the poly-crystalline grains sitting atop them. This further corroborates

173

the hypothesis that a stabilizing energetic effect could affect the growth of grains as well as their nucleation.

Number of Layers	100kx	200kx
5		
10		
20		
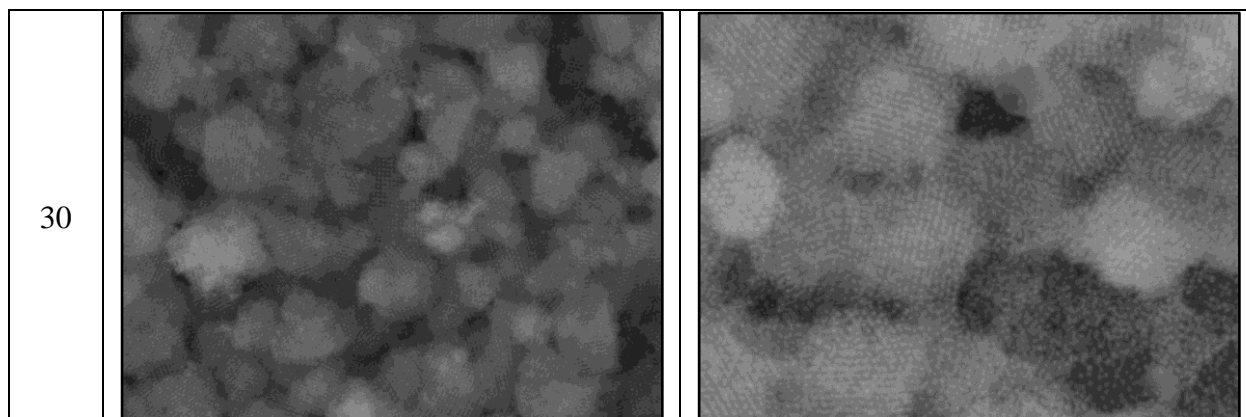
Figure A.10: Top-down SEM micrographs of the final, rearranged morphology of annealed bcc thin films consisting of various numbers of PAE layers (noted on the left). The SEM micrographs noted as 100kx (middle column) are 3 µm wide and the 200kx (right column) are 1.5 µm wide.

The final microstructures as observed in the SEM micrographs provide support for the orientation-stabilizing substrate hypothesis, but do not provide conclusive evidence for the pathway. A large research question remains whether the thin film reorganizes at the substrate surface with preferentially aligned grains first crystallizes upwards or whether the entire thin film reorganizes into polycrystalline orientations and those that are preferentially aligned outgrow or outpace the non-aligned grains. To answer this question, SAXS scans were collected *in-situ* during the reorganization process (Section A.2.1) of the above thin films. Time-elapsed videos of this process as a function of layer number (Videos S1, S2, S3, and S4)[177] distinctly reveal the conclusions presented in the main text and Figure 2.1B.

Foremost, it is observed from the *in-situ* videos that the relative presence and intensity of the third scattering peak (211) differs greatly depending on thin film thickness. To more easily visualize and compare the differences, the intensity of the first and third SAXS peaks over time were calculated and plotted started from the SAXS scan that shows the first sign of higher order peaks (Figure A.11). These values were then correlated to an orientation parameter and summarized in Figure 2.1B. As a reminder, the suppression of the third peak relative to the others indicates an increasing amount of {001}-preferentially aligned grains, while an increasing relative third peak intensity is indicative of increasingly poly-crystalline thin film morphology. From both these figures and corresponding videos, the following conclusions can be derived.
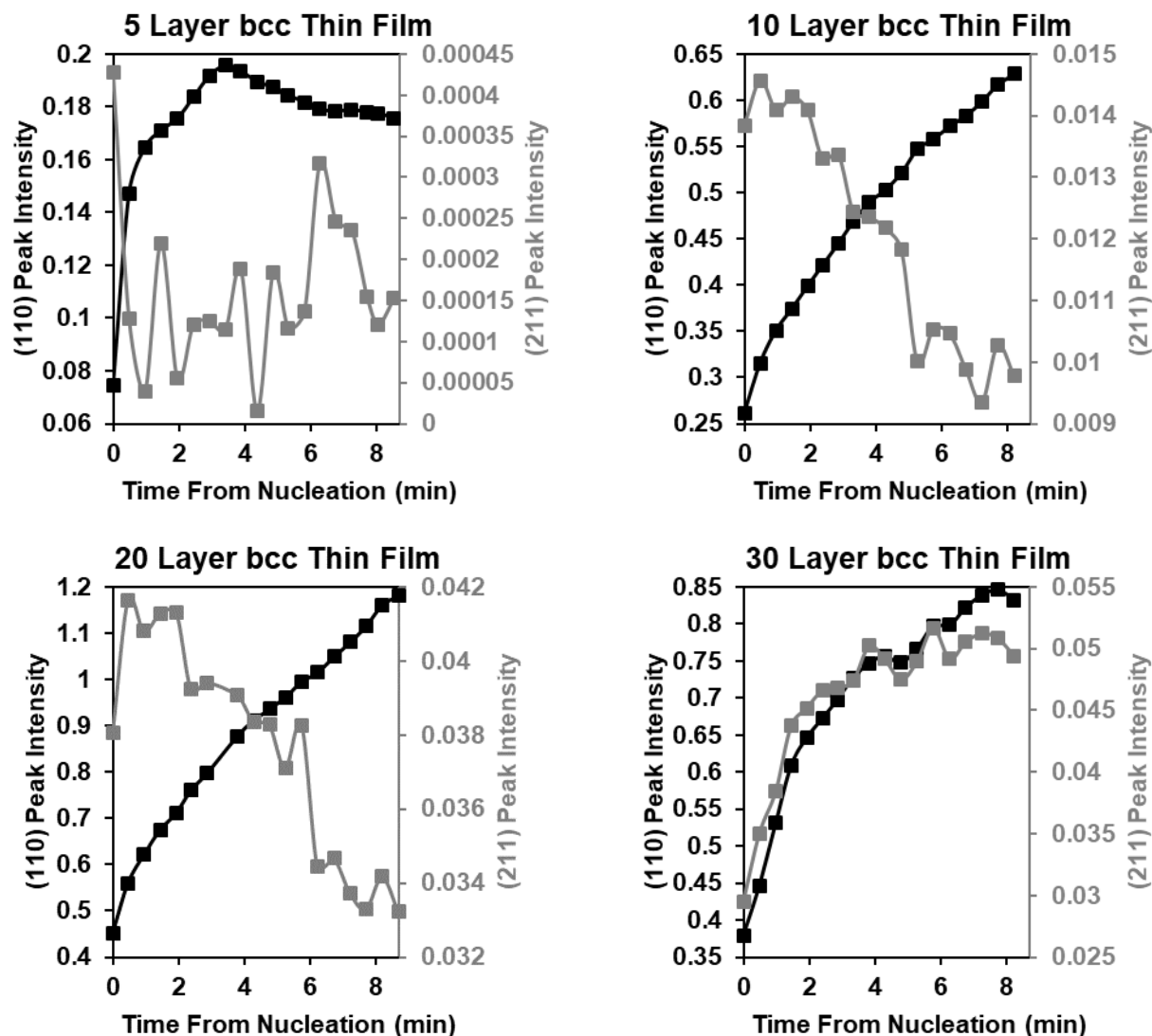
Figure A.11: Integrated peak intensities of the (110) peak (left, black axis) and the (211) peak (right, gray axis) as a function of the annealing (T = 48.5 °C) time from the onset of nucleation for bcc PAE thin films of varying thicknesses (noted on each graph).

Importantly, in all cases, the intensity of the first scattering peak increases with annealing time. This means that each sample in becoming increasingly ordered until reaches a fully ordered state and plateaus. The degree of alignment with the substrate can then be determined by comparing this growth to that of the third peak. First, in the 5-layer sample, the third scattering peak is never observed and its intensity remains virtually zero throughout the annealing process, resulting in a relatively flat order parameter over time. In this case, no un-aligned grains even

nucleate. Second, in the 10-layer sample, some unaligned grains nucleate (evidenced by the (211) peak intensity at nucleation), but these grains steadily decrease in amount (shown by decreasing intensity) as the thin film anneals. The 20-layer sample shows a similar trend, only with the initial nucleated amount and final amount of un-aligned grains being higher than that of the 10-layer sample. In both these cases, the order parameter increases over time as the thin film continues to crystallize with annealing and the unaligned grains slowly disappear.

Finally, the 30-layer sample reveals a different trend. The third peak intensity simply rises in virtually the same fashion as the first peak. In contrast to the 10- and 20-layer samples where a significant amount of the thin film was in contact with the substrate such that the substrate could drive the formed grains to align with it, a large majority of the PAEs in the 30-layer sample are so far from the substrate's influence, that the nucleated poly-crystalline grains just continue to grow with annealing without be significantly converted to a preferential alignment. The resulting order parameter *versus* time is therefore roughly flat at a low value since the alignment with the substrate is not changing (improving or worsening) with annealing.

The investigation described in this section only covers the effects of thickness for the simple case of a bcc thin film rearranging on a monofunctionalized substrate. The same general trends and conclusions were observed for a bifunctionalized substrate, only the alignment favored {011} planes parallel to the surface as opposed to {001}. Similarly, the CsCl and AlB_2 PAE systems showed comparable results when investigating both the final texture and the *in-situ* development of alignment as a function of thickness. Therefore, all other cases are omitted from this SI for succinctness.

A.5.3. Thin Film Morphology as a Function of Annealing Temperature and Time

To explore the effects of annealing time and temperature on PAE thin film rearrangement and the resulting microstructure, a larger bcc PAE system was synthesized. The larger (19.1 nm) AuNPs were functionalized with Linker Y-2d20-B and Linker X-2d20-A DNA linkers. A larger length scale system was devised and explored to make SEM analysis more readily accessible. These PAEs were found to crystallize into a bulk, bcc unit cell in the same manner as the small bcc system, with a melting temperature of 40 °C. After monofunctionalizing several substrates and depositing 5 layers of PAEs on each, the amorphous thin films were placed in heated PBS solutions

177

(equilibrated in heat blocks overnight) for a specific length of time (1 min to 23 hours). The annealed thin films were then embedded and imaged by SEM both in a top-down manner and cross-sectionally (after FIB milling). The micrographs are summarized in Figure 2.1D of the main text and Figure A.12 and Figure A.13.
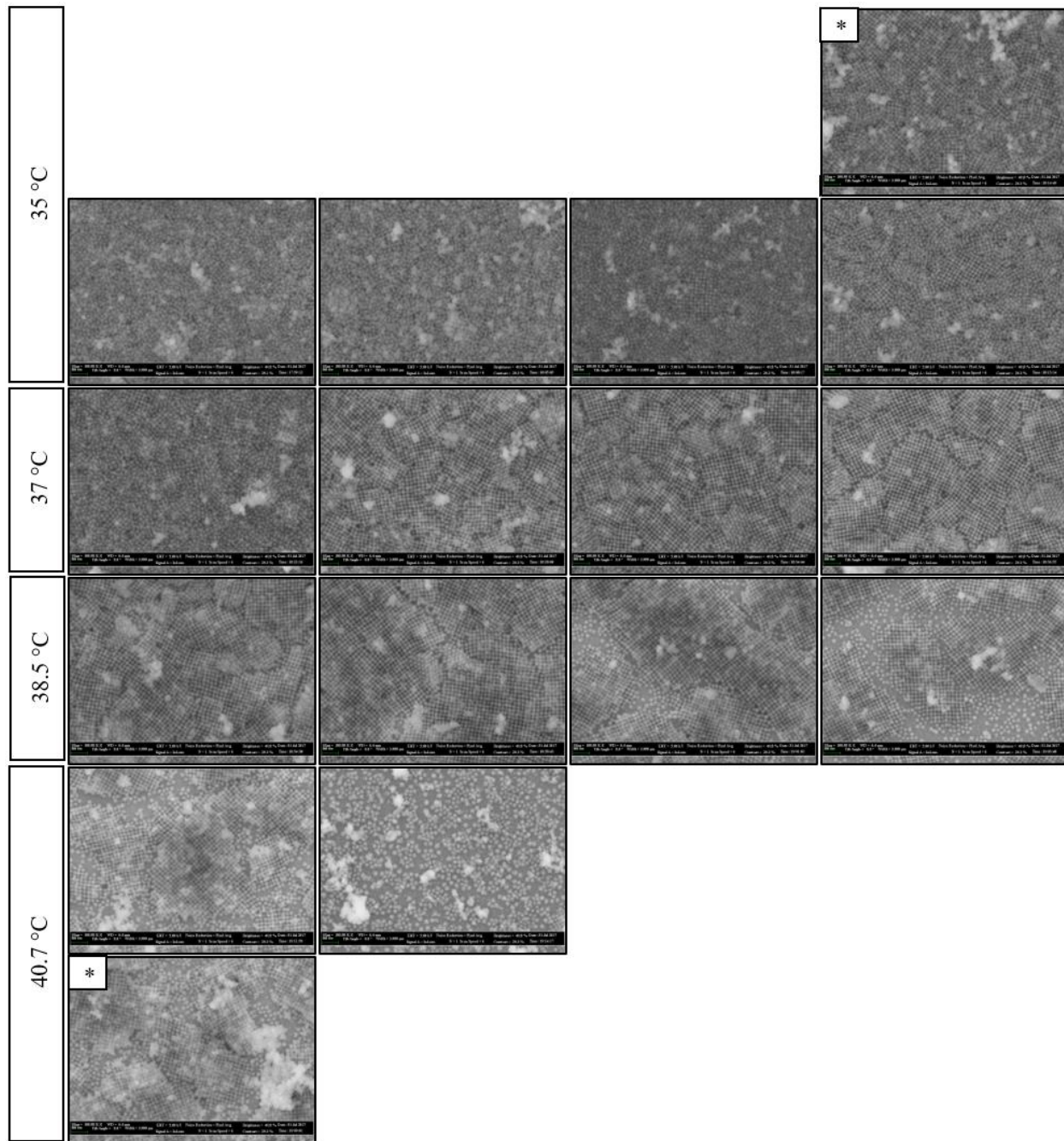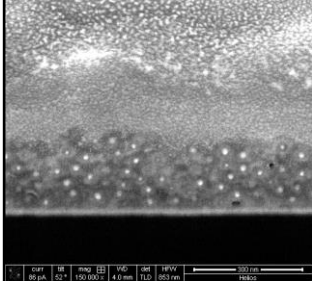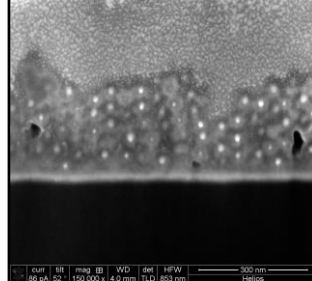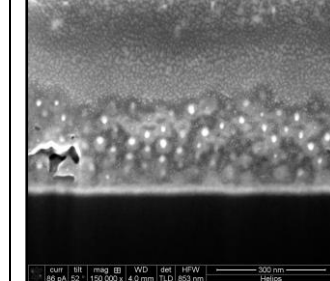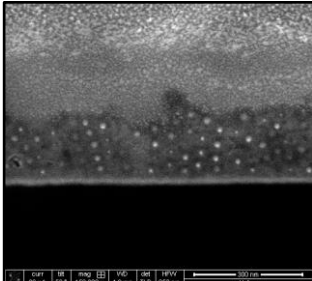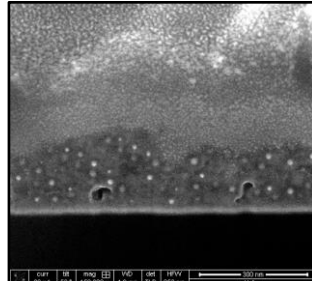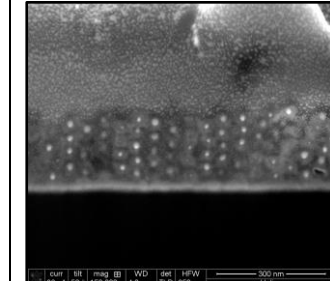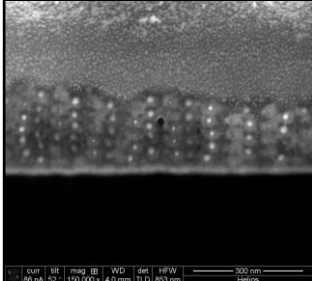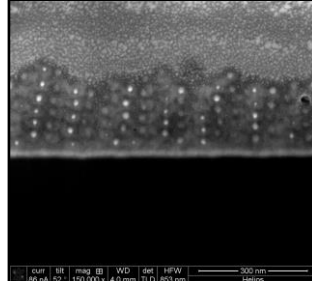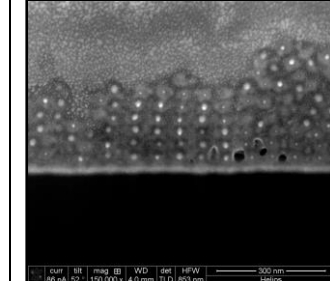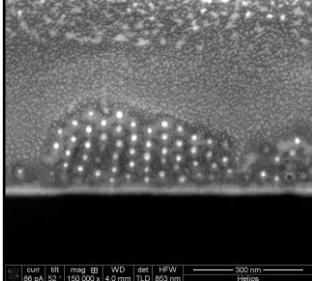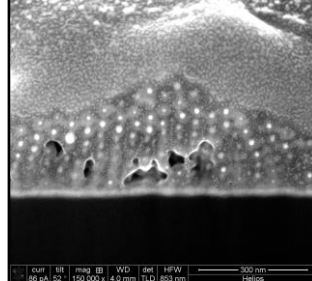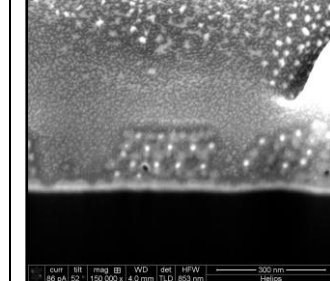
Figure A.12: Top-down SEM micrographs of embedded bcc thin films (bulk T_m = 40.0 °C) that have been annealed at various temperatures (noted at the start of each row) for various lengths of time (columns, from left to right, 5 min, 15 min, 1 hr, 4 hr). Micrographs denoted by * refer to 35 °C for 23 hr and 40.7 °C for 1 min. All micrographs are 3 µm wide.

Annealing Temperature	Time	Representative Cross-Sectional SEM Micrographs		
37 °C	5 min			
37 °C	15 min			
37 °C	1 hour			
37 °C	4 hours			

38.5 °C	1 hour			
38.5 °C	4 hours			
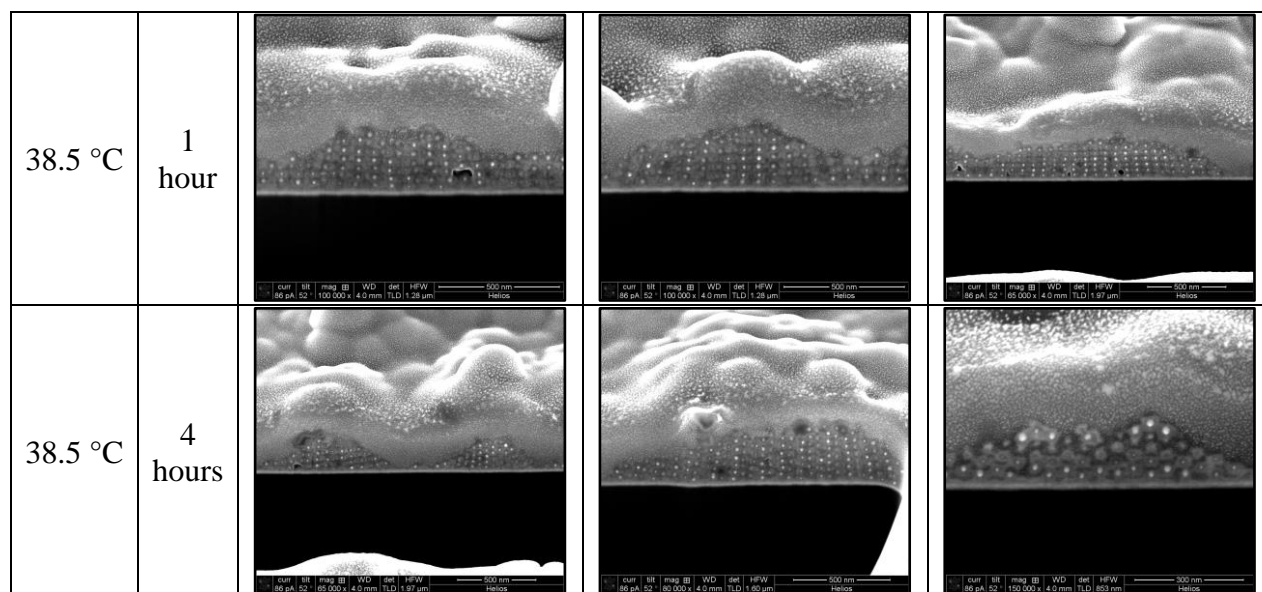
Figure A.13: Representative cross-sectional SEM micrographs of select embedded bcc thin films (bulk Tm = 40.0 °C) that have been annealed at various temperatures for various lengths of time (noted at the start of each row). The width of 37 °C micrographs are 853nm. The widths of the 38.5 °C, 1-hour micrographs are 1.28 µm, 1.28 µm, and 1.97 µm (left to right). The 38.5 °C, 4-hour micrographs are 1.97 µm, 1.6 µm, and 853 nm wide (left to right).

These SEM data corroborate the conclusions stated in the main text that were elucidated by SAXS analysis. It is clear that as the rearrangement temperature approaches the bulk T_m, the thin film more quickly orders into a crystalline lattice. However, at temperatures near and above T_m, while the PAE mobility is greatly increased, the thin film begins to melt from the surface, mainly along grain boundaries resulting in individual crystalline islands. This transition from continuous thin film containing grain boundaries to agglomeration of separated grains is particularly evident when comparing the cross-sectional SEM micrographs for the 1-hour and 4-hour time points (Figure A.13). At every temperature, the longer the thin film is allowed to anneal, the degree of crystallinity (transformation) improves and the larger the crystalline grain domain sizes grow. Specifically, non-aligned grains only appear in small quantities early in the rearrangement process and are quickly outpaced and absorbed by the increasingly larger aligned grains. This specific behavior is highlighted for the bcc in Video S5.[177] Ultimately, this dependence on time and temperature is consistent with classic TTT-type behavior with the upper half of the C-curve truncated due to non-reversible PAE melting from the substrate.

An increasing grain size with annealing time is corroborated by the *in-situ* SAXS data where the peak breadth is observed to sharpen over time, indicative of an increasing domain size of the grains (Videos S1-S9).[177]

Finally, this investigation into the effects of annealing time and Temperature demonstrate a large dependence on the annealing time and temperature of PAE thin films. While having similar characteristics, the overall microstructure and morphology of a PAE thin film can have striking differences depending on the specific thermal processing strategy. Therefore, significant care for precise thermal annealing is critical to garner specific desired microstructures and textures of PAE thin films.

A.5.4. Five Layer (5L) Thin Film Texture as a Function of Surface Functionality

Given the nearly identical design of PAE A and PAE B in the bcc system, differing only in sticky end functionality, it was hypothesized that the reorganization behavior of bcc thin films would be identical regardless of which PAE type was allowed to bind to the surface. This would be consistent with prior findings in previous literature.[69,163] To investigate this hypothesis, 5L bcc thin films were prepared (Section A.1) and SAXS scans were collected (Section A.2.1) on the amorphous thin films (Figure A.14, left). This data reveals very little structural difference between deposited films, regardless of PAE type deposited first or surface functionalization (all substrates examined appeared the same, only select cases shown for clarity). Upon rearrangement (Section A.2.1), the final, equilibrium structures of the reorganized bcc thin films were examined (Figure A.14, right) and found to have only slight variations between which PAE type was present at the surface (hypothesized to be based on thermal variations between ramping experiments; annealing temperature was different by 0.5 °C between the two experiments). This data indicates that PAEs of identical NP and hydrodynamic radius size behave nearly identically when reorganizing at an interface.
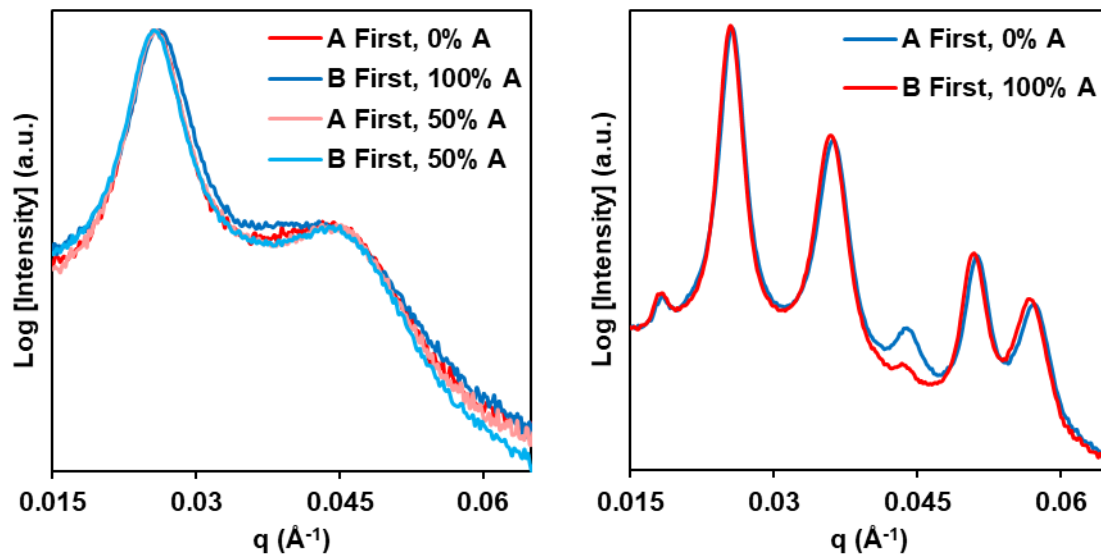
Figure A.14: 1D SAXS curves for five layer (5L) bcc thin films, deposited on monofunctionalized substrates (0% A and 100% A) or 50/50 bifunctionalized substrates (50% A); (left) amorphous state prior to annealing and (right) crystallized state after annealing at 48-48.5 °C. These scans reveal the nearly identical reorganization behavior of PAE A and PAE B for the bcc system.

To examine whether the final crystalline structure, particularly the preferred orientational alignment, of a thermally-reorganized PAE thin film would be consistent with the structures observed for deposition of PAE thin films under elevated temperature,[163] 5L bcc thin films were reorganized at 48.5 °C and their final structures determined by SAXS (Figure A.15). The previous investigation found that {001} grain alignment parallel to the substrate was preferred for monofunctionalized substrates, while {011}-alignment was preferred in the 50/50 functionalized case. Consistent with this finding, reorganized thin films were driven to those equilibrium states as well. Between the extremes of 0% A, 50% A, and 100% A, the thin films contained mixtures of {001} and {011} aligned grains in amounts that create a fairly symmetric distribution (Figure A.15).

These SAXS results can be corroborated by viewing the SEM micrographs of the resulting thin film morphologies (Figure A.17) and comparing them to computer-generated visualizations of the top-down view of oriented grains (Figure A.16). Exactly as the SAXS data predicts, the SEM data shows only {001}-alignment in the 100% and 0% A functionality, only {001}-alignment for 50% A, and a mixture of alignments for the cases in between.
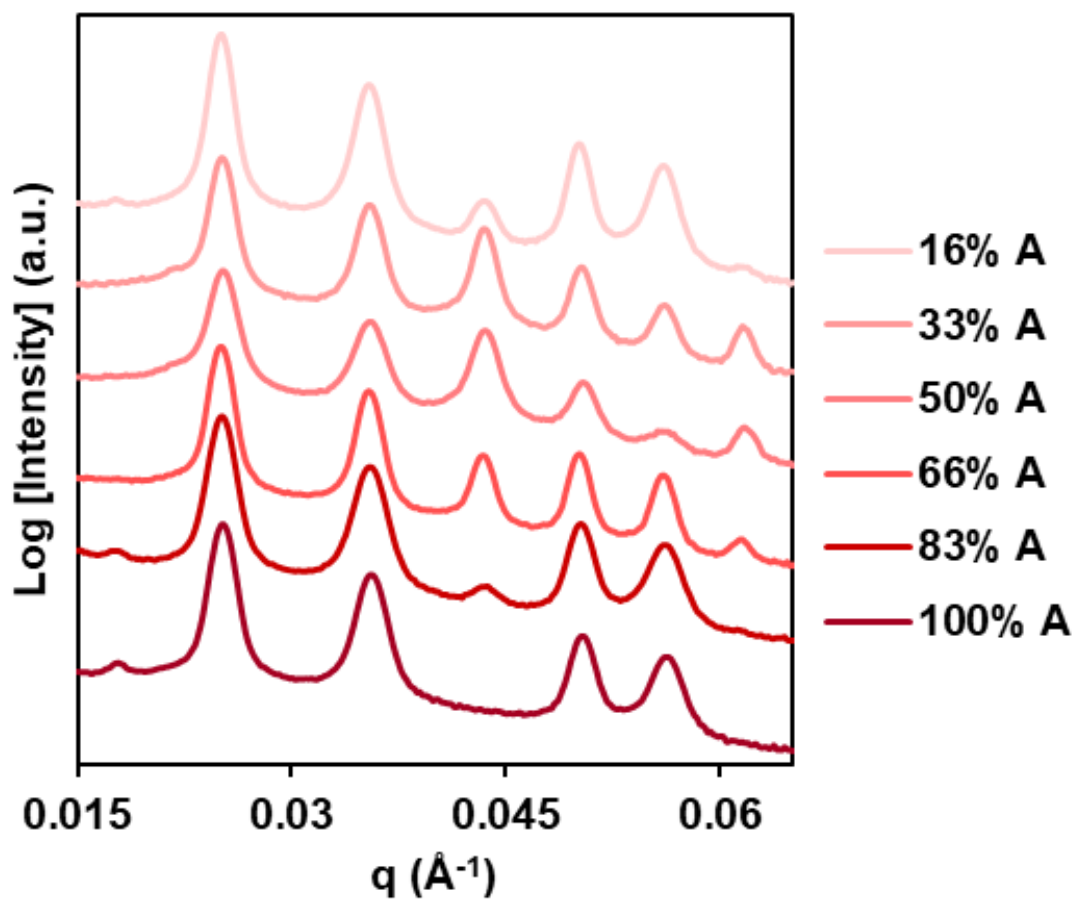
Figure A.15: Equilibrium SAXS state for five layer (5L) bcc thin films having been annealed at 48.5 °C. All cases had PAE B deposited first on substrates with varying degrees of functionality (16% A to 100% A). The SAXS curves have been offset in intensity for clarity.
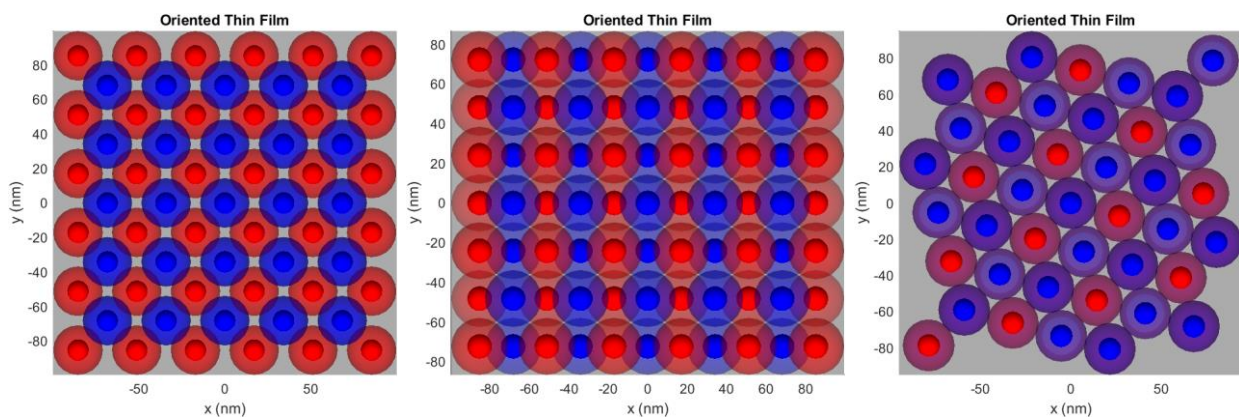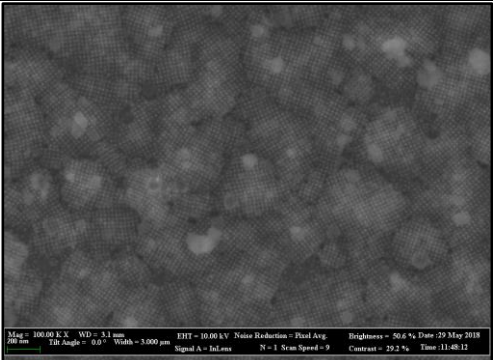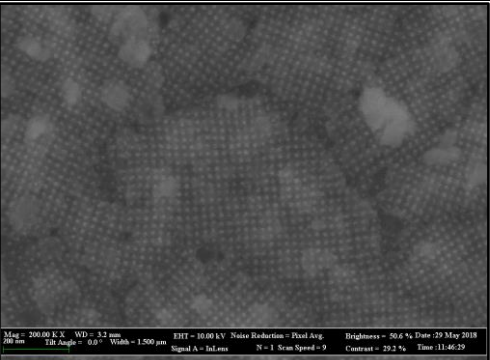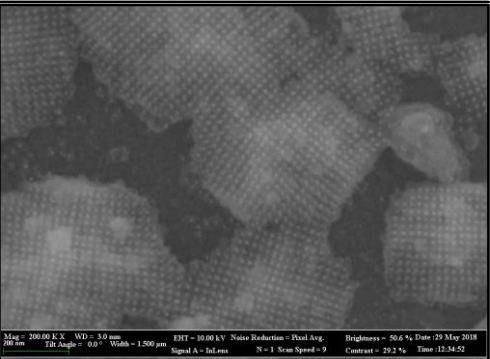
Figure A.16: Visualizations of the top-down arrangement of a bcc PAE grain with the (from left to right) {001}, {011}, or {111} plane aligned parallel to the substrate.

Surface Functionality	A/B First	100kx	200kx
0% A	A		
16% A	A		
33% A	A		

50% A	A		
66% A	A		
83% A	A		
100% A	B		
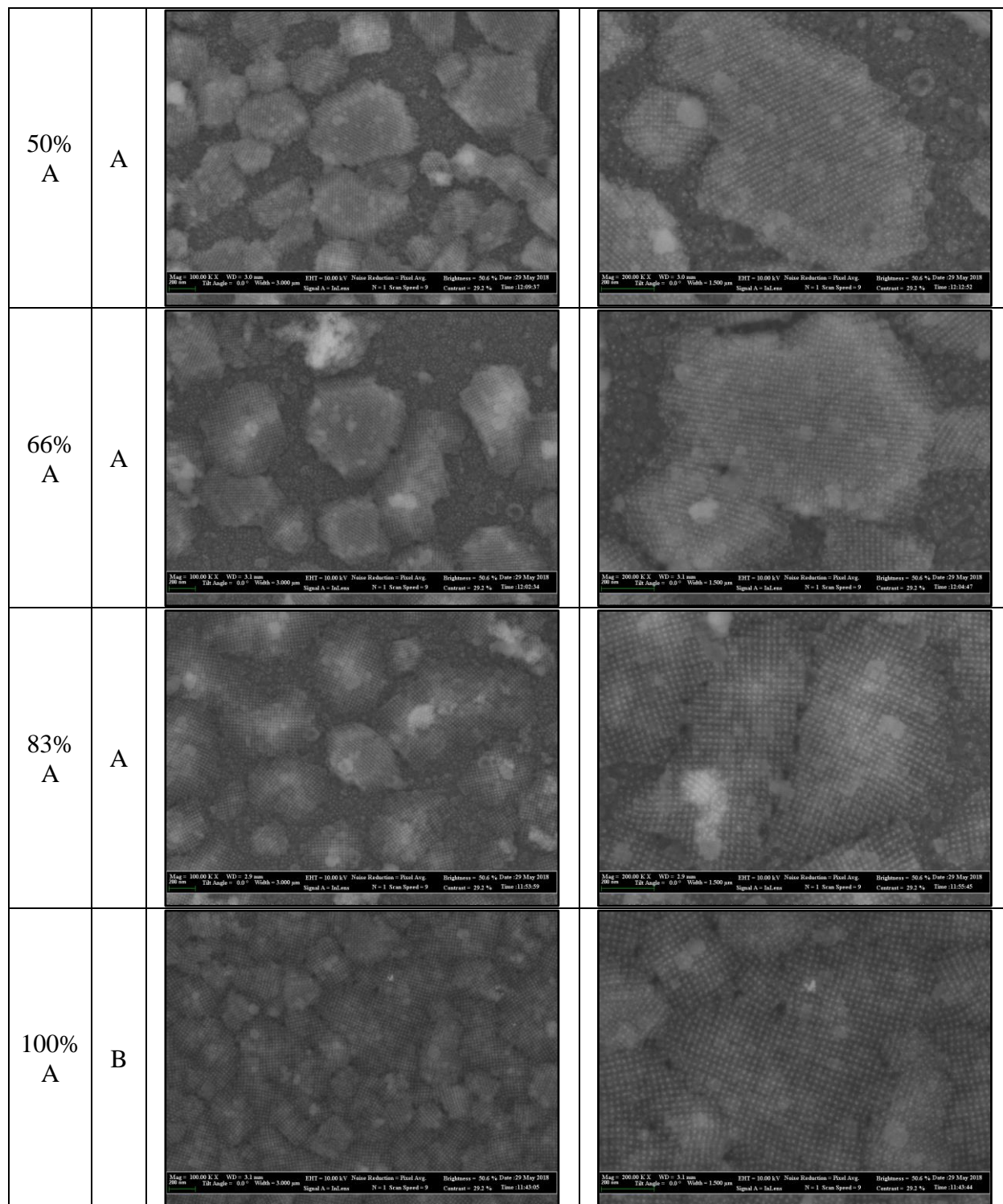
Figure A.17: Top-down SEM micrographs showing final texture of five layer (5L) bcc thin films having been annealed at 48.5 °C. The SEM micrographs noted as 100kx (middle column) are 3 µm wide and the 200kx (right column) are 1.5 µm wide.

Interestingly, other morphological trends can be observed with the texture of these thin films. Notice, the monofunctionalized substrates promote flatter thin films while the thin films on the bifunctionalized surfaces tend to island. This observed better "wetting" of the surface in the former case is hypothesized because each particle can bind to more "sticky ends" on a monofunctionalized surface, making its binding stronger and more preferred. Additionally, in several of these micrographs (specifically 50% A functionality, which was measured with SAXS *in-situ* during cooling), an inconsistent lattice parameter can be observed as a function of distance from the substrate surface. This is consistent with the asymmetric "shrinkage" concluded to occur in Figure 2.4 of the main text. Finally, strong amounts of faceting can be observed to arise in several of the oriented PAE islands. Specifically, the {001}-aligned grains produce pyramid-like structures whereas the {001}-aligned grains have large flat faces parallel to the substrate. This type of faceting is reminiscent of a Winterbottom construction[267] and proves promising for future work in controlling PAE crystal shape and creating well-defined single-crystal PAE superlattices. However, significant future work concerning appropriate thermal annealing or deposition conditions is needed in this research direction to achieve this aim.

A.6. Additional CsCl System Data

A.6.1. Indexing of Possible Orientation Alignments

Using the protocol outlined in Section A.4.1, the CsCl system peaks were indexed for the bulk, polycrystalline sample (Section A.3.3) and confirmed to align well to a CsCl lattice with a lattice parameter of 57.3 nm (Figure A.18). Additionally, following the analysis in Section A.4.2, the suppressed peaks were determined for thin film alignments with various proposed planes parallel to the substrate (Table A.9). Note, that only alignments of {001} and {011} were observed in this manuscript data, the other alignment possibility is simply tabulated for reference.
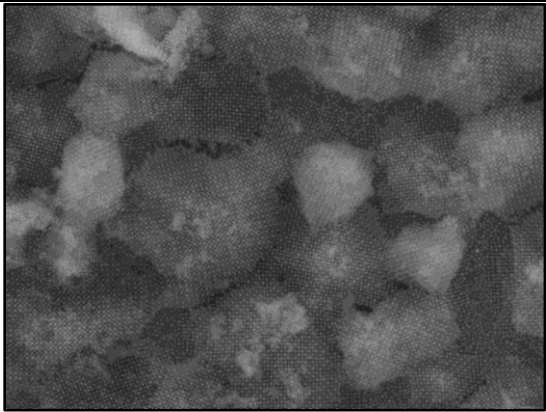
Figure A.18: Indexed 1D SAXS data for the CsCl PAE system (polycrystalline, bulk sample shown).

Table A.9: Indexed CsCl (a = 57.3 nm) peak positions (q) and suppressed peaks for given alignments.

Indexed Planes Bulk	q	Indexed Planes Present		
		{001}-Aligned	{011}-Aligned	{111}-Aligned
{100}	0.0110	(100), (010), (0-10), (-100)	(100), (-100)	Suppressed Entirely
{110}	0.0155	(110), (1-10), (-110), (-1-10)	(01-1), (0-11)	(1-10), (-110), (10-1), (01-1), (0-11), (-101)
{111}	0.0190	Suppressed Entirely	(11-1), (1-11), (-11-1), (-1-11)	Suppressed Entirely
{200}	0.0219	(200), (020), (0-20), (-200)	(200), (-200)	Suppressed Entirely
{210}	0.0245	(210), (2-10), (120), (1-20), (-120), (-1-20), (-210), (-2-10)	Suppressed Entirely	Suppressed Entirely
{211}	0.0269	Suppressed Entirely	(21-1), (2-11), (-21-1), (-2-11)	(11-2), (-1-12), (2-1-1), (1-21), (-12-1), (-211)
{220}	0.0310	(220), (2-20), (-220), (-2-20)	(02-2), (0-22)	(2-20), (-220), (20-2), (02-2), (0-22), (-202)
{221}, {300}	0.0329	(300), (030), (0-30), (-300)	(300), (12-2), (1-22), (-12-2), (-1-22), (-300)	Suppressed Entirely
{310}	0.0347	(310), (3-10), (130), (1-30), (-130), (-1-30), (-310), (-3-10)	Suppressed Entirely	Suppressed Entirely
{311}	0.0364	Suppressed Entirely	(31-1), (3-11), (-31-1), (-3-11)	Suppressed Entirely
{222}	0.0380	Suppressed Entirely	(22-2), (2-22), (-22-2), (-2-22)	Suppressed Entirely
{320}	0.0395	(320), (3-20), (230), (2-30), (-230), (-2-30), (-320), (-3-20)	Suppressed Entirely	Suppressed Entirely
{321}	0.0410	Suppressed Entirely	Suppressed Entirely	(21-3), (12-3), (-1-23), (-2-13), (3-1-2), (3-2-1), (2-31), (1-32), (-13-2), (-23-1), (-321), (-312)

A.6.2. Demonstration of Thin Film Nucleation Occurring at Top Surface

Similar to the investigation described in Section A.5.2, CsCl PAE thin films were deposited for 5, 10, 20, and 30 layers and annealed just below their bulk melting temperature (40.5 °C) (Figure A.19). In conjunction with the bcc SEM micrographs of the thin film morphology as a function of thickness, the CsCl micrographs indicate the likelihood that thin film nucleation occurs either at the film-solution interface or throughout the bulk of the thin film rather than at the substrate-film interface.

Number of Layers	50kx	100kx
5		
10		
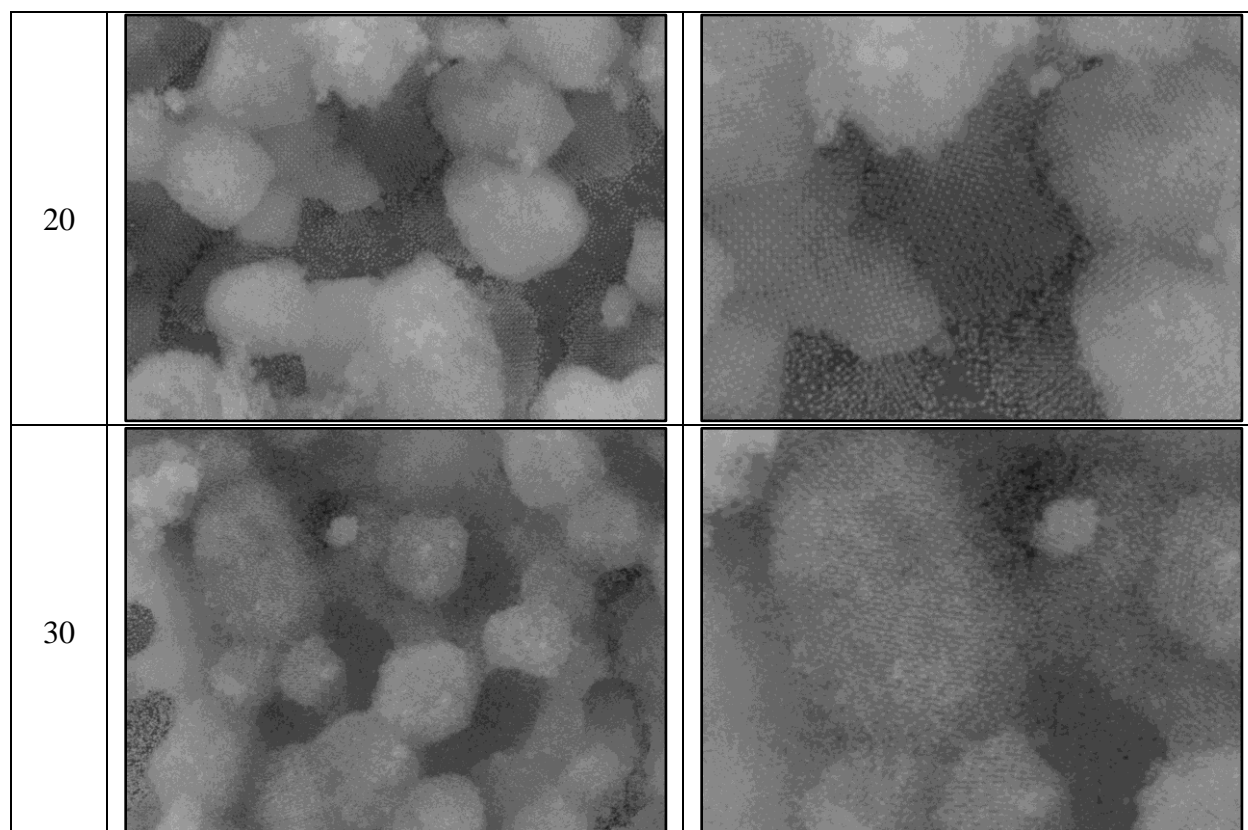
Figure A.19: Top-down SEM micrographs showing final texture of CsCl thin films of various thicknesses (denoted on left) having been annealed at 40.5 °C. The SEM micrographs noted as 50kx (middle column) are 6 µm wide and the 100kx (right column) are 3 µm wide.

The key insight garnered form Figure A.19 is that polycrystalline crystallites appear to be resting atop larger, aligned grains along the surface. In fact, the bottom of these crystallites often appears to "bleed out" into the aligned grain. This would be hypothesized if the thin film nucleated grains of random orientations at the top of the thin film and crystallized towards the substrate. When the growing grains contacted the substrate surface, the PAEs in the misaligned grain would be removed and driven to coalesce into the aligned grain.

To further investigate this hypothesis, a cross-sectional analysis was done on thick CsCl samples partway through a total reorganization. Specifically, a 10-layer and 30-layer CsCl thin film was annealed for 18 hours at 37 °C. Giving the rearrangement significant time allowed for the analysis of an equilibrium structure and not a kinetically trapped one. A lower temperature was chosen based on the findings in Section A.5.3 such that the thin film would not be entirely

191

reorganized. After embedding, the films were milled with FIB and the cross-section was analyzed by SEM (Figure A.20 and Figure A.21).

Indeed, the FIB-milled cross-sections corroborate a hypothesis that the films nucleate at the top and crystallize toward the substrate where the aligned grains are preferentially stabilized and grow more rapidly/absorb neighboring unaligned grains to dominate the final structure. Figure A.20 is a demonstrative cross-section of the 30-layer sample where it can be seen that an amorphous, not-yet reorganized section of PAE thin film exists between the crystalline region and the substrate. This same behavior is seen across the 15 µm cross-section for both the 10- and 30-layer sample and can be highlighted in the representative SEM micrographs (Figure A.21).
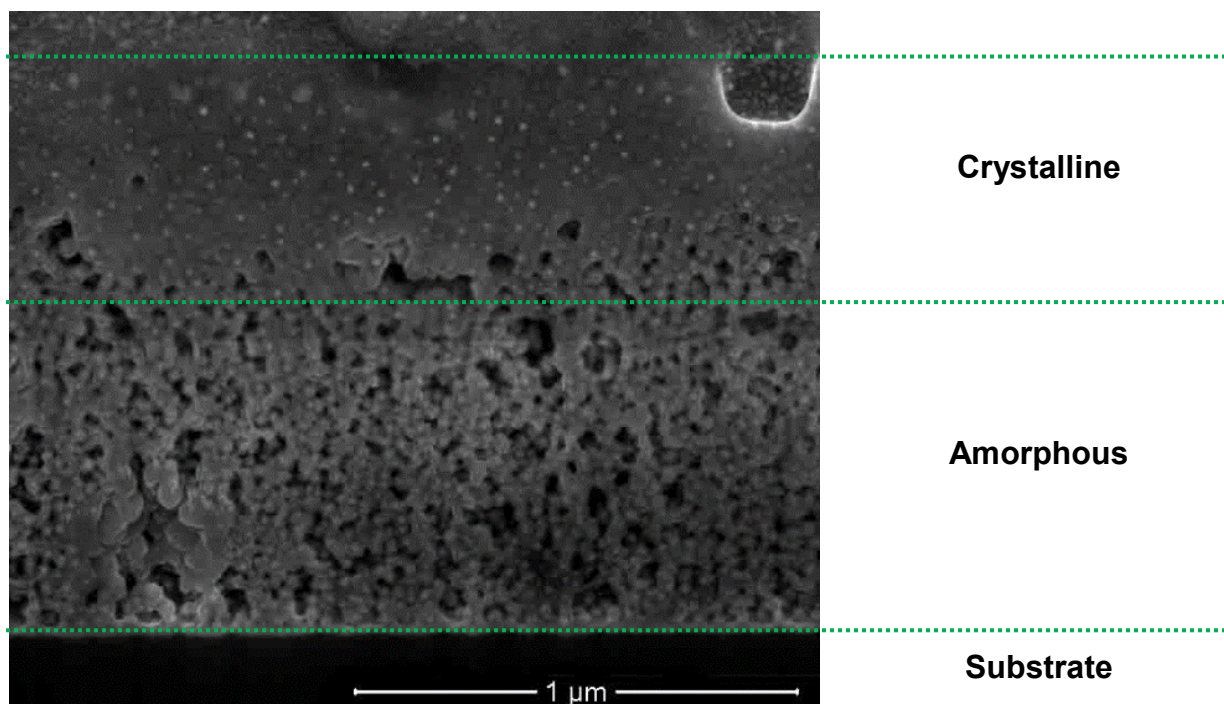
Figure A.20: Demonstrative SEM cross-sectional micrograph of a 30-layer CsCl PAE thin film halted in its rearrangement process showing nucleation at the top surface not at the substrate-film interface.

Sample	Representative Cross-Sectional SEM Micrographs		
10L 50% A A First			
30L 50% A B First			
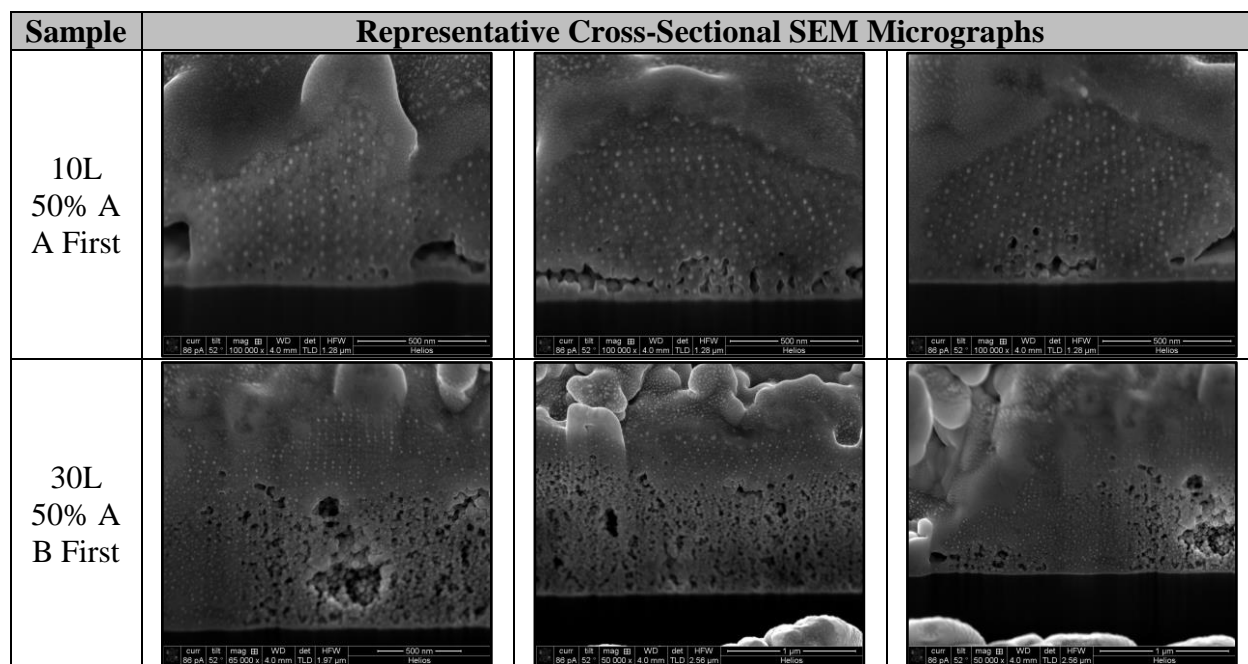
Figure A.21: Representative SEM cross-sectional micrographs of 10- and 30-layer CsCl PAE thin films halted in their rearrangement process revealing strong preferential grain alignment only upon contact with substrate surface. The widths of the SEM micrographs are as follows: (top row, all) 1.28 µm, (bottom row, left to right) 1.97 µm, 2.56 µm, and 2.56 µm.

A.6.3. Five Layer (5L) Thin Film Texture as a Function of Surface Functionality

Unlike the bcc PAE system, the CsCl system utilizes two different PAE constructs with different architectures to create a binary system. Because of this distinctiveness between PAE A and PAE B in this system, it is not obvious whether allowing PAE A versus PAE B to bind to the substrate surface will change the resulting thin film morphology or texture. Therefore, several 5-layer thin film samples were synthesized (Section A.1) with various surface functionalities and with both PAE A deposited first and B deposited first. These films were then annealed and their resulting structures were probed with SAXS and SEM. The main conclusions from this analysis are highlighted in Figure 2.2 of the main text; further supplementary data concerning this investigation is consolidated in this section.

Foremost, it was observed that depositing PAE A first versus B first yielded different amorphous structures even before annealing (Figure A.22). It should be noted that while these states are often referred to as "amorphous," there is a significant amount of short-range ordering present in PAE aggregates prior to annealing (as evidenced by several broad peaks in the SAXS

pattern); the structures have a somewhat regular nearest neighbor correlation length. In all surface functionalization cases, when PAE A was deposited first, the first broad peak occurs closer to the largest structural peak (only 0%, 50%, and 100% A functionalization is shown in Figure A.22 for clarity). While understanding the exact local structure around NPs from such broad SAXS peaks is very difficult, this data does conclude a distinct difference in the amorphous structures. It is hypothesized that this difference arises from the "softer" (less dense) DNA corona around PAE B allows them to pack closer together on the substrate surface. Consistent with this hypothesis, the final crystalline structures after annealing for 0% A and 100% A functionality display a slightly different lattice parameter (Figure 2.2B) where the NPs are closer together when PAE B is deposited first.

Once allowed to reorganize at a temperature near their T_m (40.5 °C), (see Videos S6, S7, and S8 for the *in-situ* SAXS pattern development)[177] the 5-layer CsCl thin films annealed into crystalline arrangements that showed grain alignments roughly similar to those expected in the bcc case, but with a distinctly different distribution dependent upon the particle deposited first. The asymmetric nature of the {001}-aligned and {011}-aligned grains as a function of surface functionality can be observed in both the 2D SAXS patterns (Figure A.23, only the data corresponding to the 1D curves in Figure 2.2B and C is included for brevity) and 1D SAXS patterns (Figure 2.2B and C, and Figure A.24), then verified with the top-down SEM micrographs of the final texture (Figure A.26). The SAXS patterns were analyzed consistent with the protocol described in Section A.4.3 and the calculated amounts of the two orientations in each mixture is summarized in the main text (Figure 2.2D). Finally, computer-generated visualizations of the real-space placement of the PAEs within an oriented thin film grain are provided for easy comparison to SEM data and identification of observed thin film texture (Figure A.25).
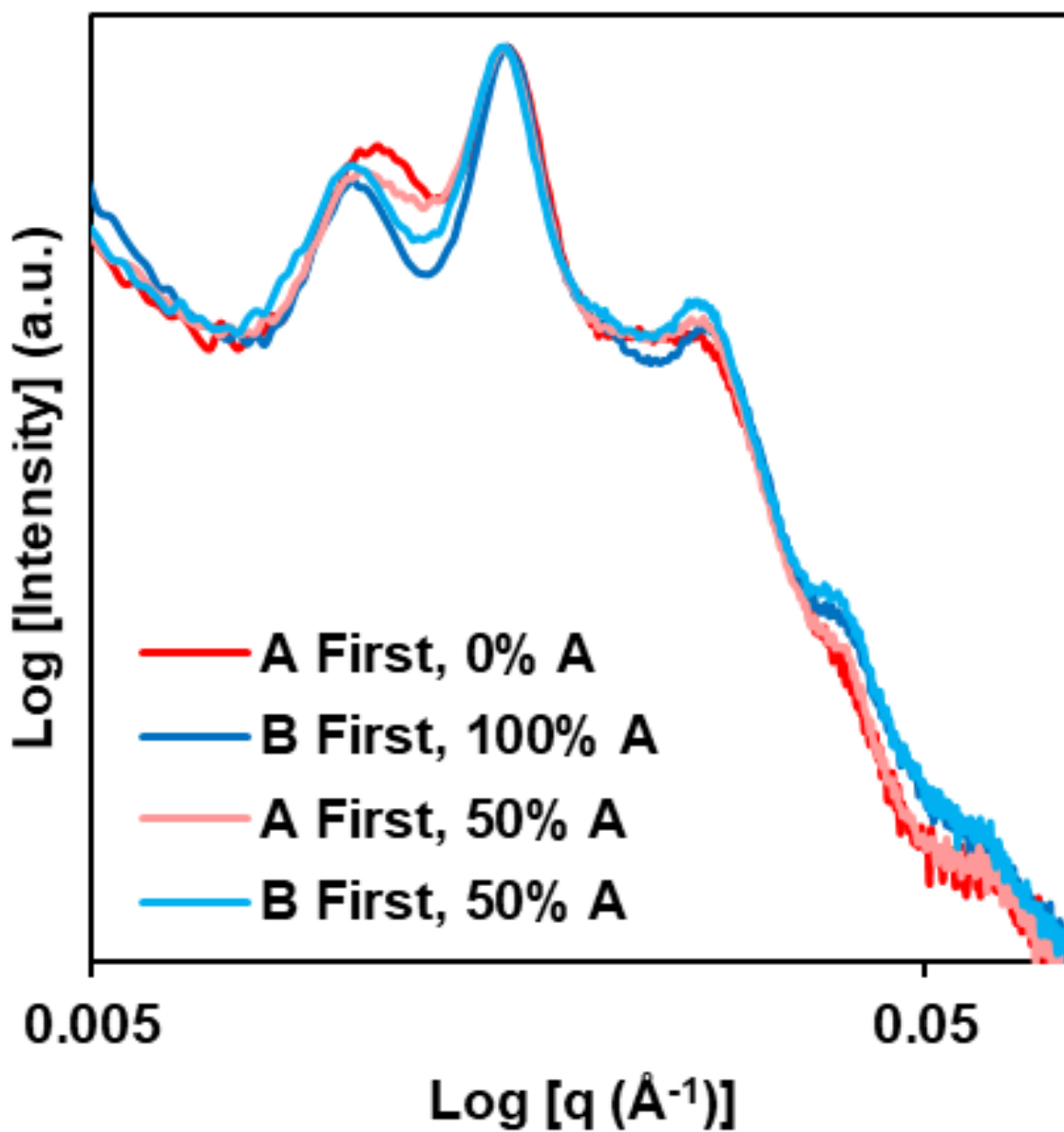
Figure A.22: 1D SAXS curves for five-layer (5L) CsCl thin films prior to annealing, deposited on monofunctionalized substrates (0% A and 100% A, dark colors) or 50/50 bifunctionalized substrates (50% A, light colors). Red curves represent PAE A deposited first, blue B first.

	A First	**B First**
(Left) 0% A (Right) 100% A		
(Both) 50% A		
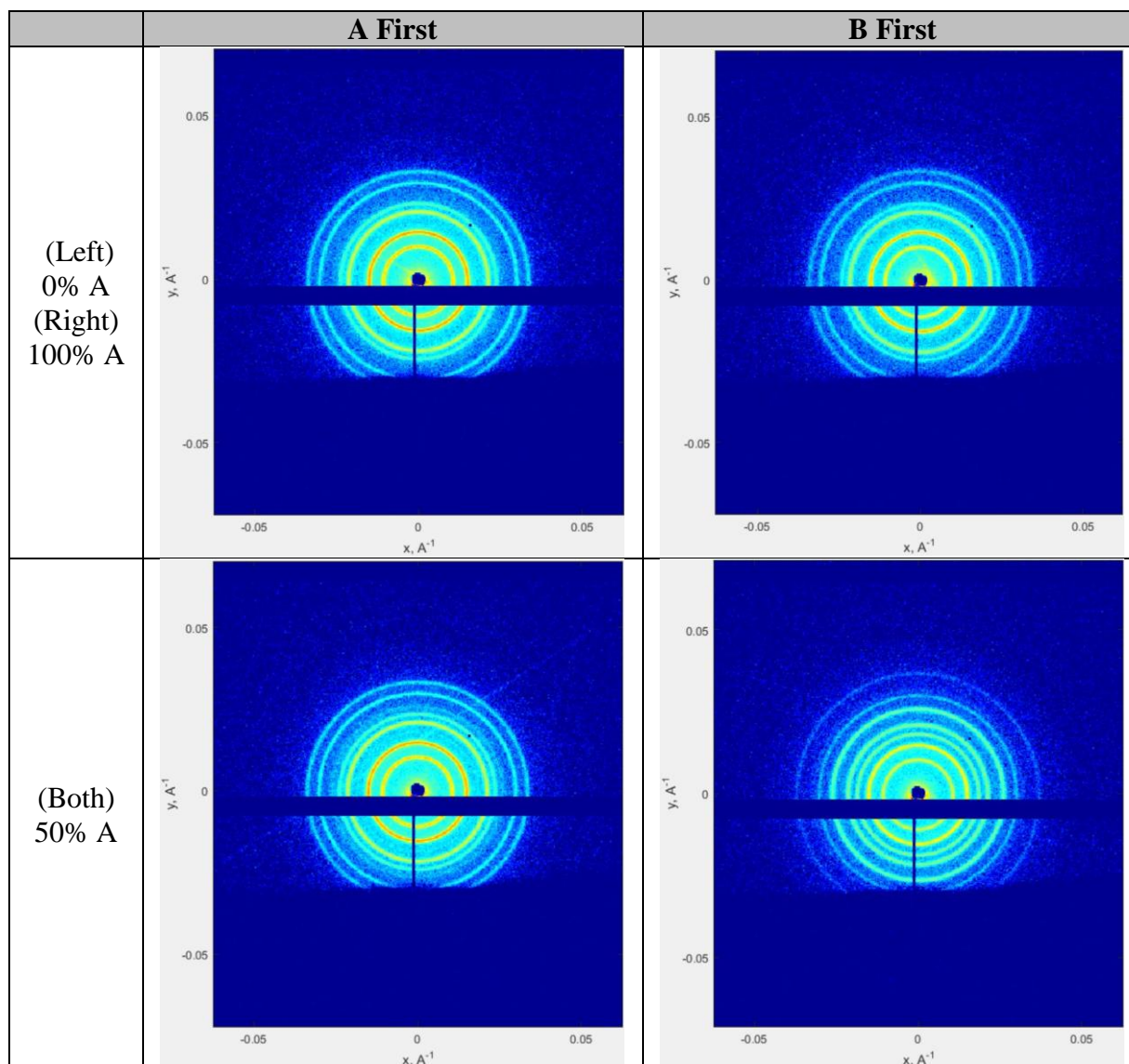
Figure A.23: 2D equilibrium SAXS data for five-layer (5L) CsCl thin films having been annealed at 40.5 °C at various surface functionalities with either PAE A or B deposited first.

0% A

16% A

33% A

50% A

66% A

83% A
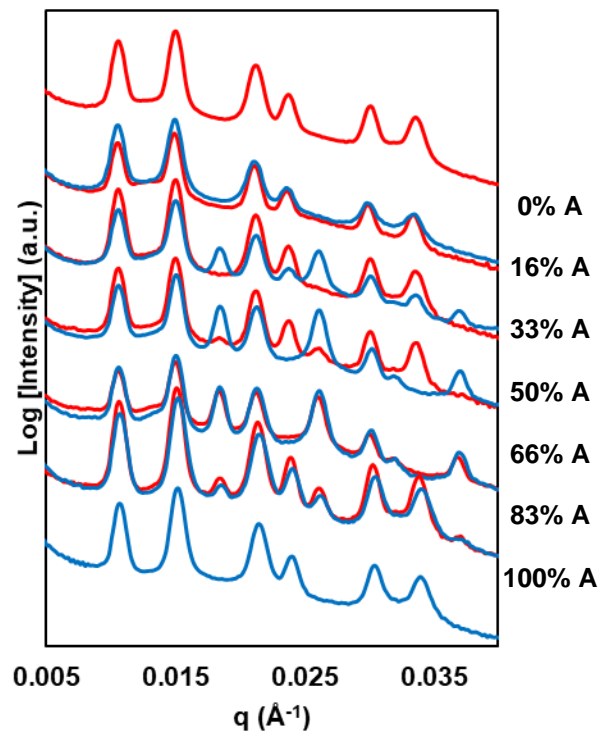
100% A

Figure A.24: Equilibrium 1D SAXS state for five-layer (5L) CsCl thin films having been annealed at 40.5 °C at various surface functionalities (0% A to 100% A). Red curves correspond to PAE A deposited first, blue curves 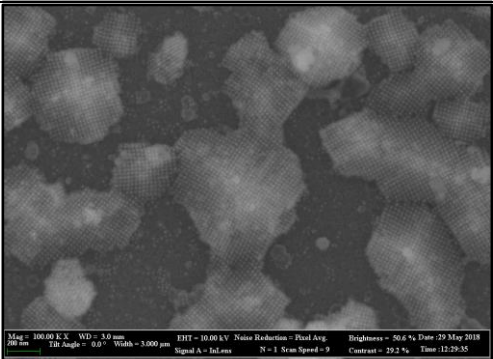to B first. The SAXS curves have been offset in intensity for clarity. A clear difference in orientation mixture arises at 33% and 50% A functionality.
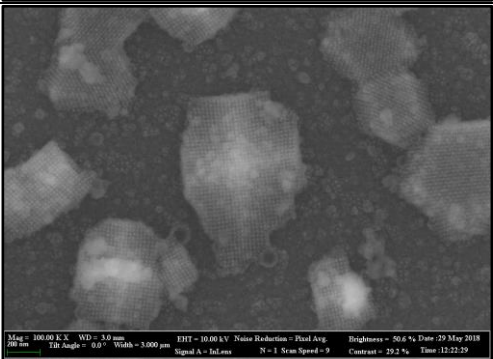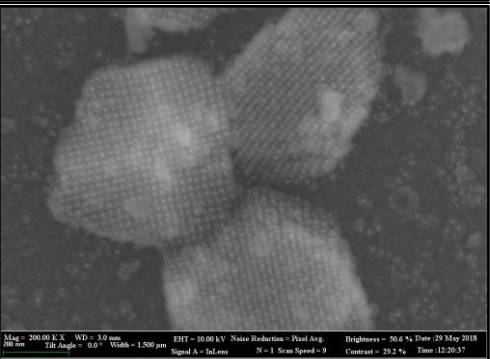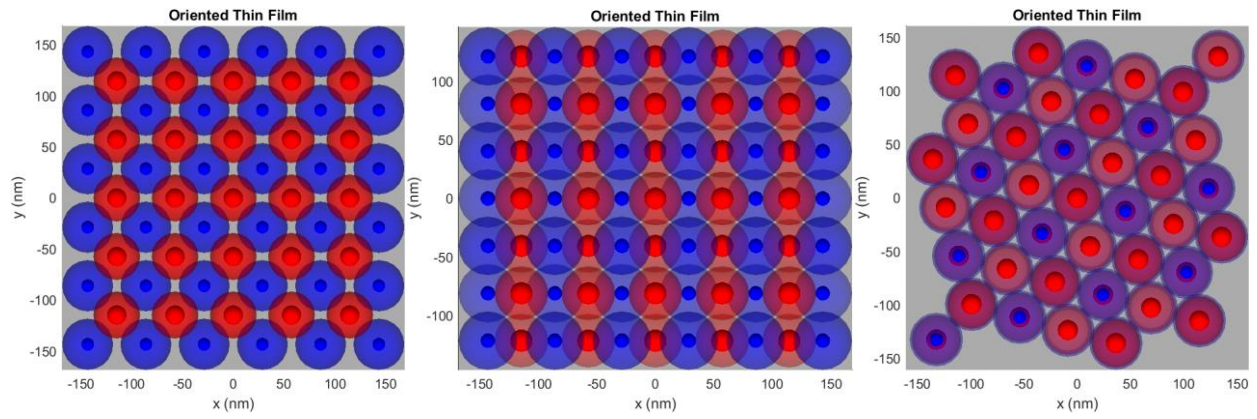
Figure A.25: Visualizations of the top-down arrangement of a CsCl PAE grain with the (from left to right) {001}, {011}, or {111} plane aligned parallel to the substrate.

| Surface Functionality	A First	B First
0% A		N/A
16% A		
33% A		

50% A		
66% A		
83% A		
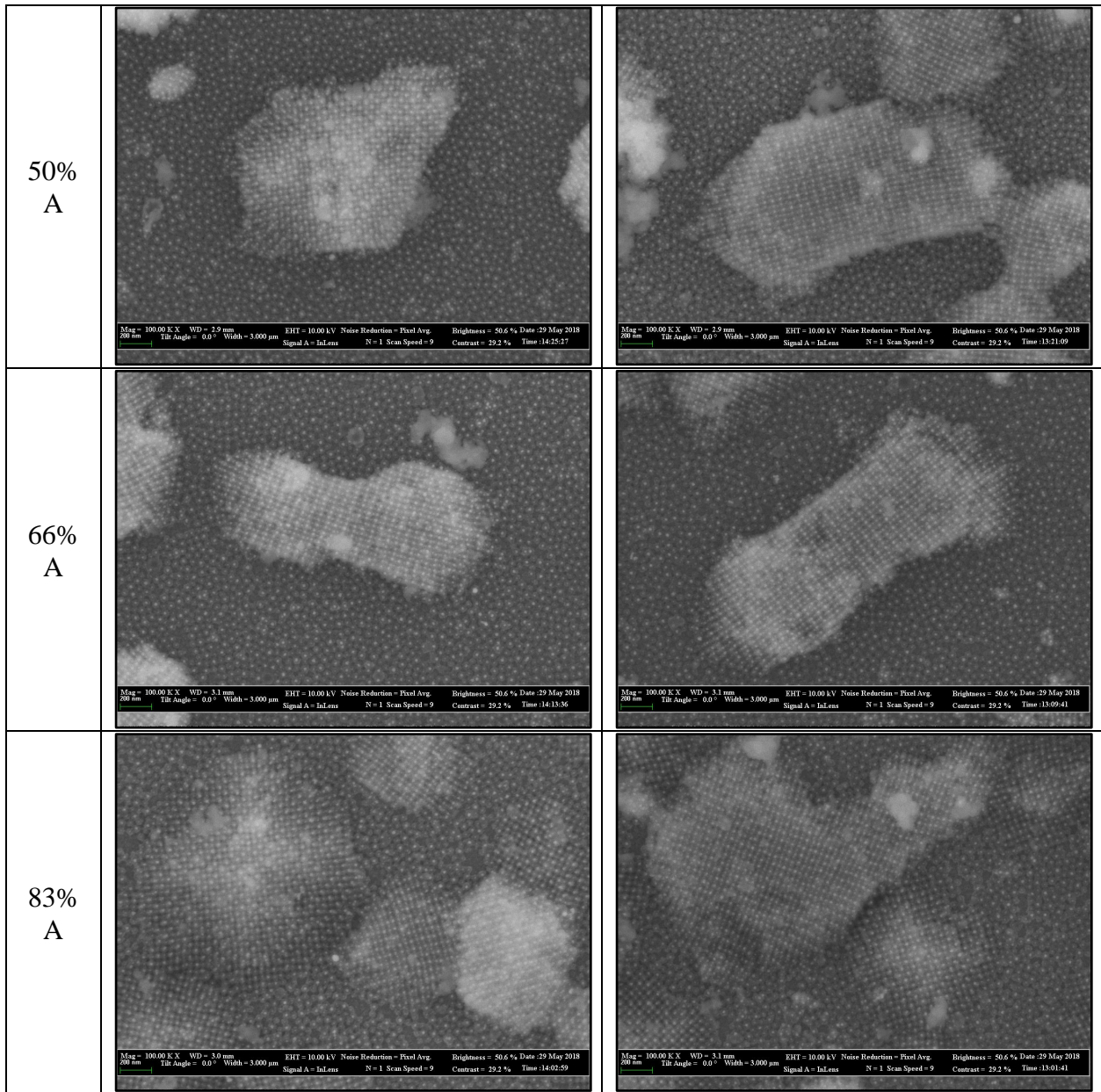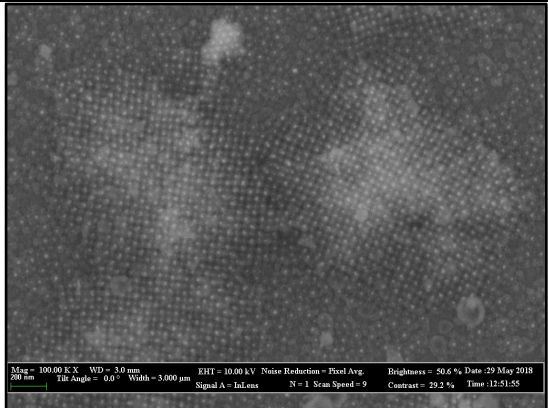
100% A	N/A	

Figure A.26: Top-down SEM micrographs showing final texture of five layer (5L) CsCl thin films deposited on various substrate functionalities (0% to 100% A, noted in left column) with either PAE A deposited first (middle) or B first (right) after being annealed at 40.5 °C. All SEM micrographs are 3 µm wide.

A.7. Additional AlB$_2$ System Data

A.7.1. Indexing of Possible Orientation Alignments

Using the protocol outlined in Section A.4.1, the AlB$_2$ system peaks were indexed for the bulk, polycrystalline sample (Section A.3.3) and confirmed to align well to an AlB$_2$ lattice with lattice parameters a = 61.5 nm and c = 50 nm (Figure A.27). Additionally, following the analysis in Section A.4.2, the suppressed peaks were determined for thin film alignments with various proposed planes parallel to the substrate (Table S10). Note, that only alignments of {001} were observed in this manuscript data, the other alignment possibilities are tabulated for reference.

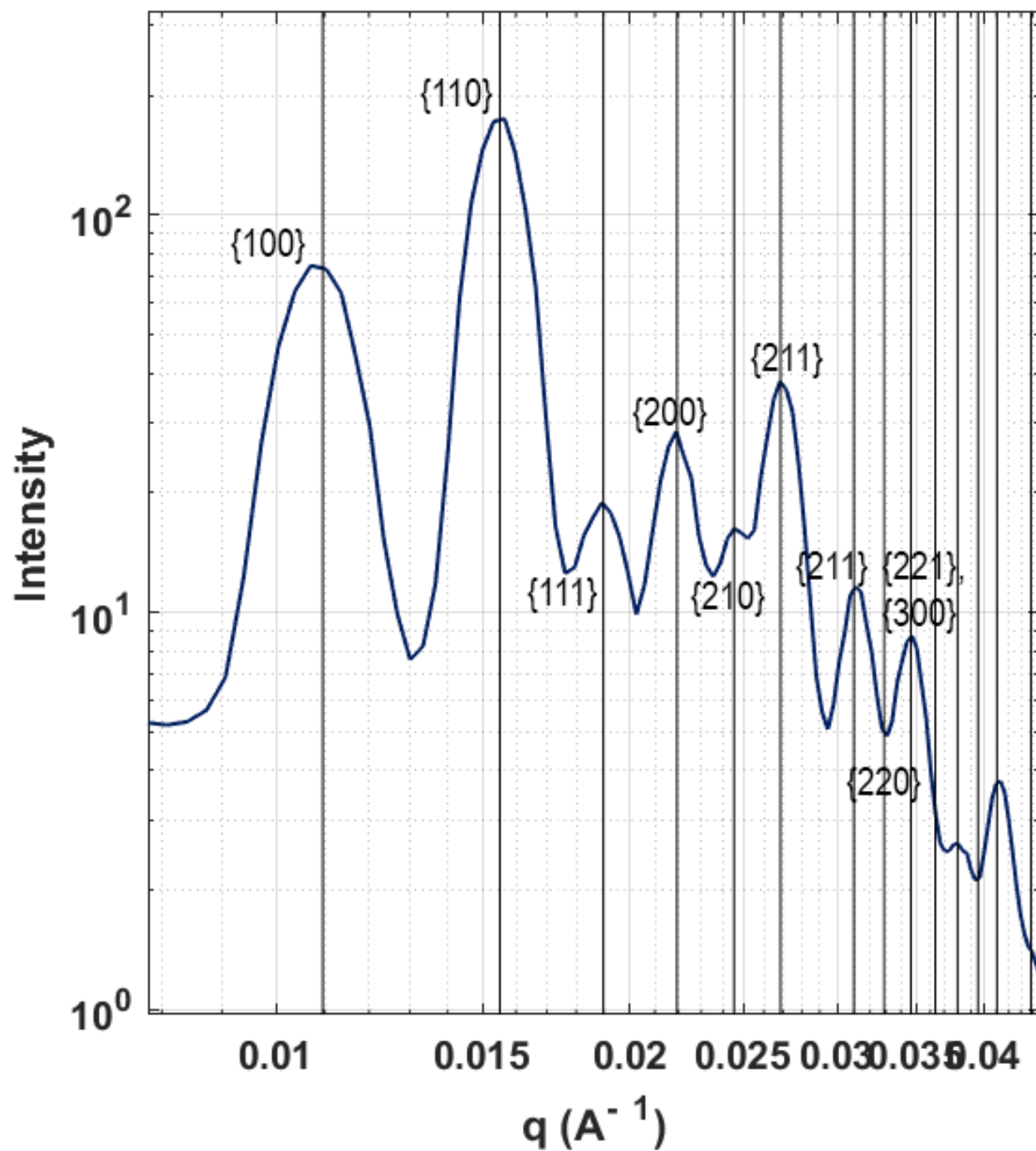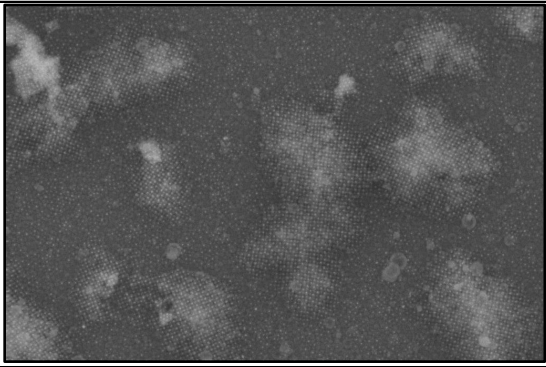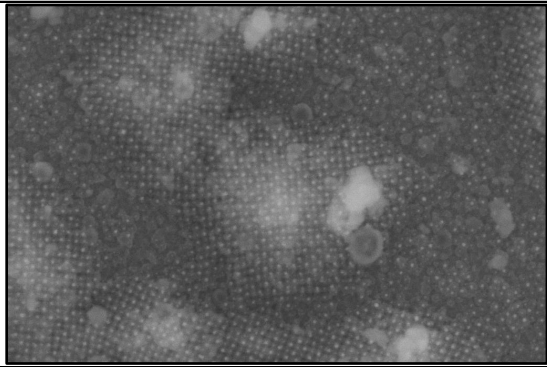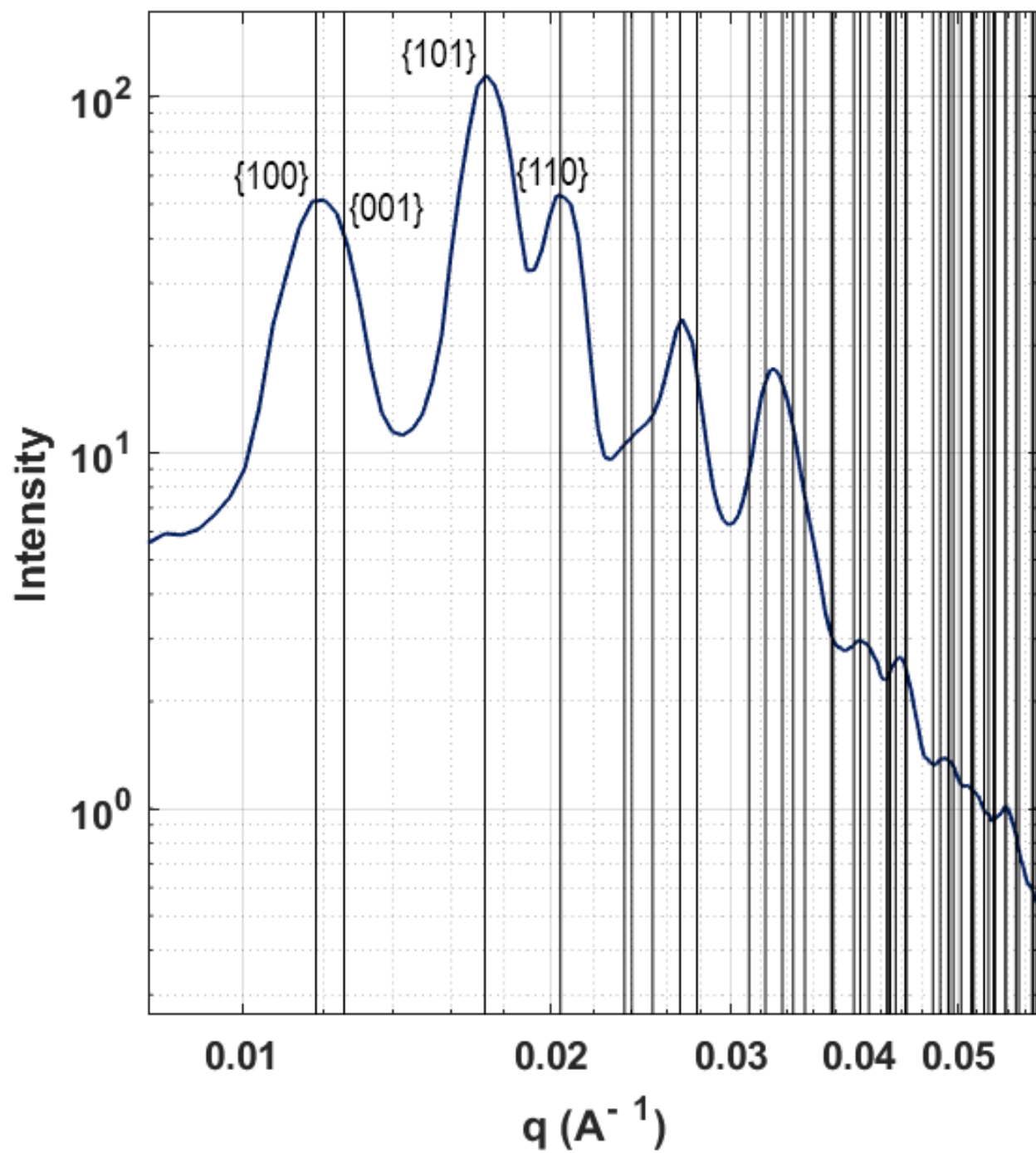Figure A.27: Indexed 1D SAXS data for the AlB_2 PAE system (bulk, polycrystalline sample shown).

Table A.10: Indexed AlB$_2$ (a = 61.5 nm, c = 50 nm) peak positions (q) and suppressed peaks for given alignments. (Note: {010}-Aligned Thin Films exhibit same suppressed peaks as {100}-Aligned; likewise, {011}- and {101}-Aligned Thin Films have the same suppressed peaks.)

Indexed Planes Bulk	q	Indexed Planes Present			
		{001}-Aligned	{100}-Aligned	{110}-Aligned	{101}-Aligned
{100}	0.0118	(1 0 0),(1 -1 0),(0 1 0),(0 -1 0),(-1 1 0),(-1 0 0)	(0 1 0),(0 -1 0)	(1 -1 0),(-1 1 0)	(0 1 0),(0 -1 0)
{001}	0.0126	Suppressed Entirely	(0 0 1),(0 0 -1)	(0 0 1),(0 0 -1)	Suppressed Entirely
{101}	0.0172	Suppressed Entirely	(0 1 1),(0 1 -1),(0 -1 1),(0 -1 -1)	(1 -1 1),(1 -1 -1),(-1 1 1),(-1 1 -1)	(1 0 -1),(1 -1 -1),(-1 1 1),(-1 0 1)
{110}	0.0204	(2 -1 0),(1 1 0),(1 -2 0),(-1 2 0),(-1 -1 0),(-2 1 0)	Suppressed Entirely	Suppressed Entirely	Suppressed Entirely
{200}	0.0236	(2 0 0),(2 -2 0),(0 2 0),(0 -2 0),(-2 2 0),(-2 0 0)	(0 2 0),(0 -2 0)	(2 -2 0),(-2 2 0)	(0 2 0),(0 -2 0)
{111}	0.0240	Suppressed Entirely	Suppressed Entirely	Suppressed Entirely	(1 1 -1),(1 -2 -1),(-1 2 1),(-1 -1 1)
{002}	0.0251	Suppressed Entirely	(0 0 2),(0 0 -2)	(0 0 2),(0 0 -2)	Suppressed Entirely
{201}	0.0267	Suppressed Entirely	(0 2 1),(0 2 -1),(0 -2 1),(0 -2 -1)	(2 -2 1),(2 -2 -1),(-2 2 1),(-2 2 -1)	Suppressed Entirely
{102}	0.0278	Suppressed Entirely	(0 1 2),(0 1 -2),(0 -1 2),(0 -1 -2)	(1 -1 2),(1 -1 -2),(-1 1 2),(-1 1 -2)	Suppressed Entirely
{210}, {120}	0.0312	(2 1 0),(1 2 0),(-1 -2 0),(-2 -1 0),(3 -1 0),(3 -2 0),(2 -3 0),(1 -3 0),(-1 3 0),(-2 3 0),(-3 2 0),(-3 1 0)	Suppressed Entirely	Suppressed Entirely	Suppressed Entirely
{112}	0.0324	Suppressed Entirely	Suppressed Entirely	Suppressed Entirely	(2 -1 -2),(-2 1 2)

{211}, {121}	0.0336	Suppressed Entirely	Suppressed Entirely	Suppressed Entirely	(1 2 -1),(-1 -2 1),(1 -3 -1),(-1 3 1)
{202}	0.0345	Suppressed Entirely	(0 2 2),(0 2 -2),(0 -2 2),(0 -2 -2)	(2 -2 2),(2 -2 -2),(-2 2 2),(-2 2 -2)	(2 0 -2),(2 -2 -2),(-2 2 2),(-2 0 2)
{300}	0.0354	(3 0 0),(3 -3 0),(0 3 0),(0 -3 0),(-3 3 0),(-3 0 0)	(0 3 0),(0 -3 0)	(3 -3 0),(-3 3 0)	(0 3 0),(0 -3 0)
{301}	0.0376	Suppressed Entirely	(0 3 1),(0 3 -1),(0 -3 1),(0 -3 -1)	(3 -3 1),(3 -3 -1),(-3 3 1),(-3 3 -1)	Suppressed Entirely
{003}	0.0377	Suppressed Entirely	(0 0 3),(0 0 -3)	(0 0 3),(0 0 -3)	Suppressed Entirely
{103}	0.0395	Suppressed Entirely	(0 1 3),(0 1 -3),(0 -1 3),(0 -1 -3)	(1 -1 3),(1 -1 -3),(-1 1 3),(-1 1 -3)	Suppressed Entirely
{212}, {122}	0.0401	Suppressed Entirely	Suppressed Entirely	Suppressed Entirely	(2 1 -2),(2 -3 -2),(-2 3 2),(-2 -1 2)
{220}	0.0409	(4 -2 0),(2 2 0),(2 -4 0),(-2 4 0),(-2 -2 0),(-4 2 0)	Suppressed Entirely	Suppressed Entirely	Suppressed Entirely

A.7.2. Five Layer (5L) Thin Film Texture as a Function of Surface Functionality

Akin to the conclusions elucidated in Section A.6.3 for the amorphous CsCl thin films, the AlB$_2$ PAE system also contains two distinctly different PAE constructs and therefore are hypothesized to exhibit different structures depending on the PAE type deposited first. Indeed, slight differences between the A and B first states exist in the 1D SAXS data (Figure A.28), indicating different local arrangement of particles. More interesting, however, is the comparison of these AlB$_2$ amorphous structures with their counterparts in the CsCl system (Figure A.22). It is worth drawing attention to the fact the patterns have striking similarities. This strengthens the hypothesis that the AlB$_2$ PAEs, when deposited, adopt a roughly CsCl-like arrangement which must be lost before an AlB$_2$ conformation can be adopted.
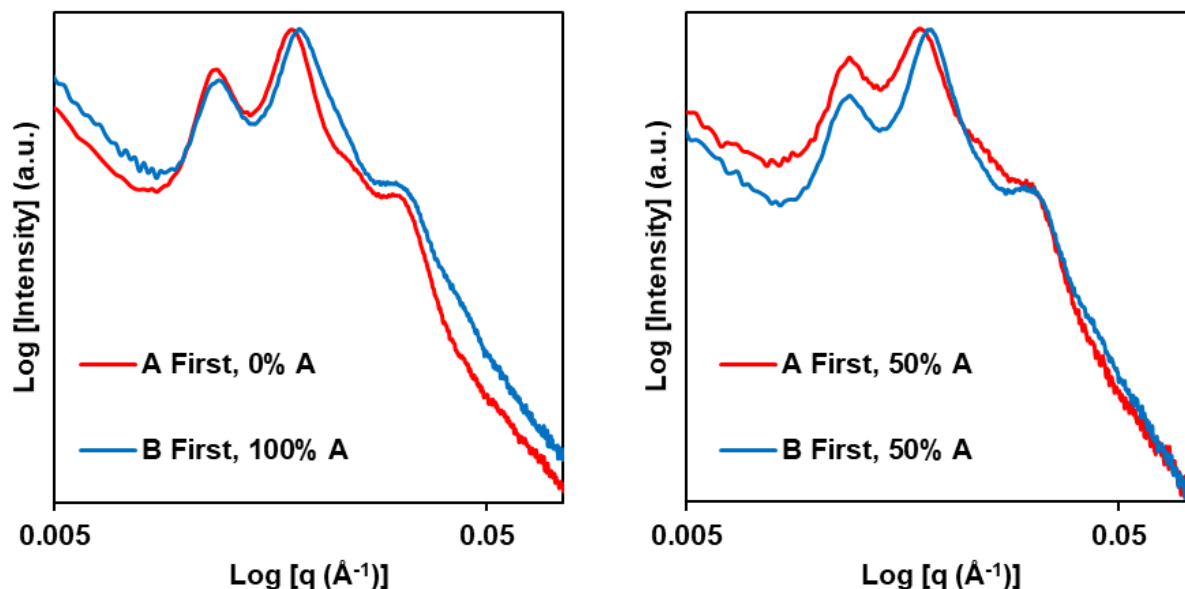
Figure A.28: 1D SAXS curves for five-layer (5L) AlB_2 thin films prior to annealing, deposited on monofunctionalized substrates (0% A and 100% A, left) or 50/50 bifunctionalized substrates (50% A, right). Red curves represent PAE A deposited first, blue B first.

These thin films were then reorganized into crystalline states while under the observation of *in-situ* SAXS measurements. Uniquely, the AlB_2 system displayed significantly different reorganization behavior (Video S9)[177] when compared to either the bcc system (Video S1)[177] or the CsCl system (Videos S6, S7, and S8).[177] Namely, the AlB_2 system required temperatures higher relative to their T_m than the other two systems to induce nucleation and crystallization. Additionally, the process of reorganization took significantly longer to reach equilibrium than bcc or CsCl thin films. Finally, and most prominently, the AlB_2 rearrangement process uniquely exhibited a 'fluidic'-like state (Figure 2.3B and Video S9[177]) where nearly all short-range ordering (SAXS peaks) were lost prior to crystalline peaks arising. Conversely, in the bcc and CsCl systems, the broad SAXS peaks present in the amorphous states simply sharpen into crystalline peaks.

The final thin film textures, as determined by SAXS analysis of the equilibrated AlB_2 thin films, reveal only one orientation alignment (consistent with the hexagonal plane – {001} – parallel to the substrate regardless of surface functionality or which PAE is deposited first (Figure A.29).

The {001} plane is hypothesized to be the singly preferred alignment because the hexagonal arrangement maximizes PAE-substrate binding compared to the other possible alignments.
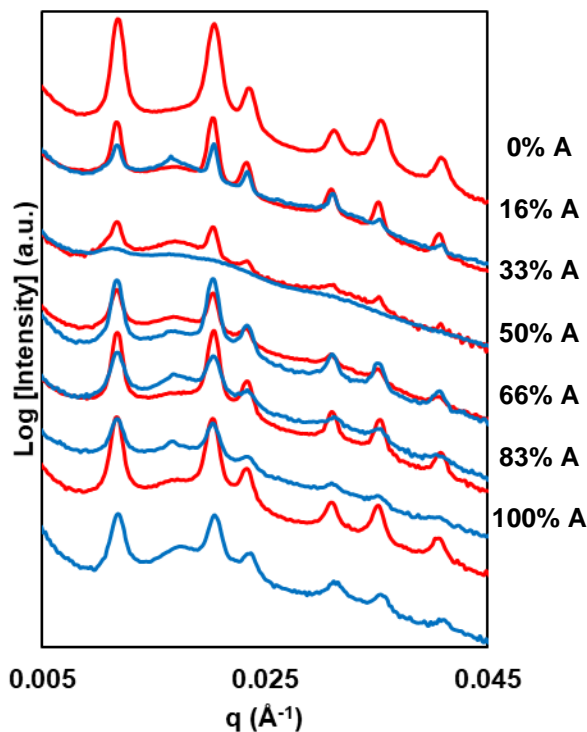
Figure A.29: Equilibrium SAXS state for five-layer (5L) AlB_2 thin films with various surface functionalities (0% A to 100% A). Red curves correspond to PAE A deposited first, blue curves to B first. The SAXS curves have been offset in intensity for clarity. Only patterns of suppressed peaks consistent with {001}-alignment are observed.

A.7.3. Arise of CsCl Crystals Upon Cooling

When the AlB_2 thin films were allowed to cool, embedded, and observed under SEM, a unique result arose with the unexpected presence of crystalline regions with rectangular symmetry. This result is explored in the main text (Figure 2.3C). It is hypothesized that the regions with particle planes at 90° angles are either the described AlB_2 phase oriented without the {001} plane aligned parallel to the substrate or consist of a CsCl lattice that was driven to form from PAE A and PAE B originally designed to create AlB_2. It is posited in the main text that both AlB_2 and CsCl can be driven to occur from the same binary PAE system due to local stoichiometric differences.[69]

206

To deduce which of the cases is more consistent with the observed data, SEM micrographs of the cooled and embedded AlB_2 thin films were collected and compared against computer-generated visualizations of various AlB_2 orientations (Figure A.30) and CsCl orientations (Figure A.31). A CsCl lattice with a 53 nm lattice parameter was chosen for comparison as that is consistent with what would be expected to form based on the hydrodynamic radii of the two particle types (Section A.3.1) as well as consistent with indexing the observed SAXS structures to a CsCl arrangement (Figure A.31). In all of the cases investigated, the microstructure of these thin films contained localized regions of crystallinity surrounded by swaths of amorphous PAEs (Figure A.32, Figure A.33, and Figure A.34). Based on comparison with the "ideal" particle positions and measurement of the interparticle spacings (Figure A.30 and Figure A.31), the crystalline regions were determined to be a mixture of {001}-oriented AlB_2 lattices (summarized with representative SEM micrographs in Figure A.33) and {011}-oriented CsCl lattices with roughly a 53 nm lattice parameter (representative micrographs in Figure A.34).
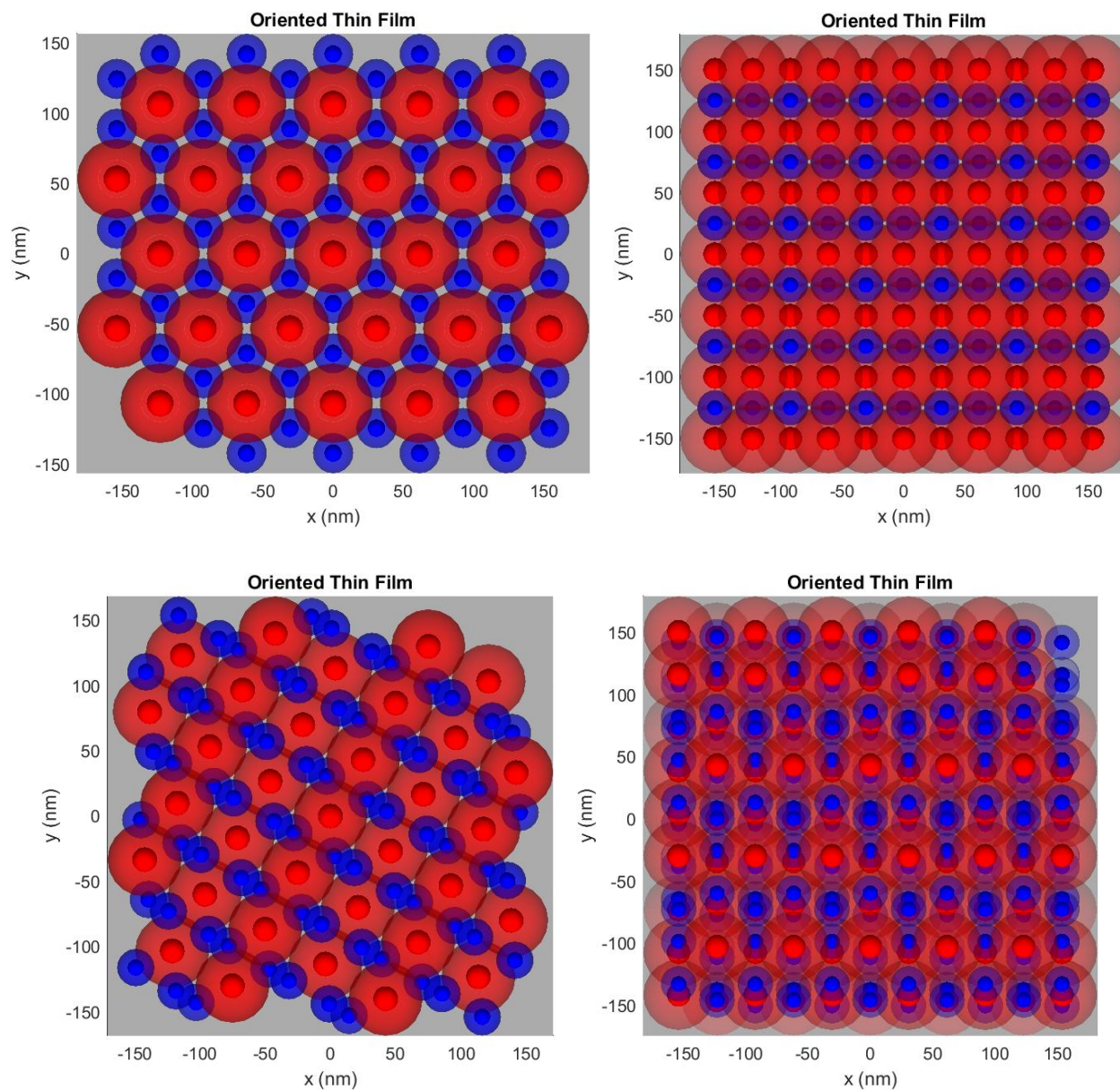
Figure A.30: Visualizations of the top-down arrangement of an AlB$_2$ PAE grain (a = 61.5 nm, c = 50nm) with the (clockwise from top left) {001}, {010}, {011}, or {110} aligned parallel to the substrate. Note: {100}-alignment structure is identical to {010}, and {101} is the same as {011}.
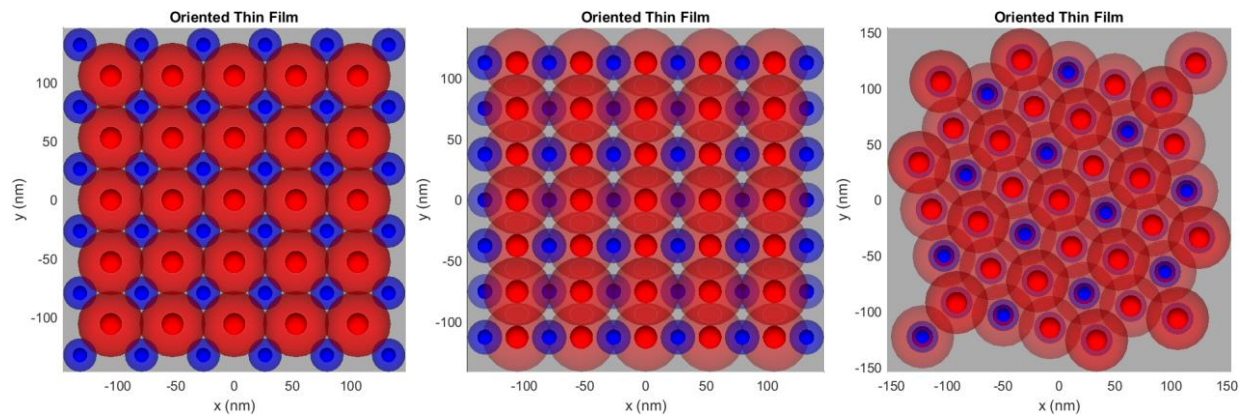
Figure A.31: Visualizations of the top-down arrangement of a CsCl PAE grain (a = 53 nm) with the (from left to right) {001}, {011}, or {111} plane aligned parallel to the substrate.

Surface Functionality	A/B First	50kx	100kx
0% A	A		
16% A	A		
16% A	B		
33% A	B		

50% A	B		
66% A	A		
83% A	A		
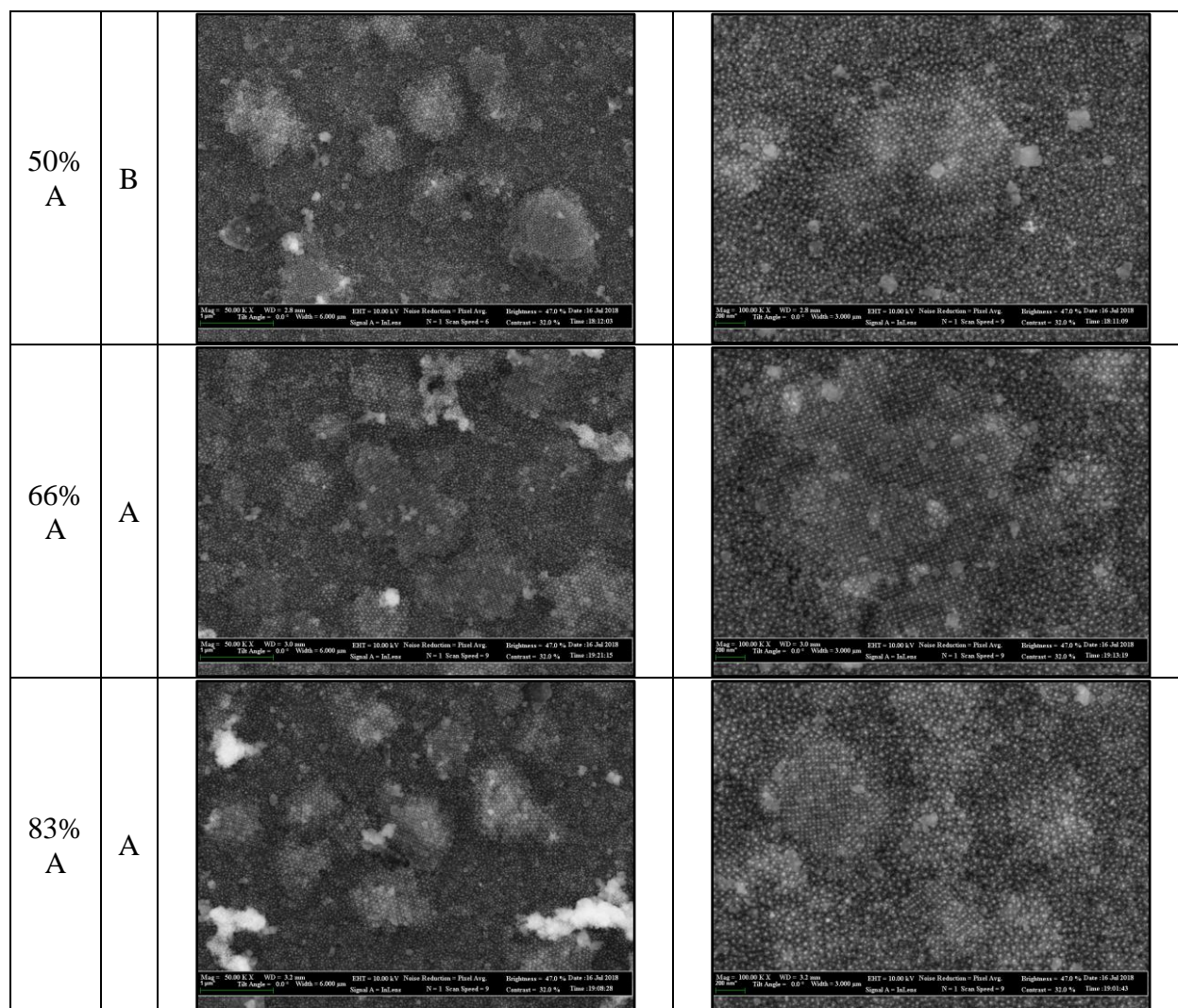
Figure A.32: Top-down SEM micrographs showing final texture and morphology of five-layer (5L) AlB$_2$ thin films deposited on various substrate functionalities and PAE type deposited first (noted in left columns) after being annealed and cooled. The SEM micrographs noted as 50kx are 6 µm wide and the 100kx are 3 µm wide.
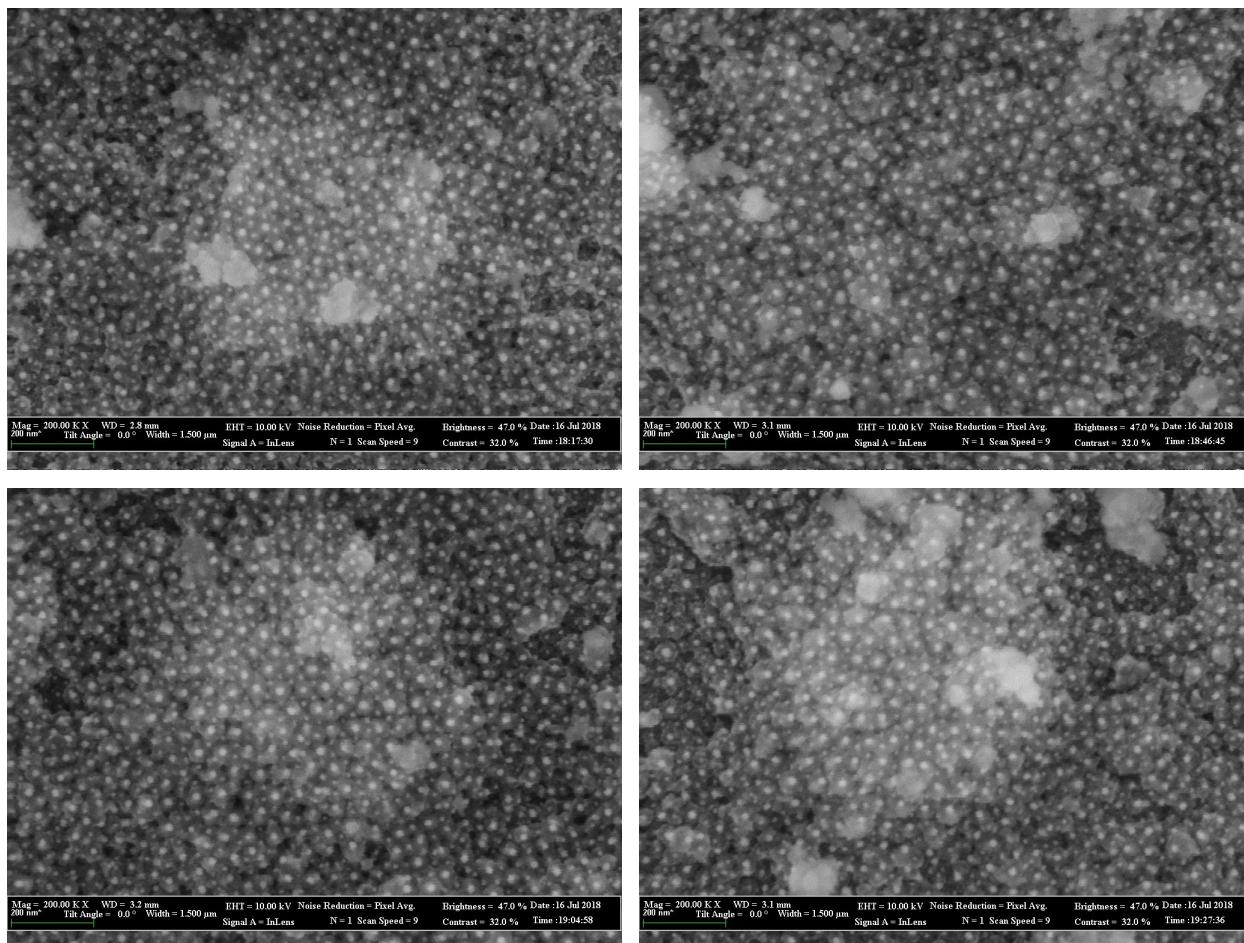
Figure A.33: Representative, top-down SEM micrographs showing crystalline domains with hexagonal symmetry observed in five-layer (5L) AlB2 thin films after being annealed and cooled. The grains' structures and lattice parameters are consistent with the hexagonal {001} plane of the AlB_2 lattice aligned parallel to the substrate (as observed in SAXS). All micrographs are 1.5 µm wide.
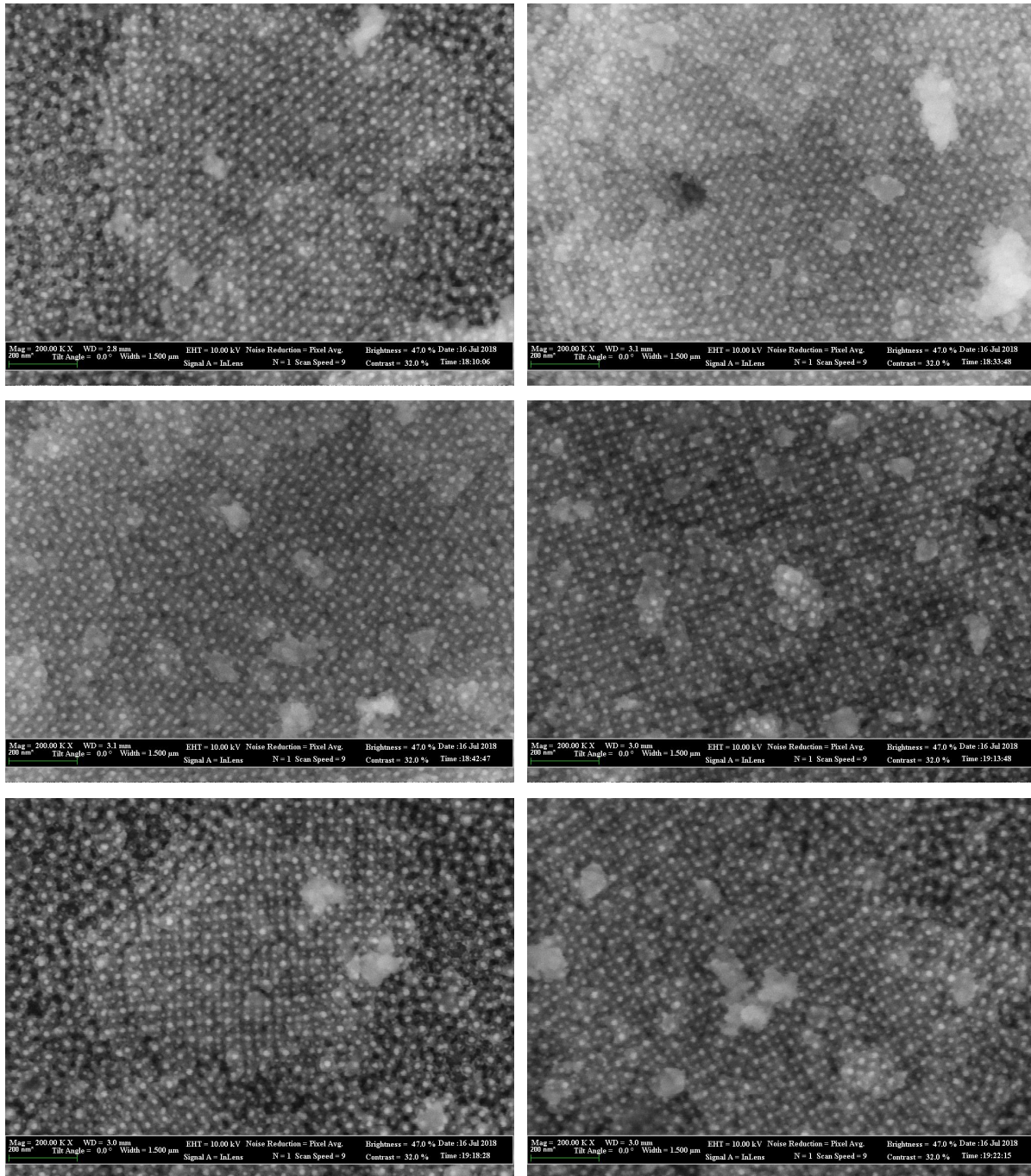
Figure A.34: Representative, top-down SEM micrographs showing crystalline domains with rectangular symmetry observed in five-layer (5L) AlB$_2$ thin films after being annealed and cooled. The grains' structures and lattice parameters are consistent with the a {011} plane of a CsCl lattice aligned parallel to the substrate. All micrographs are 1.5 µm wide.

The SEM micrographs strongly indicate the presence of localized CsCl crystal phases within the bulk "AlB$_2$" thin film. To corroborate this conclusion, the SAXS pattern of an AlB$_2$ thin film at equilibrium after being annealed near its melting temperature (where only {001}-aligned grains are observed) was compared to its 1D SAXS pattern after cooling to room temperature (Figure A.35). For reference the corresponding 2D SAXS data for these curves, as well as the 1D curves presented in Figure 2.3 of the main text (during heating of the AlB$_2$ films) are also presented (Figure A.36). This data clearly shows the appearance of at least one distinctly new peak upon cooling. When indexed following the procedure in Section A.4.1, the SAXS structure, particularly the positions of the new peaks correlate strongly to a CsCl lattice of 53 nm lattice parameter (Figure A.37). Importantly, the strong new peak that appears upon cooling would be not be suppressed in a {011}-aligned CsCl grain as observed in SEM (the suppressed peaks for this CsCl lattice are the same as in Table A.9, only the q-values are different). However, it is worth noting, that the peak positions of this proposed CsCl lattice are very near the peak positions of the measured AlB$_2$ lattice, making the SAXS data not definitive but still consistent with the SEM data conclusions.
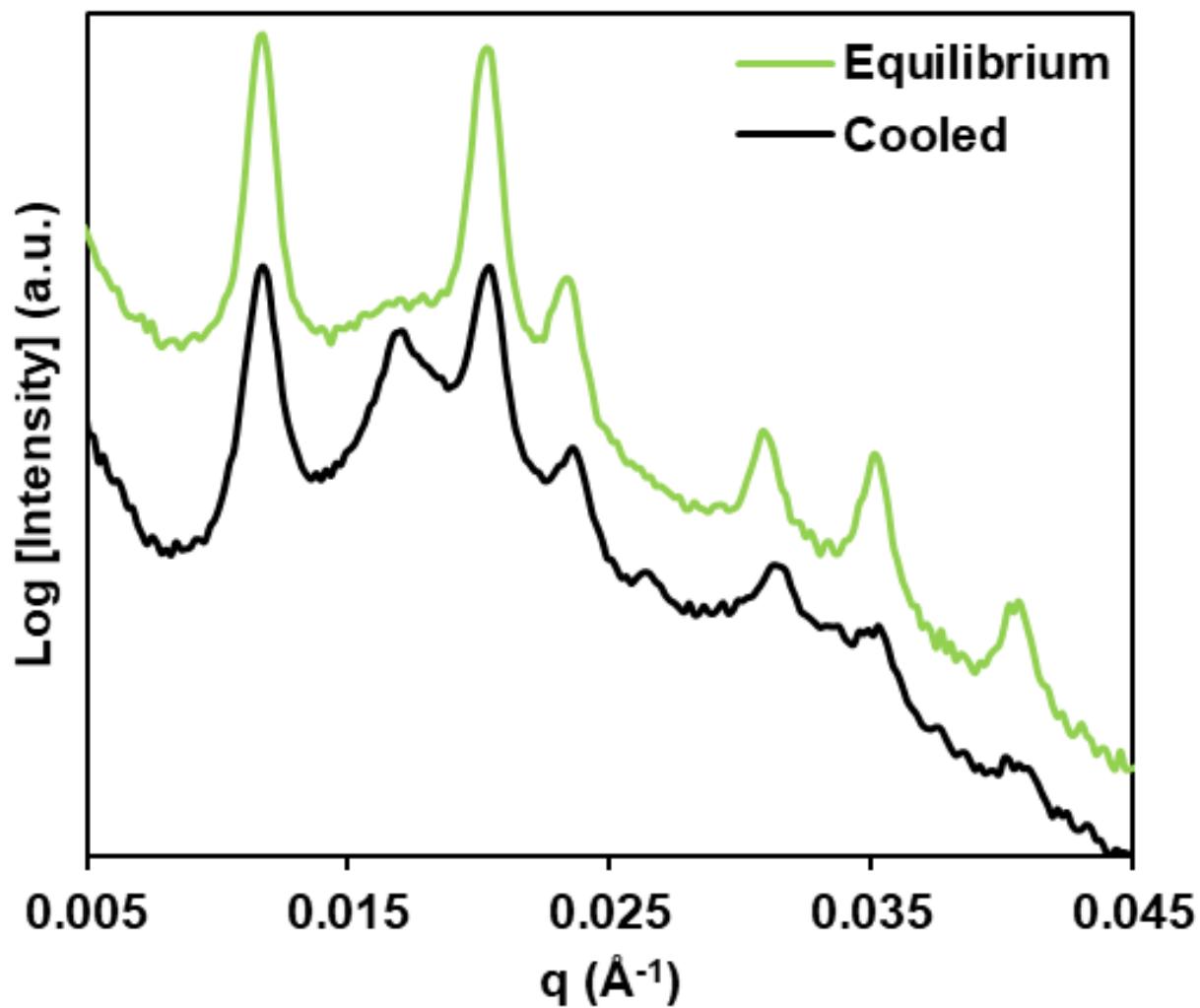
Figure A.35: Representative 1D SAXS curves for a five-layer (5L) AlB2 PAE thin film upon reaching an equilibrium state during annealing (green) and after cooling to room temperature (black). The SAXS curves have been offset in intensity for clarity.
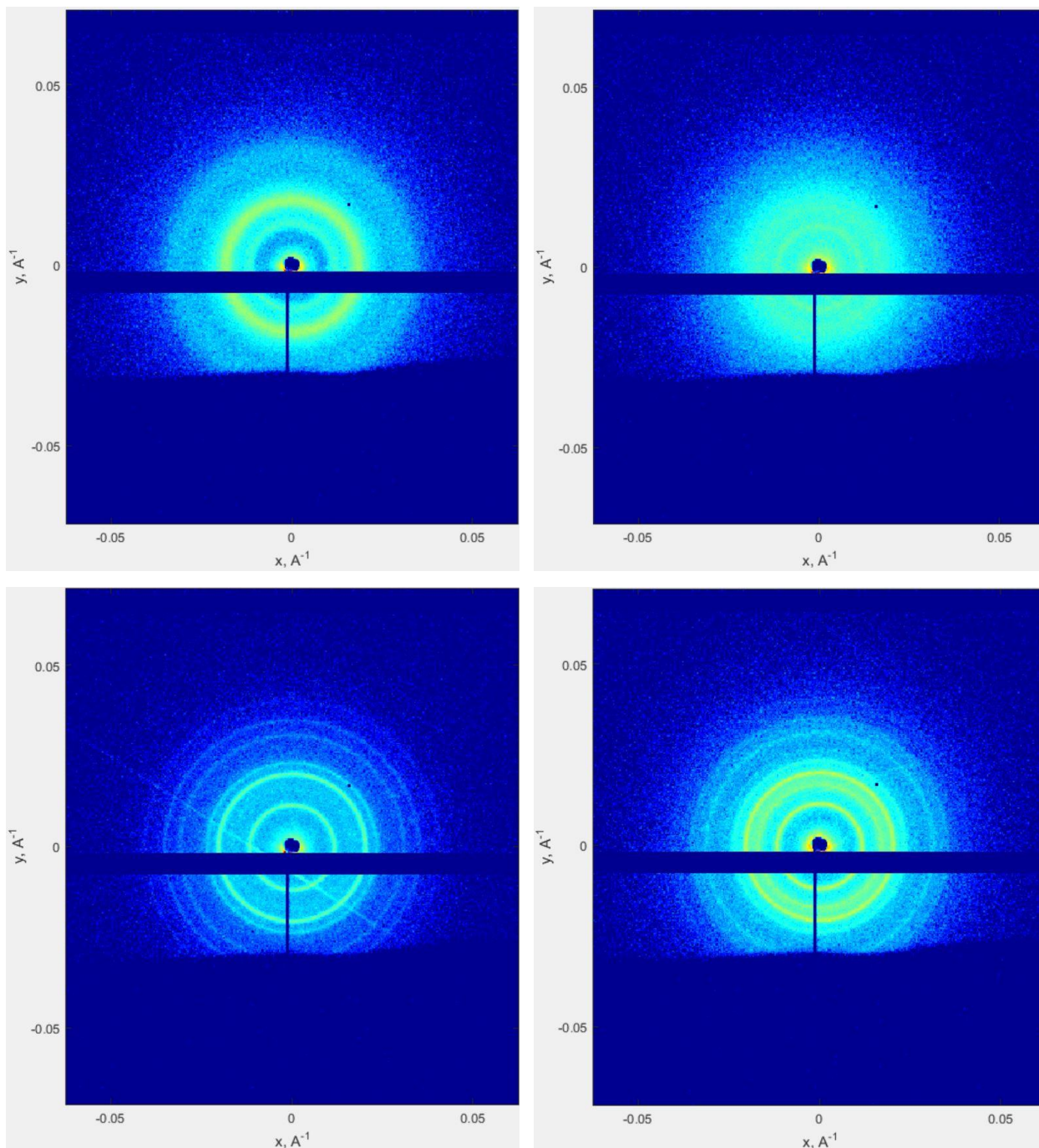
Figure A.36: Representative 2D SAXS curves for a five-layer (5L) AlB2 PAE thin films during in-situ heating and subsequent cooling: (top left) 25 °C, 0 min (as-deposited amorphous); (top right) 41 °C, 4.5 min ('fluidic' transition state); (bottom left) 40.5 °C, 9 min ({001}-oriented equilibrium state); (bottom right) 25 °C, 15 min (cooled post-annealing).
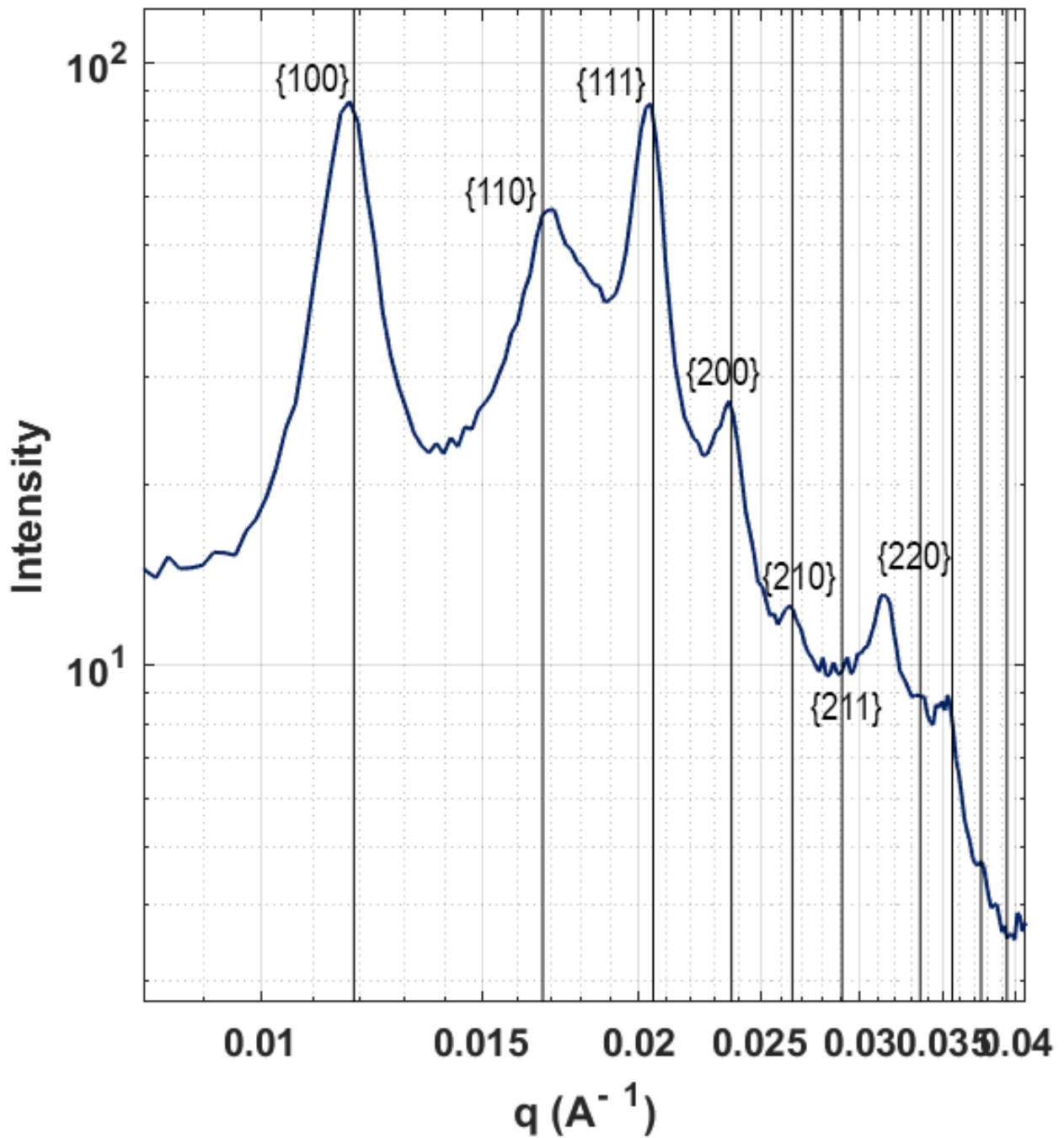
Figure A.37: Indexed 1D SAXS data of a cooled AlB_2 thin film showing theoretical peak positions for a polycrystalline CsCl lattice of 53 nm lattice parameter. (See Table A.9 for hkl-index of each peak and which are suppressed for various alignments.)

A.7.4. Stoichiometry of the AlB$_2$ Lattice

Following the analysis methodology in Section A.4.4, the stoichiometry of the AlB$_2$ system thin films was estimated. First, both the A and B PAEs individually were measured in SAXS and had their background (PBS-filled sample chamber) subtracted (Figure A.38). Likewise, a SAXS scan of a 10-layer AlB$_2$ thin film (0% A, A First) prior to annealing had a different background (PBS-filled sample chamber with bare substrate) subtracted (Figure A.38). Theoretical form factors were calculated for various stoichiometries of A to B PAEs in a mixture (values of x were varied from 0 to 1 using Equation A.15). A residual between this curve and the measured SAXS curve was calculated using Equation A.16 using only q-values from 0.034 to 0.13 (excluding the structure factor peaks and noisy region) and plotted against the relative amount of PAE A (x) (Figure A.39). The best fit was determined to be the minimum (0.51) of the residual versus relative amount of PAE A (x) and confirmed visually (Figure A.38).

Equation A.16:

$$Residual = \log\big(I(q)\big) - \log(P(q)_{Mixture})$$
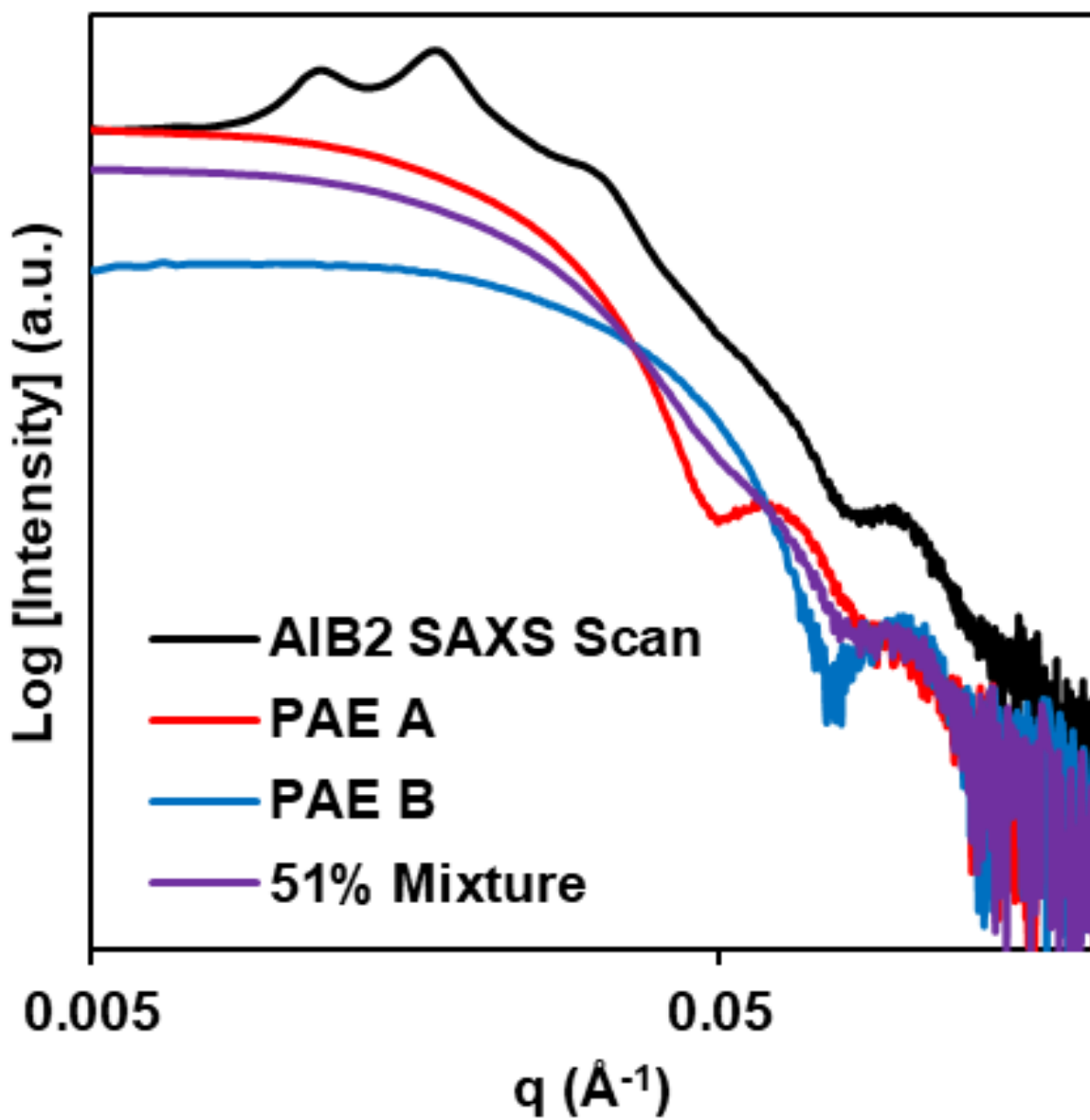
Figure A.38: Background-subtracted 1D SAXS curves for (black) a representative AlB_2 thin film prior to annealing, (red) measured form factor of PAE A, (blue) measured form factor of PAE B, and (purple) calculated best-fit form factor of a 51% PAE A and 49% PAE B mixture.
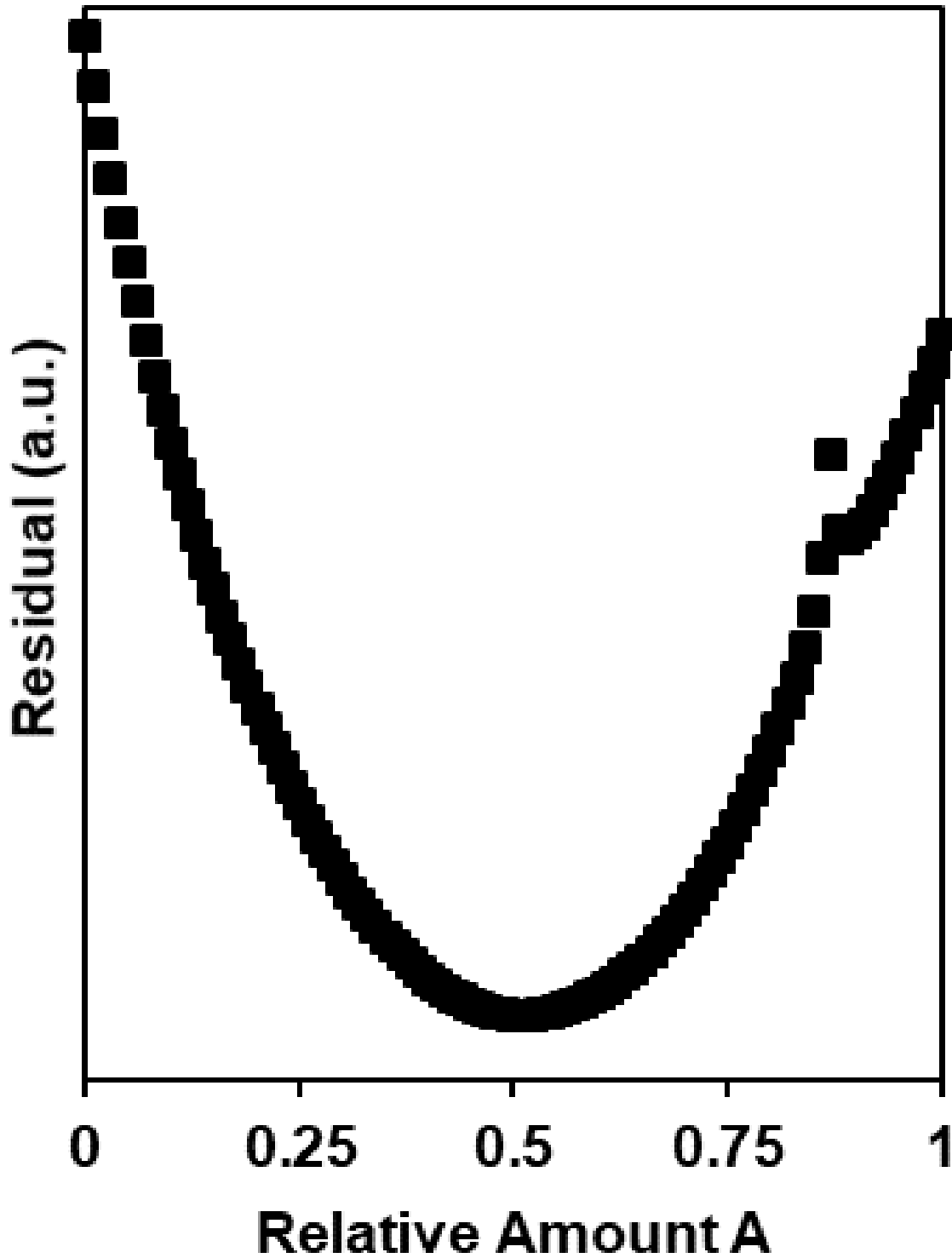
Figure A.39: Residual between mixture form factor calculated from various linear combinations of PAE A and PAE B form factors and AlB_2 SAXS scan revealing a best-fit minimum at 0.51 relative amount PAE A.

Appendix B. Supporting Information for Epitaxy: Programmable Atom Equivalents *versus* Atoms (Chapter 3)

B.1. Oligonucleotide Synthesis

Table B.1: DNA sequences used for functionalizing AuNPs and the substrate. Thiolated strands (X-SH) that had a 3' propyl thiol-modifier were functionalized onto AuNPs. These strands consisted of two of six ethylene glycol units (denoted as (EG6)$_2$) close to 3' propyl thiol to increase the flexibility of the DNA. HS-A DNA strands used for nanoparticles and the substrate are identical, and so are Linker A strands.

DNA Type	Sequence (5'-3')
Nanoparticles	
HS-A	TCA ACT ATT CCT ACC TAC (EG6)$_2$-SH
HS-B	TCC ACT CAT ACT CAG CAA (EG6)$_2$-SH
Linker A	GTA GGT AGG AAT AGT TGA A TTT AGT CAC GAC GAG TCA TT A TTT AGT CAC GAC GAG TCA TT A TTCCTT
Linker B	TTG CTG AGT ATG AGT GGA A TTT AGT CAC GAC GAG TCA TT A TTT AGT CAC GAC GAG TCA TT A AAGGAA
Duplexer	AAT GAC TCG TCG TGA CTA AA
Substrate	
HS-A	TCA ACT ATT CCT ACC TAC (EG6)$_2$-SH
Linker A	GTA GGT AGG AAT AGT TGA A TTT AGT CAC GAC GAG TCA TT A TTT AGT CAC GAC GAG TCA TT A TTCCTT
Duplexer	AAT GAC TCG TCG TGA CTA AA

Oligonucleotides were synthesized on an ABI 394 (Applied Biosystems) automated oligonucleotide synthesizer using standard phosphoramidite chemistry on controlled pore glass (CPG) beads. Phosphoramidite reagents and CPG beads (GlenUny Support) were purchased from Glen Research (Sterling, VA). After synthesis, oligonucleotides were deprotected using a fast deprotection method, where 1 µmole of synthesized oligonucleotides was mixed with 1 mL of a 1:1 mixture (*v*) of 40 % aqueous methylamine and 30 % ammonium hydroxide solution, then was allowed to sit at 25 °C for 2 hours. After deprotection, the solvent containing the DNA was evaporated with nitrogen, and the sample was filtered through a 0.2 µm pore syringe filter to remove the CPG beads and impurities. To remove failure strands from the success strands, the DNA was purified using reverse-phase high performance liquid chromatography (Varian RP-HPLC) on an Agilent C18 column. After the purification step *via* RP-HPLC, the DNA was lyophilized overnight. To cleave the acid-labile 4,4'-dimethoxytrityl (DMT) protecting group off

the DNA, 1-2 mL of 20% acetic acid was added per 1-2 µmole columns of dry DNA. After the solution was allowed to sit for approximately 1 hour, 2 mL of water and 3-4 mL of ethyl acetate were added to remove hydrophobic DMT groups and extract the purified DNA from the solution. All oligonucleotides were characterized and confirmed by matrix-assisted laser desorption/ionization time-of flight (MALDI-TOF) mass spectrometry to ensure that all molecular weights corresponded to the theoretical masses. The MALDI-TOF mass spectrometry matrix was prepared by dissolving 30 mg of 3-hydroxypicolinic acid (Fluka) in 1 mL of a 1:1 MeCN:H_2O solution and mixed with 10 mg of ammonium citrate dibasic (Sigma-Aldrich). 1.5 µL of diluted oligonucleotide was aliquoted and mixed with 1.5 µL of this matrix on a steel plate to crystallize prior to MALDI-TOF analysis. The absorbance of oligonucleotides was measured on a Cary 5000 UV-Vis-NIR spectrophotometer (Agilent) using calculated extinction coefficients from Integrated DNA Technologies (IDT) website.

B.2. Degree of Ordering
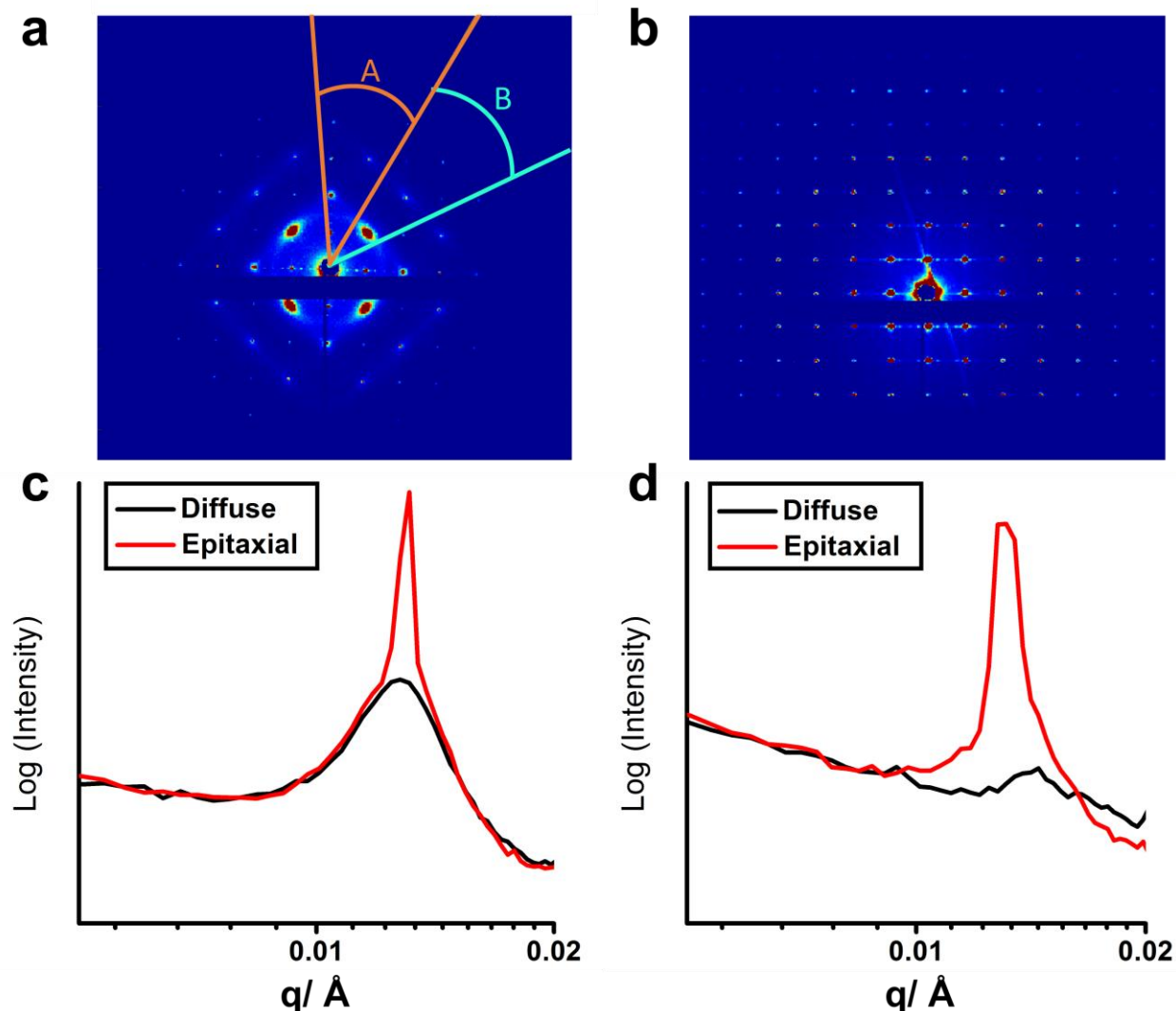
Figure B.1: Analysis of SAXS Data. a) Sector averaging to determine degree of epitaxy. The background signal from the diffuse ring is determined from azimuthally averaging arc A. The signal corresponding to the epitaxial NPs is determined from the azimuthally averaging arc B. b) SAXS scattering pattern of a blank patterned substrate. The scattering intensity comes from the gold posts on the pattern. The 1D averaged data from the 2D pattern is shown for the 10-layer thin film samples assembled at c) 25 °C and d) (T_m-4) °C and annealed.

Since epitaxial PAEs are oriented in the bcc [100] direction, their in-plane scattering produces a strong signal intensity present as a spot. On the other hand, PAEs that are not epitaxial are randomly oriented in the z-direction, even if they possess bcc symmetry, and their scattering

produces a circular ring. Therefore, by comparing the integrated signal intensity from the (110) peak produced by scattering of the epitaxial PAEs to that of the diffuse ring produced by scattering from the non-oriented PAEs, we can determine the degree of epitaxy. SAXS 2D diffraction patterns were azimuthally averaged (Figure B.1a). The background signal from the diffuse ring is determined from azimuthally averaging across the angles corresponding to arc A. Azimuthally averaging across the angles corresponding to arc B gives the signal intensity from a combination of 1) PAEs epitaxial with the pattern, 2) the pattern itself (Figure 3.1 middle row and Figure B.1b) the background signal. The 1D data (examples given in Figure B.1c&d) obtained for the region corresponding to the bcc (110) peak (Figure 3.1) were then fit to a Voigt profile and integrated to find the area. Relative degree of epitaxy was then calculated according to Equation B.1.

Equation B.1:

$$X_A = \frac{\int I_{arc\,B} - \int I_{arc\,A}}{\int I_{arc\,B}}$$
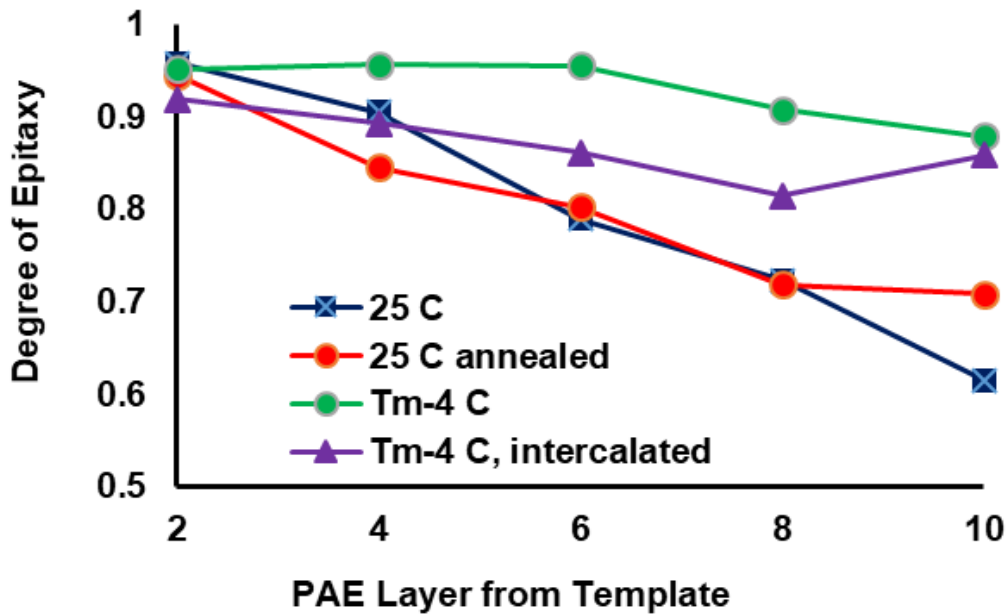
Figure B.2: Quantitative analysis of FIB-SEM cross-section. Degree of epitaxy for 10-layer thin films as a function of layer distance from the template, calculated from analysis shown in Figure B.5.

Table B.2: Mean height and roughness for films of varying layer number grown using different deposition conditions.

Layer #	Mean Height (nm)	Roughness (nm) Arithmetic Average	Roughness (nm) Root Mean Squared
1. 25 °C deposition			
2	130.56	28.46	34.34
5	311.49	38.46	47.91
10	775.95	63.87	82.66
2. 25 °C deposition, annealed at (T_m-2) °C			
5	321.78	46.96	58.82
10	883.43	79.58	100.09
3. (T_m-4) °C deposition, annealed at (T_m-2) °C			
2	97.22	20.47	25.76
5	170.38	36.44	47.52
10	257.56	29.80	40.31
4. (T_m-4) °C deposition, annealed at (T_m-2) °C, and intercalated			
2	87.36	23.99	30.42
10	220.86	46.35	66.95
Unpatterned substrate			
5	226.34	40.93	53.60

B.3. Growth Condition Details

Table B.3: Growth Conditions for Templated DNA-NP Superlattice Thin Films.

Condition **1**	Thin films were grown at 25 °C up to 2, 5, and 10 layers
Condition **2**	Thin films were grown to their full thickness at 25 °C, followed by annealing at (T_m-2) °C for 15 minutes in Buffer A. Annealing temperatures varied depending on layer number. Typically, 2-layer thin films were annealed at (T_m-6) °C, and 5 and 10-layer thin films were annealed at (T_m-2) °C due to melting temperature depression observed for thin films.
Condition **3**	The first 2 layers were grown at 25 °C, in which the sample was then annealed at (T_m-2) °C. For 3rd and 4th layers, substrates were immersed in particle solutions at (T_m-6) °C and annealed at (T_m-4) °C. For the rest of the layers, the thin films were grown at (T_m-4) °C and annealed at (T_m-2) °C.
Condition **4**	The growth protocol was same as condition **3**, with the addition of a 2-hour incubation step in 80 µM intercalator after each annealing step to ensure complete intercalation.

B.4. Melting Point Depression
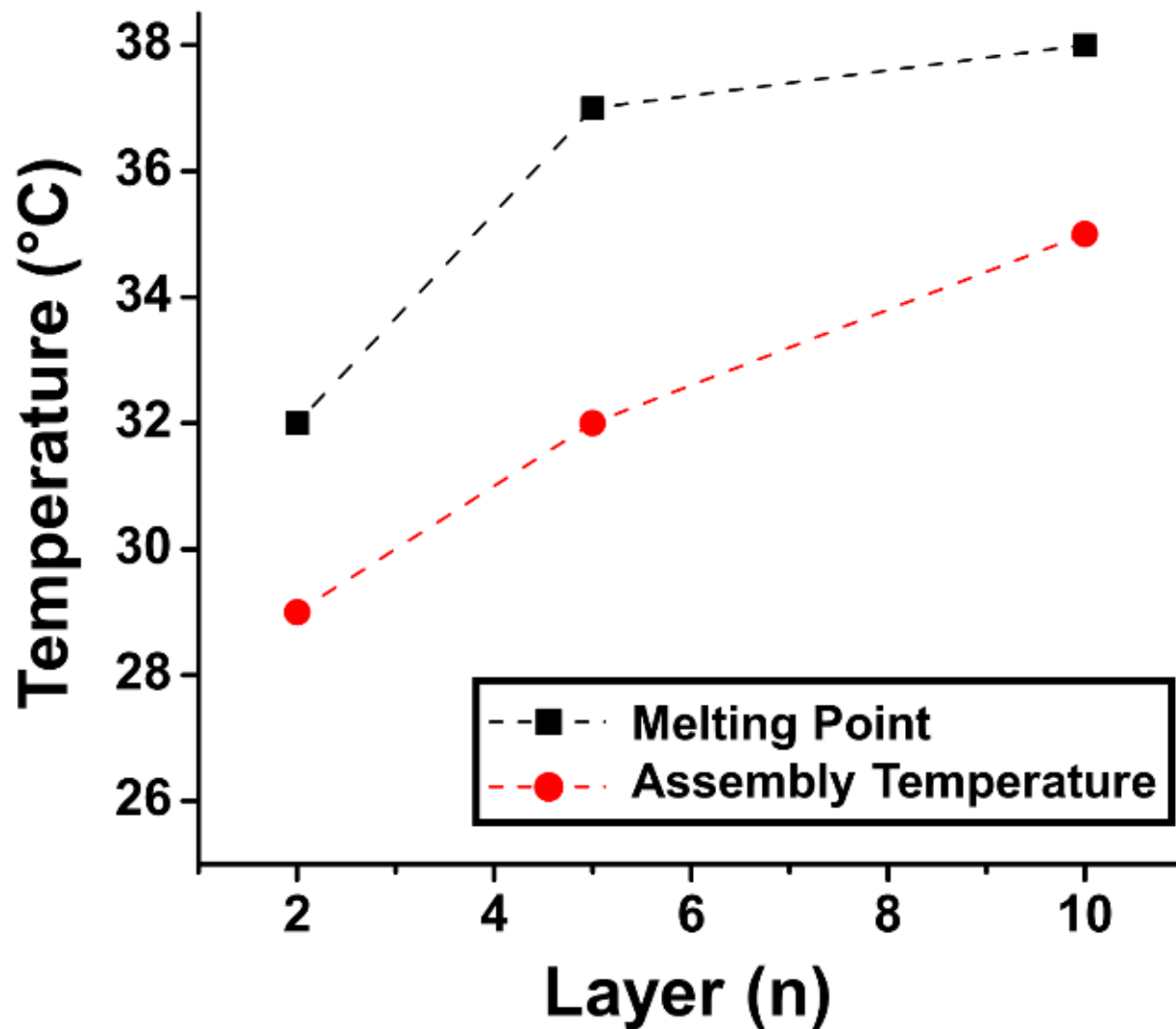
Figure B.3: Melting point depression of the templated thin film superlattice as a function of nanoparticle layer number, as determined by SAXS.

B.5. Additional Data for Growth Conditions

B.5.1. GISAXS Data
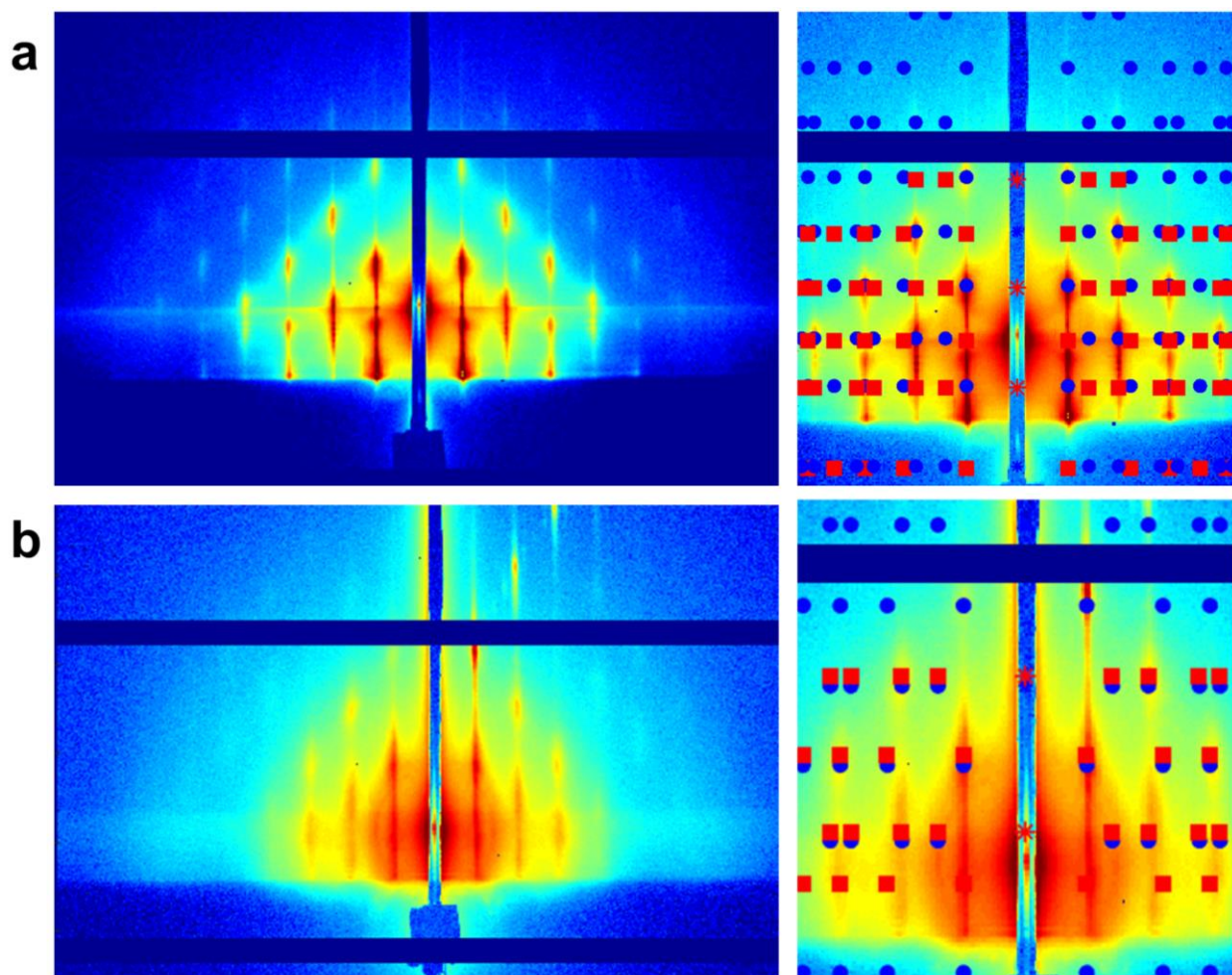
Figure B.4: GISAXS of a) 5-layer and b) 10-layer thin films grown at equilibrium conditions. On the right-hand side, the scattering patterns were indexed to bcc crystals with (100) orientation corresponding to space group I4/mmm (#139). The higher order peaks evident in the scattering patterns are indicative of long-range order. The high levels of diffuse scattering in the 10-layer film are hypothesized to be due to the thickness of the film, making it difficult for X-ray penetration.

B.5.2. Degree of Epitaxy from FIB Data
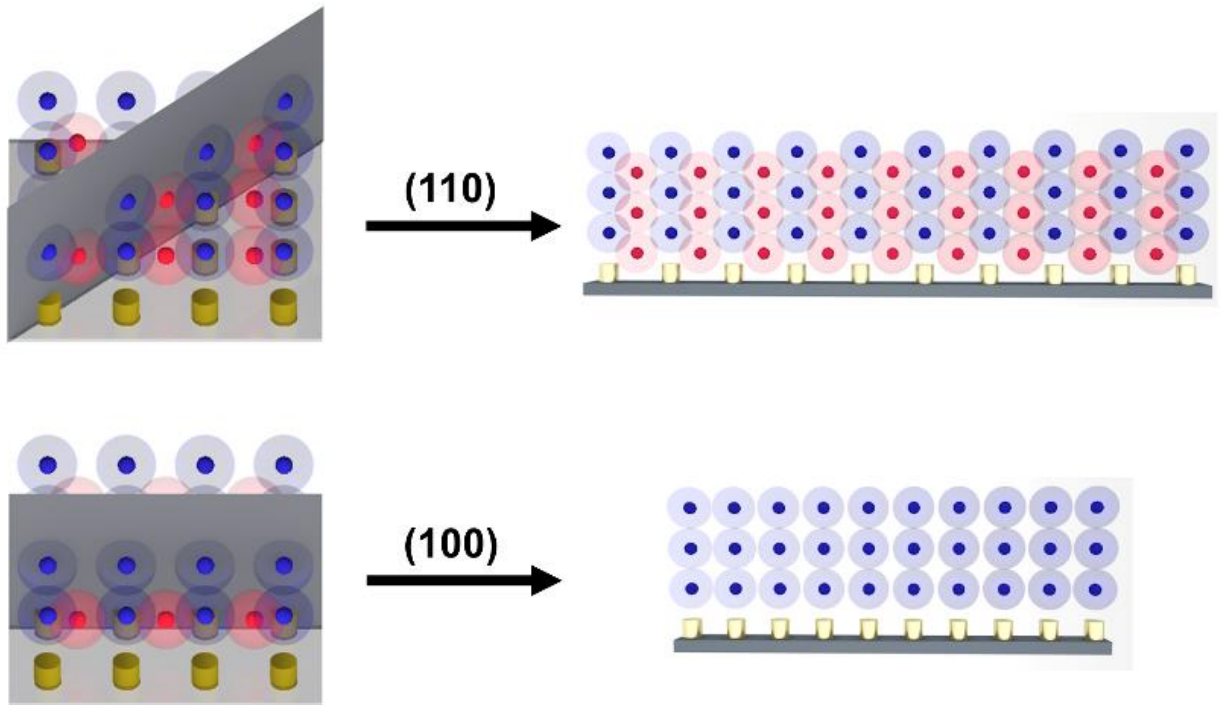
Scheme B.1: Demonstration of FIB-SEM cut in different plane orientations.
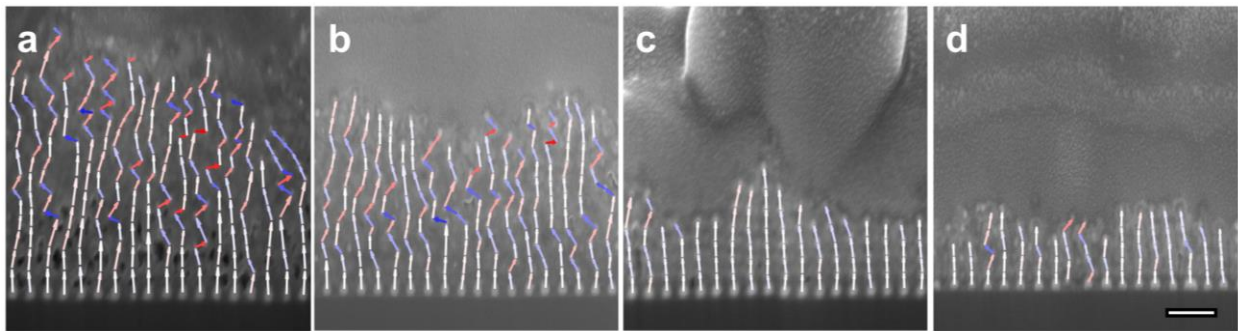
Figure B.5: Degree of epitaxy analysis for FIB-SEM cross-sections of 10-layer films grown at a) 25 °C, b) 25 °C and annealed, c) (T_m-4) °C and annealed, and d) (T_m-4) °C, annealed, and intercalated. Scale bar is 200 nm.

Photoshop and Matlab were used to track the positions of internal PAEs relative to the positions of the templated posts. After correcting for tilt, vectors were calculated between adjacent particles in the [001] direction and plotted atop the cross-section of the SEM image. Perfectly epitaxial superlattices would display vectors completely vertical from the posts up throughout the

layers; this direction was taken to be 0° (and displayed as white arrows on the overlaid image). Any deviation in z-direction was calculated in terms of degrees where the limits are therefore -90 to 90° (with arrows becoming increasingly blue or red, respectively, as they deviate); note that this vector exists as the projection onto the plane of the cross-section, not as a 3D vector. The first row of vectors was then aggregated and the standard deviation (σ) of their angles was calculated using Matlab. If the vectors were all vertically aligned, i.e. the superlattices were perfectly epitaxial, $\sigma = 0$. However, if the vectors were completely random, i.e. the superlattices were completely disordered, the maximum standard deviation for this system would be $= \sqrt{((-90 - 90)2/4)} = 90$. Therefore, to calculate X_A or "Degree of Epitaxy" for that row of vectors such that 1 is perfect epitaxy and 0 is completely disordered, $X_A = (90 - \sigma)/90$. This process was repeated for each row of vectors in the superlattices and plotted in Figure B.2. These data corroborate the SAXS results on effects of deposition protocol on epitaxy. While SAXS data provides an averaged information on degree of epitaxy, the analysis on FIB-SEM highlights the waning force of epitaxy the template exhibits over the PAEs as a function of layer number. PAEs within the bulk crystal are more tightly bound and networked with neighboring particles, limiting their vibrational motion. PAEs near the surface of the thin film have fewer neighboring particles, thus have many near-equilibrium positions to easily oscillate between. This indicates the importance of annealing each layer so that as few defects as possible in the surface layer exist upon the deposition of the subsequent layer to avoid trapping defects in the bulk crystal.

B.5.3. Additional Data for Condition 3
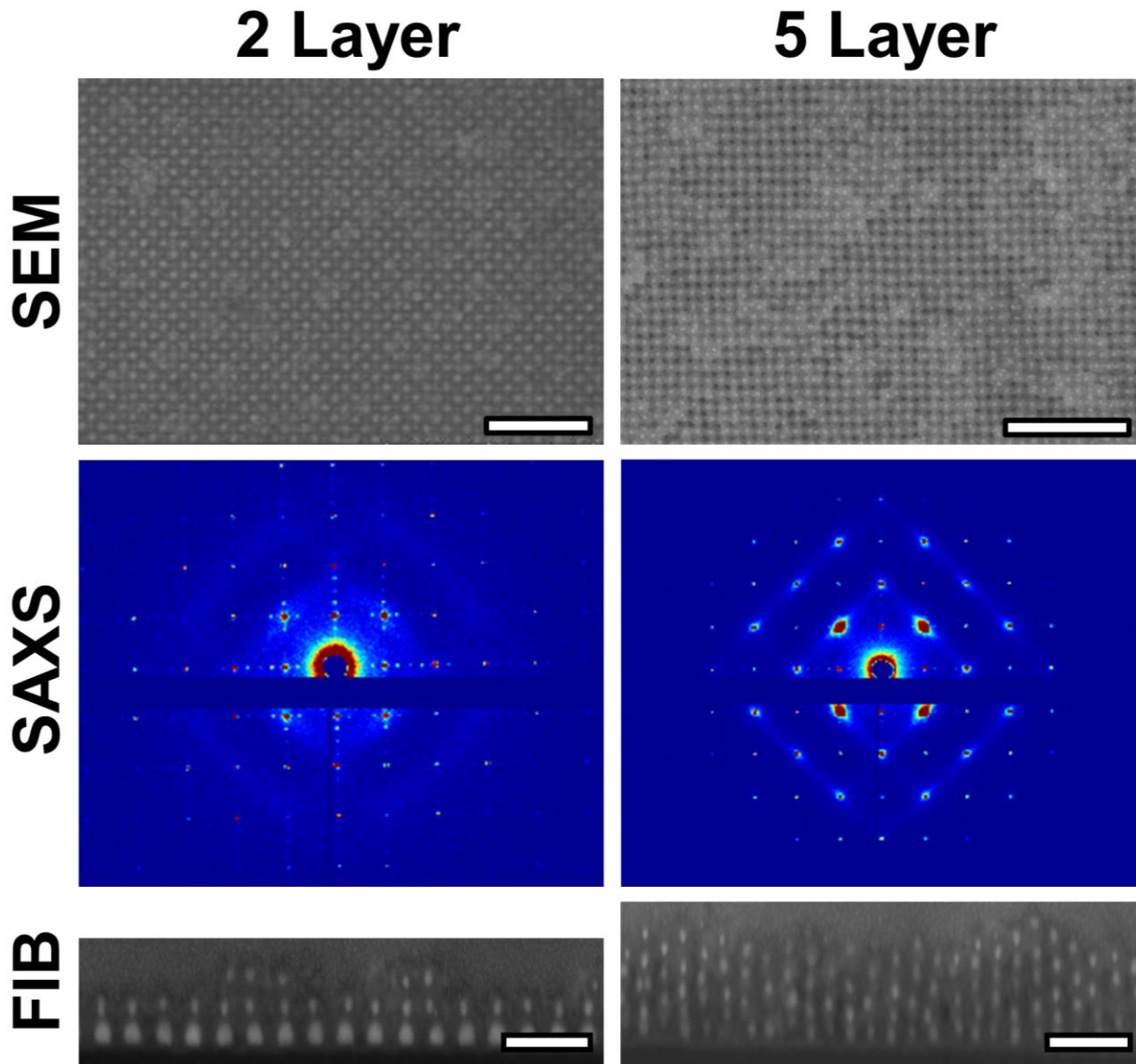
Figure B.6: Epitaxial growth of DNA-functionalized nanoparticle thin films at 2 and 5 layers is observed when they are assembled at $(T_\mathrm{m}{-}4)$ °C and annealed. SEM, SAXS, and FIB-SEM show crystalline, epitaxial thin films at 10 layers of nanoparticles. Scale bars for SEM and FIB-SEM are 500 nm and 200 nm, respectively.

B.5.4. FIB-SEM Cross-Sections
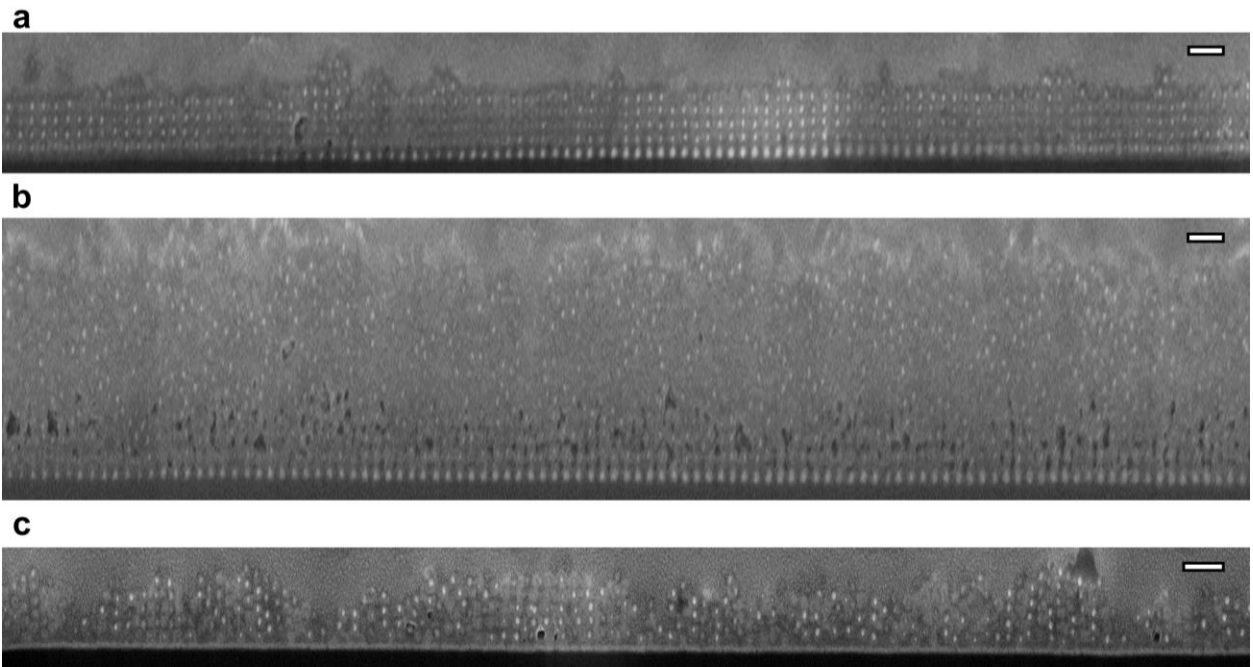
Figure B.7: FIB-SEM cross-sections of a) 10-layer film grown on a patterned substrate at $(T_\mathrm{m}\text{-}4)$ °C, b) 10-layer film grown on a patterned substrate at 25 °C, and c) a 5-layer film assembled on an unpatterned substrate and annealed at $(T_\mathrm{m}\text{-}2)$ °C. Scale bars are 200 nm.

10 Layer

Figure B.8: Intercalated 10-layer thin film presenting roughened surface morphology (SEM) and defect propagation along the z-axis (FIB-SEM). SAXS was used to determine the degree of epitaxy ($X_A = 0.65$). Scale bars for SEM and FIB-SEM are 500 nm and 200 nm, respectively.

B.5.6. Annealed Thin Film on Unpatterned Substrate
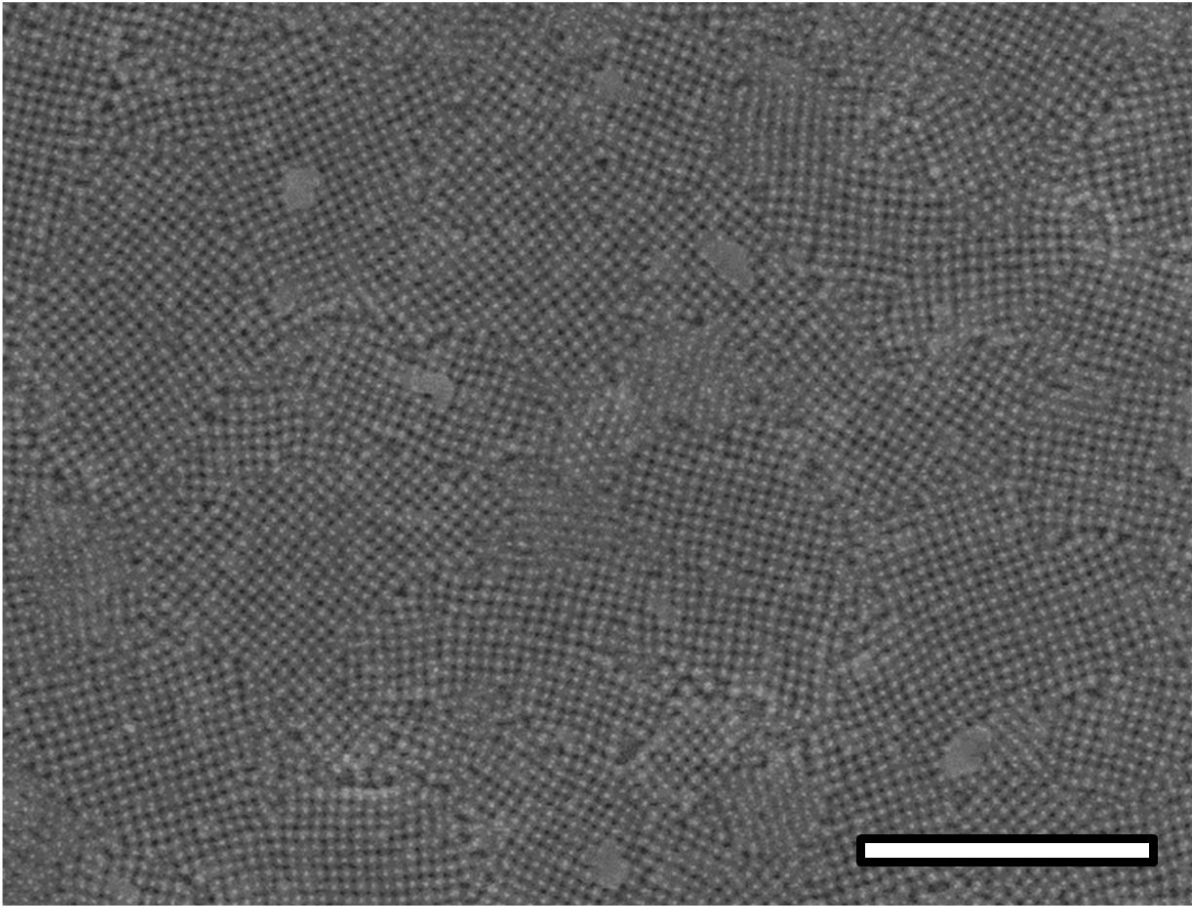
Figure B.9: Polycrystalline 5-layer thin film grown on an unpatterned substrate. Scale bar is 1 μm.

Appendix C. Supporting Information for Lattice Mismatch in Crystalline Nanoparticle Thin Films (Chapter 4)

C.1. Potential Energy Calculations for PAE Thin Films

Lattice energies of superlattices for each interparticle spacing were calculated by summing all pair potentials between the first nearest neighbor PAEs based on previously described method.[132] Pair potential calculation mainly considered attractive energy from DNA hybridization interactions between sticky ends and repulsive energy from excluded volume repulsion between DNA duplexes.

C.1.1. Attractive Interaction Potential

The attractive interaction potential ($E_{attractive}$) from hybridization between two complementary particles is calculated using geometric considerations based on the complementary contact model (Equation C.1), where the hybridization energy is proportional to the area fraction of the overlap between adjacent particles.[132] In this calculation, we assume that each hybridization event of sticky ends is additive and the DNA strands are homogeneously distributed around the PAE. Therefore, the attractive energy is proportional to the number of sticky ends within the overlap:

Equation C.1:

$$\sigma_h = \sigma f_s$$

where σ_h is the number of sticky ends that can hybridize, σ is the total number of sticky ends on the PAE, and f_s is the area fraction occupied by the overlap between adjacent PAEs. The attractive interaction potential from DNA hybridization can be calculated by:

Equation C.2:

$$\frac{E_{attractive}}{kT} = -\sigma f_s e_h$$

where $E_{attractive}$ is the attractive energy potential, e_h is the hybridization energy of each sticky end, k is the Boltzmann constant, and T is the temperature (Equation C.2). e_h for the sticky end sequence used in our study is -14 kT from the IDT website.

C.1.2. Repulsive Interaction Potential

The dominant repulsion that counterbalances the DNA hybridization attraction is the excluded volume repulsion between DNA duplexes, and thus the interaction potential energy can be simplified to contributions from $E_{attractive}$ and $E_{excluded\ volume}$ (repulsive energy from excluded volume).[132] While there are different modes of repulsion from stretching, bending or compressing the DNA duplexes and surrounding counterions (entropic effect) between particles grafted with polyelectrolyte brushes, their contributions are projected to be minimal relative to two main forces considered in our study based upon previous literature.[132] In these systems, the long-range electrostatic repulsion between particles is effectively screened by supporting electrolytes. While the long-range Coulombic repulsion is neglected, calculation of effective radius of the DNA chains accounted for the Debye length which changes as a function of salt concentration. To calculate the repulsive interaction potential between noncomplementary and complementary particles, a mean field approximation was used.

Effective radius of the DNA chains (R_{DNA}) was calculated using following equation:
Equation C.3:

$$R_{DNA} = R_0 + \kappa^{-1}$$

where R_0 is the DNA chains and κ^{-1} is the Debye length.

Then, by adopting the grafted polymer brush theory, $E_{excluded\ volume}$ was calculated using following equation:[309]1
Equation C.4:

$$E_{excluded\ volume} = \Pi V_0$$

Here, Π is the osmotic pressure due to pressure difference between the overlap and the environment and V_0 is the volume of the overlap. In this work, we approximated $\Pi/kT = vc^2/2$, where v is the excluded volume of a monomer unit and c is the concentration of the monomers within the overlap. Detailed mathematical description for the calculation of $E_{excluded\ volume}$ can be found in published literature.[132]

C.1.3. Lattice Energy

First, interaction potential energies were calculated for the system of particles over a range of lattice parameters in the x and y planes. Each PAE was modeled as having 205 hybridized linkers

around 20 nm NPs (determined experimentally, SI section 2.3). Theoretical calculation of ideal (bulk) lattice parameter was corroborated with experimentally determined lattice constant of 65 nm (Section C.2.5). For each lattice parameter in the x,y-plane, a range of z heights were modeled, with thermodynamic minimum occurring at the ideal height. For each of these systems, using the ideal height, the interaction potential energy was calculated based on contributions from $E_{attractive}$ and $E_{excluded\ volume}$. The potential energies shown in Figure 4.1 are calculated assuming a single unit cell (in the x,y-plane) and an appropriate number of unit cells (5 or 10 layers) in the z-direction for ease of data presentation. The potential calculated for the bulk assumes particles on all exposed surfaces of the lattice have broken bonds whereas the potential calculated for the thin film case assumes particles located on the bottom face of the lattice are bound to a substrate via DNA hybridization interactions. Specifically, the particles sitting at the center of four posts forms four bonds with the substrate when a lattice is in a bcc crystallographic symmetry. This attractive force draws the total thin film energy below the bulk at low degrees of lattice mismatch.

C.2. PAE Synthesis and Characterization

C.2.1. DNA Sequences

The following oligonucleotides (Table C.1) were purchased from Integrated DNA Technologies (IDT).

Table C.1: DNA Sequences. Thiol-modified strands (X-SH) with a 3' propylthiol-modifier were functionalized onto AuNPs. These strands consisted of two of six ethylene glycol units (denoted as $(EG_6)_2$) to increase the flexibility of the DNA chains.

Sequence Name	Sequence (5'-3')
HS-A	TCA ACT ATT CCT ACC TAC $(EG_6)_2$-SH
HS-B	TCC ACT CAT ACT CAG CAA $(EG_6)_2$-SH
Linker A	GTA GGT AGG AAT AGT TGA A TTT AGT CAC GAC GAG TCA TT A TTT AGT CAC GAC GAG TCA TT A TTCCTT
Linker B	TTG CTG AGT ATG AGT GGA A TTT AGT CAC GAC GAG TCA TT A TTT AGT CAC GAC GAG TCA TT A AAGGAA
Duplexer	AAT GAC TCG TCG TGA CTA AA

C.2.2. PAE Synthesis

DNA-AuNPs were synthesized by functionalizing 20 nm diameter (Ted Pella) citrate capped AuNPs with a dense shell of thiol-modified DNA. The 3'-propylmercaptan protecting group of the thiol-modified DNA sequences was cleaved by treating the sequences with 100 mM dithiolthrietol for 1 hour. The strands were desalted using a size exclusion column (GE Healthcare) and added to a solution of AuNPs (6 nmol DNA per 1 mL of colloid). After incubating for 1 hour, the solution was brought up to a concentration of 0.01% sodium dodecyl sulfate and 10 mM sodium phosphate. A salt aging process was used to increase the DNA loading by adding phosphate buffer solution (PBS) with 2 M sodium chloride stepwise over the course of several hours until a final concentration of 0.5 M NaCl was reached. After the final NaCl addition, the solutions were set overnight. Unbound DNA was removed by three rounds of centrifugation (12,000 rpm for 20 min), removal of supernatant, and resuspension in nanopure water. The final resuspension was done in PBS with 0.5 M NaCl.

Linker strands were pre-hybridized by incubating with 2 equivalents of duplexer in 0.5 M NaCl PBS. Stock solutions of 100 µM linker were incubated at 35°C for 1 hour to ensure full hybridization. Type A and B DNA-NPs were mixed with 400 linkers/particle of the appropriate duplexed linker stock solutions and PBS to yield 15 nM PAEs.

C.2.3. Linker Loading

To determine the loading of complementary linkers on the particles, aggregates were assembled. The solution was incubated for 15 min at a temperature slightly below that of the melting temperature to anneal the lattices and allow the linkers to fully hybridize. The assembled lattices were spun down using a desktop centrifuge. The supernatant with unhybridized linkers was removed and unassembled particles were centrifuged down (14,000 rpm for 30 min). The concentration of linkers in the supernatant was determined using UV/vis spectroscopy. Based on the assumption that linkers absent from the supernatant were hybridized to the PAEs, it was determined that ~204 linkers were hybridized per particle.

C.2.4. Bulk Melting Temperature Characterization

The homogenous melting transition of PAE aggregates in solution was monitored with UV-Vis spectroscopy using established literature protocols.[62] 15 µL of each PAE type at 15 nM

was mixed together and allowed to aggregate. The mixture was then diluted to 1 mL with PBS and placed in a capped cuvette with a stir bar. Under continuous stirring and monitoring at 520 nm with a Cary 5000 UV-Vis, the solution was heated from 20°C to 43°C at a ramp rate of 0.25°C/min. The bulk phase melting temperature was taken to be the inflection point of the melt curve (Figure C.1). The PAEs studied in this manuscript had a melting temperature (T_m) of 38.5°C.
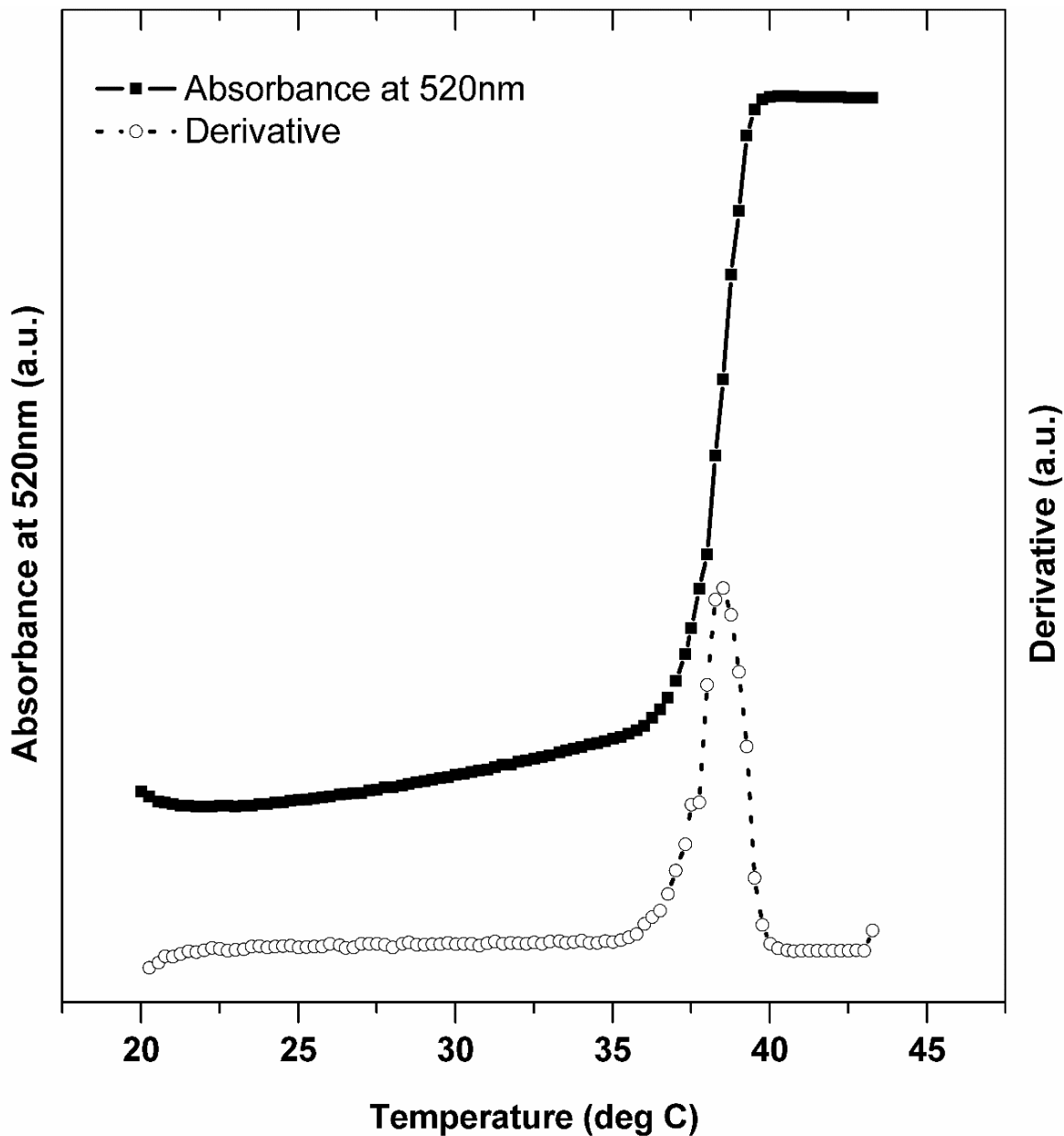
Figure C.1: Bulk (homogeneous) melting transition of PAEs aggregated in solution.

C.2.5. Bulk Lattice Parameter Calculation

Verification of the bulk crystallography and measurement of the bulk lattice parameter for PAEs used in this manuscript were determined from transmission SAXS of annealed PAE aggregates in solution. 15 µL of each PAE type at 15 nM was mixed together and allowed to aggregate. The mixture was then annealed at a temperature slightly below where the aggregate begins to dissociate (bulk melting temperature), allowing the PAEs enough thermal energy to rearrange and crystallize. After being allowed to cool, the aggregates were sealed in a quartz capillary (Charles Supper) with 5 min epoxy (Home Depot).

SAXS measurements were performed at the Massachusetts Institute of Technology (MIT) Center for Materials Science and Engineering (CMSE) X-ray Diffraction Shared Experimental Facility on a SAXSLAB system. The Rigaku 002 microfocus X-ray source produced Cu Kα1 X-rays of wavelength 1.5409 Å; Osmic staggered parabolic multilayer optics focused the beam crossover at the second pinhole. Two sets of JJ X-ray jaw collimation slits set at 0.45 mm and 0.2 mm, respectively, were used to define the beam. The system was calibrated using silver behenate as a standard.

The capillary was placed horizontally in the sample chamber and pumped down to 0.08 mbar. The sample was exposed for 20 min. The scattered radiation was detected with a Dectris Pilatus 300K detector set at a distance of 1,400 mm. The 2D SAXS data is presented in Figure C.2. The 1D SAXS data was obtained *via* radial averaging of the 2D scattering pattern (Figure C.3). These data were then transformed into profiles of scattering intensity as a function of scattering vector q.
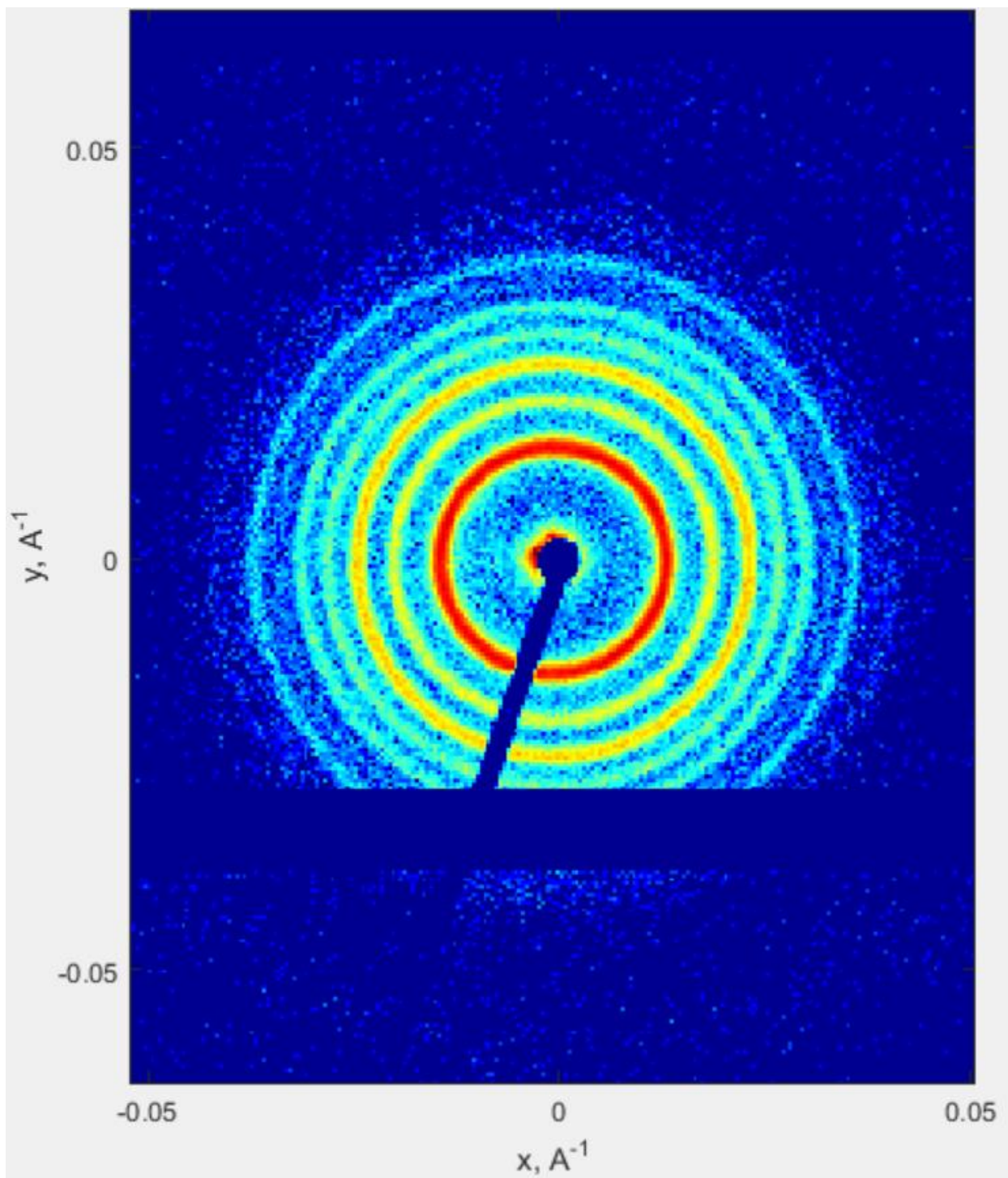
Figure C.2: 2D SAXS image of bulk PAE crystals showing bcc ordering.
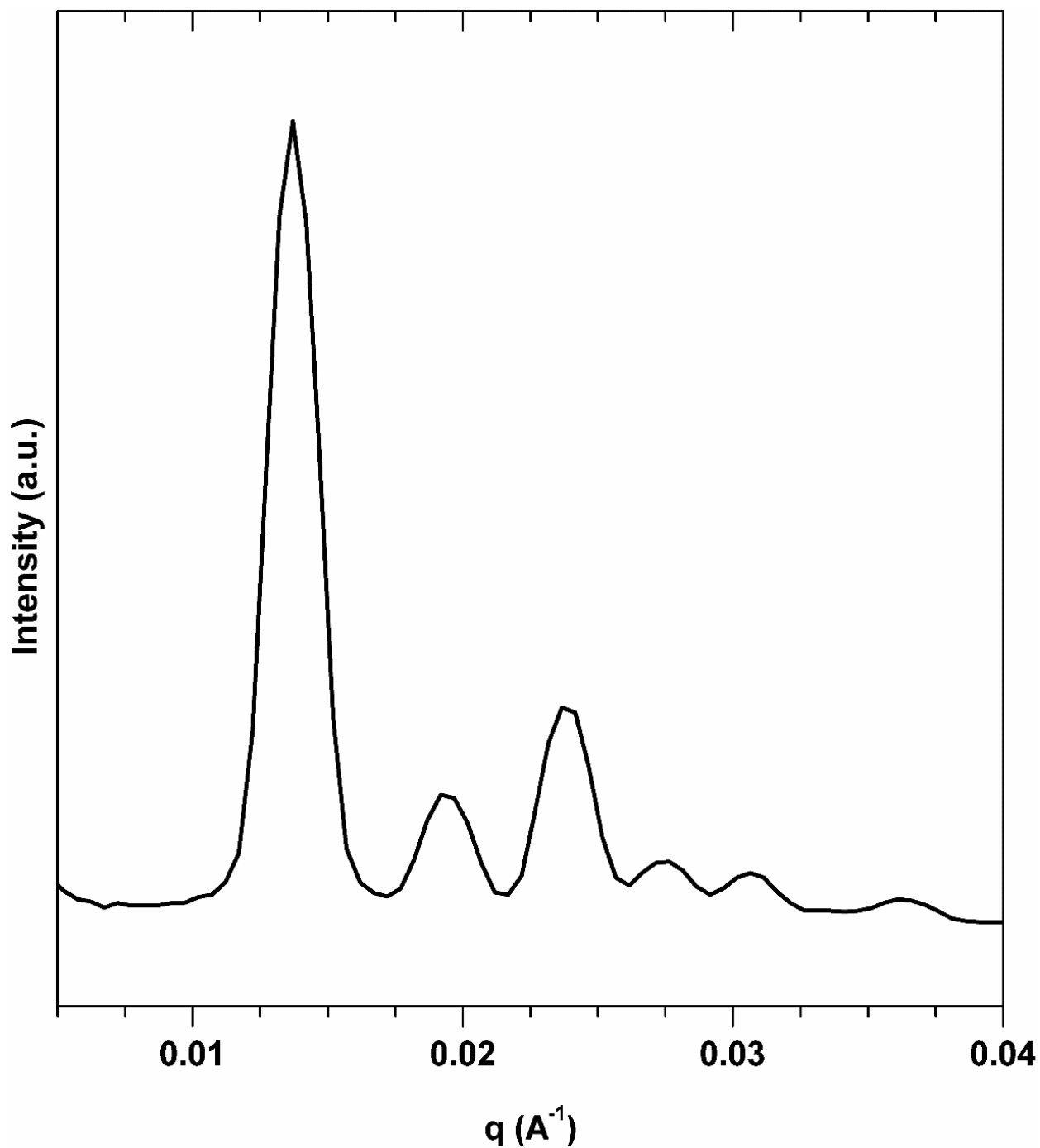
Figure C.3: 1D SAXS circular average of bulk PAE crystals showing bcc ordering.

Body-centered cubic (bcc) ordering was confirmed with comparison to previous work on PAEs.[69] After identifying the first peak position (q_0) – corresponding to the (110) peak in bcc – the relevant crystalline parameters were then calculated as follows:

Equation C.5:

$$Interparticle\ Distance = d = \frac{\sqrt{6}\pi}{q_0}$$

Equation C.6:

$$Lattice\ Parameter = a = \frac{2d}{\sqrt{3}}$$

The PAEs used in this manuscript exhibited a $q_0 = 0.01371$ Å^{-1}, $d = 56$ nm, and $a = 65$ nm.

C.3. Substrate Preparation

C.3.1. Substrate Fabrication

The templated substrates for PAE thin film deposition were fabricated using standard fabrication techniques at the Materials Technology Laboratory (MTL) at MIT. 150 mm P-Type Prime (100) silicon wafers with polished surfaces and resistivity 1-100 Ωcm were purchased from Wafernet. The wafer was then spun coat with 950 A2 PMMA (MicroChem). ~5 mL of PMMA was added to a static wafer then the speed was ramped to 1,900 rpm for 1 min to coat the entire wafer evenly. The coated wafer was then post baked for 5 min at 180°C and allowed to cool. Thickness of the deposited PMMA layer was verified with a Dektek Profilometer to be ~90 nm.

After dicing the wafer into appropriately sized pieces, the desired pattern was written using a Elionix ELS-F100 electron beam lithography (EBL) system at 125 kV accelerating voltage. The patterns were designed to mimic the (100) plane of a bcc superlattice with various lattice parameters. To achieve this pattern, 350×350 µm square arrays of dots with x and y pitches (lattice parameters) of 58, 60, 62, 64, 66, 68, 70, and 72 nm were exposed. Each dot was exposed with one shot of a 2 nA beam for 10 µsec. Two of each lattice parameter (for 5L and 10L samples) was patterned.

The exposed chip was developed in a ~5°C solution of 3:1 Isopropyl Alcohol (IPA):Methyl Isobutyl Ketone (MIBK) for 90 sec; IPA was purchased from Sigma Aldrich, MIBK from MicroChem. The chip was immediately rinsed in ~5°C IPA for 5 sec to remove remaining MIBK then blown dry with nitrogen gas. 5 nm of chromium (Cr) followed by 25 nm of gold (Au) were deposited on the developed chip at a rate of 0.2 Å/sec in an AJA eBeam evaporator under vacuum

(6 x 10^{-6} Torr). The chip was then diced such that each array was on its own small chip. To lift-off the gold layer and remove PMMA, each chip was placed in a heated (120°C) solution of Remover PG (MicroChem) and gently swirled until the gold layer was removed as one sheet. The chip was then rinsed in IPA and blown dry. Due to difficulties in lift-off only one 58 nm substrate was created.

The amount of lattice mismatch induced by each substrate was then calculated using Equation C.7, given the bulk PAE lattice parameter (l.p.) of 65 nm, and is summarized in Table C.2.

Equation C.7:

$$Lattice\ Mismatch = \frac{(Substrate\ l.p.) - 65\ nm}{65\ nm} \times 100\%$$

Table C.2: Amount of lattice mismatch induced by each templated substrate.

Substrate Lattice Parameter	Lattice Mismatch
58 nm	-10.8%
60 nm	-7.7%
62 nm	-4.6%
64 nm	-1.5%
66 nm	+1.5%
68 nm	+4.6%
70 nm	+7.7%
72 nm	+10.8%

C.3.2. Substrate Functionalization

DNA functionalization of the substrates was performed by incubating each patterned substrate in 5 µM HS-B DNA solution in buffer (0.5 M NaCl PBS) overnight, after the propylmercaptan protecting group of the thiol-modified DNA was cleaved (Section C.2.2). To remove unbound DNA, the substrates were rinsed 3 times in buffer with vigorous agitation. Linkers were hybridized to the substrates by incubating the substrates in 0.5 µM hybridized Linker B solution at 0.5 M NaCl at 35°C overnight. Unhybridized linkers were removed by rinsing the solution 5 times in buffer.

C.4. Epitaxial PAE Thin Film Assembly

C.4.1. Protocol

The layer-by-layer deposition of PAE thin films onto the functionalized lithographically defined templates was done rapidly at elevated temperatures. PAEs of both types were diluted to 5 nM using buffer solution. Each pair of identical substrates was placed back-to-back in 1 mL of the appropriate PAE type and incubated for 45 min (verified to be sufficient for near full monolayer coverage, Figure C.4).
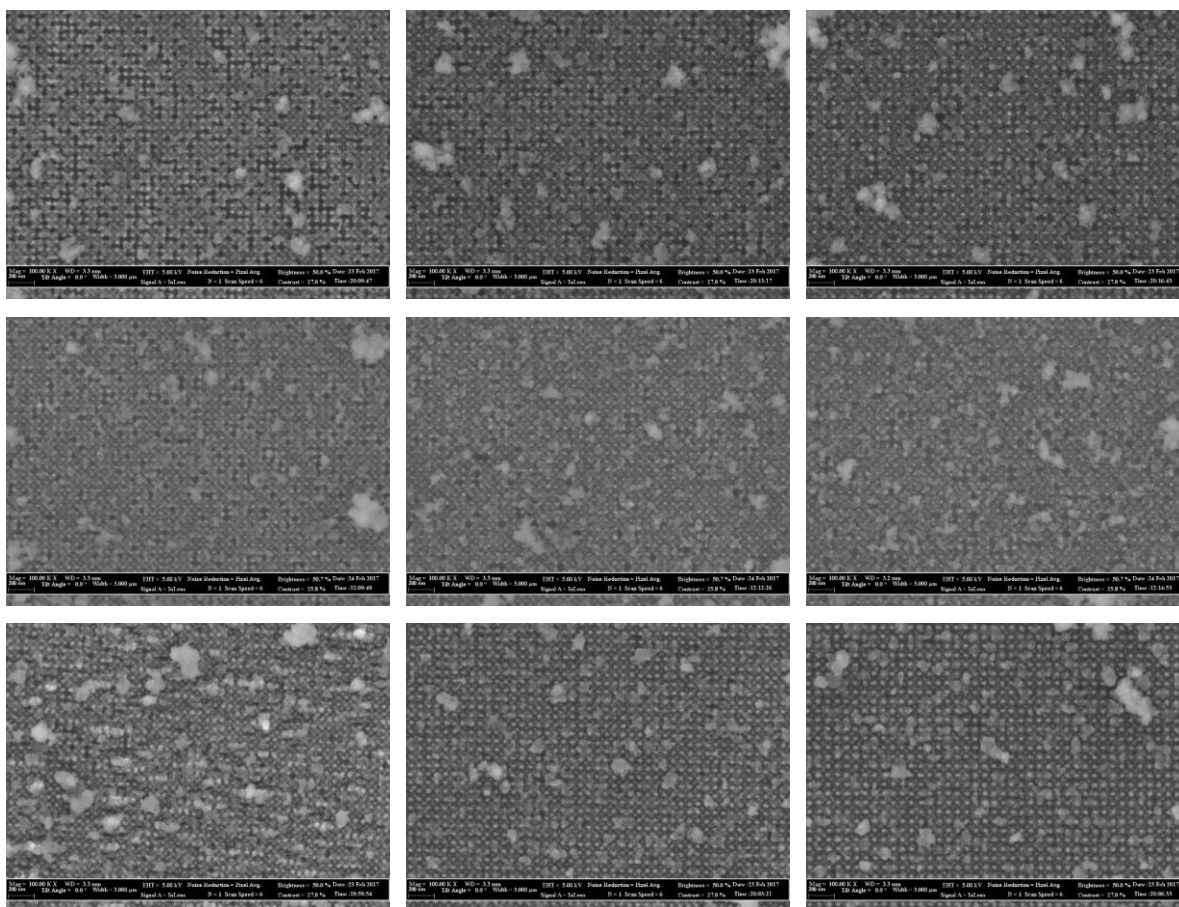
Figure C.4: SEM micrographs of embedded (see SI section 4.2) PAE monolayers on templated lattice mismatch substrates revealing near full coverage after 45 min. Rows (top to bottom): 15 min deposition, 45 min, 8 hr. Columns (left to right): -7.7% lattice mismatch, +1.5%, +10.8%.

The substrates were then removed and washed 5 times in buffer and placed back-to-back in 1 mL 0.5 M NaCl PBS and annealed for 15 min. The PAE solution was refreshed with the addition of 3 µL 15 nM PAE solution to return it to its original concentration (5 nM). Finally, the

substrates were removed from the PBS and placed in the complementary PAE solution where the protocol was then repeated. After 5 layers of deposition, the substrates were allowed to set at 25°C overnight; similarly, after 10 layers of deposition, they set overnight before embedding (Section C.4.2). The temperatures of the deposition solutions and the annealing solutions were controlled by an Eppendorf Thermomixer and were as described in Table C.3. The rising pattern of deposition/annealing temperatures is similar to previously reported protocols.[147]

Table C.3: Temperature protocols for layer-by-layer epitaxial PAE thin film deposition and annealing.

Layer #	PAE Type	Deposition Temp	Annealing Temp
1	A	Room Temperature (25°C)	Room Temperature (25°C)
2	B	Room Temperature (25°C)	$T_m - 9.5°C = 29°C$
3	A	$T_m - 8.5°C = 30°C$	$T_m - 6.5°C = 32°C$
4	B	$T_m - 7.5°C = 31°C$	$T_m - 5.5°C = 33°C$
5	A	$T_m - 6.5°C = 32°C$	$T_m - 4.5°C = 34°C$
6	B	$T_m - 6.5°C = 32°C$	$T_m - 4.5°C = 34°C$
7	A	$T_m - 6.5°C = 32°C$	$T_m - 4.5°C = 34°C$
8	B	$T_m - 6.5°C = 32°C$	$T_m - 4.5°C = 34°C$
9	A	$T_m - 6.5°C = 32°C$	$T_m - 4.5°C = 34°C$
10	B	$T_m - 6.5°C = 32°C$	$T_m - 4.5°C = 34°C$

C.4.2. Silica Embedding

In order to transfer solution-phase PAE thin films to the solid state for characterization by SEM, transmission-SAXS, and AFM, samples were embedded in silica using a sol-gel process modified from the literature.[176] First, 3 μL of *N*-(trimethoxysilyl)-propyl-*N,N,N*-trimethylammonium chloride (TMSPA, Gelest, 50% in methanol) was added to each deposited substrate in 1 mL of 0.5 M NaCl PBS and left to encapsulate DNA bonds within the superlattices for 20 min on an Eppendorf thermomixer (1,400 rpm, 25°C). 5 μL of triethoxysilane (Sigma-Aldrich) was then added, and the samples were left on shaker for another 30 min before being rinsed with nanopure water 3 times under vigorous agitation. The samples were finally blown dry with compressed air.

C.5. PAE Thin Film Characterization

The embedded PAE thin films were characterized using SEM, transmission SAXS, FIB cross-sectioning followed by SEM imaging, and atomic force microscopy (AFM).

C.5.1. SEM Data

The top-down micrographs in Figure S5 were collected on a Zeiss SEM. (Note the tilt angle listed in the information bar is inaccurate due to a software malfunction; should be listed as 0°) The SEM data clearly shows that the deposited PAEs adopt the patterned, single-crystal (100) bcc crystallographic alignment. As the amount of lattice mismatch increases (moving from left to right in Figure S5), the surface of the PAE thin film is increasingly amorphous. This conclusion is visual verification of the conclusion in Figure 4.2 of the manuscript – the thin films maintain coherency up to 7.7% lattice mismatch in both the positive and negative directions.
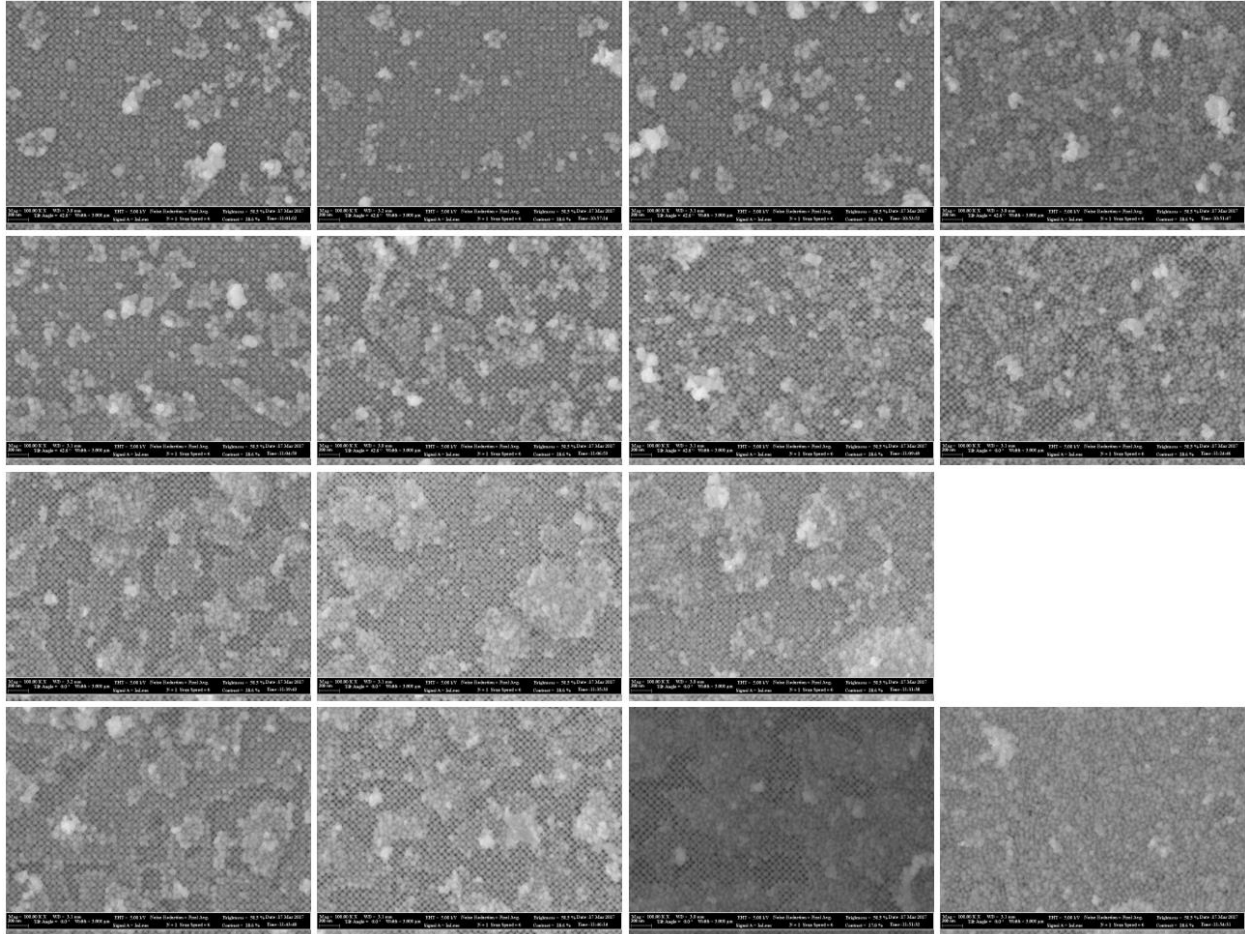
Figure C.5: Representative SEM micrographs of the embedded thin films revealing single crystal epitaxial alignment. Rows (top to bottom): 5 layer (5L), negative lattice mismatch; 5L, positive; 10L, negative; and 10L, positive. Columns (left to right): 1.5% lattice mismatch, 4.6%, 7.7%, and 10.8%.

C.5.2. SAXS Data

All SAXS experiments carried out on the embedded PAE thin films were conducted at the 12-ID-B station at the Advanced Photon Source (APS) at Argonne National Laboratory (ANL). The samples were probed using 13.3 keV X-rays, and the sample-to-detector distance (3603.5631 mm) was calibrated with a silver behenate standard. The beam was collimated using two sets of slits and a pinhole. The beam size was ~200 μm × 20 μm. Scattered radiation was detected using a Pilatus 2M detector.

Full 2D SAXS scattering patterns for all the PAE thin films studied in this manuscript are collected below in Figure C.6 and reveal excellent alignment and lattice matching to the patterned

substrates. Each 2D pattern was averaged circularly across the entire q-range, and the resulting 1D averages are plotted in Figure C.7. Note: the intensity of each 1D curve is normalized such that the maximum value is 1 and then linearly offset from the other curves for clarity.
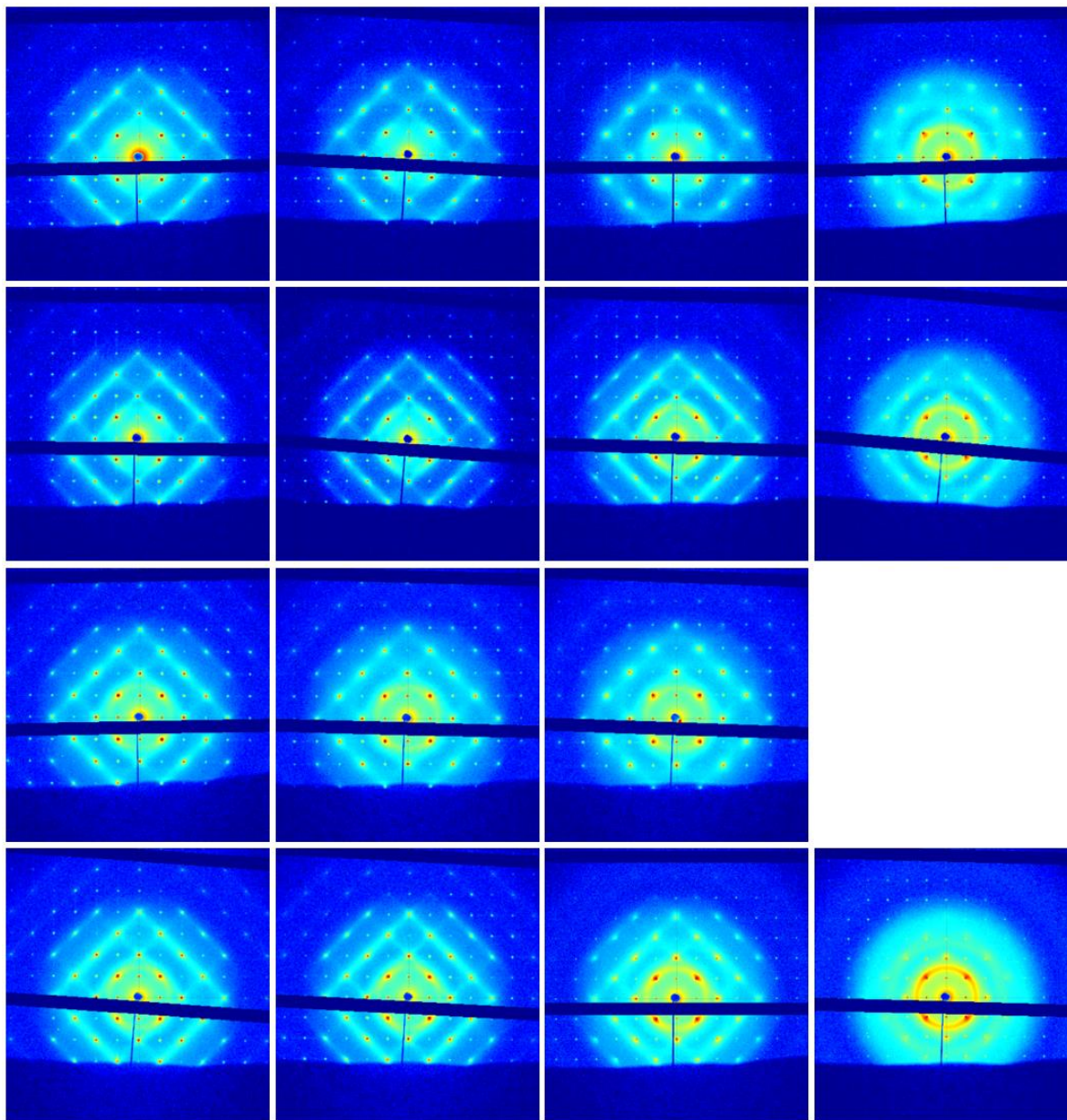
Figure C.6: 2D transmission SAXS patterns of the embedded thin films revealing high degree of ordering. Rows (top to bottom): 5 layer (5L), negative lattice mismatch; 5L, positive; 10L, negative; and 10L, positive. Columns (left to right): 1.5% lattice mismatch, 4.6%, 7.7%, and 10.8%.
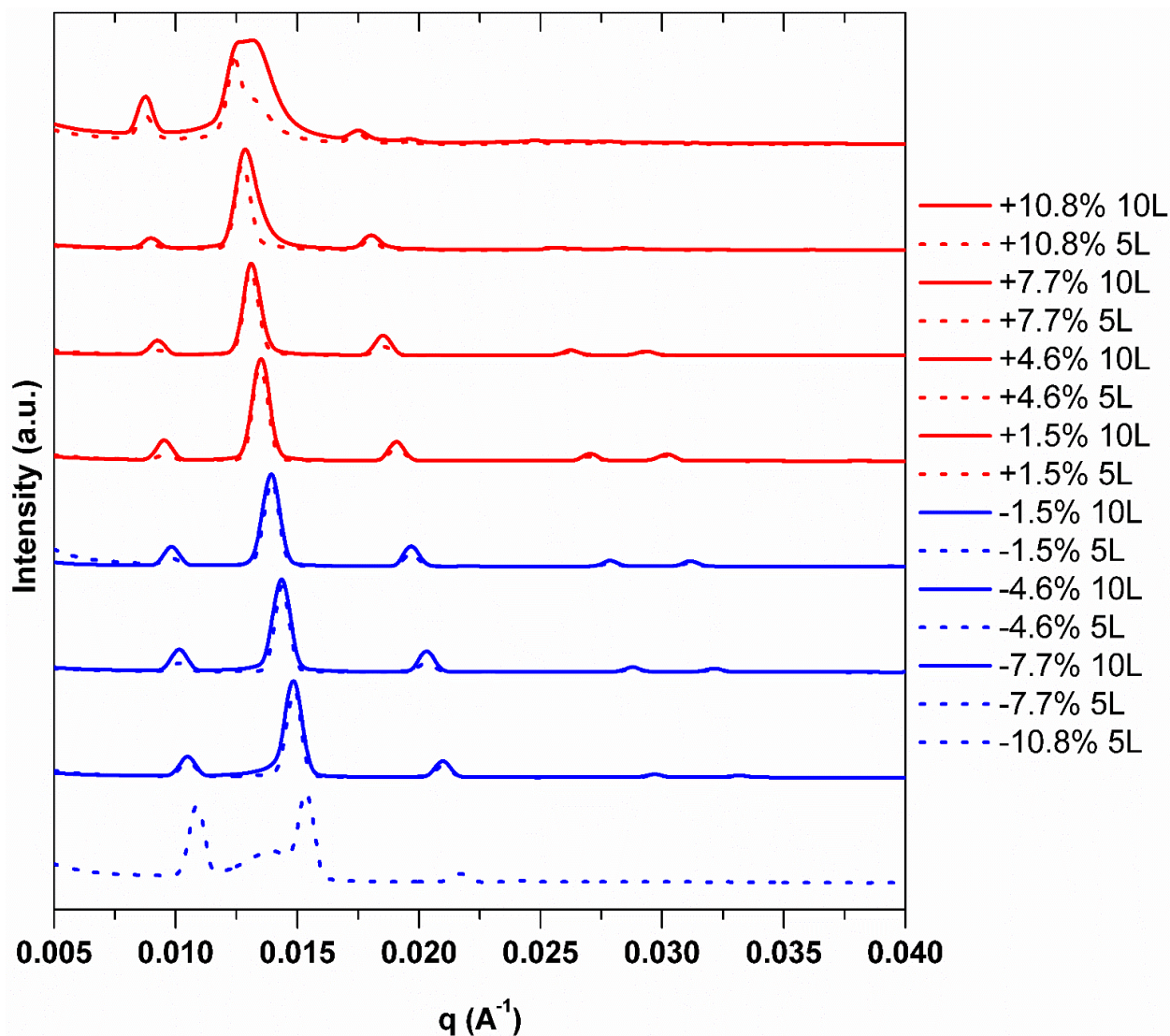
Figure C.7: 1D circular averaging SAXS data of the embedded thin films. Curves (from top to bottom) correspond to the legend order.

C.5.3. SAXS Order Parameter Calculations

To better compare the degree of ordering between samples, an arbitrary order parameter was established and plotted in Figure 4.2b of the manuscript such that "perfectly" ordered samples – all PAEs in ideal epitaxial positions – would have a value of 1 and "perfectly" disordered samples – no correlation between templated substrate and PAE positions – would have a value of 0. To calculate the relative degree of epitaxy/ordering, first, azimuthal linecuts (averaging the intensity of q-values between 0.0045 and 0.0138 Å^{-1} for each azimuthal angle) of each sample's 2D SAXS

data were taken (Section C.5.6 for more details). The q-range of the azimuthal cuts was selected to ensure that the (110) spot of each sample and any elastic relaxation would be included while excluding any other diffraction peaks. Each of these 1D curves was then normalized such that the maximum intensity was at an azimuthal angle of 45°. As described in the manuscript, PAEs that are in a lattice position relative to the substrate's patterned crystallography will add to the intensity of the diffraction spots while PAEs that are in amorphous arrangements or within a crystalline domain not aligned with the substrate (polycrystalline) will add intensity to a diffuse ring encircling the beam center. Thus, to compare the relative number of PAEs ordered *vs* disordered to the substrate, the following equation was used, where I is the intensity and θ is the azimuthal angle of Figure C.9.

Equation C.8:

$$Order\ Parameter = \frac{\int_{30°}^{60°} Id\theta - \int_{75°}^{105°} Id\theta}{\int_{30°}^{60°} Id\theta}$$

The range of 30° to 60° (±15° from 45°) was chosen to include the entire breadth of each (110) spot (*i.e.* all plastic deformation was included as "ordered"). Since the diffuse ring of "disordered" particles contributes a flat intensity from 0° to 360°, a section of this intensity (with the same integration width) must be subtracted from the integration around the (110) spot. It should be noted that the patterned dots on the substrate add a large amount of intensity to each of the diffraction spots in the 2D SAXS data. Given the experimental difficulty in accurately measuring this contribution, it was not subtracted from the "ordered" integrated intensity, thus making the order parameter reported higher than one that strictly only considers PAE contributions. However, the theoretical contribution of the dots to the measured intensity is expected to be relatively constant across all samples; therefore, using this order parameter to compare the relative ordering trends across samples in this study is justified.

C.5.4. SAXS $q_{(110)}$ Calculations

The measured $q_{(110)}$ peak position plotted in Figure 4.2c of the manuscript was taken to be the maximum q-value of each curve in Figure C.7 – full circular averages of the 2D SAXS data. The templated (theoretical) $q_{(110)}$ positions were calculated from Equation C.9 which is merely a rearrangement of Equation C.5 and Equation C.6.

Equation C.9:

$$Templated\ q_{(110)} = \frac{2\sqrt{2}\pi}{(Substrate\ lp)}$$

C.5.5. SAXS Elastic Relaxation Analysis

The elastic relaxation phenomenon described in Figure 4.3 of the manuscript was deduced from radial averaging of the 2D SAXS data along the direction including the (110) peak, *i.e.* the 45° azimuthal angle. Each linecut was aligned to the (110) peak and allowed to average over a width of two detector pixels across the entire q-range. The peak to be investigated – (110) in the manuscript – had a modeled linear background subtracted such that the local minima surrounding the peak were at a value of 0 and had its intensity normalized such that the local maximum was at a value of 1 (Figure 4.3a). The *q*-values at intensity 0.5 (half max) and 1 (peak max) of these curves were found, interpolating linearly between neighboring data points if necessary. The value for "$q_{(110)}$ Deviation" in Figure 4.3b was calculated with the following equation.

Equation C.10:

$$q_{(110)}\ Deviation = q_{(Peak\ Max\ of\ Radial\ Linecut)} - (Templated\ q_{(110)})$$

The length of the error bar (peak width at half max) in the high-*q* and low-*q* directions was then calculated using the appropriate half max *q*-value and the following equation.

Equation C.11:

$$Peak\ Width\ at\ Half\ Max = \left| q_{(Half\ Max\ of\ Radial\ Linecut)} - q_{(Peak\ Max\ of\ Radial\ Linecut)} \right|$$

As described in the main text, intensity deviation along the radial direction is indicative of elastic relaxation of the PAEs within the thin film. Notably, the shape of the overall 1D curve (namely, the directional width) can be used to elucidate whether the PAEs in the film are expanding or compressing relative to the patterned lattice parameter. While Figure 4.3a of the manuscript shows that the PAEs strive to return to their bulk phase lattice parameter/interparticle spacing, the relative deviation from the patterned lattice mismatch can be more clearly seen from Figure C.8 where the 1D curves from Figure 4.3a have been normalized relative to their appropriate Templated $q_{(110)}$ such that all the peak maximums are aligned.
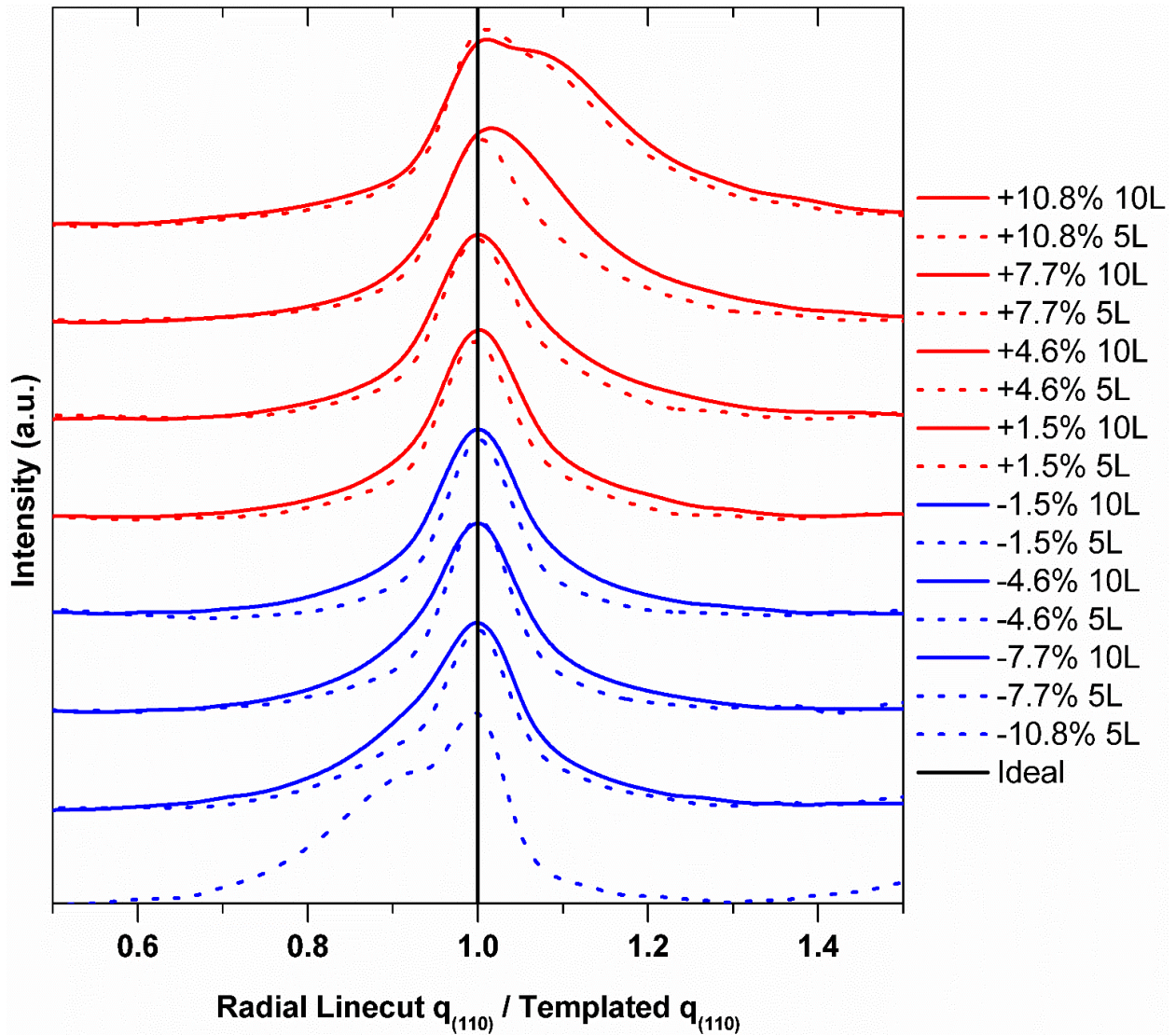
Figure C.8: 1D SAXS averages of radial linecut along the 45° direction normalized to the Templated $q_{(110)}$ peak position revealing an elastic relaxation of PAEs counter to the direction of induced lattice mismatch. Curves (from top to bottom) correspond to the legend order.

In the manuscript, the (110) diffraction spot position is chosen as it is the highest intensity and easiest to observe visually in the 2D SAXS data and as it corresponds to the nearest neighbor spacing between PAEs in the bcc lattice. Thus, directional gradients in intensity from this position can be directly understood as gradients in interparticle distance. However, in principle, every diffraction spot in the 2D SAXS data should exhibit radial broadening if the PAEs are indeed elastically relaxing. Visual inspection of the 2D SAXS data reveal this phenomenon at each spot (Figure C.6).

C.5.6. SAXS Plastic Relaxation Analysis

The plastic deformation phenomenon described in Figure 4.4 of the manuscript was deduced from azimuthal averaging of the 2D SAXS data (averaging the intensity of q-values between 0.0045 and 0.0138 $Å^{-1}$ for each azimuthal angle). Each 1D linecut was then normalized such that the highest intensity occurred at 45° and was a value of 1 (Figure C.9).
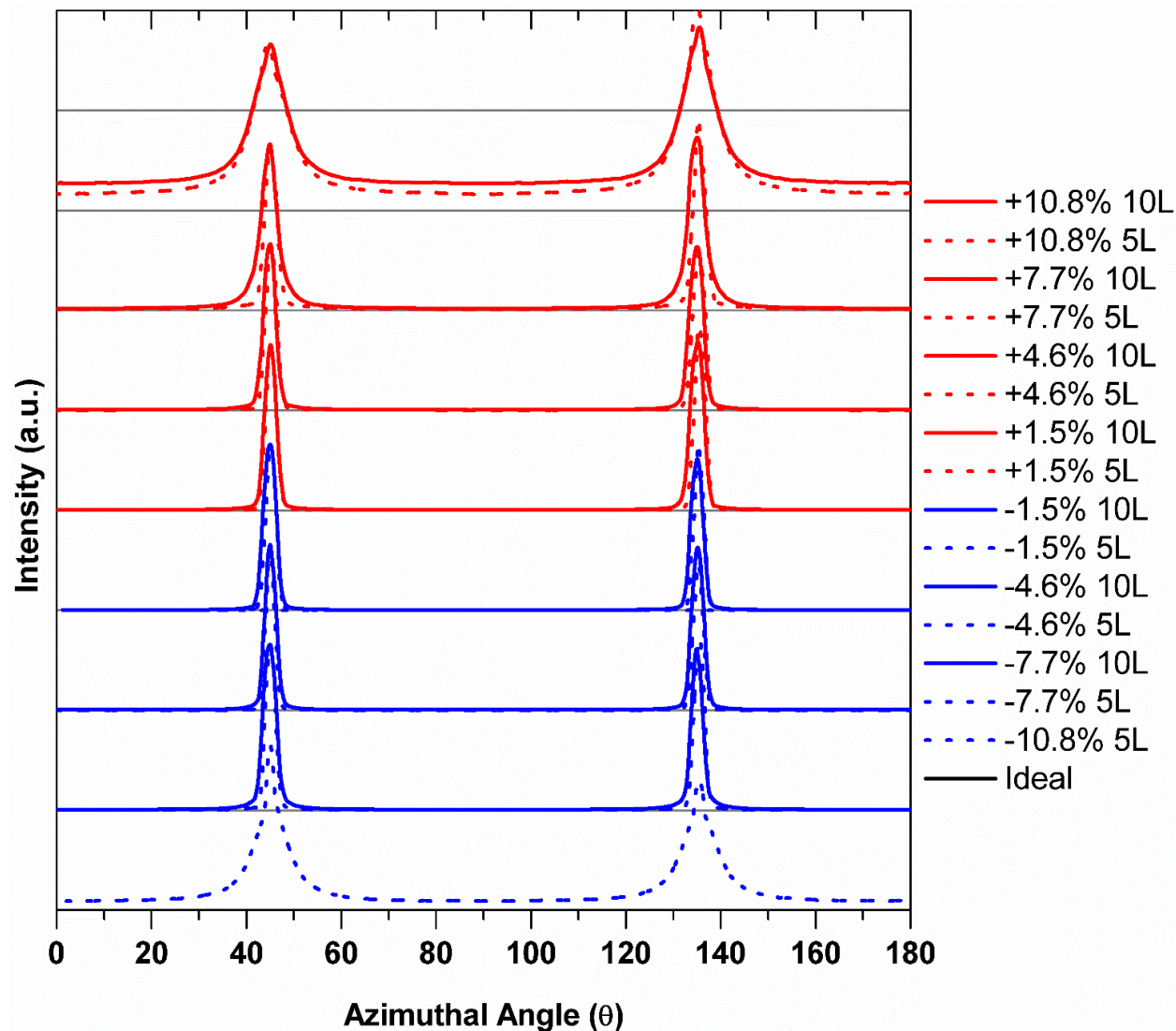
Figure C.9: 1D SAXS averages of azimuthal linecuts. Curves (from top to bottom) correspond to the legend order.

Each curve was background subtracted to remove the contributions from the disordered PAEs. To do this, the intensity value at 90° was subtracted from the entire curve. The azimuthal

angles (θ) at intensity 0.1 (10% max) above and below 45° of these curves were found, interpolating linearly between neighboring points if necessary. The value for "$q_{(110)}$ Peak Breadth" in Figure 4.4a was then calculated with the following equation.

Equation C.12:

$$q_{(110)} Peak\ Breadth = \left(\theta_{(10\%\ Max\ Above\ 45°)} - 45°\right) + \left(45° - \theta_{(10\%\ Max\ Below\ 45°)}\right)$$

C.5.7. FIB Cross-section Data

All FIB cross-sectional data was collected on a Helios Nanolab 600 dual beam focused ion beam milling system with a 52° relative difference between the ion and electron beam. After a layer of titanium was deposited over the area of interest, a 15 μm × 1 μm area, aligned lengthwise with the (100) plane of the superlattice, was milled with a 93 pA (30 kV) ion beam. Thus, the templated dots of the substrate are visible at the bottom of each cross-section. Epitaxial PAEs would be expected to align vertically to these positions and any deviations in the PAE positions could be readily observed. Each cross-section was imaged with an 86 pA (5 kV) electron beam using the in-lens detector on the SEM without using the software's tilt correction. SEM images were stitched together using Photoshop but not adjusted for tilt angle. Post processing of the SEM micrographs can be done to adjust the y-axis to a scale that is representative of the real space length using the following equation.

Equation C.13:

$$y_{processed} = \frac{y_{raw}}{\cos(90° - 52°)} = \frac{y_{raw}}{\cos(38°)} = 1.269 \times y_{raw}$$

Data analysis on cross-sections was done for entire 15 μm; images to be included in Figure 4.4b of the manuscript and Figure C.10 of the SI were subsequently cropped to a representative section and included for qualitative reference. The 15 μm cross-sections of each of the 10 layer samples can be found in an accompanying Supporting Information file (.tif) in the literature.[26]

C.5.8. FIB Plastic Deformation Analysis

Since PAEs have been shown to mimic the behavior of atoms in numerous situations, we hypothesize the presence of even more intricate plastic strain relief mechanisms in these PAE films that often arise in atomic, heteroepitaxial thin films. In systems with lattice mismatch, the accumulation of strain energy can reach a point where incurring the energy penalty of forming a

lattice defect relieves enough strain energy to lower the film's total potential energy. For example, a crystalline material under compressive strain can manifest a vacancy such that the building blocks surrounding the empty lattice site can locally expand into the space, relieving their strain energy. Even more collectively, a heteroepitaxial lattice mismatched thin film is able to locally expand/shrink the *x,y*-direction spacing, relaxing the strain energy present in those planes, by excluding/beginning the continuation of an entire lattice plane. This type of defect is known as a misfit dislocation is common to atomic heteroepitaxial systems with lattice mismatch. Both vacancies and misfit dislocations were observed in the FIB cross-sections and are highlighted below in Figure C.10. To investigate whether the observed defects could be removed with annealing, a second -7.7% lattice mismatch thin film was deposited with longer deposition and annealing times, allowing the PAEs more time to reorganize. The cross-section of this thin film is included in the literature SI file (.tif)[26] with the other FIB cross-sections. Instead of annealing out the defects, the added thermal energy encouraged more dislocations to form, as well as grain boundaries. This result indicates that the thin films studied in this manuscript may be kinetically arrested structures, but a more detailed study is required to confirm this hypothesis.
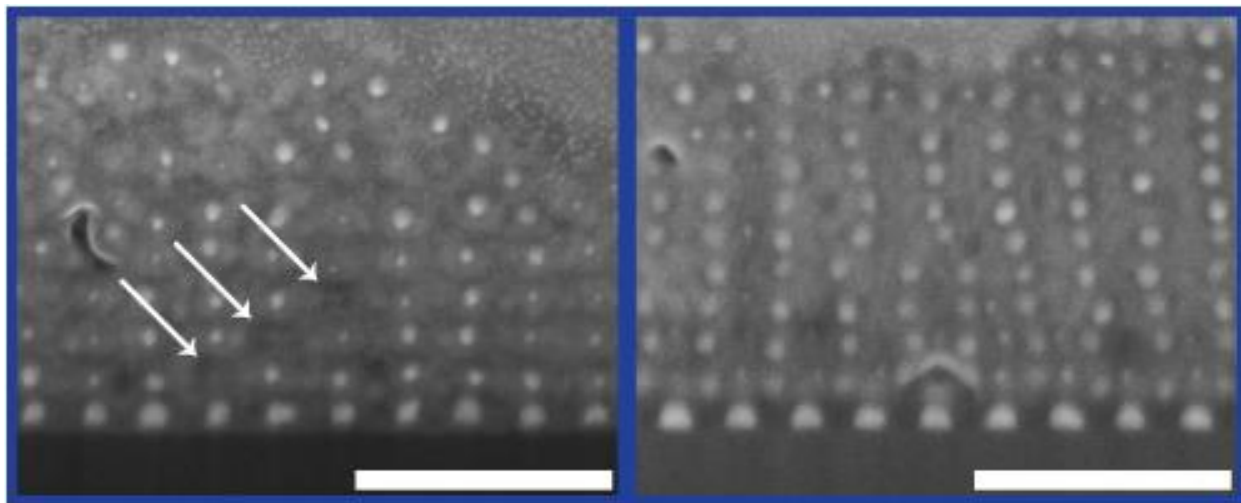
Figure C.10: Representative defects (left: vacancies, right: misfit dislocation) present in the FIB cross-sections of the medium, generally negative, lattice mismatch thin films. Scale bars are 250 nm.

C.5.9. AFM Data

In addition to the SEM data, the substrate surfaces were imaged with atomic force microscopy (AFM, Bruker Dimension ICON, Bruker, Santa Barbara, CA), which provides

information about the particle alignment and the surface roughness of films. For each sample, a 2 µm × 2 µm area was scanned in tapping mode using NCHR-50 cantilevers with a spring constant of 42 N/m (Nanoworld, Neuchâtel, Switzerland). Thermal tuning was used to find the resonance frequency. The scan speeds were restricted to 0.75 – 0.99 Hz. The imaging was carried out in ambient conditions, and images were adjusted utilizing a first order plane fit (NanoScope Analysis 1.5 software). The data are collected in Figure C.11. AFM images corroborate the data collected using SEM, and support the conclusion that the PAEs alleviate the strain from lattice mismatch by deviating from their ideal bcc positions. With increasing lattice mismatch, surface roughness of each film is increased (*i.e.* islands and amorphous structures observed atop of the film).

a)

b)
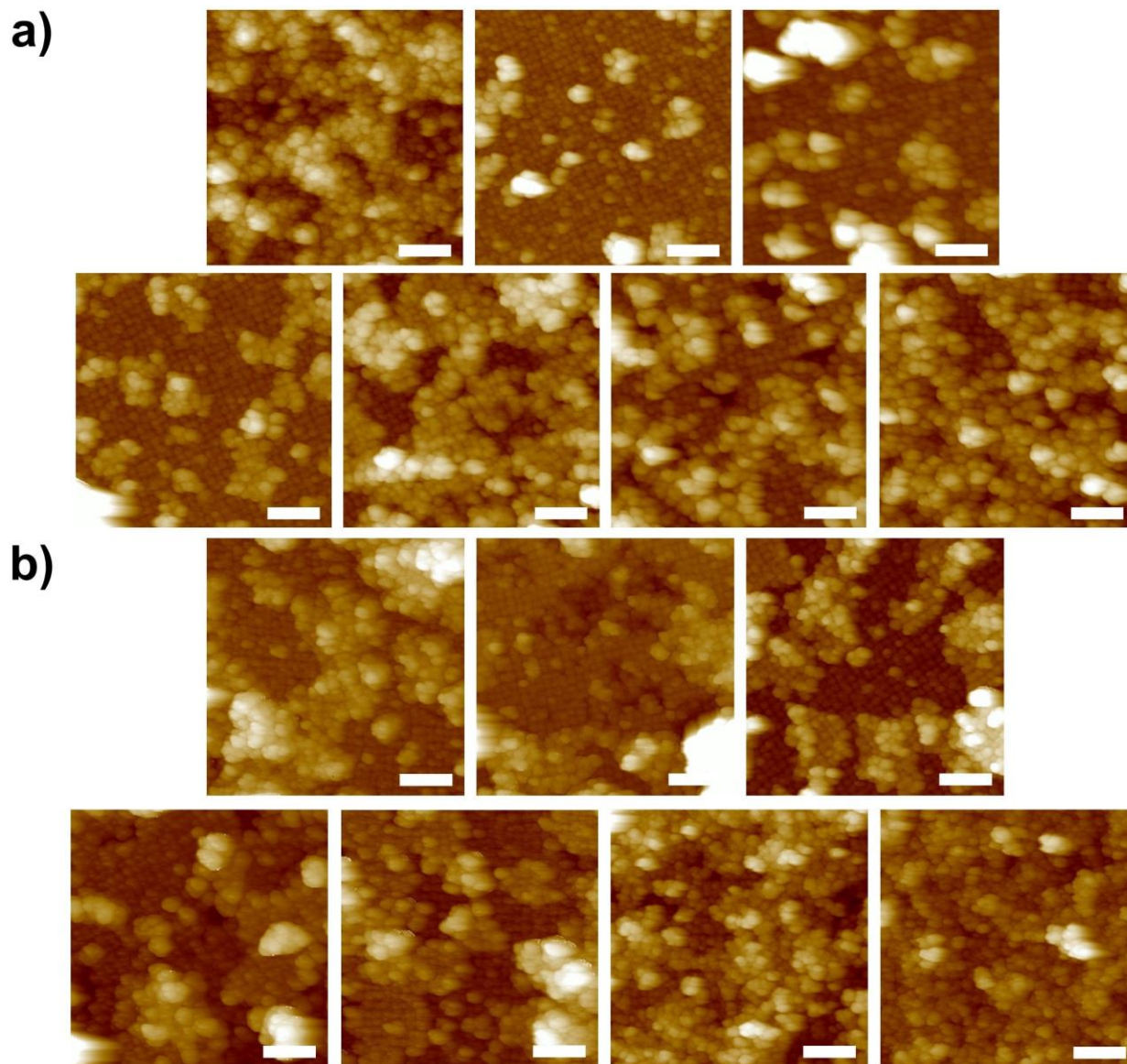
Figure C.11: AFM images of embedded PAE thin films. a) 5L films with (first row, left to right) -10.8, -4.6, -1.5, (second row, left to right) +1.5, +4.6, +7.7 and +10.8% lattice mismatch. b) 10L films with (first row, left to right) -7.7, -4.6, -1.5, (second row, left to right) +1.5, +4.6, +7.7 and +10.8% mismatch. All scale bars are 400 nm.

Appendix D. Supporting Information for Nanoparticle Composite Materials with Programmed Nanoscale, Microscale, and Macroscale Structure (Chapter 5)

D.1. Materials, Instrumentation, and Characterization Methods

D.1.1. Materials

2,6-Diaminopyridine, thymine, acetyl chloride, 11-bromoundecan-1-ol, sodium azide, ethylenediaminetetraacetic acid sodium salt, 2-Bromoisobutyryl bromide, styrene, N,N,N',N",N'"-Pentamethyldiethylenetriamine (PMDETA), propargyl alcohol, and citric acid monohydrate were purchased from Acros. Trisodium citrate dihydrate, hexamethyldisilazane, Tris[2-(dimethylamino)ethyl]amine (Me_6TREN), and tin(II) 2-ethylhexanoate were purchased from Alfa Aesar. Docosane, phosphorous acid, cyclohexamine, ferric chloride hexahydrate, oleic acid, copper (I) bromide, hydrochloric acid, and copper (II) bromide were purchased from Sigma Aldrich. N-hexane, N-octane, N-decane, and gold (III) chloride trihydrate were purchased from Beantown Chemical. Aminoethanethiol and sodium oleate were purchased from TCI America. Basic Alumina and general solvents were purchased from Fisher Scientific. A polyoxymethylene bar was purchased from McMaster Carr. All chemicals, including solvents, were used without further purification, except styrene, which was passed through a short column of basic alumina to remove inhibitor prior to polymerization.

D.1.2. Instrumentation

Centrifugation was performed with an Eppendorf 5424 centrifuge. Gel permeation chromatography (GPC) characterizations were performed on an Agilent Technologies Infinity 1260 GPC system with triple detection (refractive index, 90° light scattering, and viscometry), with Resipore columns, and with tetrahydrofuran (THF) as the eluent at 1.0 mL/min. UV-vis spectra and measurements were obtained on a Cary-5000 spectrometer. Small angle x-ray scattering (SAXS) measurements were performed at the Massachusetts Institute of Technology (MIT) Center for Materials Science and Engineering (CMSE) X-ray Diffraction Shared Experimental Facility on a SAXSLAB system. The Rigaku 002 microfocus X-ray source produced Cu Kα1 x-rays of wavelength 1.5409 Å; Osmic staggered parabolic multilayer optics focused the beam crossover at the second pinhole. Two sets of JJ X-ray jaw collimation slits set at 0.45mm and 0.2mm,

respectively, were used to define the beam. The system was calibrated using silver behenate as a standard. Solvated SAXS samples were loaded into a short section of 1.5 mm diameter Polyimide Tubing (Cole-Parmer) and sealed at both ends with epoxy. Before loading samples into the tubing, one end was sealed with epoxy and the tubing baked at 110 °C overnight. Dried SAXS samples were prepared by casting onto polyimide film, or for macroscopic samples wrapping in polyimide tape. The lowest q peak identified in SAXS (q_0) were fit using a Pseudo-Voight function, and the interparticle distance for bcc crystals was determined as:

Equation D.1:

$$d_{bcc} = \frac{\pi\sqrt{6}}{q_0}$$

And for CsCl crystals as:

Equation D.2:

$$d_{CsCl} = \frac{\pi\sqrt{3}}{q_0}$$

Transmission electron microscopy (TEM) was performed with a JEOL 2010 Advanced High-Performance transmission electron microscope, with samples cast onto formvar coated TEM grids (Ted Pella). Top-down Scanning electron microscopy (SEM) was performed on either a Zeiss Sigma 300 VP Field Emission SEM (5kV electron beam with in-lens detector) or a Helios Nanolab 600 dual beam (86 pA and 5 kV electron beam with in-lens detector). To be imaged, samples were cast and dried onto copper tape or silicon wafers (150 mm P-Type Prime (100) wafers with polished surfaces purchased from Wafernet) which had 2 nm of chromium (Cr) and 8 nm of gold (Au) deposited (*via* AJA eBeam evaporator) to aid conduction. Cross-sectional micrographs were collected on the Helios Nanolab 600 dual beam focused ion beam milling system with a 52° relative difference between the ion and electron beam. After a layer of titanium was deposited over the area of interest, the sample was milled with a 93 pA (30 kV) ion beam. Each cross-section was imaged with an 86 pA (5 kV) electron beam using the in-lens detector on the SEM without using the software's tilt correction. SEM images were stitched together using Photoshop and had the y-

axis scale adjusted for tilt angle such that it is representative of the real space length using the following equation:

Equation D.3:

$$y_{processed} = \frac{y_{raw}}{\cos(90° - 52°)} = \frac{y_{raw}}{\cos(38°)} = 1.269 \times y_{raw}$$

D.2. Synthesis of Nanocomposite Tectons (NCTs)

The synthesis of the diaminopyridine (DAP) initiator, thymine (Thy) initiator, and phosphonate anchor have been previously reported.[244]

The DAP polymers were synthesized by the Activator ReGenerated by Electron Transfer Atom Transfer Radical Polymerization (ARGET-ATRP)[310] of polystyrene using the DAP initiator as previously reported.[233] The Thy polymers were synthesized by the ATRP of polystyrene using the Thy initiator as previously reported.[21] GPC traces of the polymers used in this work are featured in Figure D.1, and the results summarized in Table D.1.
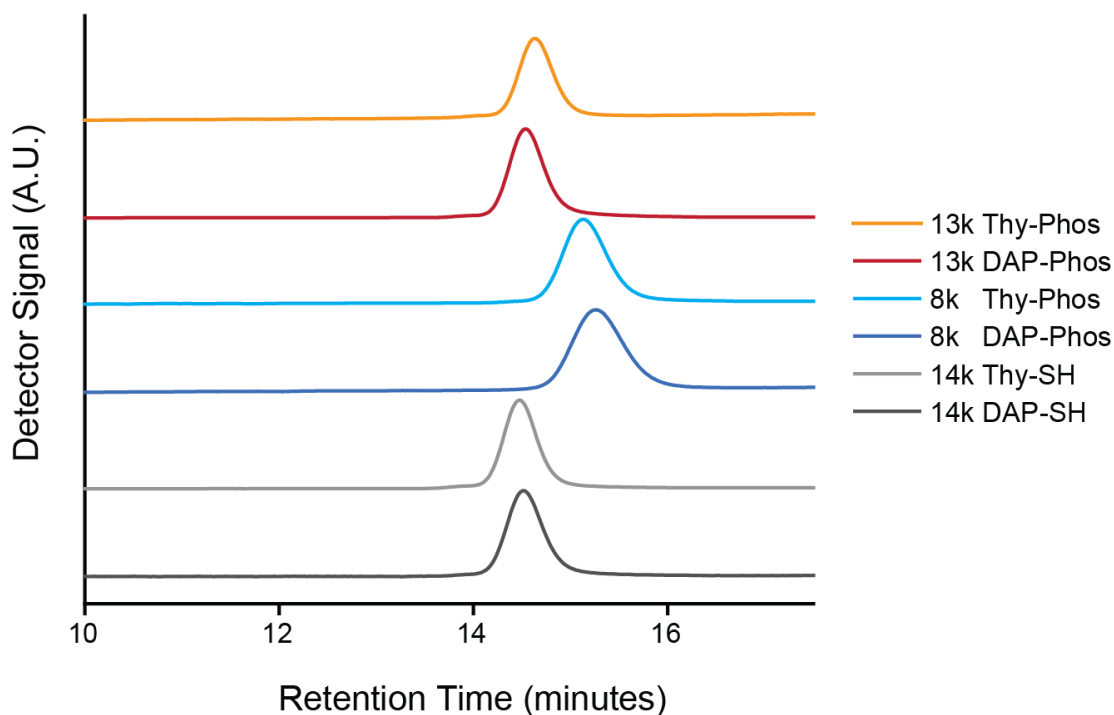
Figure D.1: GPC traces of polymers used in this work. Data is summarized in Table D.1.

Table D.1: Summary of GPC results for the polymers used in this work.

	M_n (kDa)	M_w (kDa)	M_p (kDa)	Đ
DAP-SH 14 kDa	13.1	13.6	14.0	1.036
Thy-SH 14 kDa	13.8	14.2	14.4	1.028
DAP-Phos 8 kDa	7.1	7.4	7.7	1.050
Thy-Phos 8 kDa	7.5	7.7	7.9	1.033
DAP-Phos 13 kDa	13.1	13.5	13.8	1.031
Thy-Phos 13 kDa	12.2	12.4	12.6	1.019

After polymerization, the terminal bromine of polymers that were to functionalize gold nanoparticles was substituted with aminoethanethiol, as described previously.[21] The terminal bromine of polymers that were to functionalize iron oxide nanoparticles was substituted with sodium azide, and a "click" reaction was performed to install the phosphanate anchor as described previously.[244]

Citrate capped gold nanoparticles were synthesized by a literature procedure[307] that was slightly modified.[234]

Iron oxide nanoparticles were synthesized according to a literature procedure from the thermal decomposition of an iron oleate precursor.[244,311] TEM micrographs of the nanoparticles used in this work are featured in Figure D.2, and their sizes and distributions are summarized in Table D.2.
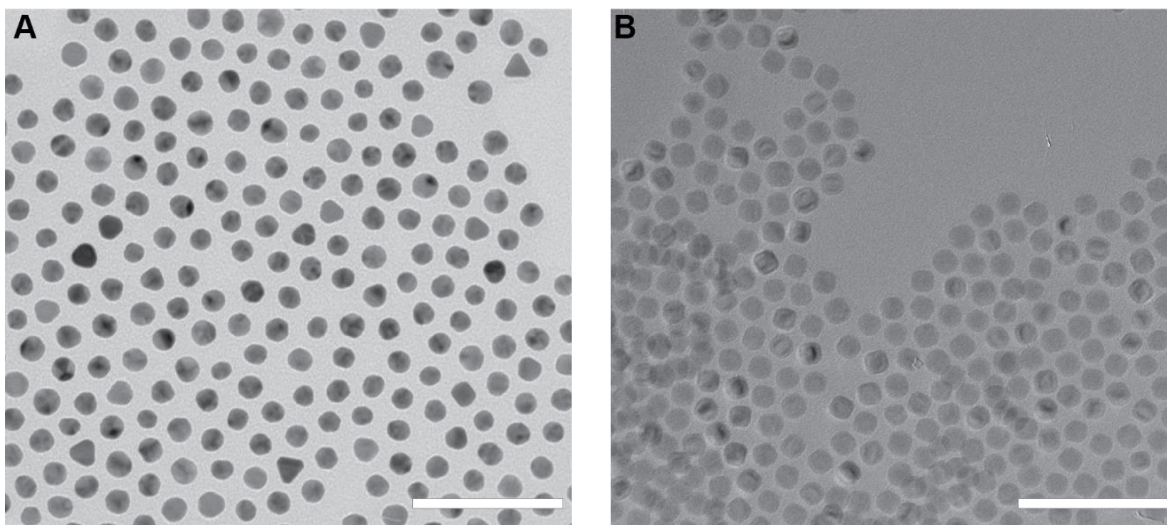
Figure D.2: TEM Micrographs of the gold (A) and iron oxide (B) nanoparticles used in this work. Nanoparticle properties are summarized in Table D.2. Scale bars are 100 nm.

Table D.2: Size and dispersity of the nanoparticles used in these experiments.

	Diameter (nm)	Relative Standard Deviation (%)
Gold Nanoparticles	15.4	8.5
Iron Oxide Nanoparticles	15.9	6.1

Gold Nanocomposite Tecton (Au-NCTs) synthesis was performed as previously reported.[21] Briefly, a solution of as-synthesized gold nanoparticles was added to an equal volume of 1 mg/mL thiolated DAP or Thy polystyrene, and vigorously shaken for 1 minute. The resulting pink precipitate was collected by a gentle centrifugation, and redispersed in N,N-dimethylformamide (DMF). The NCTs then underwent a series of 3 centrifuge cycles (5000 RCF, 45 minutes), redispersing in DMF, Toluene, and Toluene. The concentration of the NCTs was measured using Beer's Law, and adjusted to match the desired concentration for the experiment.

Iron Oxide NCTs (IO-NCTs) were synthesized as previously described.[244] Briefly, iron oxide nanoparticle docosane reaction mixture (500 mg) was dissolved in 4 mL THF. Reaction byproducts were removed by centrifugation (2 x 8,500 RCF) and redispersion in THF. The nanoparticles in THF were divided in half, and added to either DAP or Thy polymer equipped with the phosphonate anchor (40 mg). The solutions were shaken overnight, and then purified by three centrifuge cycles (8,500 RCF) redispersing in THF, Toluene, and Toluene.

D.3. NCT Crystallization

To prepare crystalline Au-NCT assemblies, equal volumes of purified DAP and Thy NCTs were combined in a PCR tube. Analysis of the melting curve (Figure D.28) indicated the standard case NCTs (15 nm Au NPs with 14 kDa polymer) were totally dissociated at 55 °C. Therefore, the annealing process was performed by slow cooling the mixed NCT solution from 55°C to 25°C in a Techne Prime Thermal Cycler at a desired cooling rate (if not mentioned, 0.1 °C / minute). IO-NCTs were crystallized by heating to 80 °C on a heat block, removing the sample, and allowing the NCTs to return to room temperature.

D.3.1. Collapsing the Polymer Brush

NCTs cast directly from toluene do not retain their ordering upon solvent evaporation (Figure D.3). As the solvent evaporates the polymer brush uncontrollably deswells, and capillary forces distort the lattice, although some local ordering is preserved.
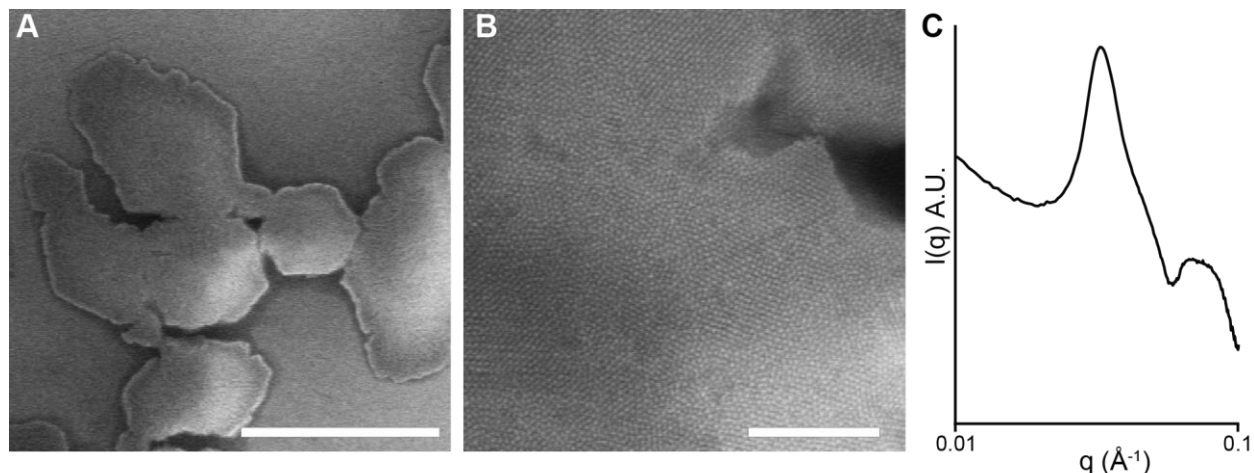
Figure D.3: SEM (A and B) and SAXS data (C) of NCTs cast directly from toluene and dried. Scale bars are (A) 5 microns and (B) 500 nm.

Ordering can be preserved by gradually adding a poor solvent that does not disrupt the hydrogen bonding interactions of the NCTs (Figure D.4). N-Decane was the preferred solvent for the experiments in the main text because its slower evaporation rate allowed for trace amounts of residual toluene to be removed before the assembly completely dried. The typical procedure was to increase the volume fraction of non-solvent by 0.2 every 30 minutes, and when the solution reached 80% non-solvent it was removed with a needle and replaced with pure alkane. The system could accommodate faster addition rates, but shaking samples to mix the solvents would frequently generate static electricity which would pull the NCTs out of solution and destroy them, making their study difficult. Therefore, a more conservative procedure that allowed ample time for solvent diffusion was preferred.

Additionally, the collapsed NCT brush can be swollen with toluene again, without any loss in ordering (Figure D.5).
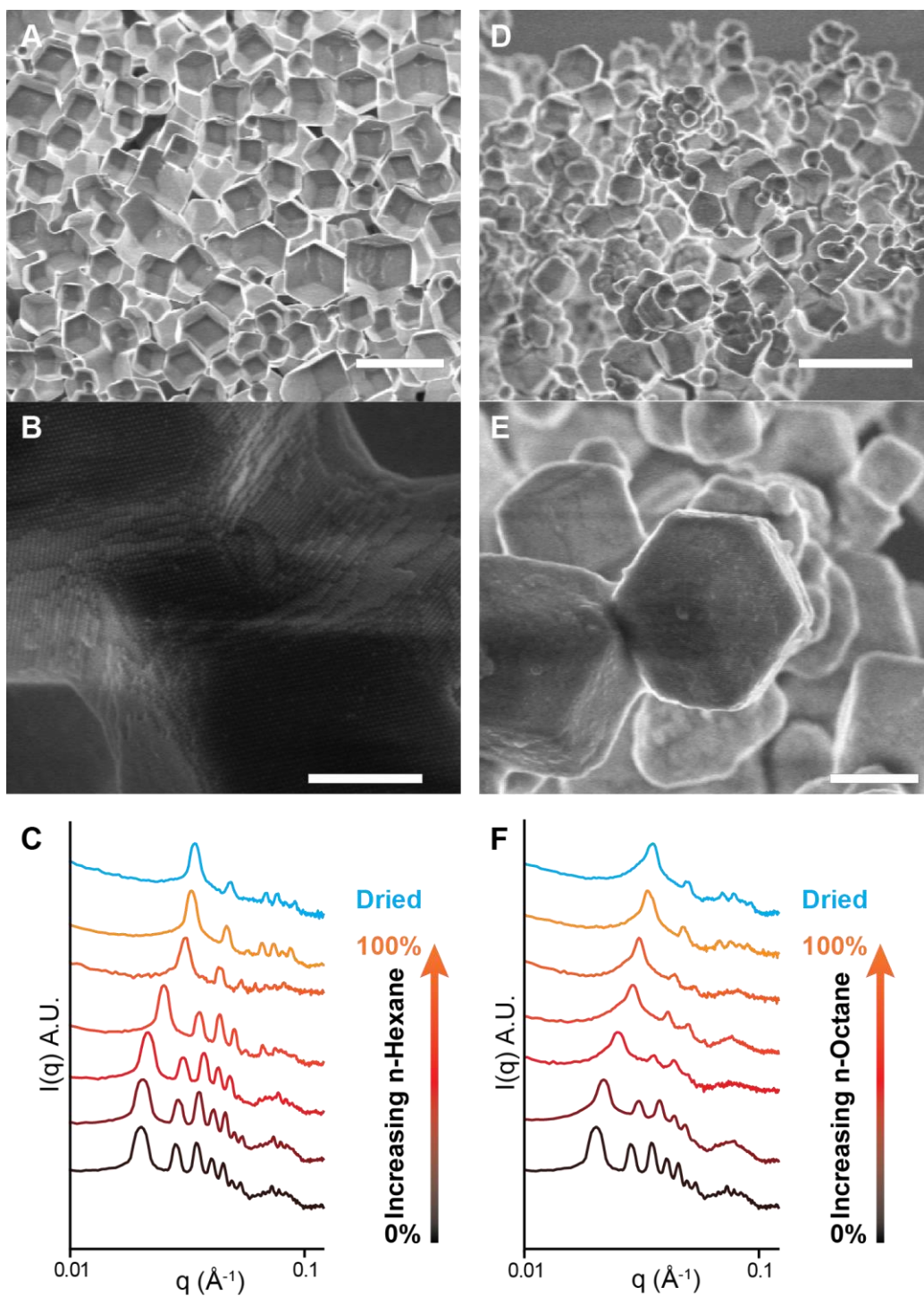
Figure D.4: (A and B) SEM micrographs of NCTs with the brushes collapsed with n-hexane. Scale bars are 5 microns (A) and 500 nm (B). (C) SAXS of NCT crystallites in 0, 20, 40, 60, 80, and 100 volume percent n-Hexane, and of a dried sample. (D and E) SEM micrographs of NCTs with the brushes collapsed with n-Octane. Scale bars are 5 microns (D) and 1 micron (E).
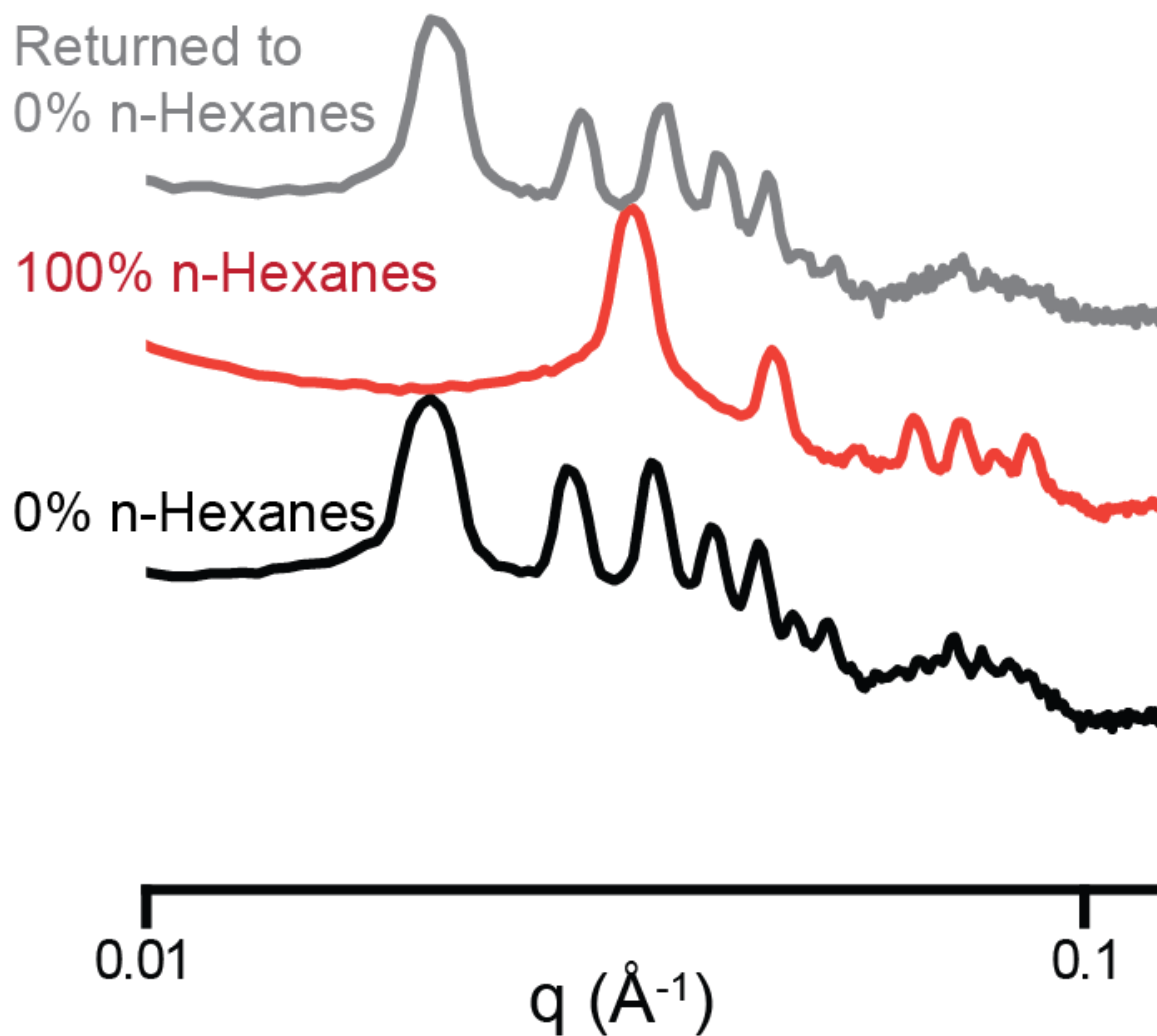
Figure D.5: Sample of Au-NCTs that was transitioned to 100% n-Hexane, and then returned to 100% toluene.

A potential key advantage of these NCT solids with collapsed polymer brushes is the ability to assemble lattices of nanoparticles with very small interparticle distances, which could find use in plasmonic, optical, or magnetic materials.[312,313] To demonstrate this, Au-NCTs were assembled with a 6 kDa polymer brush and collapsed, leading to well-ordered lattices with an interparticle distance of 19.5 nm, or a surface to surface distance of 4.1 nm (Figure D.6).
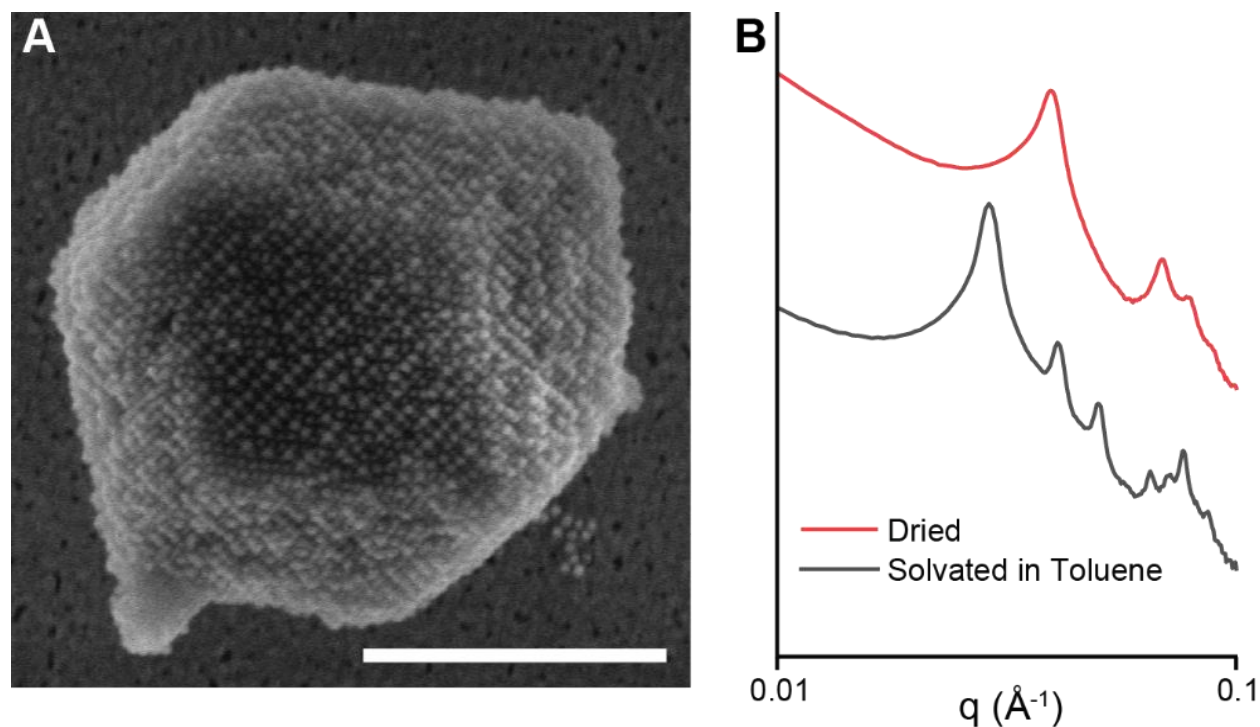
Figure D.6: SEM (A) and SAXS (B) of Au-NCTs synthesized with a shorter, 6 kDa polymer, resulting in a very short interparticle distance (19.5 nm, 4.1 nm surface to surface). Scale bar is 500 nm.

D.4. Controlling NCT Crystallite Size with Cooling Rate and Concentration

To investigate the effects of NCT concentration and cooling rate on crystallite size, several samples were crystallized *via* slow cooling as described above with various cooling rates (1sec/0.1℃ to 8min/0.1℃) and NCT concentrations (5nM to 80nM). After each of these samples had SAXS data collected on them to demonstrate that each was crystalline (key SAXS data collected in Figure D.7), the resulting crystallites were collected, their polymers collapsed, and drop cast onto substrates for SEM analysis. A minimum of 50 micrographs for each condition were collected where each image contains several crystallites, which tend to conglomerate together on the substrate. Three characteristic SEM micrographs of each condition are included for reference in Figure D.8 through Figure D.24. The individual crystallites in each micrograph were measured in ImageJ by tracing the dimensions with a stylus and averaging the major and minor axis lengths to yield a characteristic length (roughly akin to a diameter). The number of crystallites (N)

269

measured for each condition is summarized in Table D.3 and included at minimum 200 individual crystallites. Histograms of characteristic length reveal roughly gaussian size distributions for every condition (Part D of Figure D.8 through Figure D.24, Figure D.25, and Figure D.26) with increasing average values for slower cooling rates and higher concentrations. Descriptive statistics of each distribution is summarized in Table D.3.
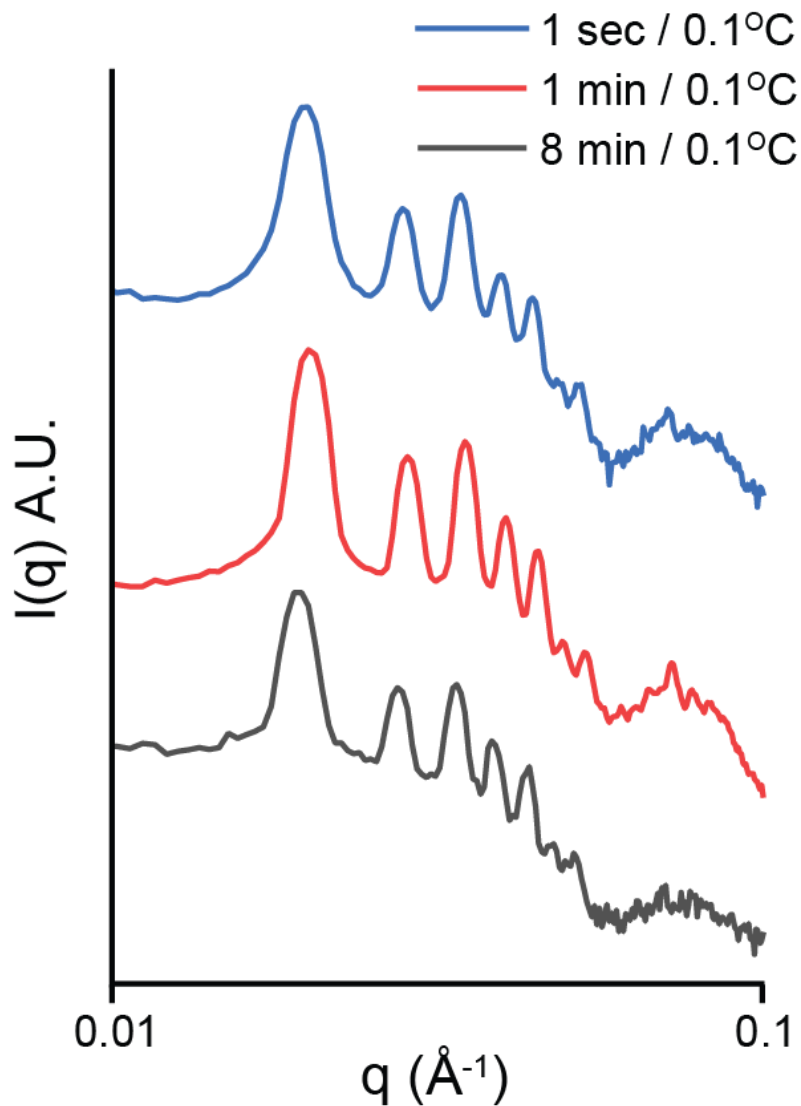
Figure D.7: NCTs form well-ordered crystals at a variety of cooling rates. Even when cooled very rapidly at extreme rates of 0.1°C/s and 0.1°C/8min, an ordered bcc lattice is formed, as evidenced by SAXS.

Table D.3: Summary and descriptive statistics of crystallite size for all conditions studied.

Cooling Rate^{-1} (Time/0.1°C)	NCT Concentration (nM)	N	Mean (nm)	Standard Deviation (nm)	Minimum (nm)	1st Quartile (Q1) (nm)	Median (nm)	3rd Quartile (Q3) (nm)	Maximum (nm)
1sec	20	988	436	103	81	370	432	499	847
15sec	20	1137	1,237	218	28	1,111	1,261	1,377	2,246
30sec	20	955	1,531	316	454	1,325	1,537	1,725	2,801
1min	20	723	1,782	574	483	1,404	1,784	2,129	3,918
2min	20	501	2,046	743	539	1,576	2,006	2,510	5,526
4min	20	468	2,231	909	527	1,595	2,049	2,735	5,473
8min	20	225	3,508	1,696	631	2,185	3,214	4,594	8,438
1min	5	223	1,150	259	403	992	1,185	1,324	1,921
1min	10	288	1,699	433	607	1,429	1,697	1,947	3,547
1min	40	517	2,233	926	28	1,780	2,206	2,588	9,903
1min	80	468	2,299	908	547	1,733	2,180	2,795	9,043
2min	20	456	2,055	657	502	1,641	2,043	2,441	5,337
4min	20	291	2,339	617	709	1,936	2,281	2,735	4,369
8min	20	318	3,509	1,471	703	2,262	3,284	4,668	8,817
2min	40	719	2,313	775	499	1,786	2,332	2,762	5,461
4min	40	373	2,804	1,245	507	2,050	2,598	3,330	8,807
8min	40	539	5,054	2,587	1,276	3,153	4,371	6,438	15,777
2min	80	495	2,952	1,217	612	2,147	2,810	3,645	10,853
4min	80	1095	3,077	1,434	863	2,286	2,793	3,529	20,169
8min	80	421	6,190	4,191	1,246	3,711	4,445	7,223	26,341

D.4.1. NCT Crystallite Size Distributions as a Function of Cooling Rate

Figure D.8: (A-C) SEM images of NCTs crystallized with a cooling rate of 1 second per 0.1 °C and a concentration of 20 nM. Scale bar is 5 microns. (D) Histogram of crystallite sizes with a Gaussian fit.
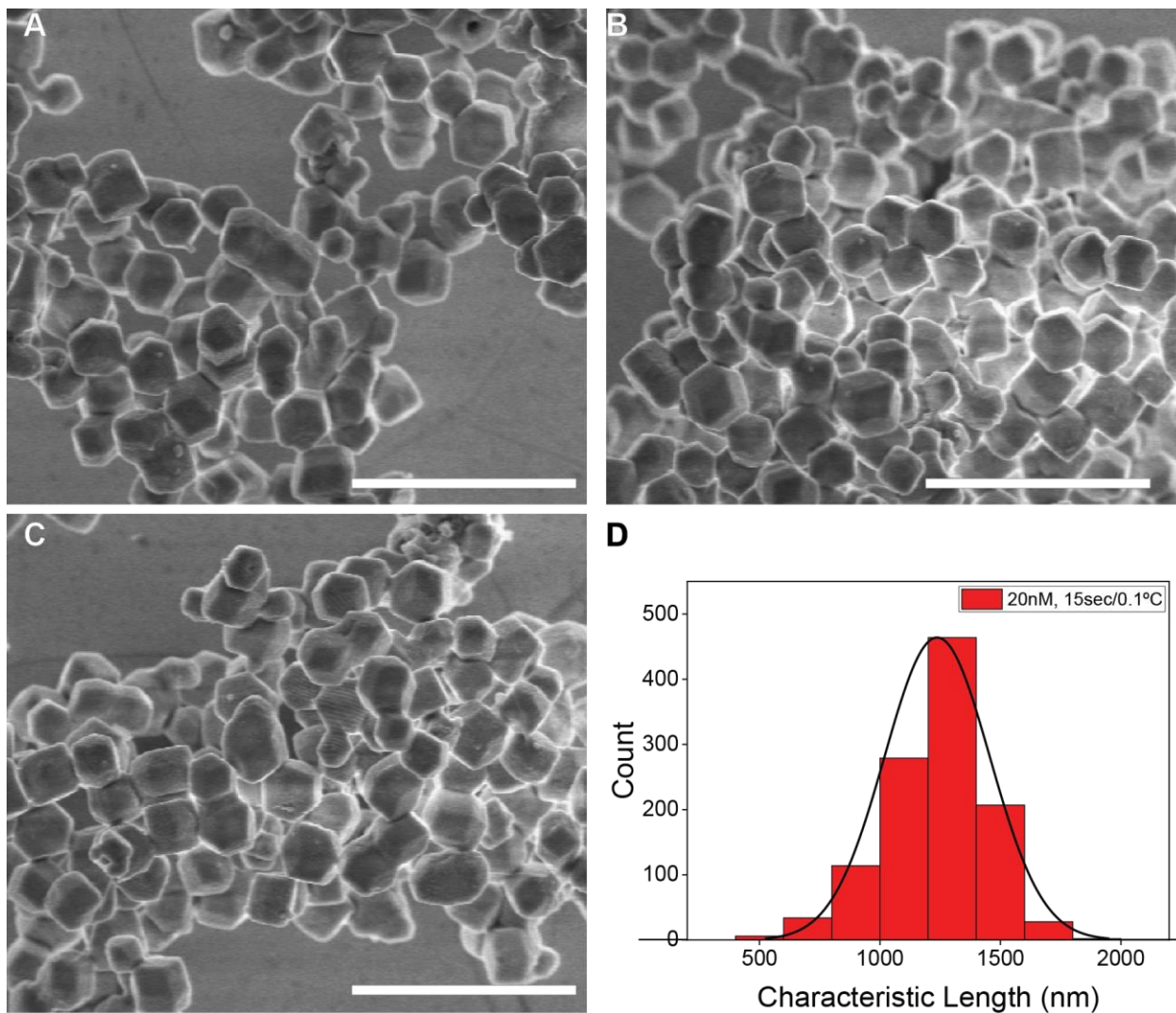
Figure D.9: (A-C) SEM images of NCTs crystallized with a cooling rate of 15 seconds per 0.1 ℃ and a concentration of 20 nM. Scale bar is 5 microns. (D) Histogram of crystallite sizes with a Gaussian fit.

Figure D.10: (A-C) SEM images of NCTs crystallized with a cooling rate of 30 seconds per 0.1 °C and a concentration of 20 nM. Scale bar is 5 microns. (D) Histogram of crystallite sizes with a Gaussian fit.
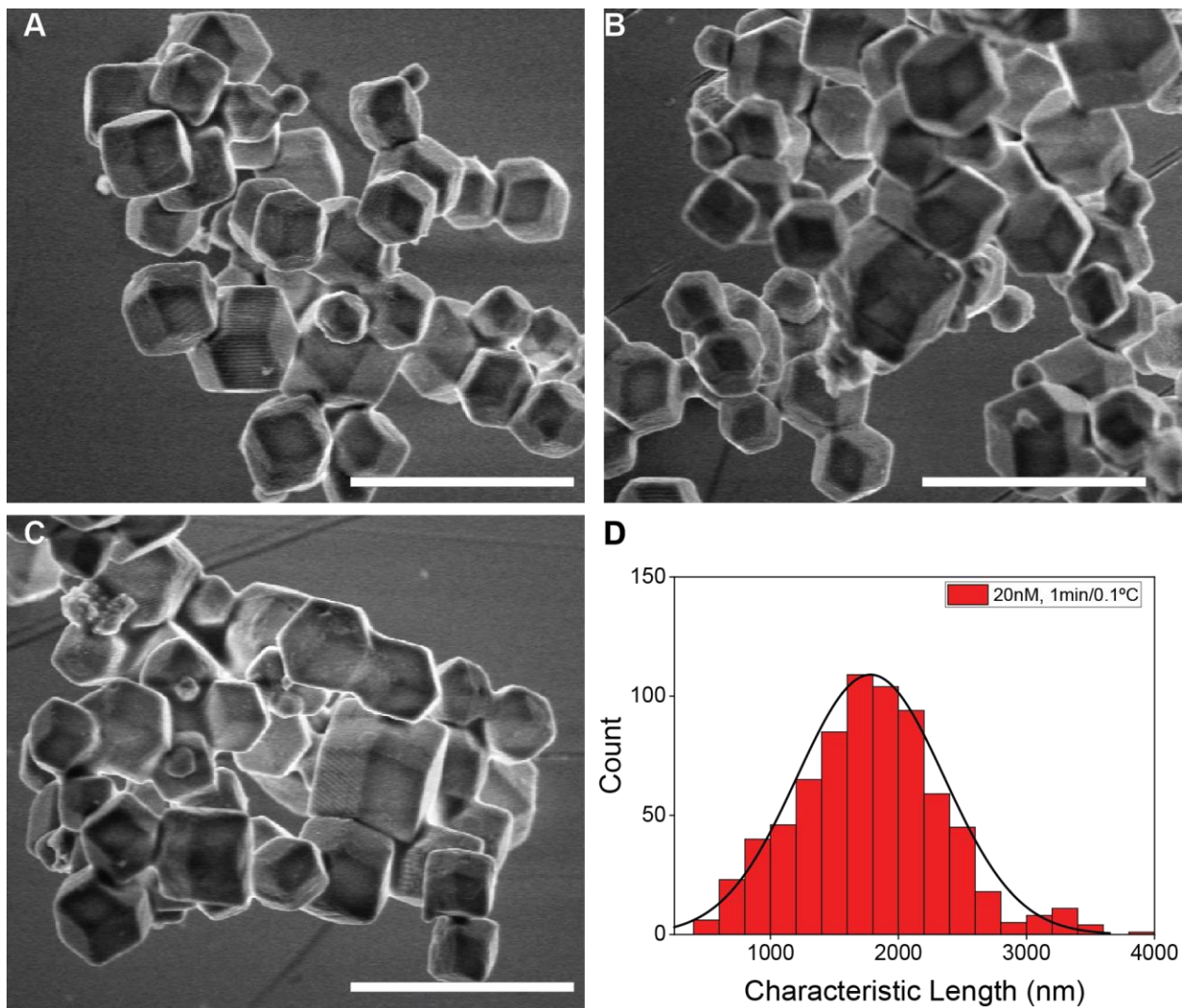
Figure D.11: (A-C) SEM images of NCTs crystallized with a cooling rate of 1 minute per 0.1 °C and a concentration of 20 nM. Scale bar is 5 microns. (D) Histogram of crystallite sizes with a Gaussian fit.
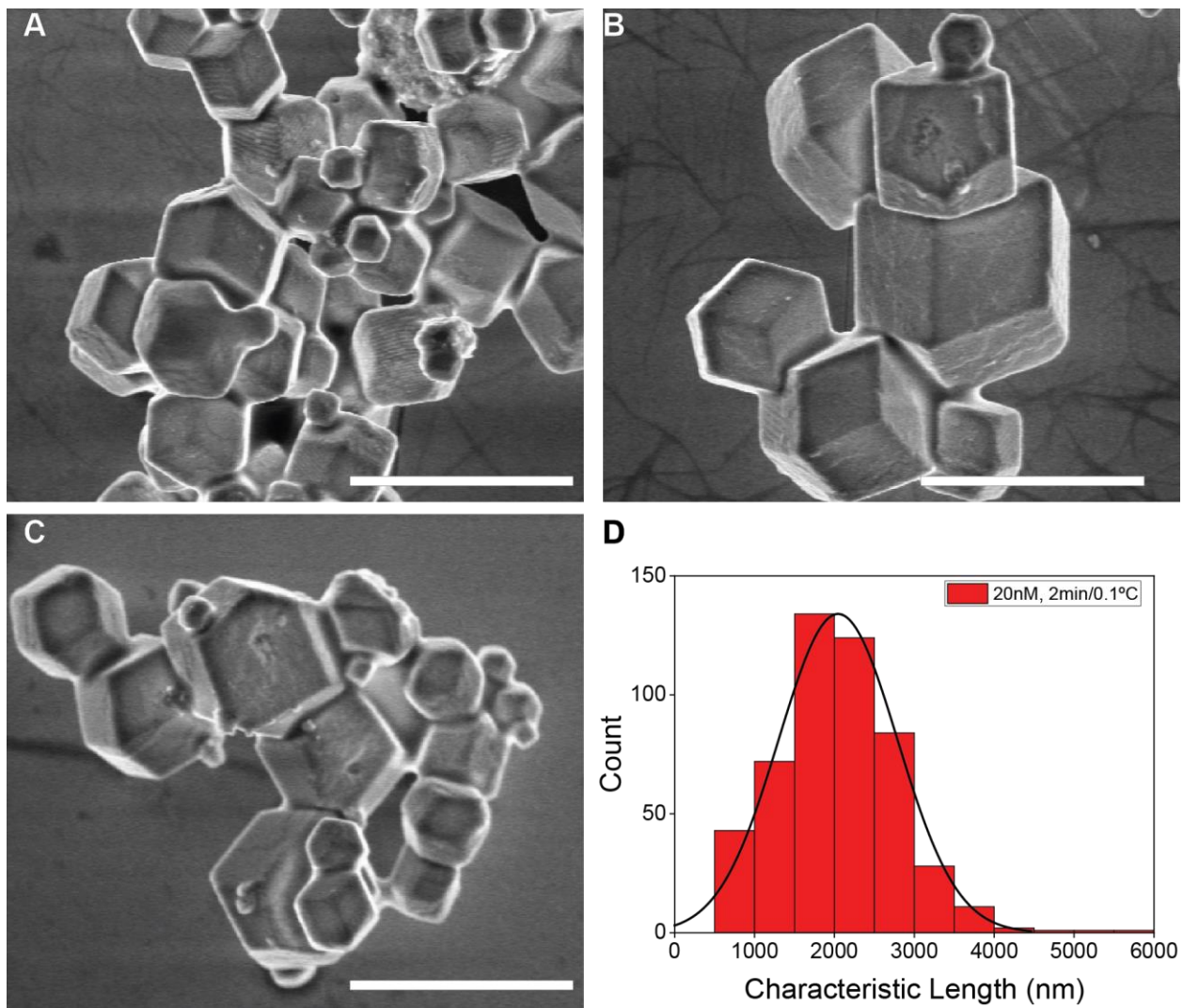
Figure D.12: (A-C) SEM images of NCTs crystallized with a cooling rate of 2 minutes per 0.1 ℃ and a concentration of 20 nM. Scale bar is 5 microns. (D) Histogram of crystallite sizes with a Gaussian fit.
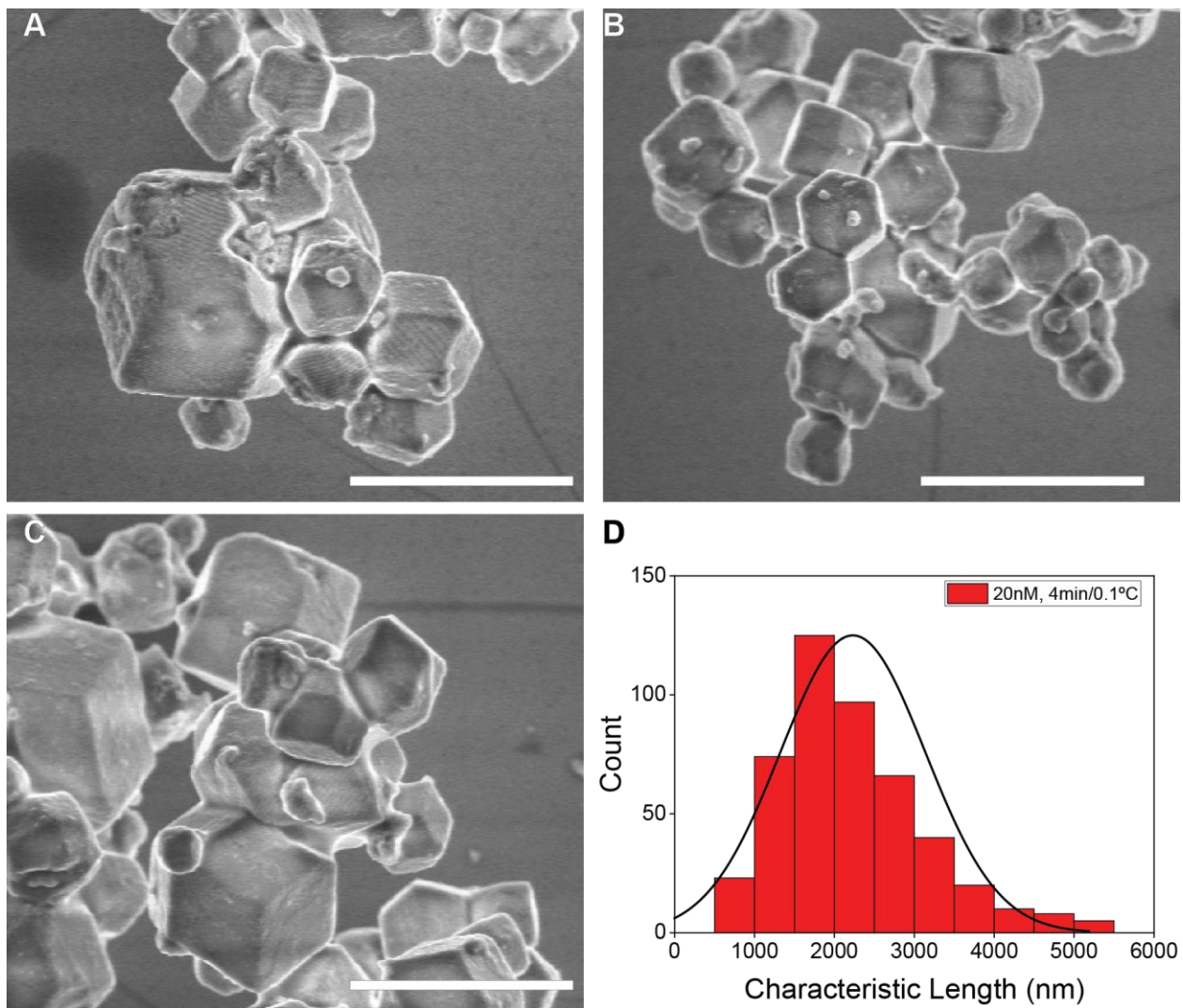
Figure D.13: (A-C) SEM images of NCTs crystallized with a cooling rate of 4 minutes per 0.1 ℃ and a concentration of 20 nM. Scale bar is 5 microns. (D) Histogram of crystallite sizes with a Gaussian fit.
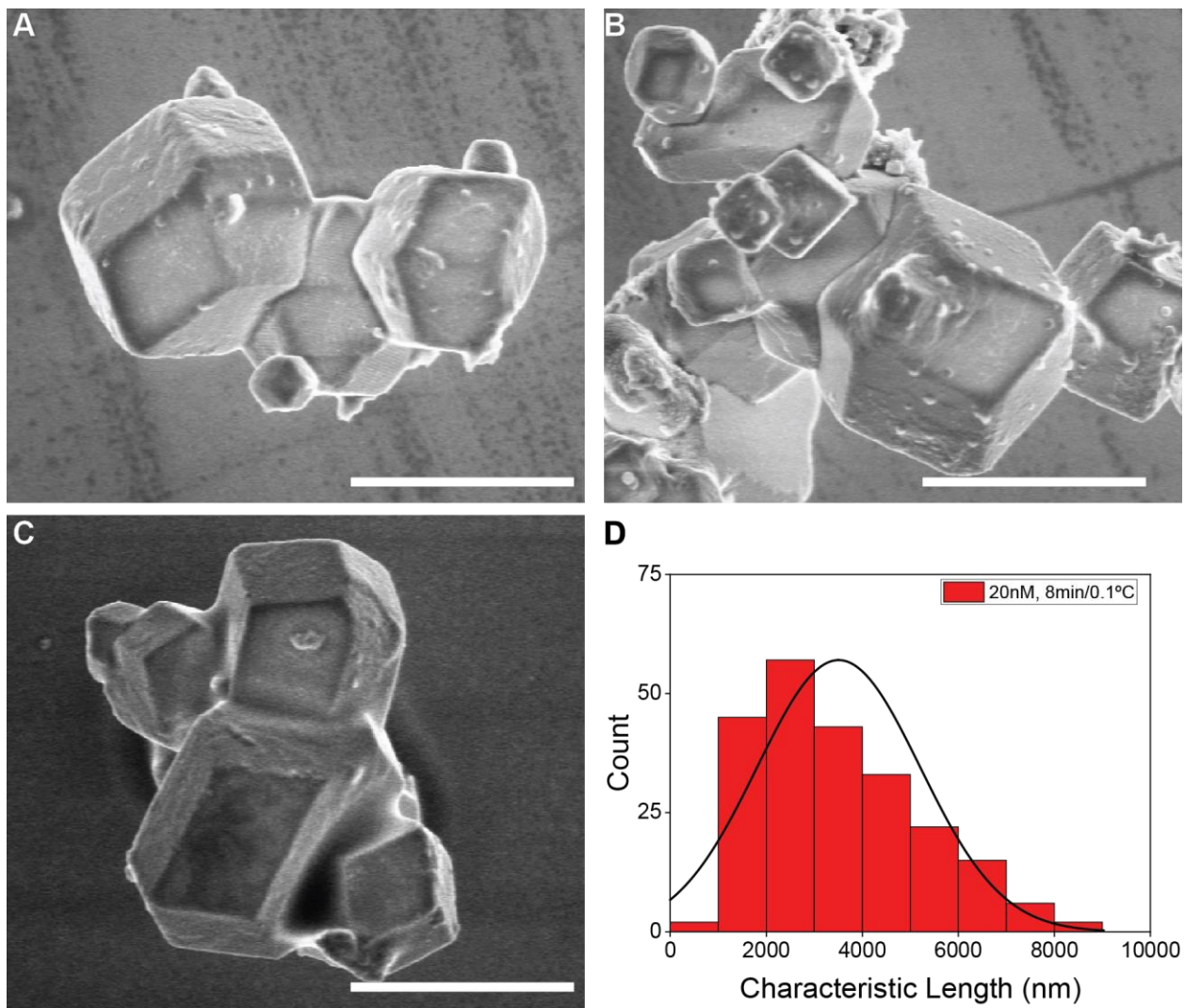
Figure D.14: (A-C) SEM images of NCTs crystallized with a cooling rate of 8 minutes per 0.1 ℃ and a concentration of 20 nM. Scale bar is 5 microns. (D) Histogram of crystallite sizes with a Gaussian fit.

D.4.2. NCT Crystallite Size Distributions as a Function of Concentration
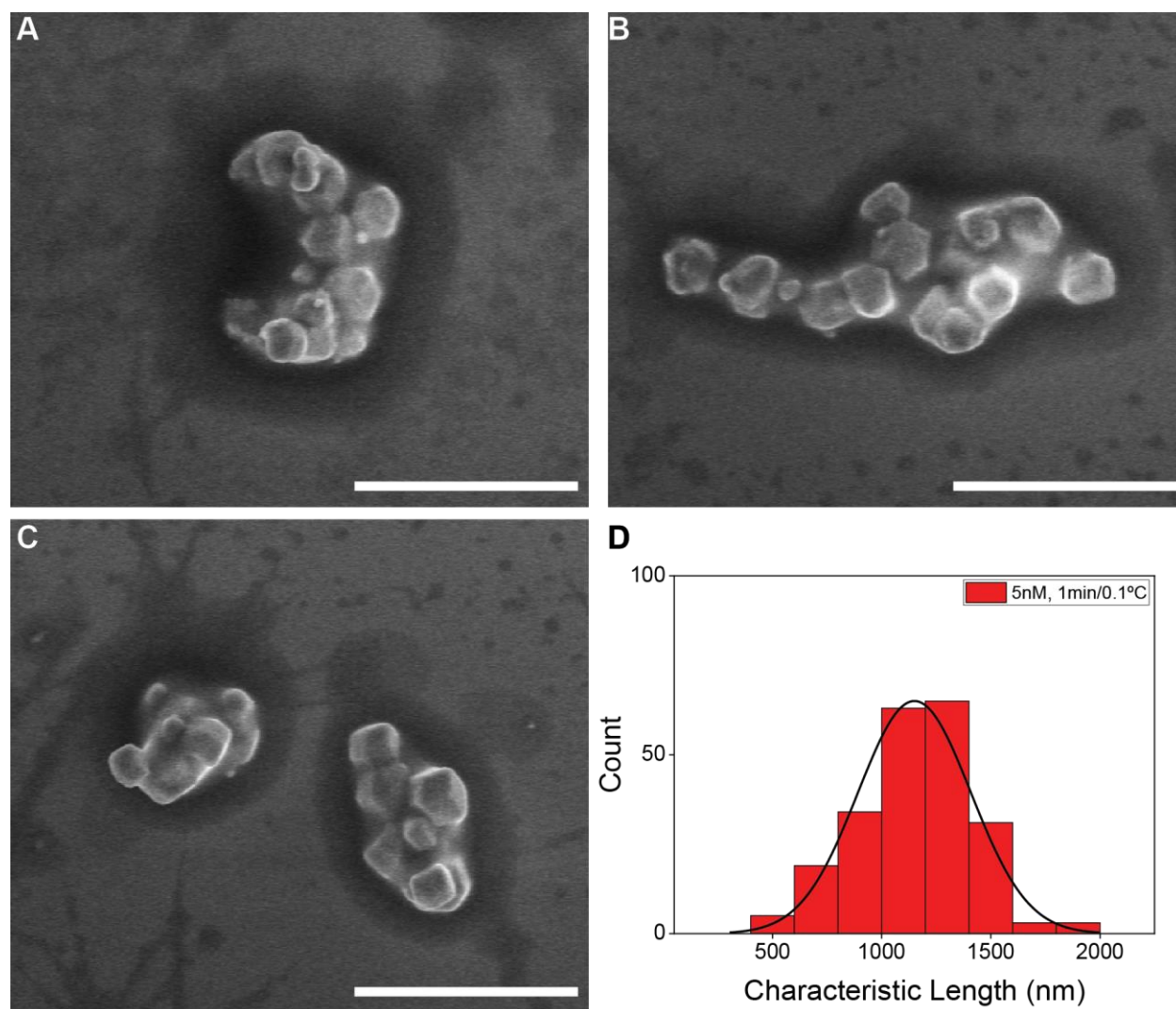
Figure D.15: (A-C) SEM images of NCTs crystallized with a cooling rate of 1 minute per 0.1 °C and a concentration of 5 nM. Scale bar is 5 microns. (D) Histogram of crystallite sizes with a Gaussian fit.
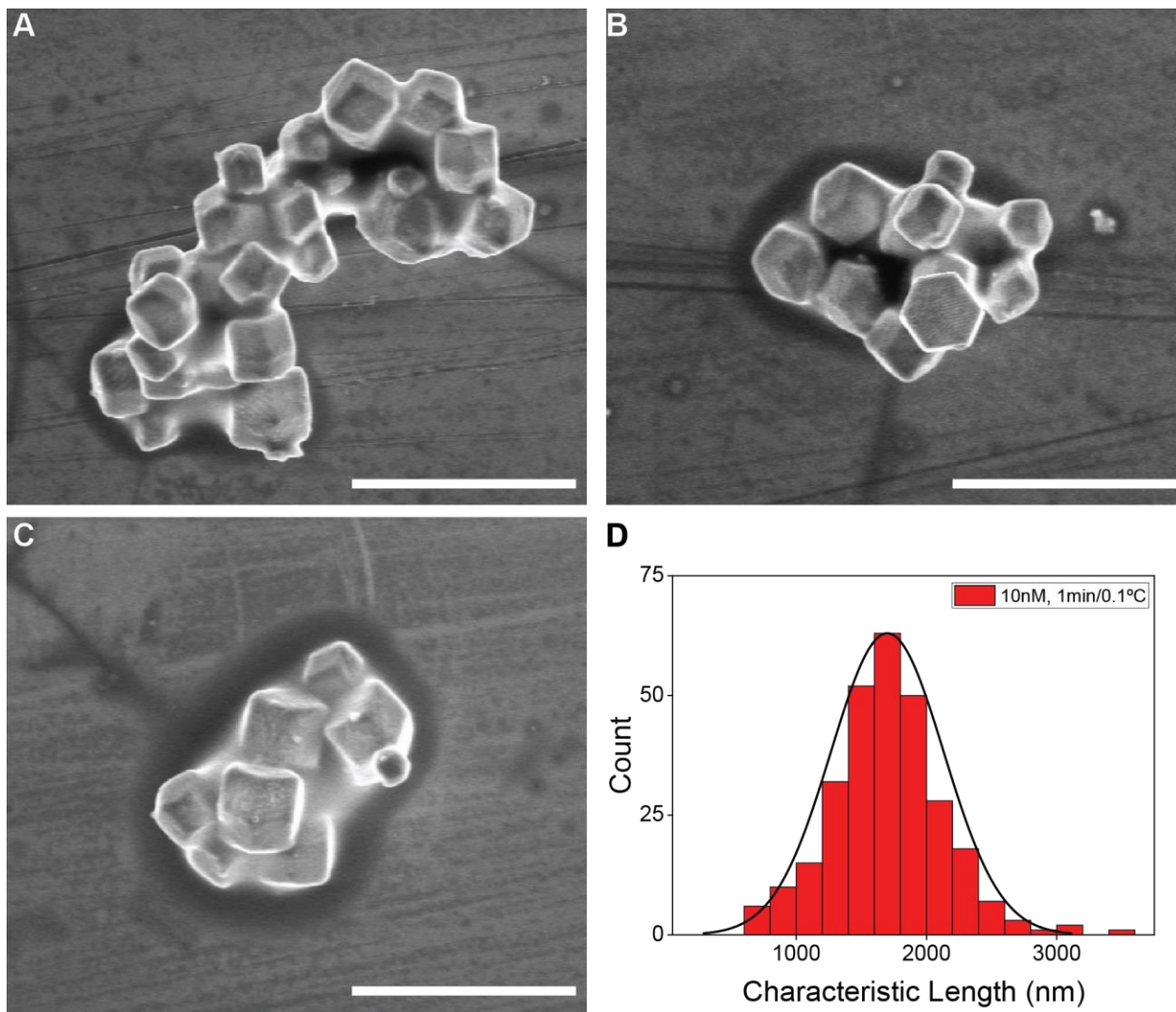
Figure D.16: (A-C) SEM images of NCTs crystallized with a cooling rate of 1 minute per 0.1 °C and a concentration of 10 nM. Scale bar is 5 microns. (D) Histogram of crystallite sizes with a Gaussian fit.
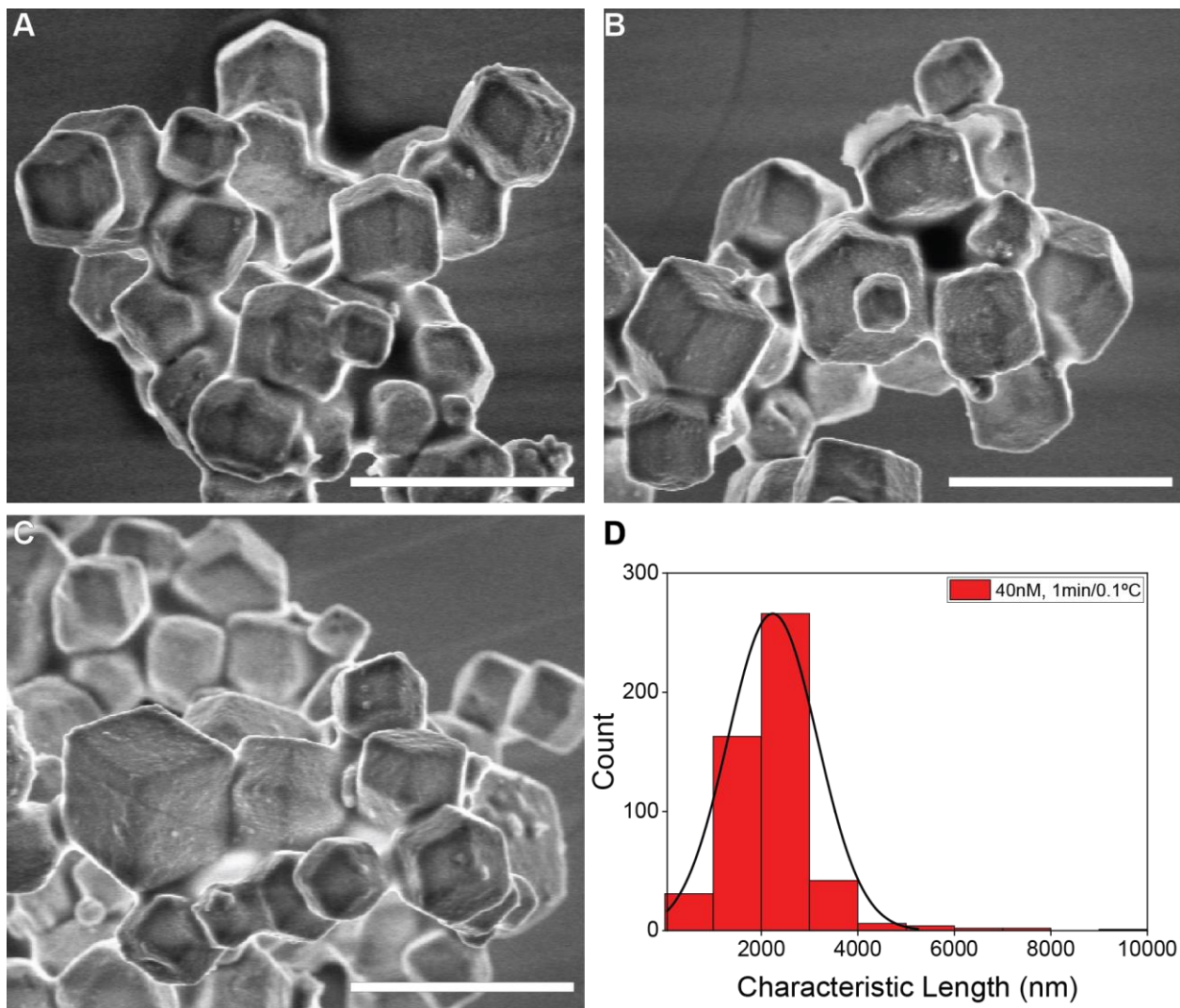
Figure D.17: (A-C) SEM images of NCTs crystallized with a cooling rate of 1 minute per 0.1 ℃ and a concentration of 40 nM. Scale bar is 5 microns. (D) Histogram of crystallite sizes with a Gaussian fit.
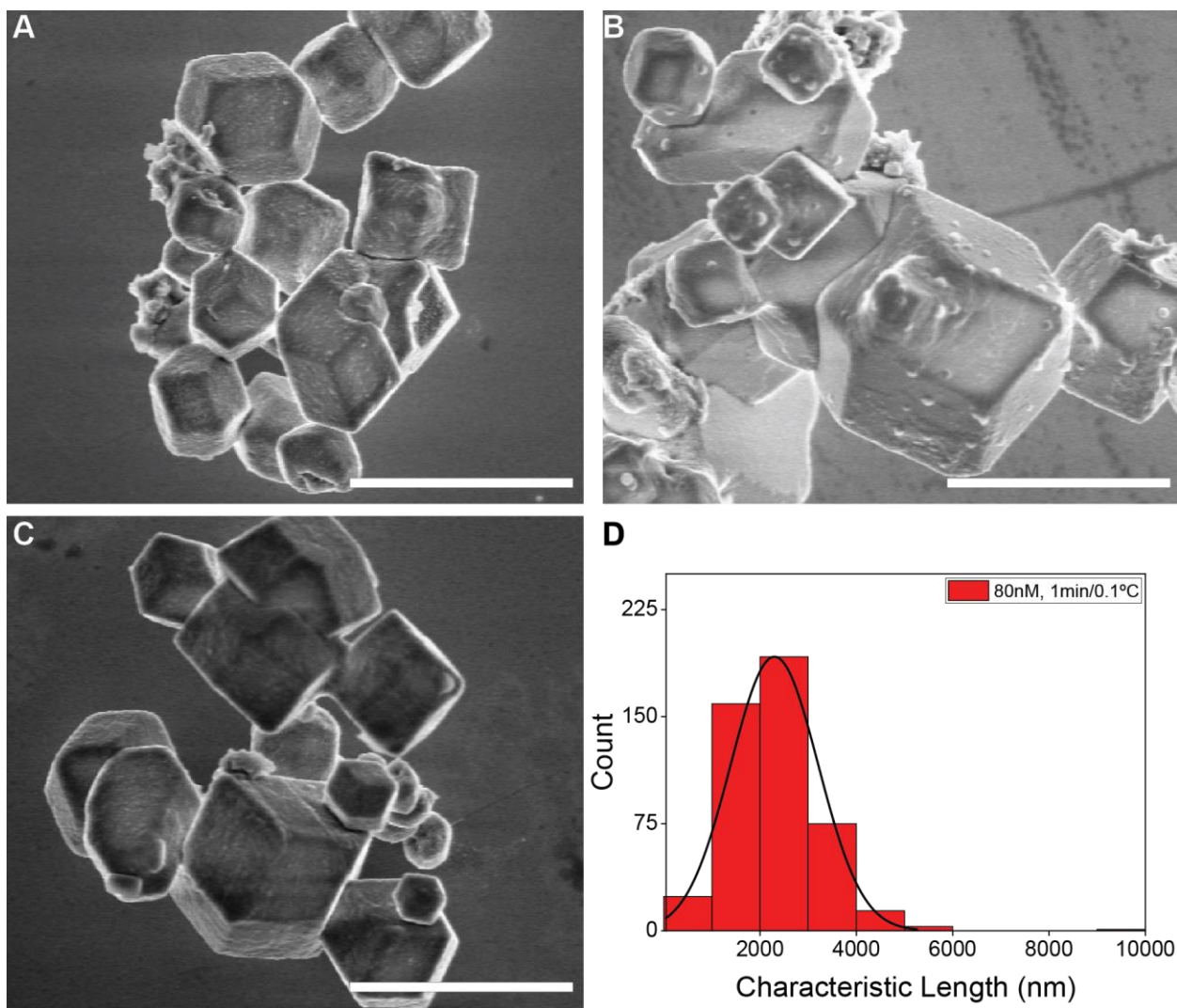
Figure D.18: (A-C) SEM images of NCTs crystallized with a cooling rate of 1 minute per 0.1 °C and a concentration of 80 nM. Scale bar is 5 microns. (D) Histogram of crystallite sizes with a Gaussian fit.

D.4.3. NCT Crystallite Size Distributions as a Function of Both Higher Concentration and Slower Cooling Rates
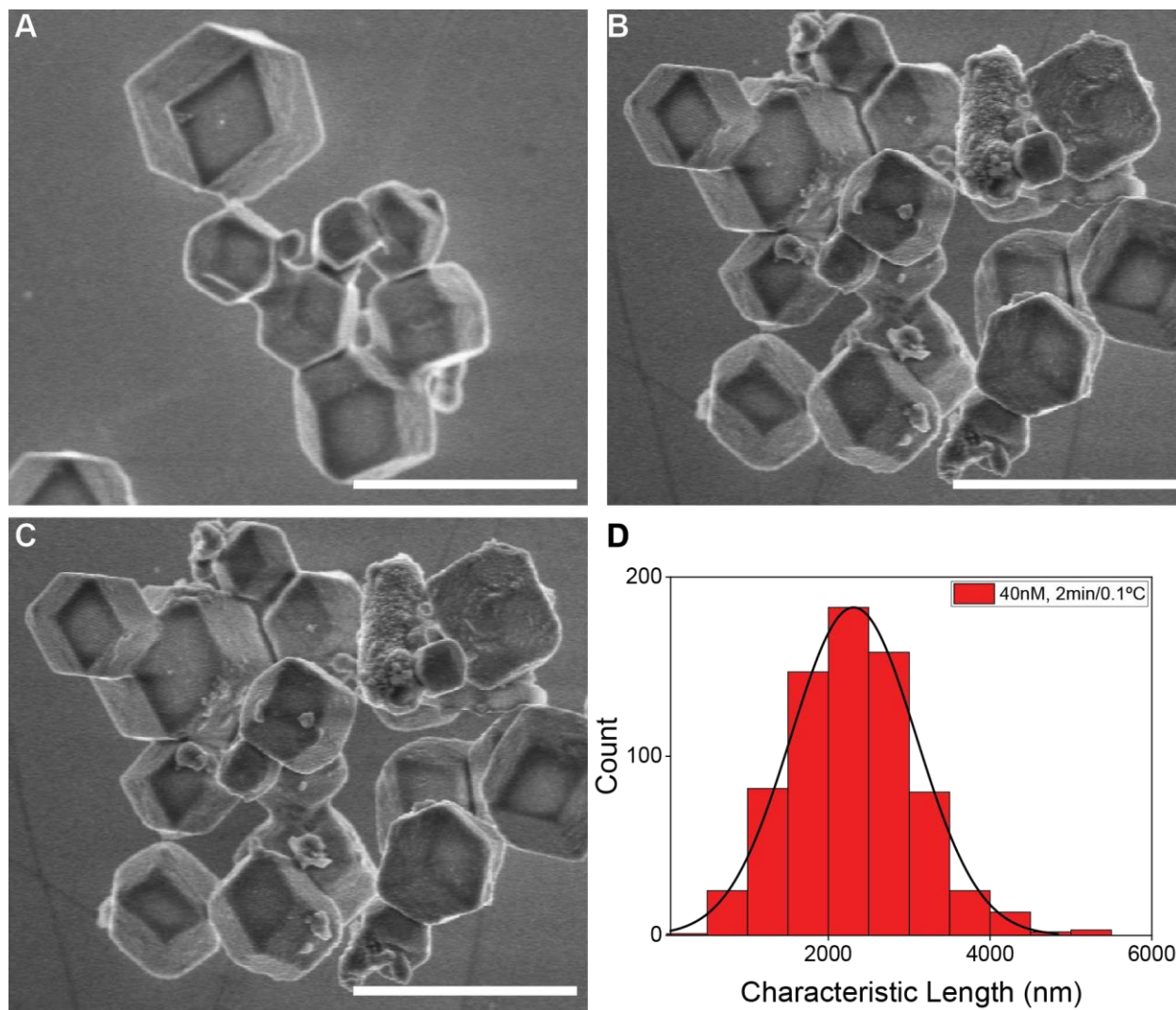
Figure D.19: (A-C) SEM images of NCTs crystallized with a cooling rate of 2 minute per 0.1 ℃ and a concentration of 40 nM. Scale bar is 5 microns. (D) Histogram of crystallite sizes with a Gaussian fit.
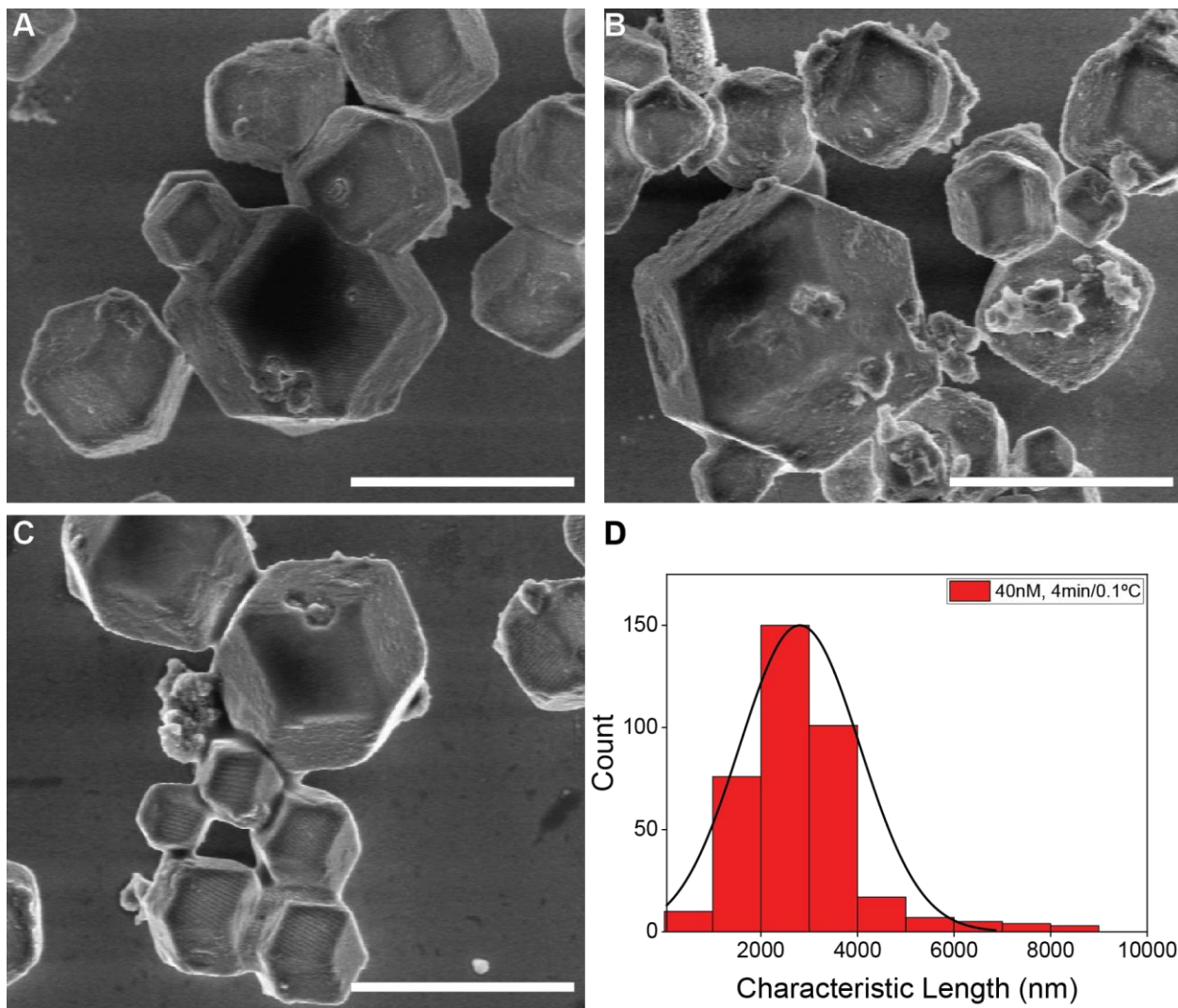
Figure D.20: (A-C) SEM images of NCTs crystallized with a cooling rate of 4 minute per 0.1 °C and a concentration of 40 nM. Scale bar is 5 microns. (D) Histogram of crystallite sizes with a Gaussian fit.
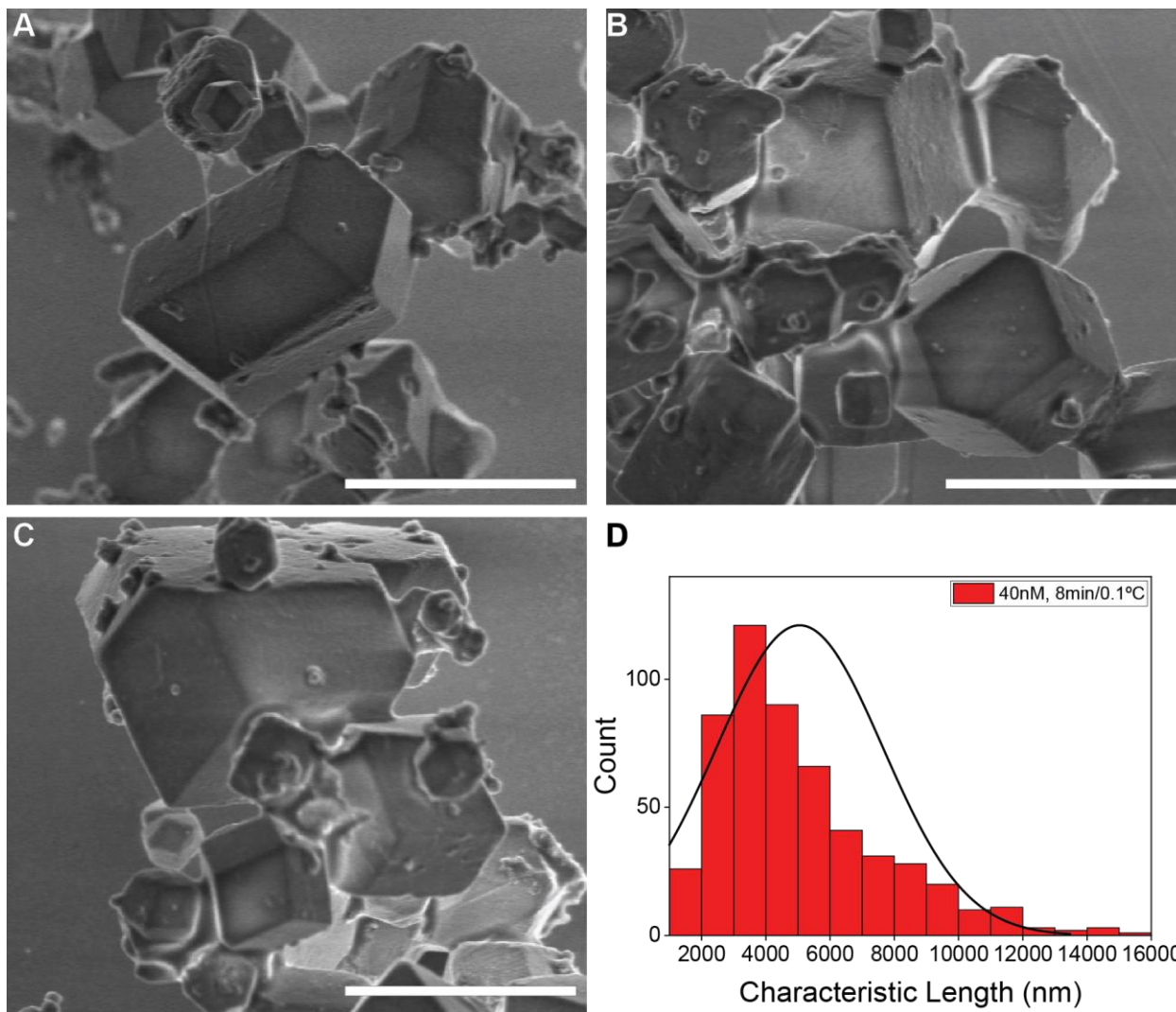
Figure D.21: (A-C) SEM images of NCTs crystallized with a cooling rate of 8 minute per 0.1 ℃ and a concentration of 40 nM. Scale bar is 10 microns. (D) Histogram of crystallite sizes with a Gaussian fit.
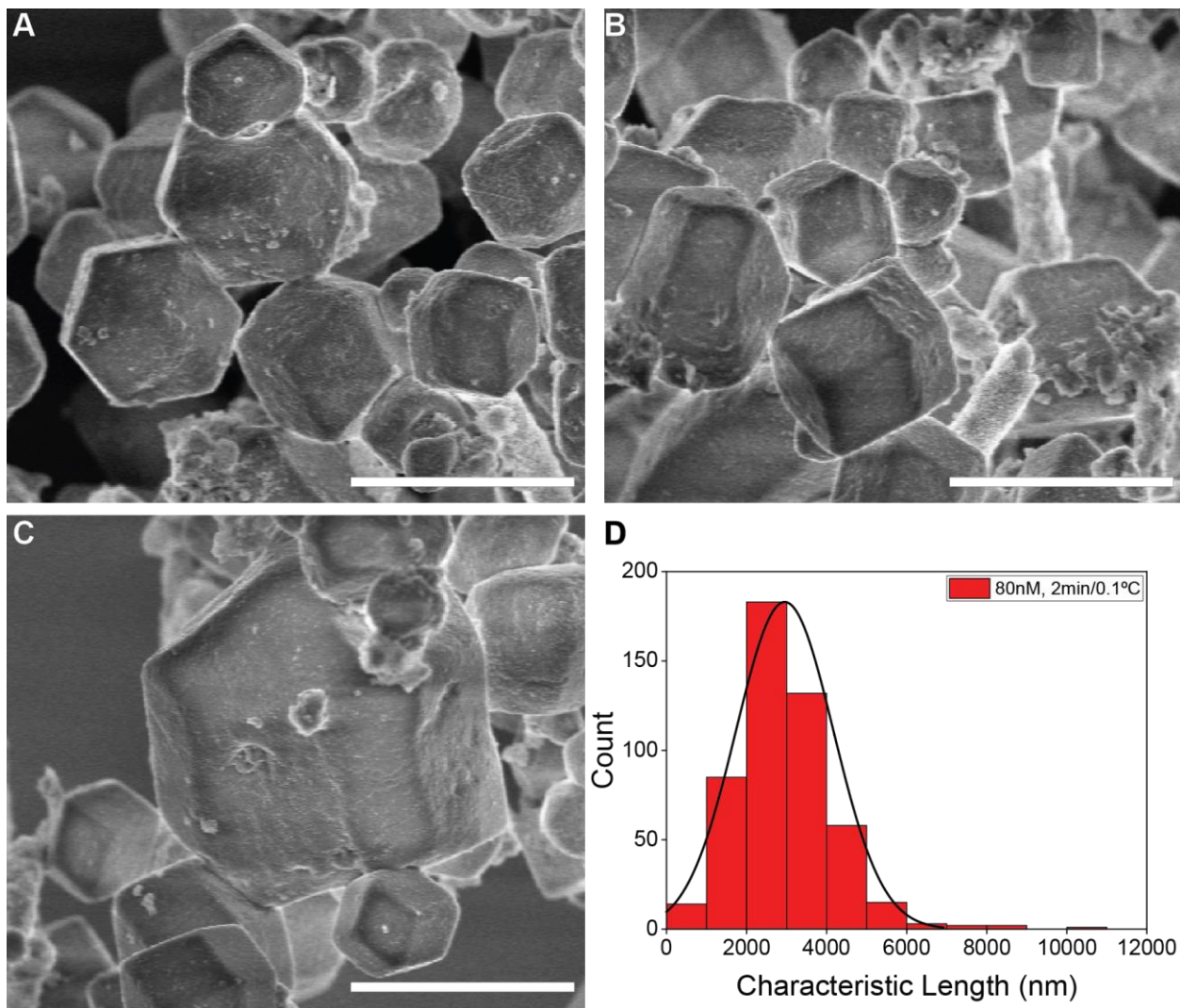
Figure D.22: (A-C) SEM images of NCTs crystallized with a cooling rate of 2 minute per 0.1 °C and a concentration of 80 nM. Scale bar is 5 microns. (D) Histogram of crystallite sizes with a Gaussian fit.
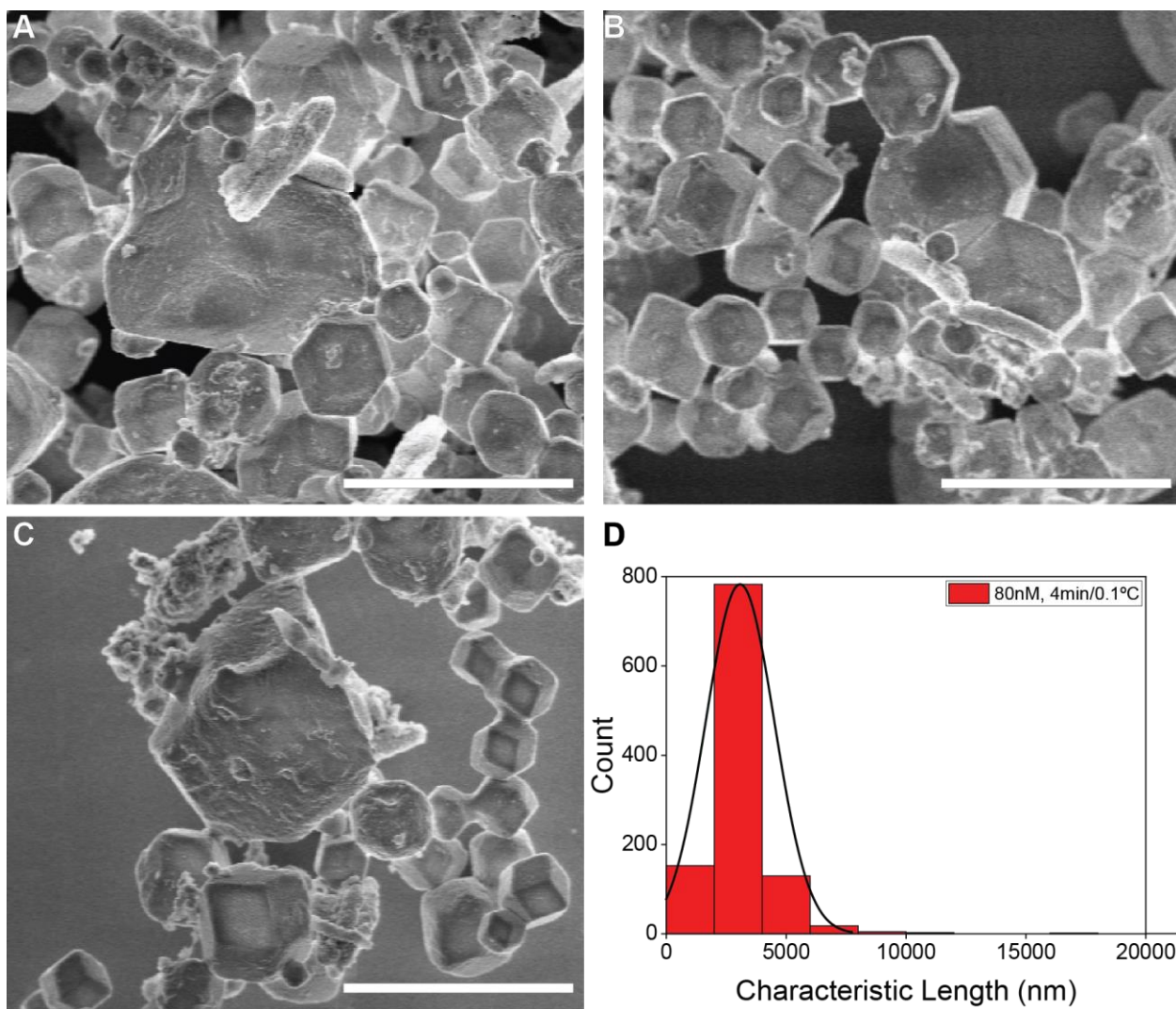
Figure D.23: (A-C) SEM images of NCTs crystallized with a cooling rate of 4 minute per 0.1 ℃ and a concentration of 80 nM. Scale bar is 10 microns. (D) Histogram of crystallite sizes with a Gaussian fit.
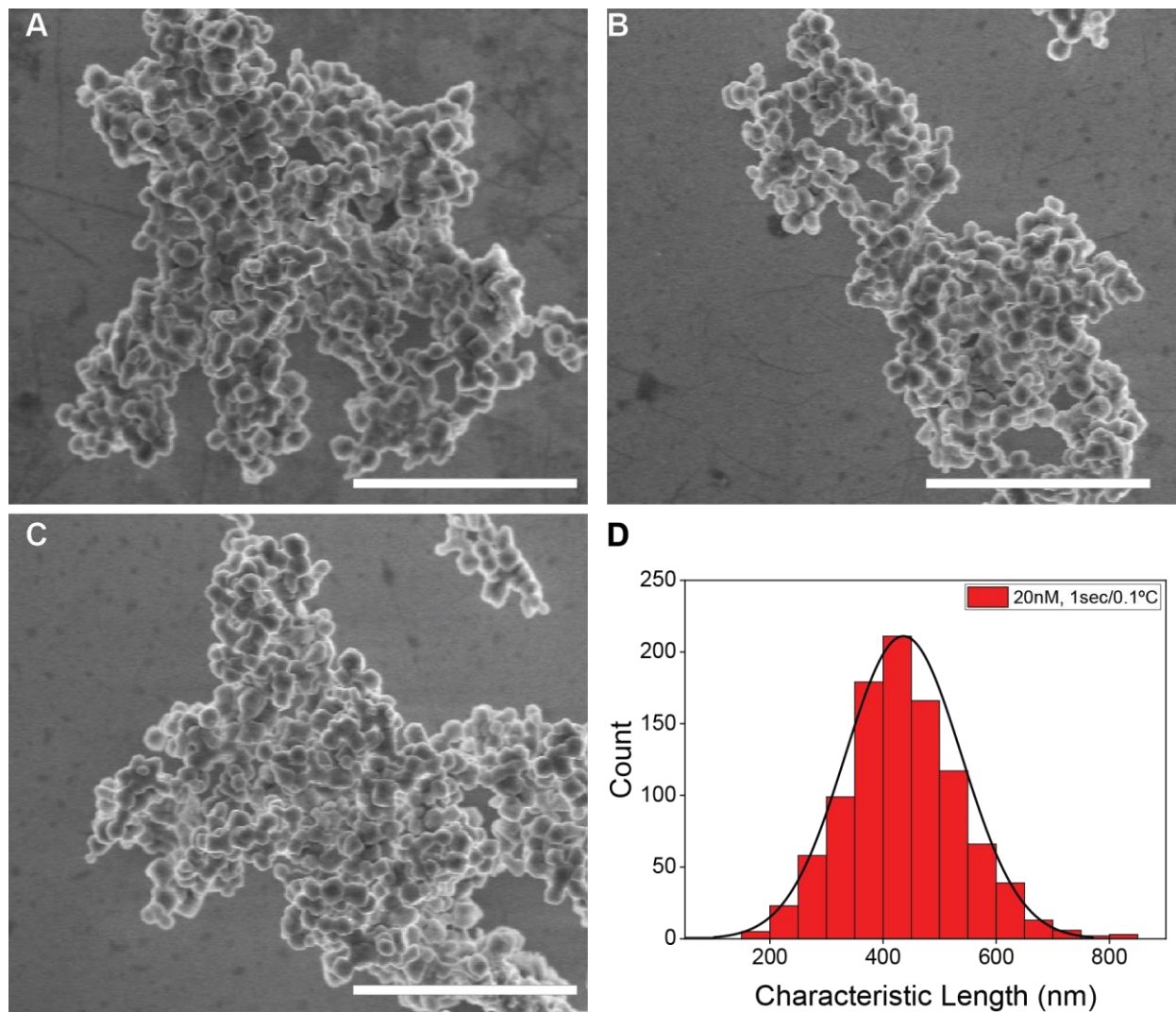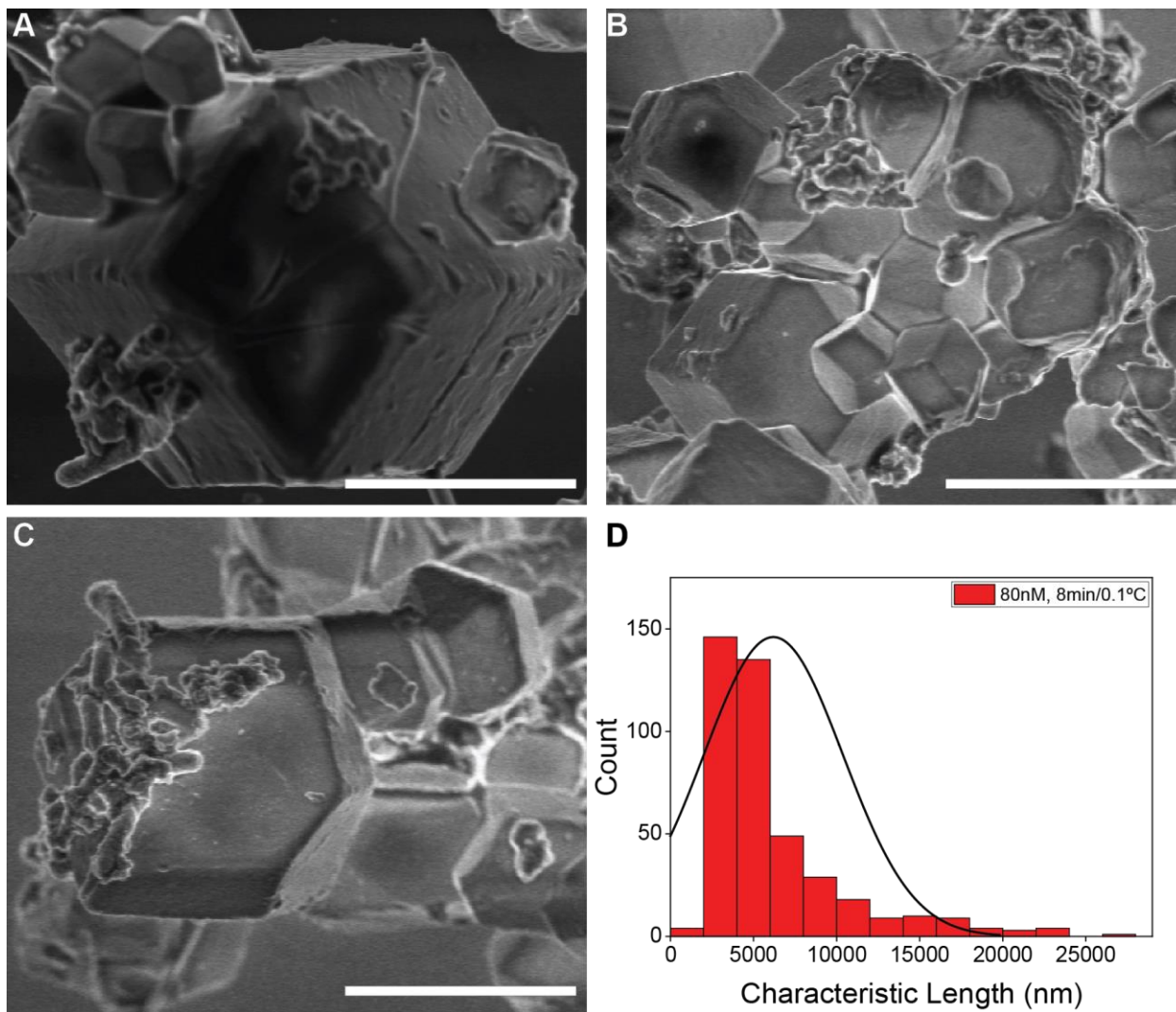
Figure D.24: (A-C) SEM images of NCTs crystallized with a cooling rate of 8 minute per 0.1 °C and a concentration of 80 nM. Scale bar is 10 microns. (D) Histogram of crystallite sizes with a Gaussian fit.
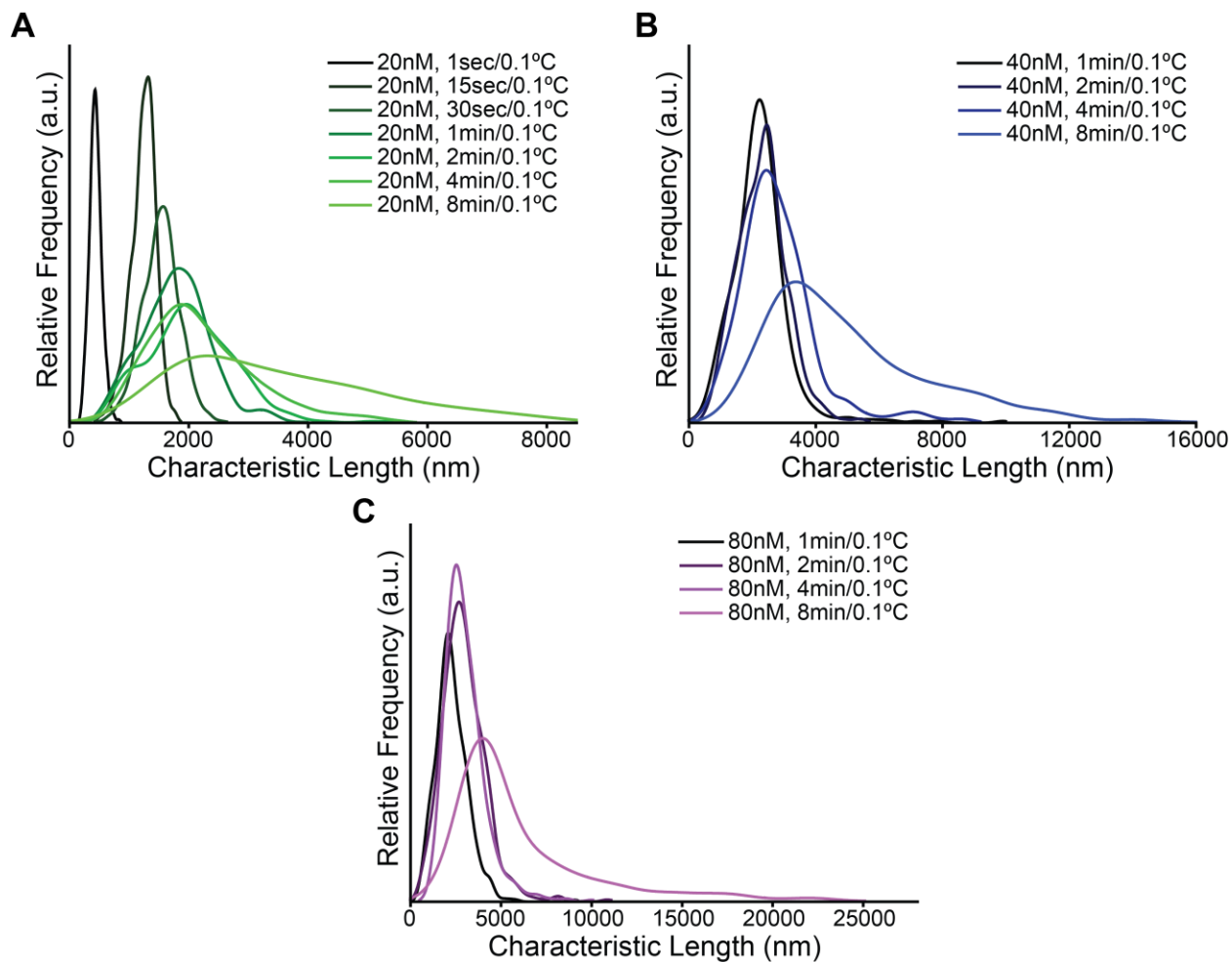
Figure D.25: Size distribution comparisons as a function of cooling rate^{-1} for samples with NCT concentration of (A) 20 nM, (B) 40 nM, and (C) 80 nM.
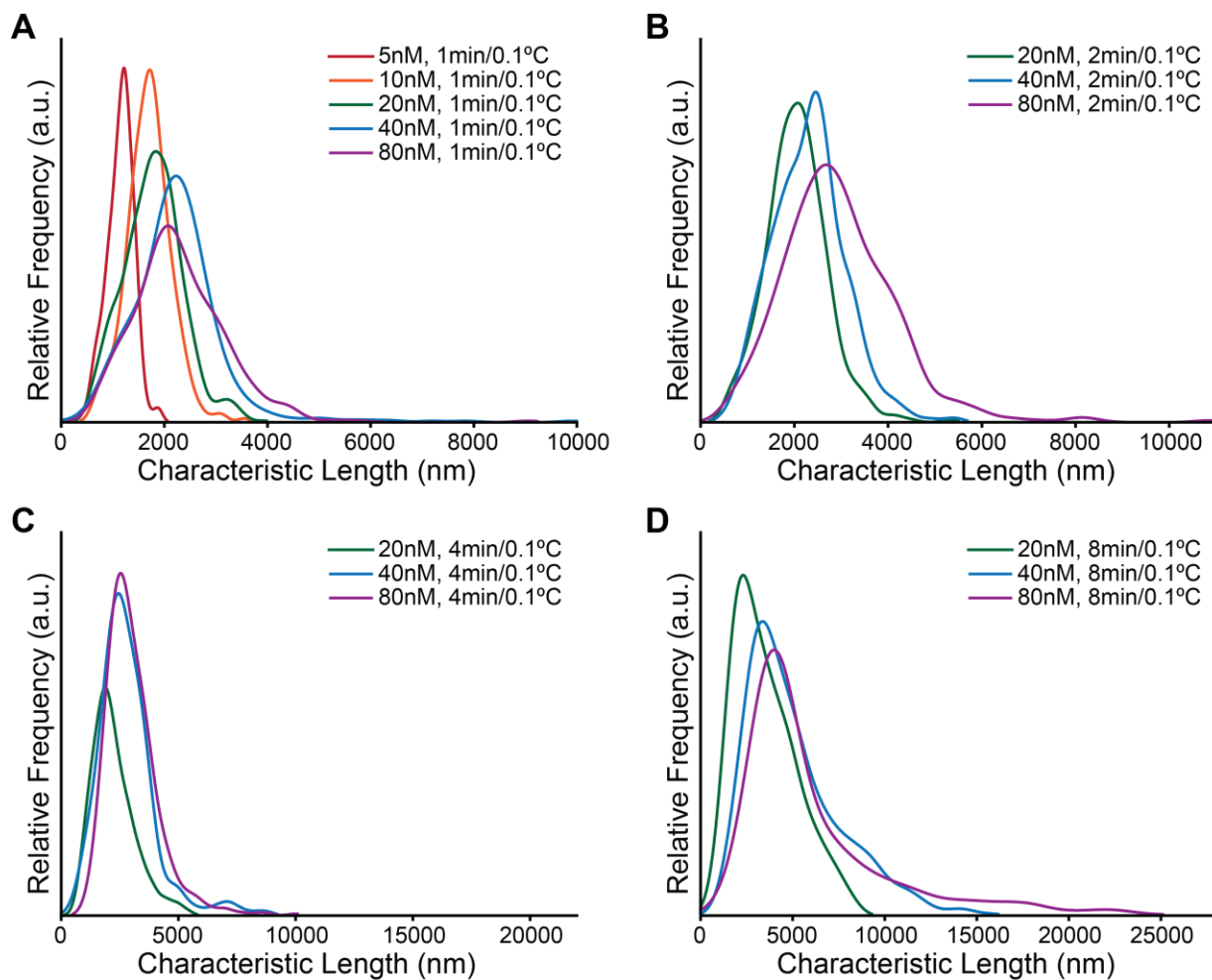
Figure D.26: Size distribution comparisons as a function of NCT concentration for samples with cooling rate^{-1} of (A) 1min/0.1°C, (B) 2min/0.1°C, (C) 4min/0.1°C, and (D) 8min/0.1°C.

Upon determining that the 80nM, 8min/0.1°C condition yielded the largest average size crystallites, the sample was searched for its largest crystallites. These crystallites were not included in the size analysis, which consisted of randomly selected regions to image. However, the SEM micrographs of the largest three observed crystallites are included in Figure D.27 for reference.
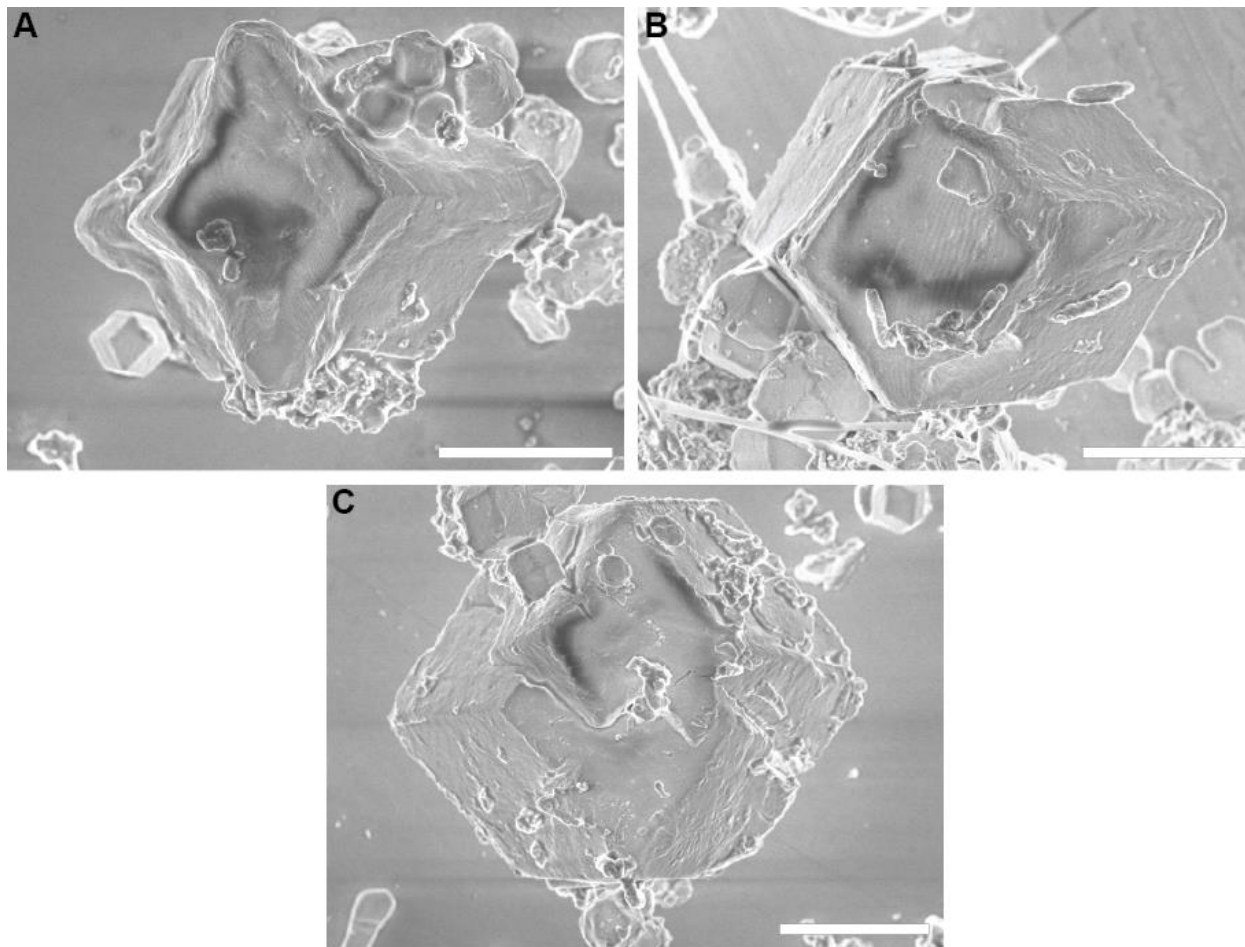
Figure D.27: SEM micrographs of the three largest observed NCT crystallites (all from the conditions of 80nM and 8min/0.1°C) with diameters of (A) 28 µm, (B) 29.5 µm, and (C) 31 µm. Scale bars are 10 µm.

D.5. Model of NCT Crystallization

D.5.1. Thermodynamics of NCT Assembly

NCTs have multiple weak supramolecular binding groups that collectively form a particle-particle bond. At low temperatures, the nanoparticles form bonds and aggregate together, forming solid-like assembled state. At higher temperatures, the bonds between particles break, forming a solute-like state of free particles in solution. Previous work[234] has captured this behavior using a simple model that assumes that particles reach an equilibrium between the "assembled" and "free" state via a unimolecular reaction.

Equation D.4:

$$NCT_a \leftrightarrow NCT_f$$
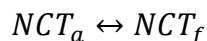
The quantities of assembled NCTs A and free NCTs F must preserve the total number of particles P

Equation D.5:

$$A + F = P$$

At equilibrium, the quantities of assembled NCTs A and free NCTs F are also related by the temperature-dependent thermodynamic relation

Equation D.6:

$$\frac{A}{F} = K = K_0 e^{-\frac{\Delta H}{RT}}$$

The quantities A and F are then given by

Equation D.7:

$$F = \frac{P}{1 + K_0 e^{-\frac{\Delta H}{RT}}}$$

Equation D.8:

$$A = \frac{P}{1 + \frac{1}{K_0 e^{-\frac{\Delta H}{RT}}}}$$

This melt may be monitored using UV-vis data at varying temperatures by assuming particles in the assembled state have an effective extinction coefficient of ϵ_a and particles in the

free state have an extinction coefficient of ϵ_f, such that the sample absorptivity may be calculated using the Beer-Lambert law:

Equation D.9:

$$\alpha_{total} = \epsilon_a * A + \epsilon_f * F$$

Equation D.10:

$$\alpha_{total} = P \frac{\epsilon_a * K_0 e^{-\frac{\Delta H}{RT}} + \epsilon_f}{1 + K_0 e^{-\frac{\Delta H}{RT}}}$$

Equation D.11:

$$\alpha_{normalized} = \frac{\alpha_{total} - \epsilon_a P}{\epsilon_f P - \epsilon_a P} = \frac{1}{1 + K_0 e^{-\frac{\Delta H}{RT}}}$$

This model allows for simple estimation of the enthalpy of the interparticle bonds while accurately capturing several key features of the NCT melt curve: not only the sigmoidal transition from assembled to free particle states, but also the proportional dependence on concentration of the total particle count, allowing for consistent normalized absorptivity curves at varying concentrations (Figure D.28). This is inconsistent with conventional transitions from the solid phase to a dissolved state; in conventional systems, a solid will dissolve up to a maximum saturation concentration regardless of the quantity of excess solid present, and additional solid material will remain in the solid form rather than dissolving. Instead, for the NCT system, increasing the amount of assembled NCTs in the system will proportionally increase the amount free NCTs in solution, and assembled NCTs added to a system at equilibrium will not remain assembled, but will partially dissociate. To account for this, we propose that NCTs in this "melting window" region behave analogously to a flocculated aggregate, with a thermodynamically determined distribution of aggregate sizes in lieu of a thermodynamically determined solubility in equilibrium with an assembled state.
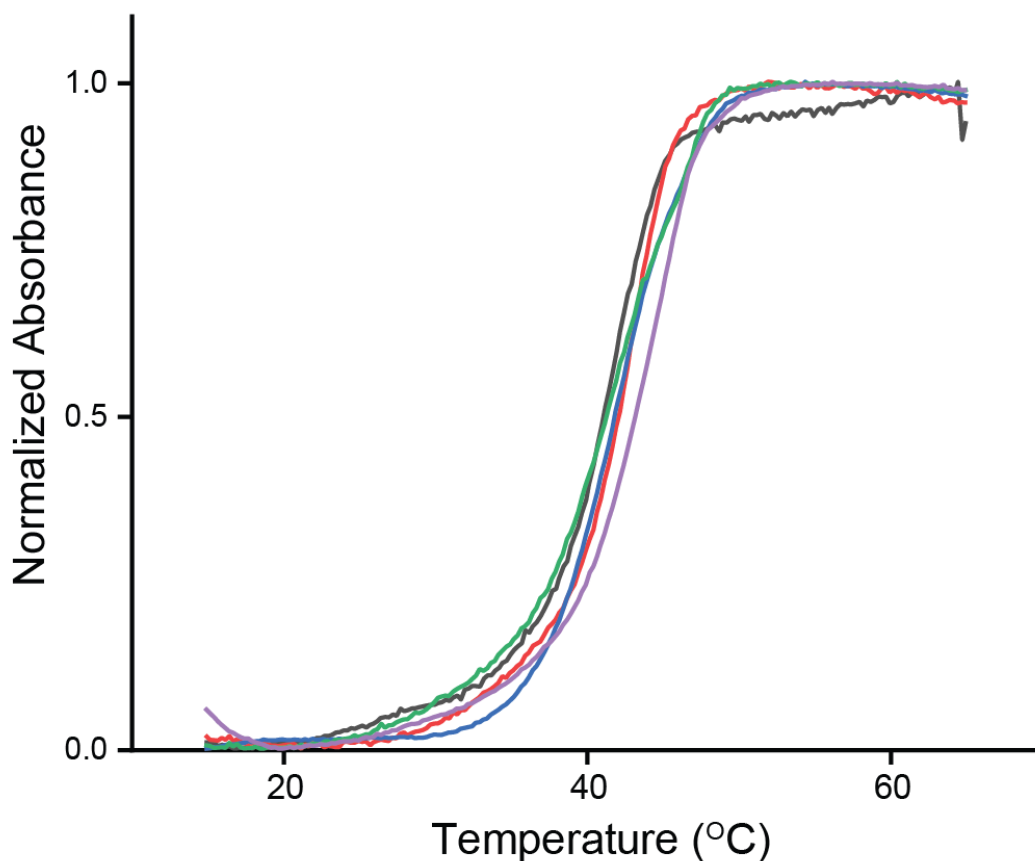
Figure D.28: Melt curves of 5 separate batches of Au-NCTs. Each experiment was performed at a different concentration, but the curves can be normalized independent of the total particle number due to the proportionality between assembled and free species.

D.5.2. Cluster Behavior of NCTs

In conventional crystallizing processes, components are initially fully dissolved in solution below the saturation concentration. Nucleation of crystals is initiated when the system transitions from an unsaturated state (in which all components are dissolved) into a supersaturated state, such as by evaporating solvent (which increases the solute concentration in the remaining solvent) or cooling the system (which lowers the saturation concentration). These nucleated crystals are all approximately the same size: specifically, the minimum size at which the enthalpy of crystallization is sufficient to offset the surface energy penalty. After nucleation, the small crystals continue to grow in the supersaturated solution, until the solvent is no longer supersaturated. The number of nucleation events increases with the amount of supersaturation, so increasing the initial

concentration will increase the number of crystallites formed, rather than increase the final crystallite size. In fact, the increased nucleation will often decrease the final crystallite size, since nucleation rate typically scales nonlinearly with degree of supersaturation.

Since the NCT system does not exhibit saturation behavior, we must instead develop a mechanism for crystal nucleation and growth that accounts for the NCT's clustering behavior. The thermodynamic distribution of NCT clusters may be approximated by replacing the single unimolecular reaction in Equation D.4 into a series of unimolecular reactions between clusters of increasing size:

$$NCT_1 \leftrightarrow NCT_2 \leftrightarrow \cdots \leftrightarrow NCT_n \leftrightarrow NCT_{n+1} \ldots$$
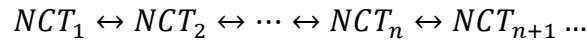
We may approximate the equilibrium constant between clusters as equivalent, since each reaction corresponds to the addition of an identical nanoparticle subunit. This allows us to express P_n, the quantity of nanoparticles in clusters of size n, by the expression:

Equation D.12:

$$\frac{P_{n+1}}{P_n} = K \rightarrow \frac{P_n}{P_1} = K^{n-1}$$

Where P_1 corresponds to the quantity of nanoparticles in clusters of size 1 (i.e. isolated nanoparticles), and K is the equilibrium constant between cluster reactions.

For K<1 (conditions that favor dissociation), this value may be normalized with a sum over all cluster sizes

Equation D.13:

$$P_n = \frac{K^{n-1}}{\sum_{m=1}^{\infty} K^{m-1}} = K^{n-1}(1-K)$$

As expected, larger cluster sizes are favored as K approaches 1, causing the distribution to broaden outwards (Figure D.29, blue curves). However, for K>1, the distribution inverts as larger clusters become thermodynamically preferred, and the distribution is no longer normalizeable (Figure D.29, red curves). This distribution is also nonphysical, as it predicts infinite particles in clusters of infinite size. However, if we truncate the distribution to a maximum cluster size N, such as the total number of particles in the system, the model remains both physical and renormalizeable.

Equation D.14:

$$P_n = \frac{K^{n-1}}{\sum_{m=1}^{m=N} K^{m-1}} = K^{n-1} \frac{1-K}{1-K^N}$$

For K<1, this system reduces to the unbound distribution as $N \to \infty$. For K>1, the cluster population rapidly collapses to the upper bound cluster size. For example, a system with maximum cluster size of 1000 is shown to be highly sensitive to population inversion, with dramatic shift towards clustered state upon equilibrium constant K shifting from 0.99 to 1.01.

This suggests that, in contrast to classical nucleation, there is no metastable barrier to nanoparticle aggregation. When decreasing temperature causes K to increase above 1, the particles are free to smoothly invert their cluster size distribution, and ultimately collapse into the maximum cluster size.
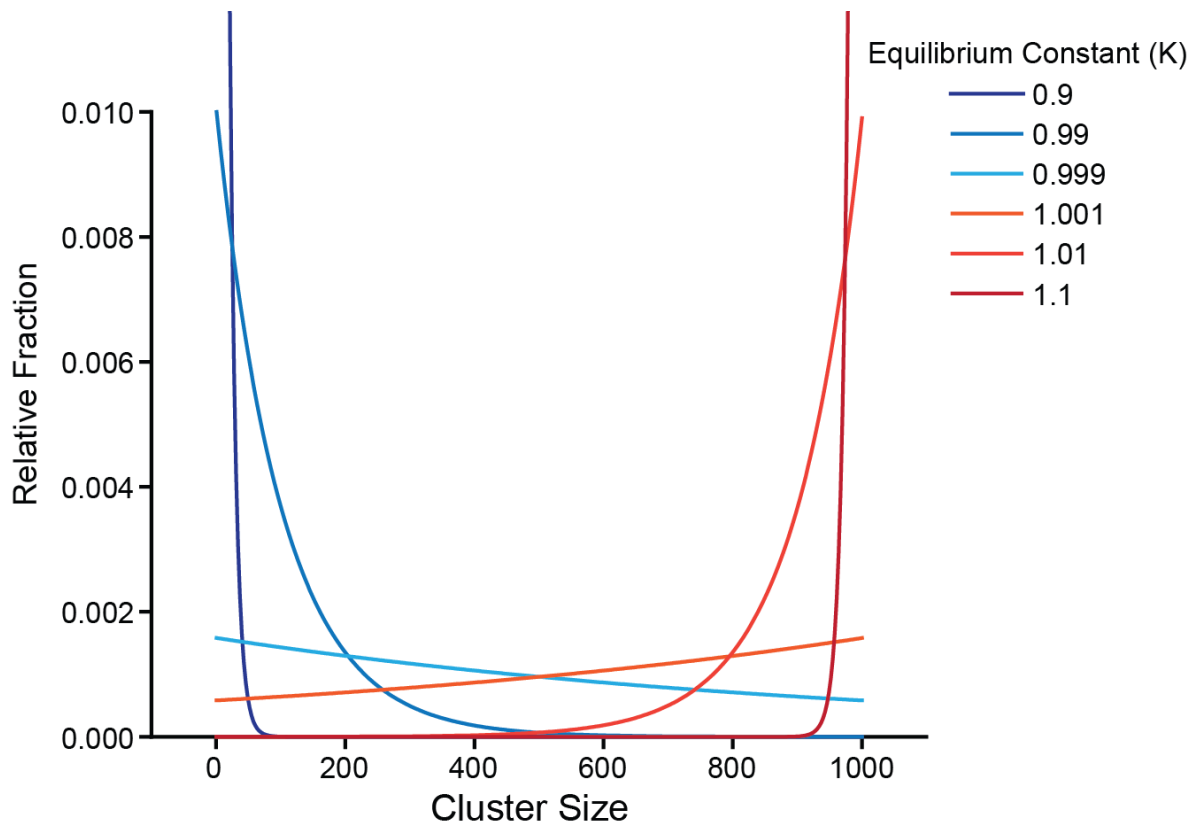
Figure D.29: Effect of the NCT equilibrium constant (K) on cluster size. For values of K below 1 (blue curves), the system strongly tends toward smaller clusters, or entirely free particles.

Conversely, for values of K above 1 (red curves), the distribution rapidly inverts to favor larger aggregates.

To confirm consistency with the observed melt curves, we may estimate the absorptivity of these clusters.

The quantity of we may consider the quantity of clusters of size n

Equation D.15:

$$C_n = \frac{P_n}{n}$$

We may approximate the absorptivity of each cluster size by scaling with the cross-sectional area of the cluster,

Equation D.16:

$$\epsilon_n \sim \epsilon_1 n^{\frac{2}{3}}$$

Then the measured absorptivity α_{total} would be given by the sum of contributions of each cluster size

Equation D.17:

$$\alpha_{Total} = \sum_{n=1}^{\infty} C_n \epsilon_n = \epsilon_1 P \sum_{n=1}^{N} K^{n-1} \left(\frac{1-K}{1-K^N} \right) n^{-\frac{1}{3}}$$

We may compare the normalized absorptivity generated by the cluster kinetic model and the existing coarse model, to real NCT melt data, and find that the general shape is in good agreement (Figure D.30).
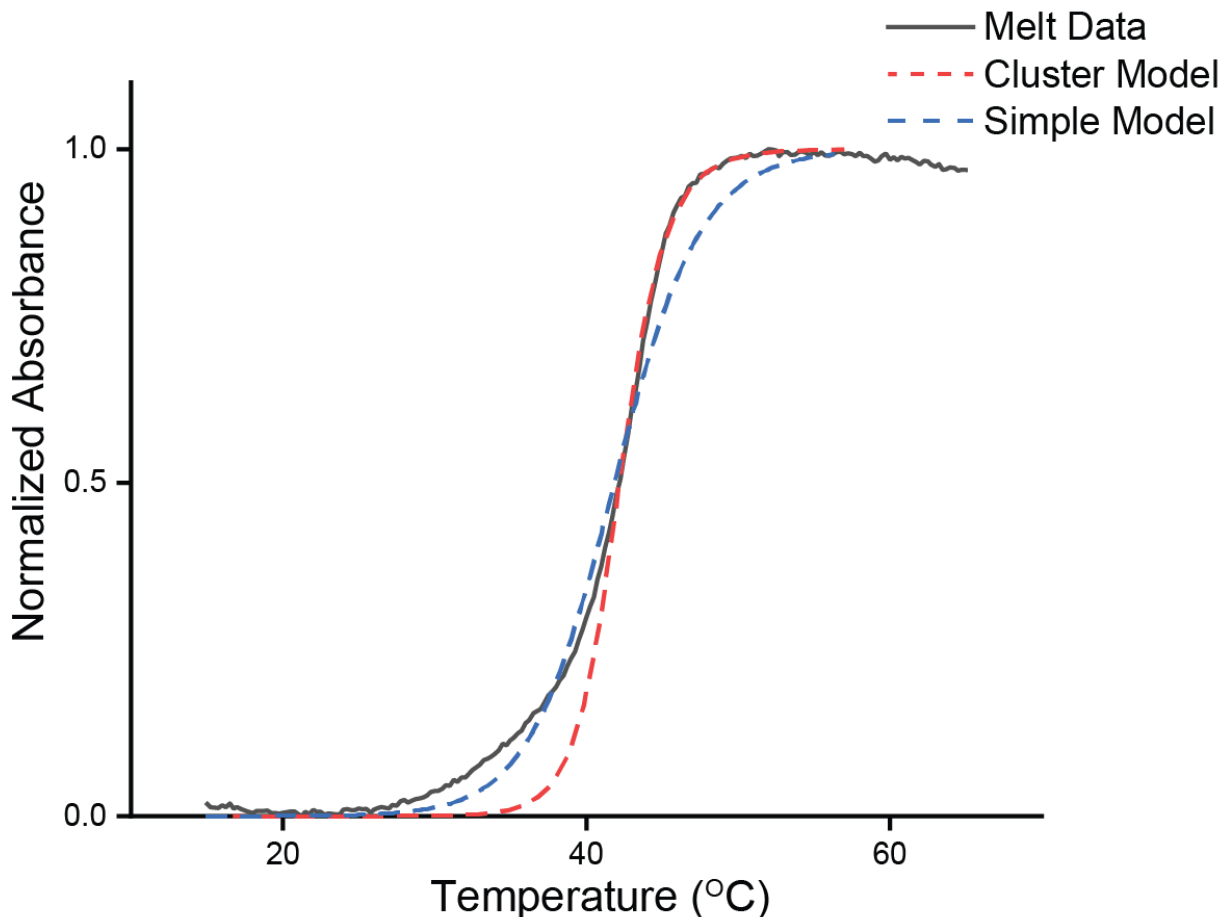
Figure D.30: The cluster model matches the general lineshape of the real melt data. The representative graphs were manually generated using nonphysical values.

D.5.3. Diffusion in NCT Crystallization

For the system at thermodynamic minimum, the maximum cluster size would correspond to the total number of particles present in the system. However, it is not kinetically feasible for the particles to all assemble into a single aggregate. Instead, we limit the maximum number of particles per cluster by the ability of nanoparticles to diffuse between clusters, resulting in an "interaction volume" that collapses when K>1 rather than the full volume of the system. This interaction volume may be estimated by calculating the characteristic diffusion length of a nanoparticle, given by:

Equation D.18:

$$l = \sqrt{Dt}$$

Where D is the diffusivity of the particle and t is the characteristic diffusion time of the system. If the particle clusters "collapse" during a finite window of temperature with range W, while cooling at a reciprocal rate of τ, then the characteristic time may be approximated as:

Equation D.19:

$$t \approx W\tau$$

The interaction volume V may then be calculated by the sphere with radius equal to the characteristic diffusion length, corresponding to the ability for other particles to diffuse towards each other from opposite ends of the sphere

Equation D.20:

$$V = \frac{4}{3}\pi l^3 = \frac{4}{3}\pi = \frac{4}{3}\pi D^{\frac{3}{2}} W^{\frac{3}{2}} \tau^{\frac{3}{2}}$$

The cluster size N is then given by the collapse of all particles in an interaction volume

Equation D.21:

$$N = cV = \frac{4}{3}\pi W^{\frac{3}{2}} * c\tau^{\frac{3}{2}}$$

Where c is the total concentration of particles in solution.

D.5.4. Prediction of Trends

Given that the crystallite volume scales with the number of particles in the crystallite, the 1D characteristic crystal size L then scales with

Equation D.22:

$$L \sim N^{\frac{1}{3}} \sim c^{\frac{1}{3}} \tau^{\frac{1}{2}}$$

This is consistent with the observed data for concentration and reciprocal rate (Figure D.31)
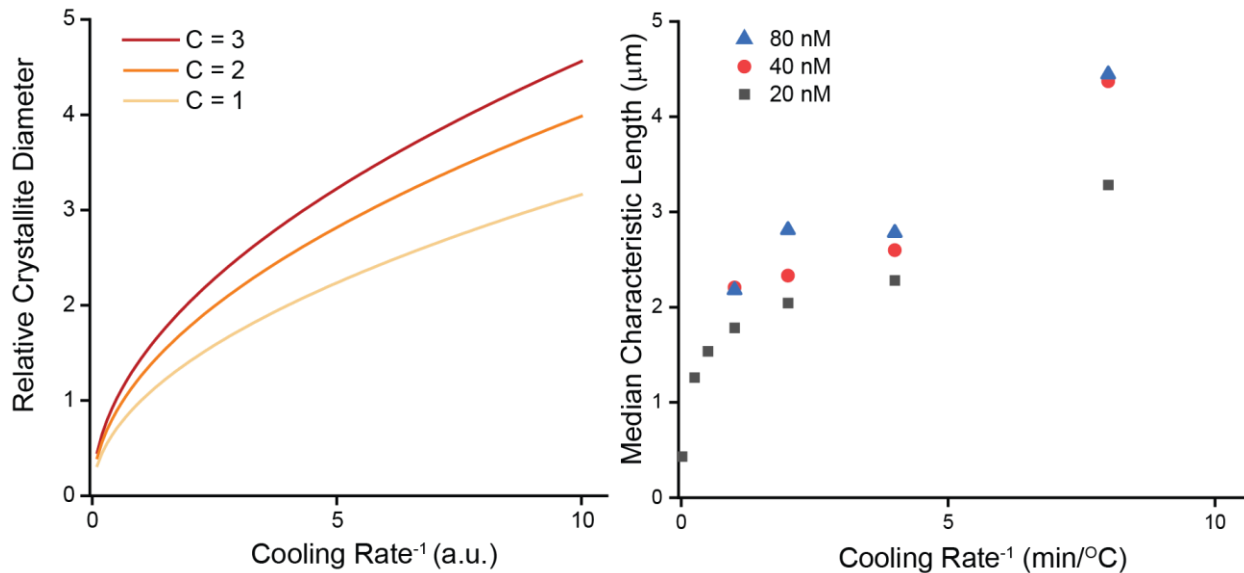
Figure D.31: Comparison of trends between the NCT crystallization model using non-physical values for concentration, rate, and diameter (left), and the data reported in this manuscript (right, adopted from Figure 5.2 in the main text). The trends in the model are consistent with the experimental data.

This model also predicts relationships between other parameters which may be used to alter crystal size, such as the breadth of the melting window (which may be controlled by binding group loading) or particle diffusivity (which may be controlled by particle size). However, these parameters are correlated to other factors in the system, such as melting temperature, and so were beyond the scope of this current work.

D.6. Sintering NCTs

D.6.1. Crystallite Preparation

The crystallites used in the sintering protocol to produce different grain sizes were synthesized *via* slow-cooling as described above. The two protocols utilized were 15s / 0.1°C (fast cool) and 4min / 0.1°C (slow cool), both at 20 nM concentration, and resulted in crystallites virtually identical to Figure D.9 and Figure D.13, respectively. However, as a control, some of the crystallites from each batch were SEM imaged and analyzed for size distribution in the same manner as described above. The measured size distributions (Figure 5.2C) are therefore from the

same batch of crystallites used to produce the sintered solids and are directly comparable to the measured distribution of grain sizes.

The mixes between Au and IO-NCTs were prepared in the same fashion (Figure D.32), with the IO-NCTs added to the Au-NCTs before sintering, and mixed with a pipette. Note, the concentration of IO-NCTs is significantly higher than that of Au-NCTs. Consequently, CsCl lattices formed slightly rounded shapes instead of polyhedral (Figure D.32B&C), and the sintered solids were predominantly IO-NCTs (Figure D.40). For the CsCl NCTs, the excess IO-NCTs were removed with a syringe before any further processing. SEM imaging of the crystallites used to make the sintered solids in the main text are presented in Figure D.32. SAXS characterization demonstrates crystallinity regardless of composition and the presence of a CsCl crystallographic phase (Figure D.33).
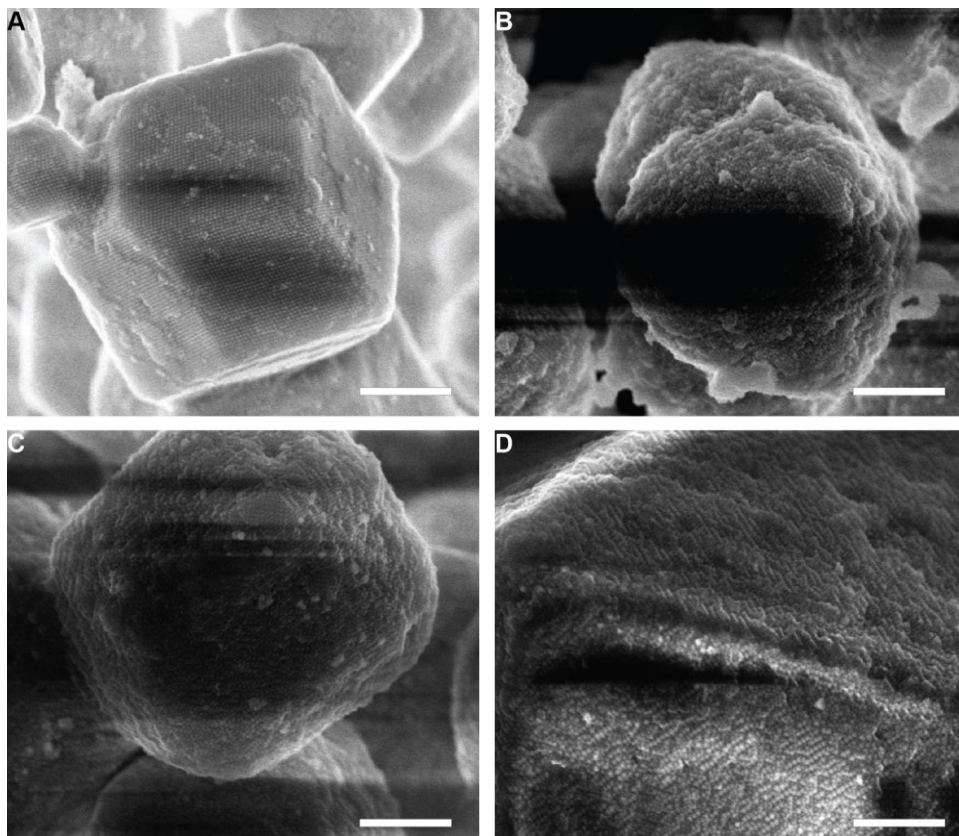
Figure D.32: NCTs prepared with different nanoparticle cores, before they were sintered together in the experiments featured in Figure 5.3 of the main text. (A) NCT crystals prepared entirely with AuNPs. (B) NCT crystals made from DAP functionalized AuNPs and Thy functionalized IONPs. (C) NCT crystals made from the coassembly of DAP functionalized IONPs and Thy functionalized AuNPs. (D) NCT crystals made entirely of IONPs. All scale bars are 500 nm.
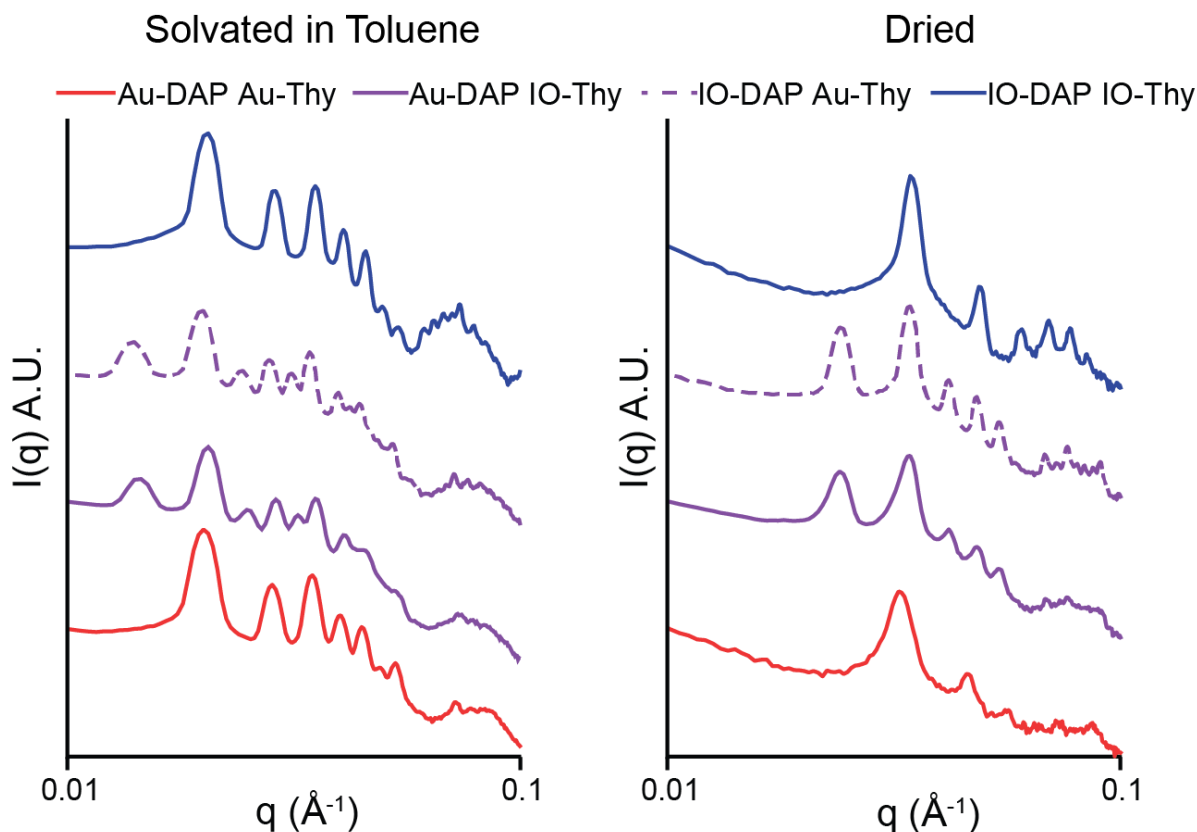
Figure D.33: SAXS of NCT crystallites prepared with Au-NCTs (red), IO-NCTs (blue), or mixtures of Au and IO-NCTs (purple). Note that the mixed samples show a larger number of peaks, indicating they have formed a CsCl lattice. These samples were then used to prepare the sintered solids in the main text.

D.6.2. Sintering Protocol

To sinter NCT crystallites into macroscopic solids, they were loaded into a microcentrifuge tube, and centrifuged for 10 minutes at 20,000 RCF. Other speeds were also effective, but gave a less dense microstructure. Moreover, the sintering process was only effective while the brush was in toluene, likely because in the collapsed state new hydrogen bonds were slower to form (Figure D.34). After centrifuging the sample underwent the standard polymer brush collapse, and were allowed to dry. The subsequent materials were then characterized by SEM (Figure D.34) and optical microscopy (Figure D.35).
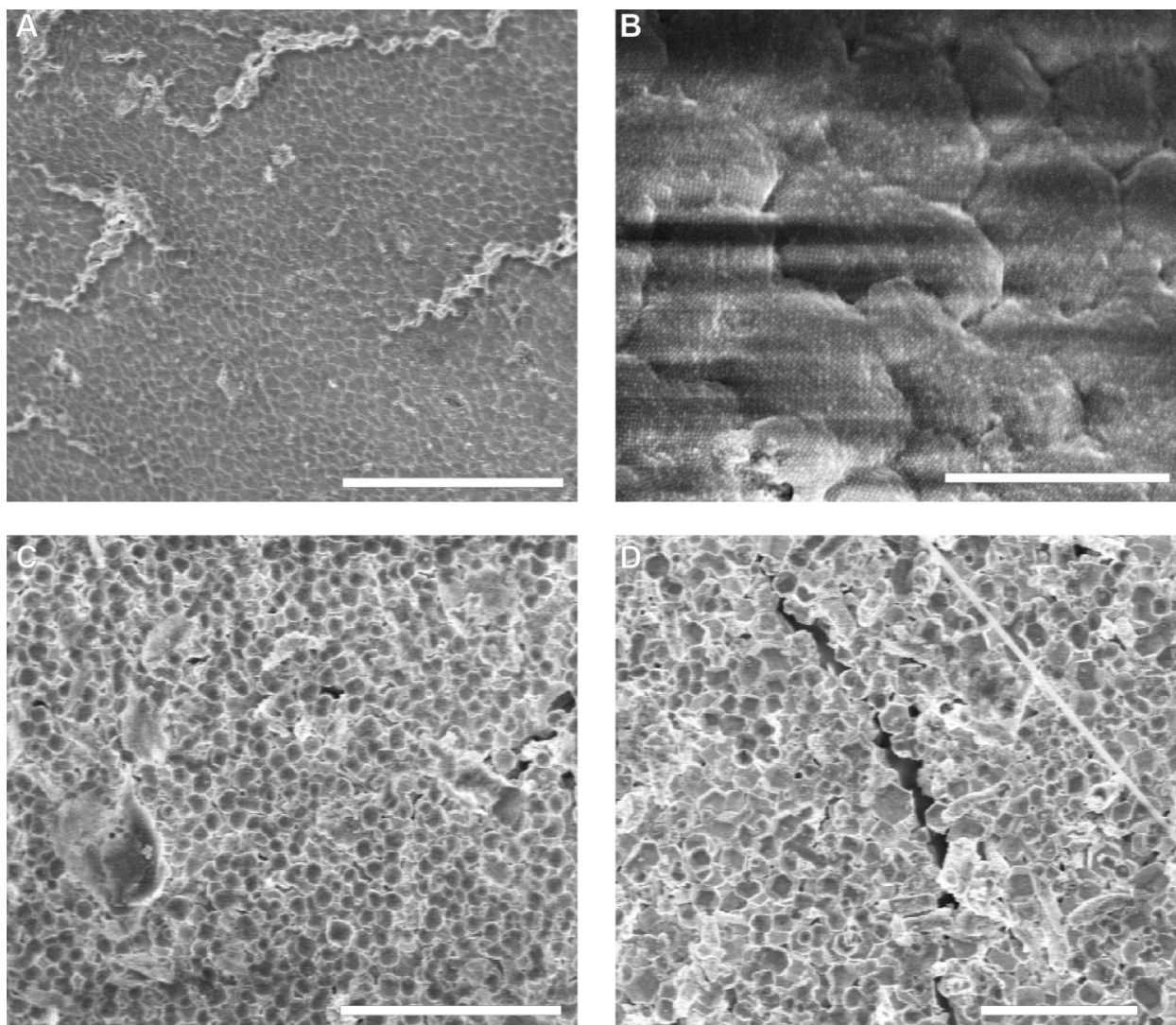
Figure D.34: Effect of sintering conditions on NCT microstructure. (A) NCTs centrifuged at 20,000 RCF in toluene. (B) Closer image of the sintered solid in A. (C) NCTs centrifuged at 10,000 RCF in toluene. The sintered solid appeared to be continuous and could be manipulated by hand, but the microstructure is less compact. (D) NCTs centrifuged at 20,000 RCF in n-Decane. The material prepared from n-Decane was significantly less compact. It was not powder like, and did not separate upon being exposed to air flow, but it could not withstand physical contact. The scale bars of A, C, and D are 10 microns, the scale bar of B is 1 micron.
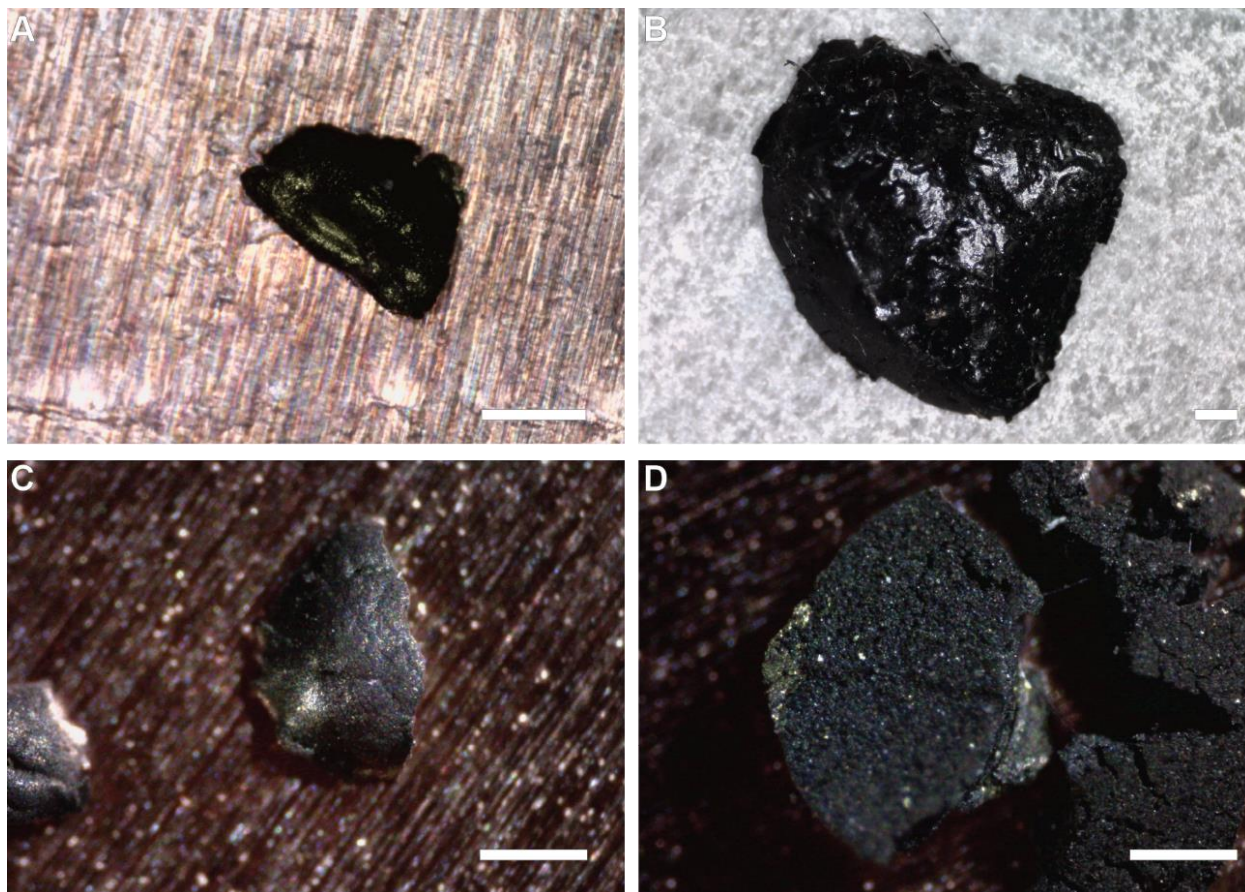
Figure D.35: Optical images of sintered NCTs with different compositions. (A) Gold NCTs in a bcc lattice (B) Iron oxide NCTs in a bcc lattice (C) Gold and Iron Oxide NCTs in a CsCl Lattice (D) Blend of Gold NCTs in a bcc lattice and Iron Oxide NCTs in a bcc lattice. All scale bars are 0.5 mm.

D.6.3. Cross-Sections

The sintered solids were subsequently cross-sectioned mechanically with a razor blade followed by FIB milling (as described above) to image the interior microstructure (Figure D.36). Each of the four sintering conditions had their cross-sections SEM imaged, stitched into one composite image in Photoshop, and adjusted for tilt *via* Equation D.3. Significant portions of the collected cross-sections are included in Figure D.37, Figure D.38, Figure D.39, and Figure D.40; smaller sections are included in Figure 5.3.

The two cross-sections demonstrating different grain sizes had individual grains within the cross-section identified by eye and colored in Photoshop. The grains were then outlined and analyzed in ImageJ in the same manner as the pre-sintering crystallites. The average of the major

and minor axis was used as the characteristic length of each grain and the distributions of sizes is included in Figure 5.3D. Note, the observed cross-section is a 2D slice of a 3D grain structure. Therefore, their measured size in cross-section is smaller than the true 3D size but can be geometrically related[314] for comparison between pre- and post-sintering.

In the cross-sections containing both Au-NCTs and IO-NCTs, the composition of each nanoparticle can be determined from the SEM contrast. Au-NCTs, with high electron density, will appear brighter while IO-NCTs, low electron density, will appear darker.
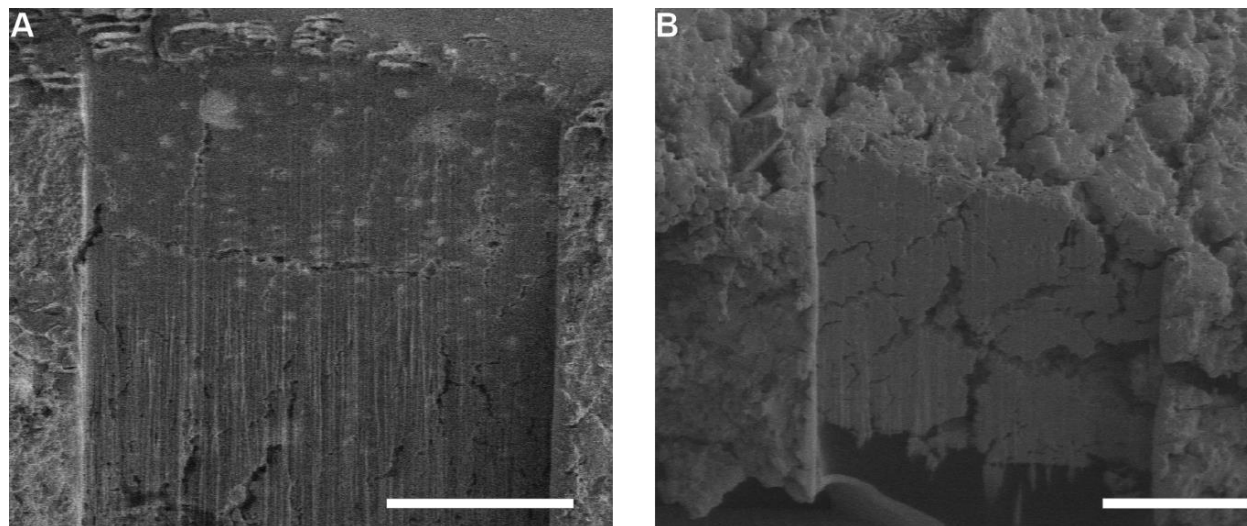
Figure D.36: Low magnification images of the FIB cross sections of the fast cooled (A) and slow cooled (B) sinter NCT samples featured in Figure 5.3. Scale bar for each image is 20 microns.
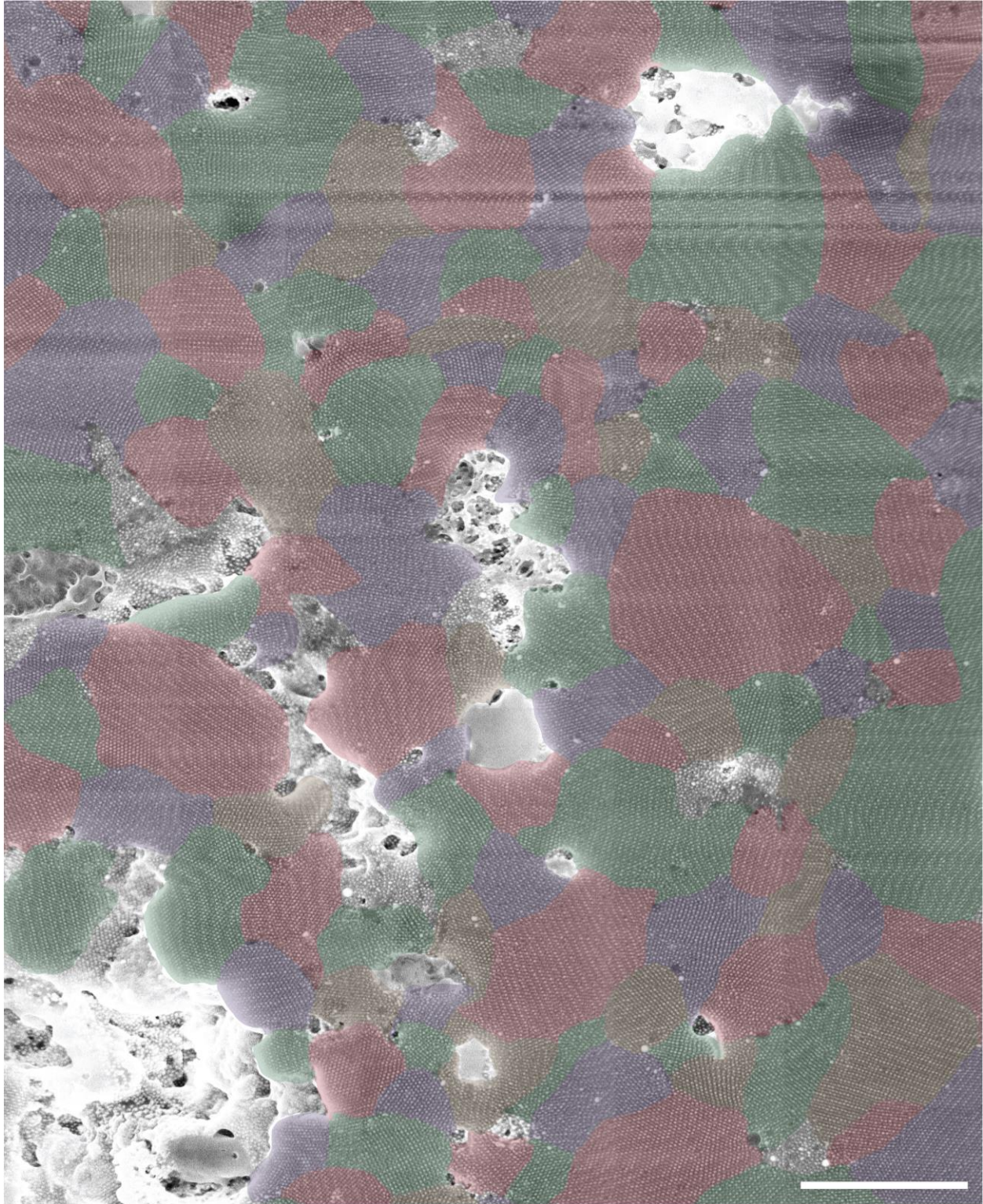
Figure D.37: FIB cross-section of Au-NCTs rapidly cooled (15s / 0.1°C) and sintered into solids. Overlaid colors highlight grains of different orientations. Scale bar is 1 micron.
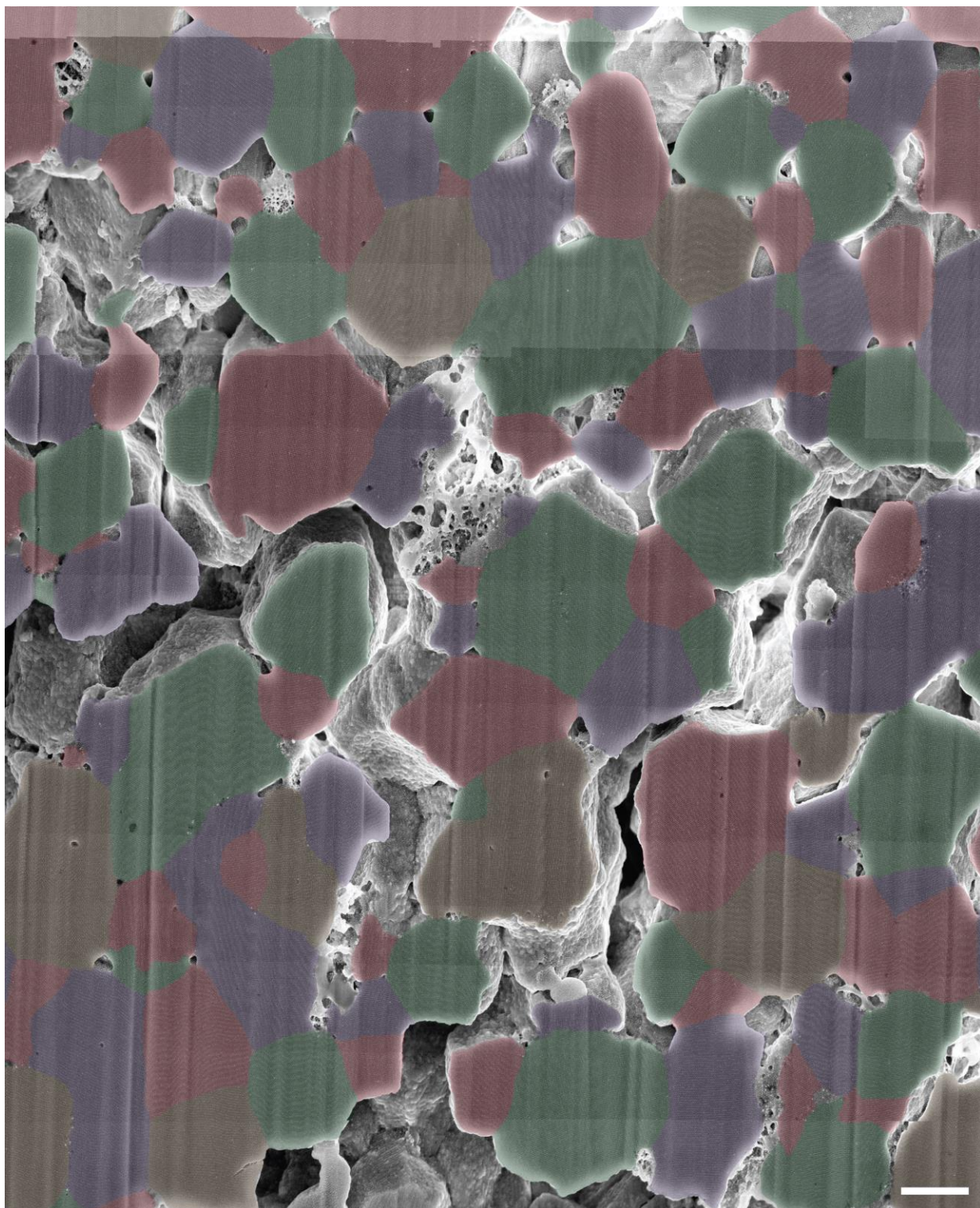
Figure D.38: FIB cross-section of Au-NCTs slowly cooled (4 min/ 0.1°C) and sintered into solids. Overlaid colors highlight grains of different orientations. Scale bar is 1 micron.
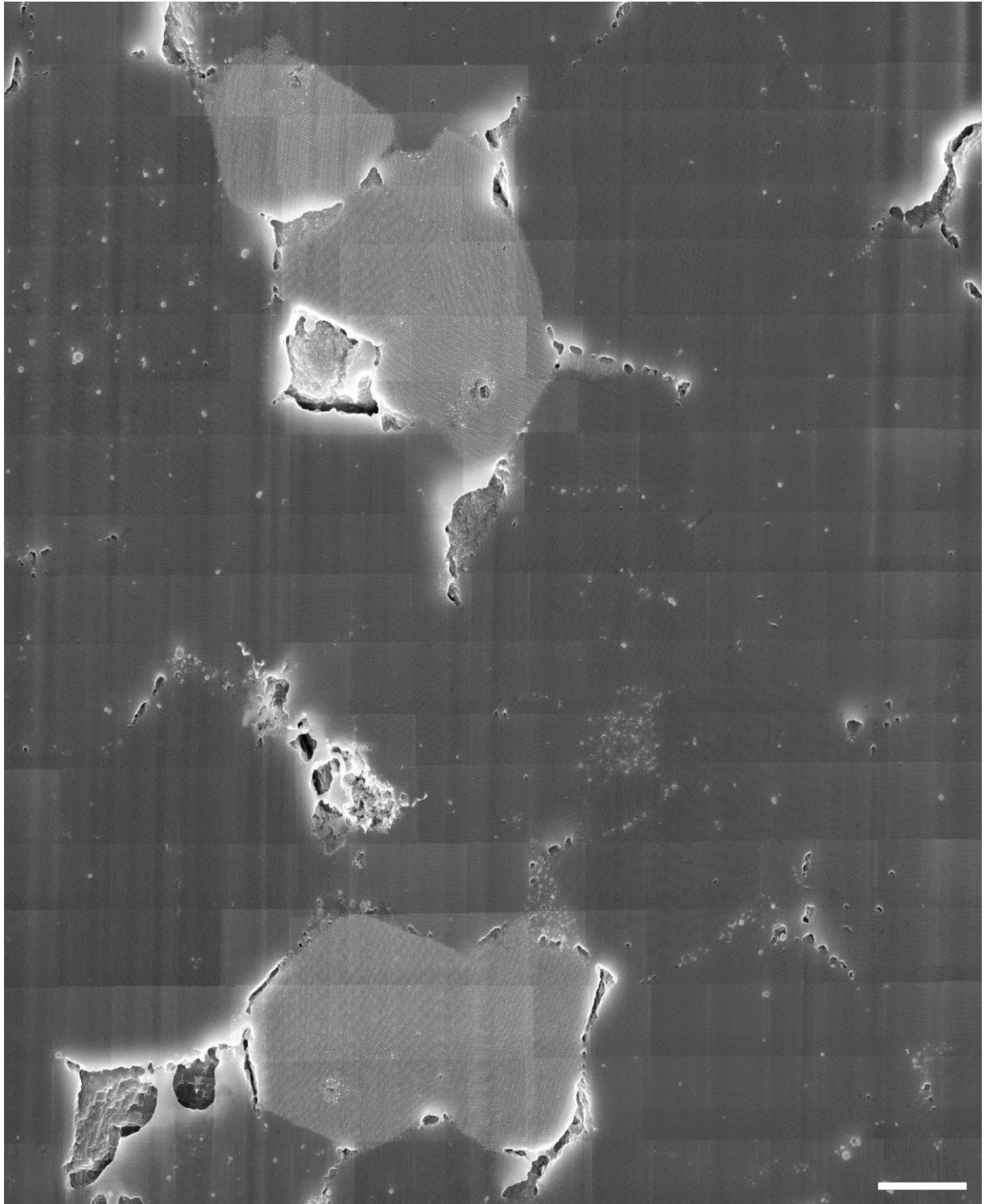
Figure D.39: FIB cross-section of Au-NCTs and IO-NCTs assembled into a bcc lattices, blended together, and sintered into solids. Dark regions are IO-NCTs, bright regions are Au-NCTs. Scale bar is 1 micron.
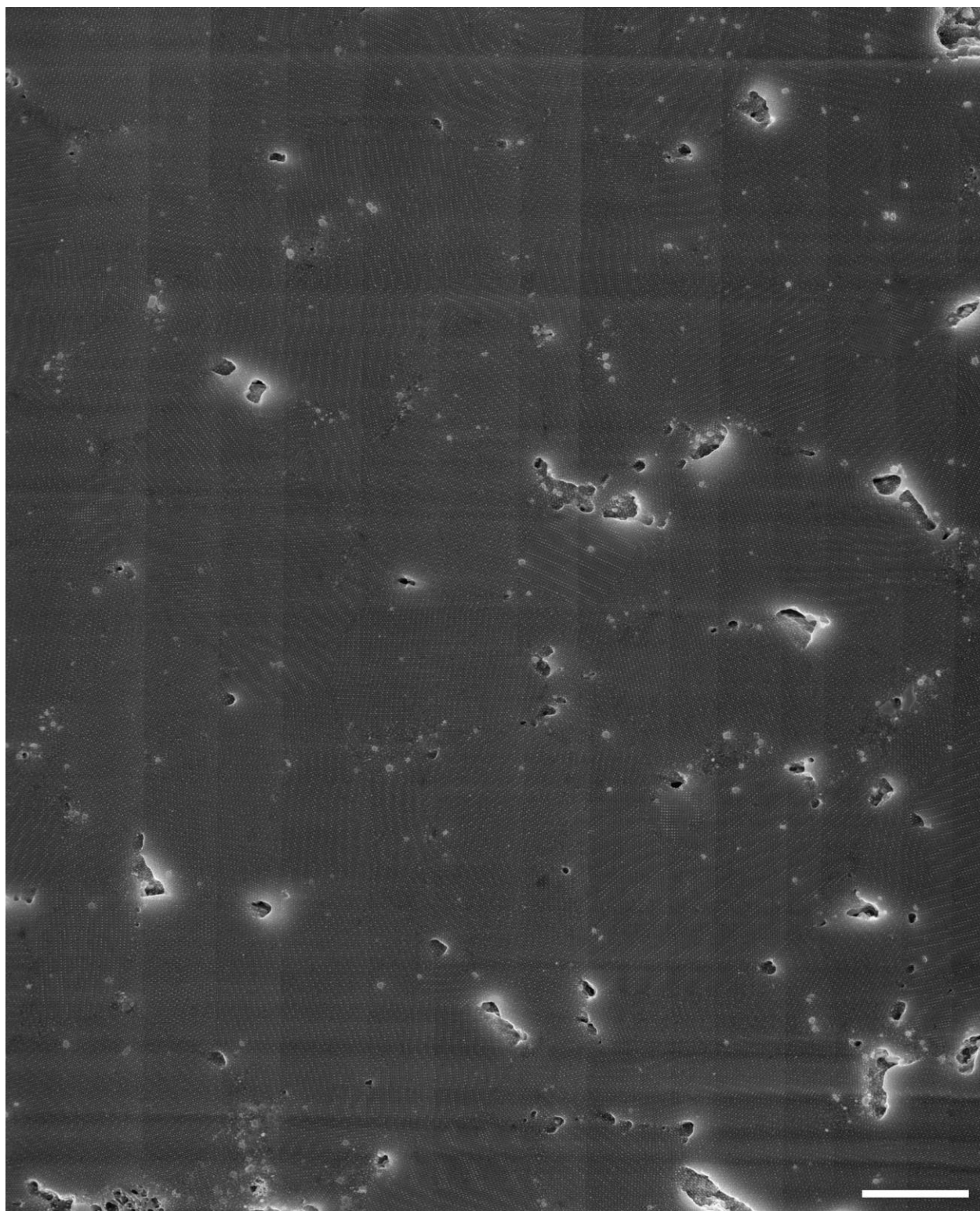
Figure D.40: FIB cross-section of Au-NCTs and IO-NCTs coassembled into a CsCl lattice and sintered into solids. Light particles are Au-NCTs, dark ones are IO-NCTs. Scale bar is 1 micron.

D.6.4. Evidence of a Sintering Mechanism and Grain Boundary Diffusion
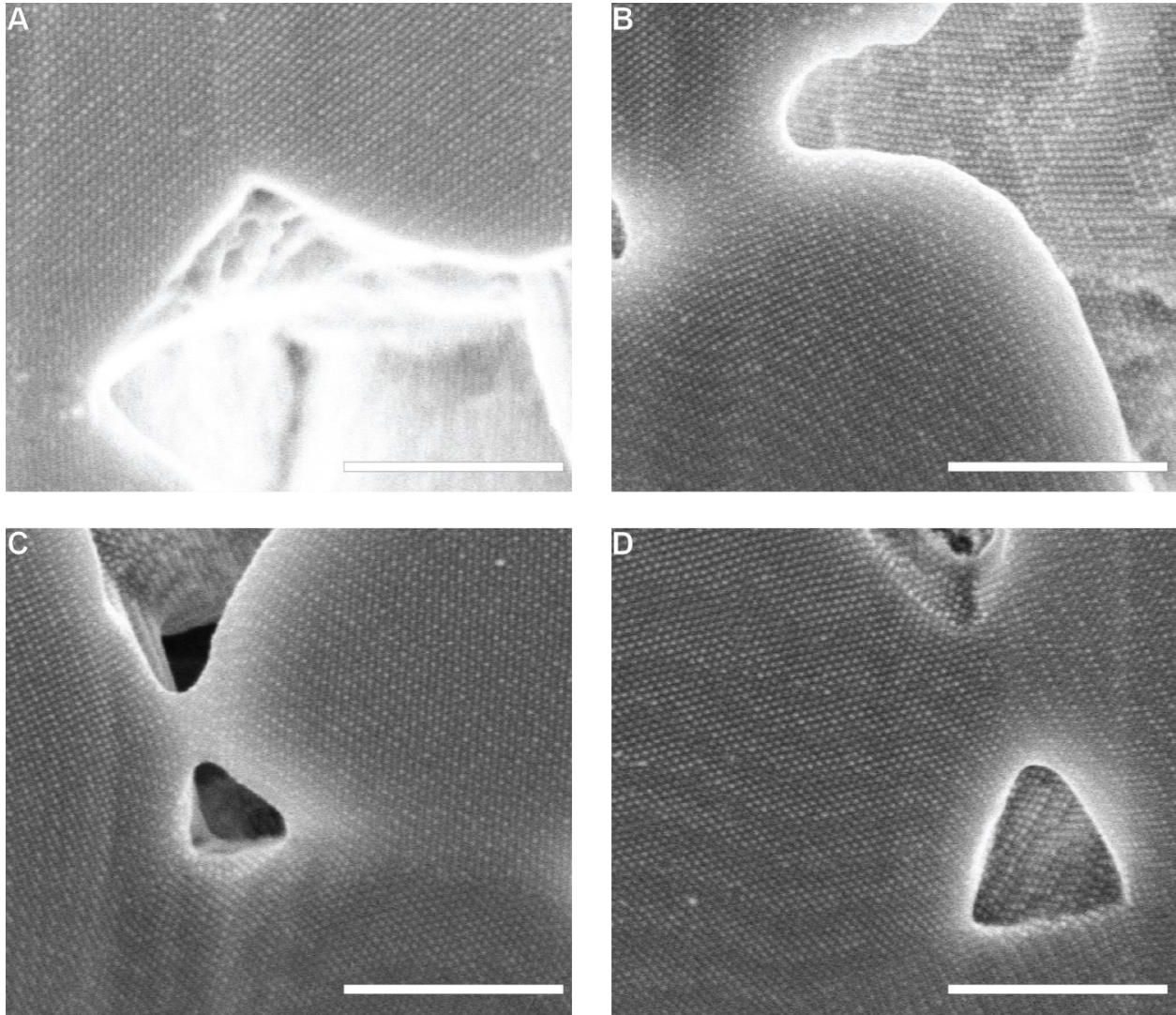
Figure D.41: Examples of necking and crystallite deformation observed in the "slower cooled" sintered sample with larger grain sizes. Scale bars for all images are 500 nm.
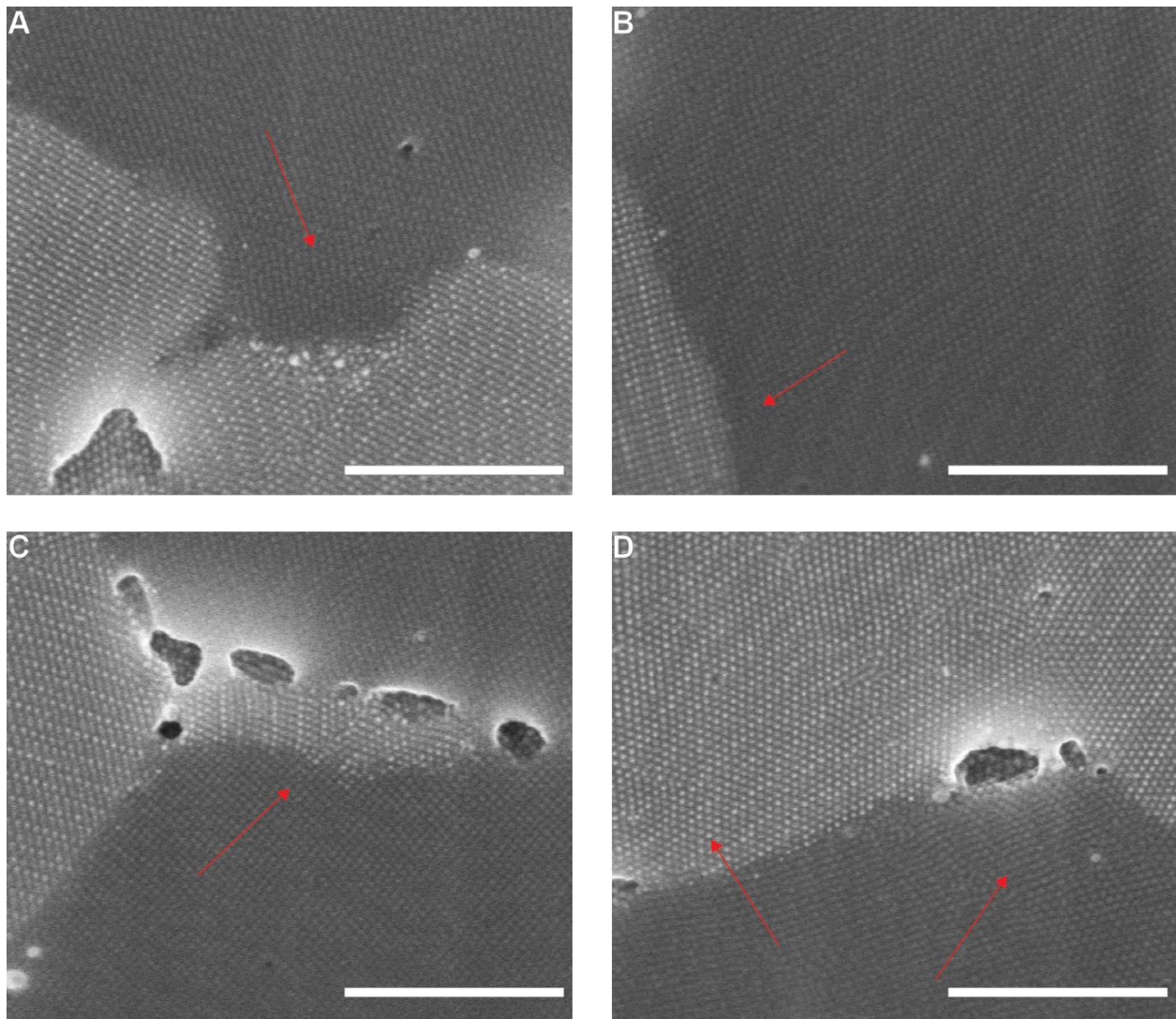
Figure D.42: The experiments in this work did not provide conclusive evidence for grain boundary diffusion during sintering, but experiments with blended IO and Au NCTs allowed for visualization of the interface between crystallites. In several regions, significant distortions of the lattice were observed, suggesting some degree of grain boundary diffusion may be possible under the correct processing conditions. (A) A small segment of IO-NCTs between two Au-NCT crystallites deforms to match the neighboring grains. (B) Lattice strain appears to orient the NCTs to align at the interface. (C) A small segment of Au-NCTs orienting to match the surrounding IO-NCTs. (D) Lattice strain in both IO and Au NCTs. Scale bars for all images are 500 nm.

D.7. Mechanically Shaping NCTs

To mechanically shape the bulk NCT materials, first a sintered solid was prepared from IO-NCTs (16 nm IO NPs and 8 kDa polymer) using the abovementioned procedure, yielding a monolithic solid easily observed by eye and manipulated by hand (Figure D.43). The sample was then placed into a polyoxymethylene mold, cut with a laser cutter (Figure D.44), and had 500 Newtons applied to it for 1 hour. The result was a material with a macroscale, well-defined embossed structure visible by eye (Figure 5.1 and Figure D.45). SEM analysis of the pressed sample revealed maintenance of crystallinity post-processing (Figure D.46). To demonstrate the robustness of this processing route, a similar sample was produced using IO-NCTs with 13 kDa polymkers and mechanically processed (Figure D.47). Ordering was slightly less well maintained in this sample than ones prepared with a shorter polymer brush, likely because the softer NCTs are more capable of deforming during sintering.
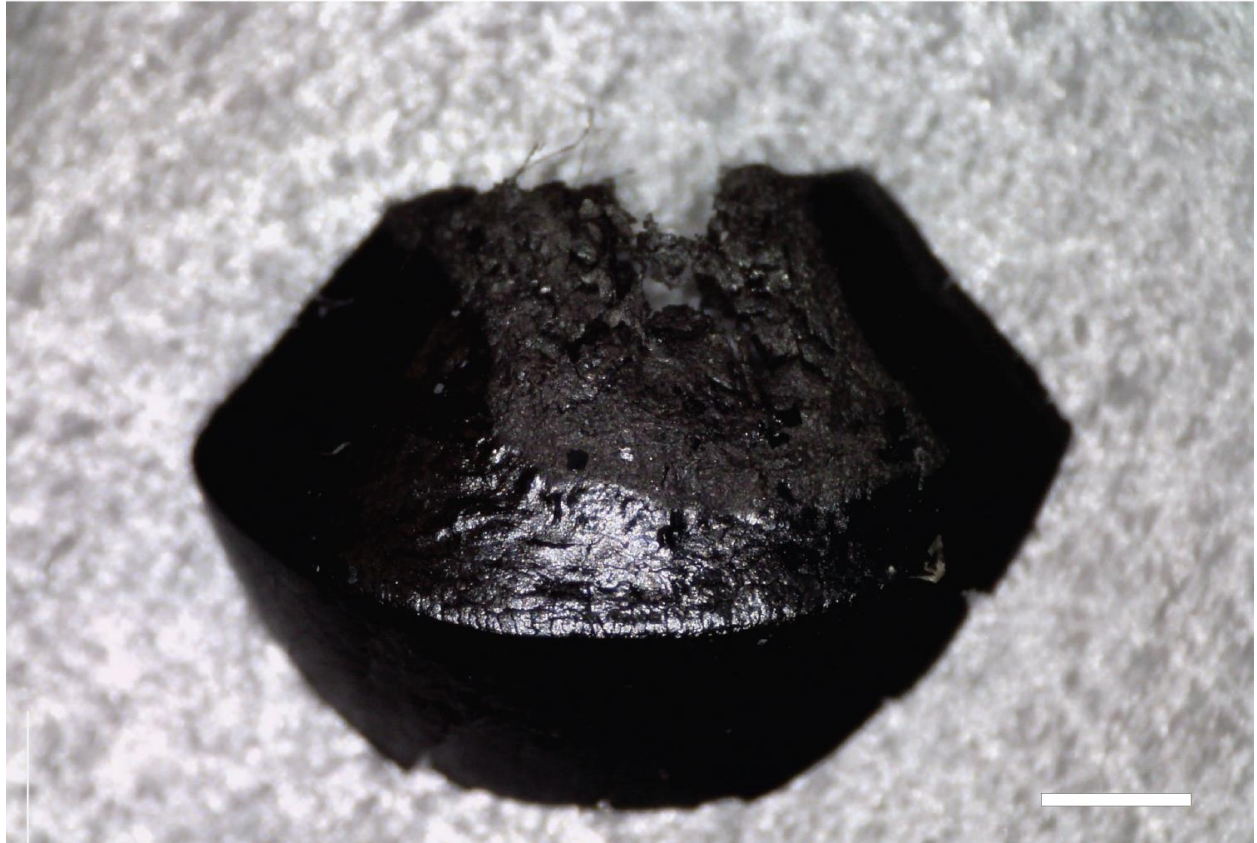
Figure D.43: Optical image of a sintered IO-NCT solid that was then pressed into a mold to form the mechanically shaped NCT materials. Scale bar is 1 mm.
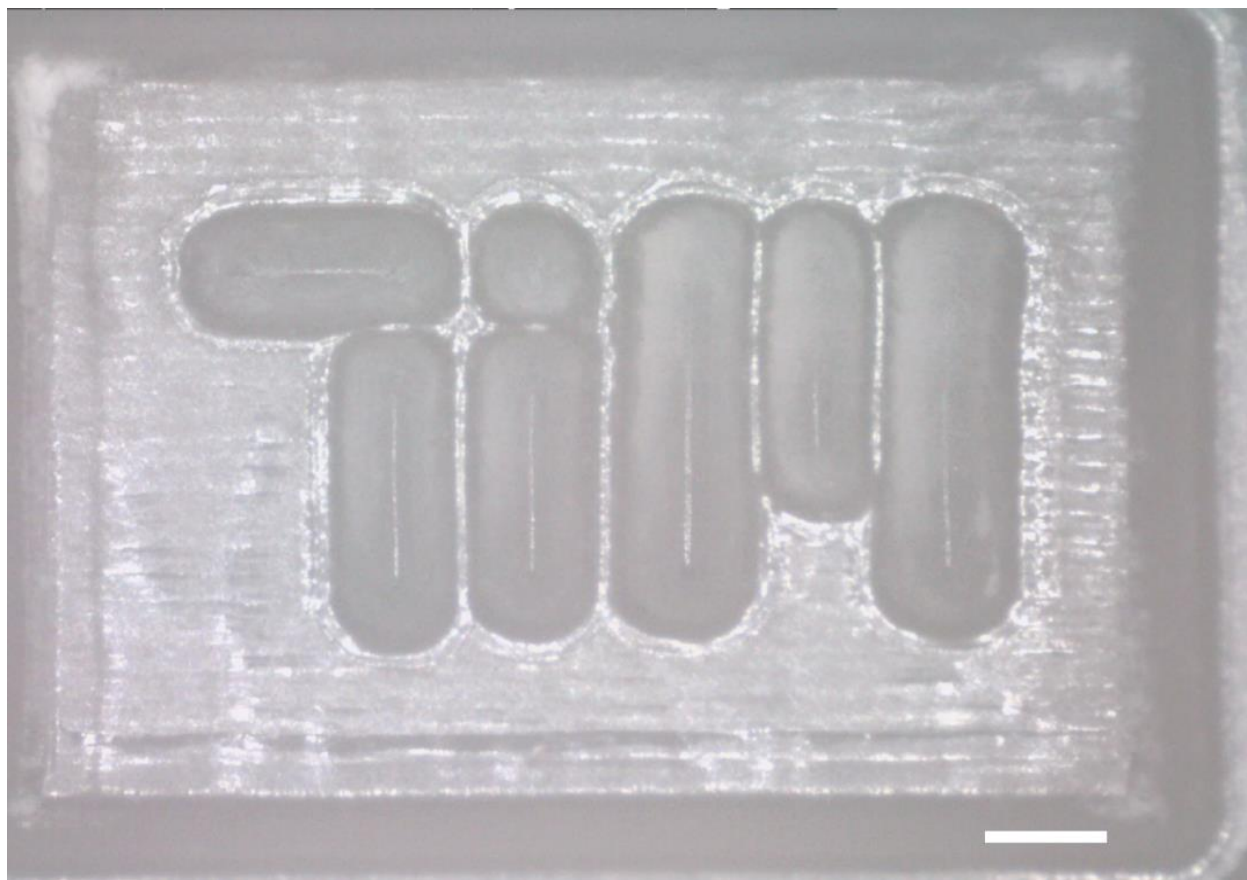
Figure D.44: Optical image of the mold used to mechanically shape the NCT solids. Scale bar is 0.5 mm.
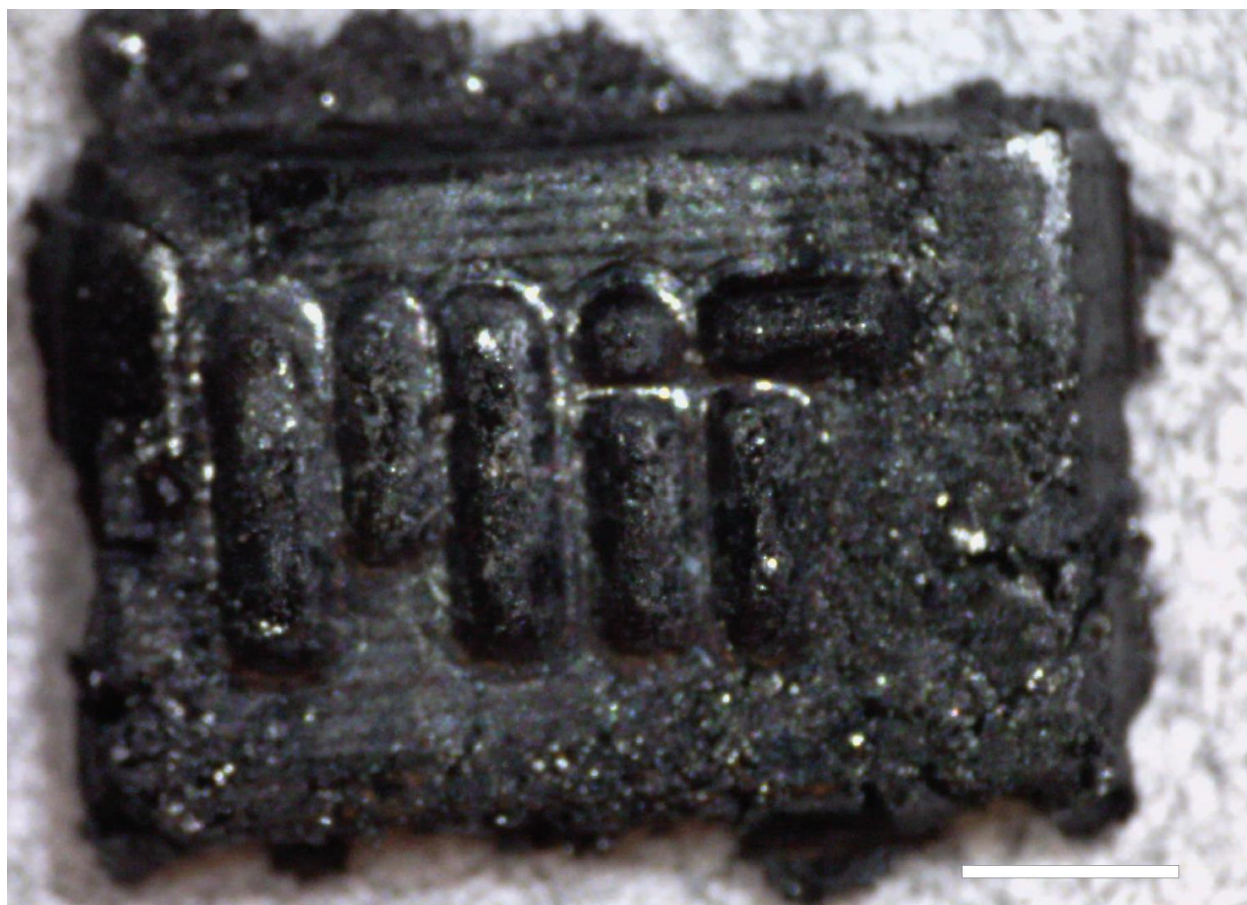
Figure D.45: Optical image of a mechanically processed NCT solid made with 16 nm IO NPs and 8 kDa polymer. This is a lower magnification image of the picture used in Figure 1 of the main text. Scale bar is 1 mm.
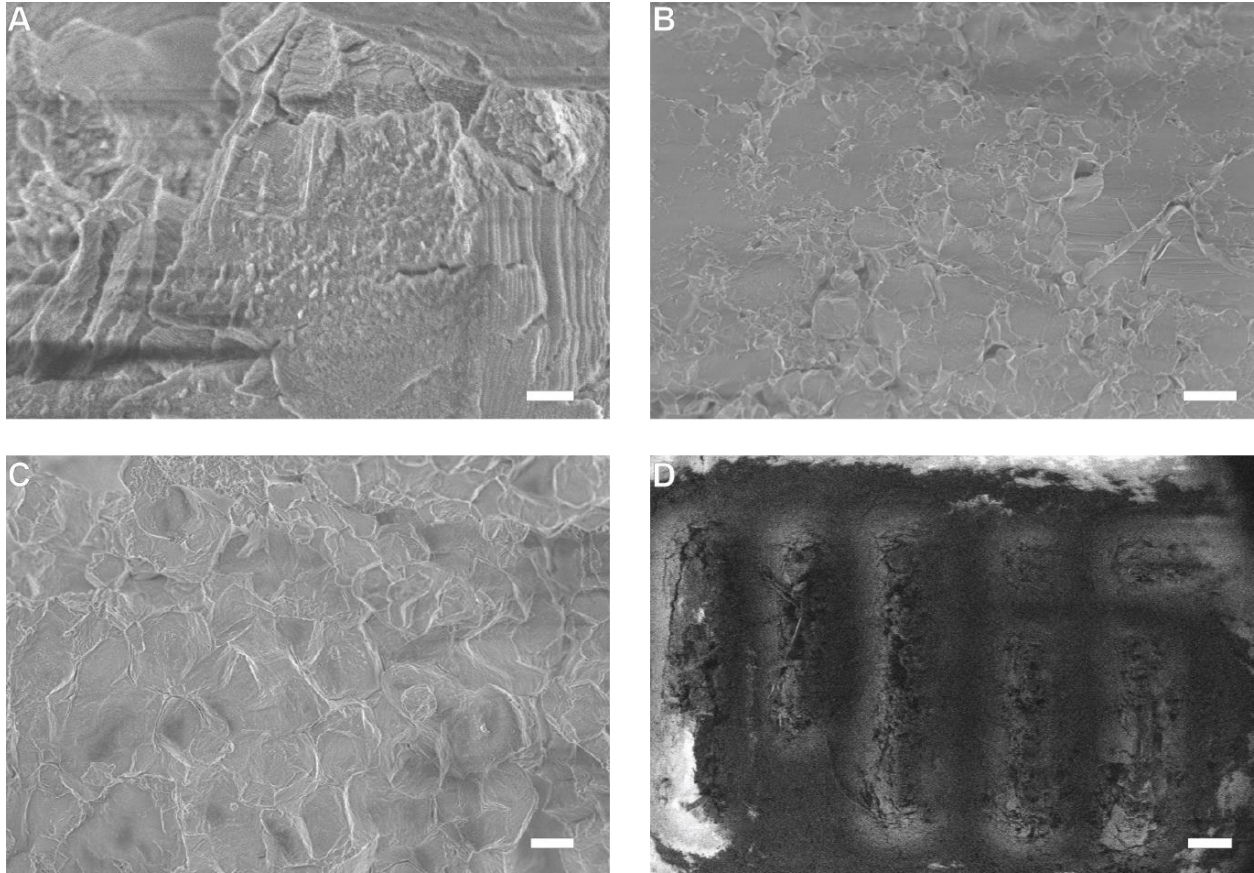
Figure D.46: SEM micrographs of the mechanically processed NCT solid. (A) High magnification image with visible particles. Scale bar 400 nm. (B) Lower magnification image of the area in (A). Scale bar 10 microns. (C) Image of a rougher region where Wulff polyhedra are still visible. Scale bar 4 microns. (D) SEM image of the MIT school logo. Scale bar 200 microns.
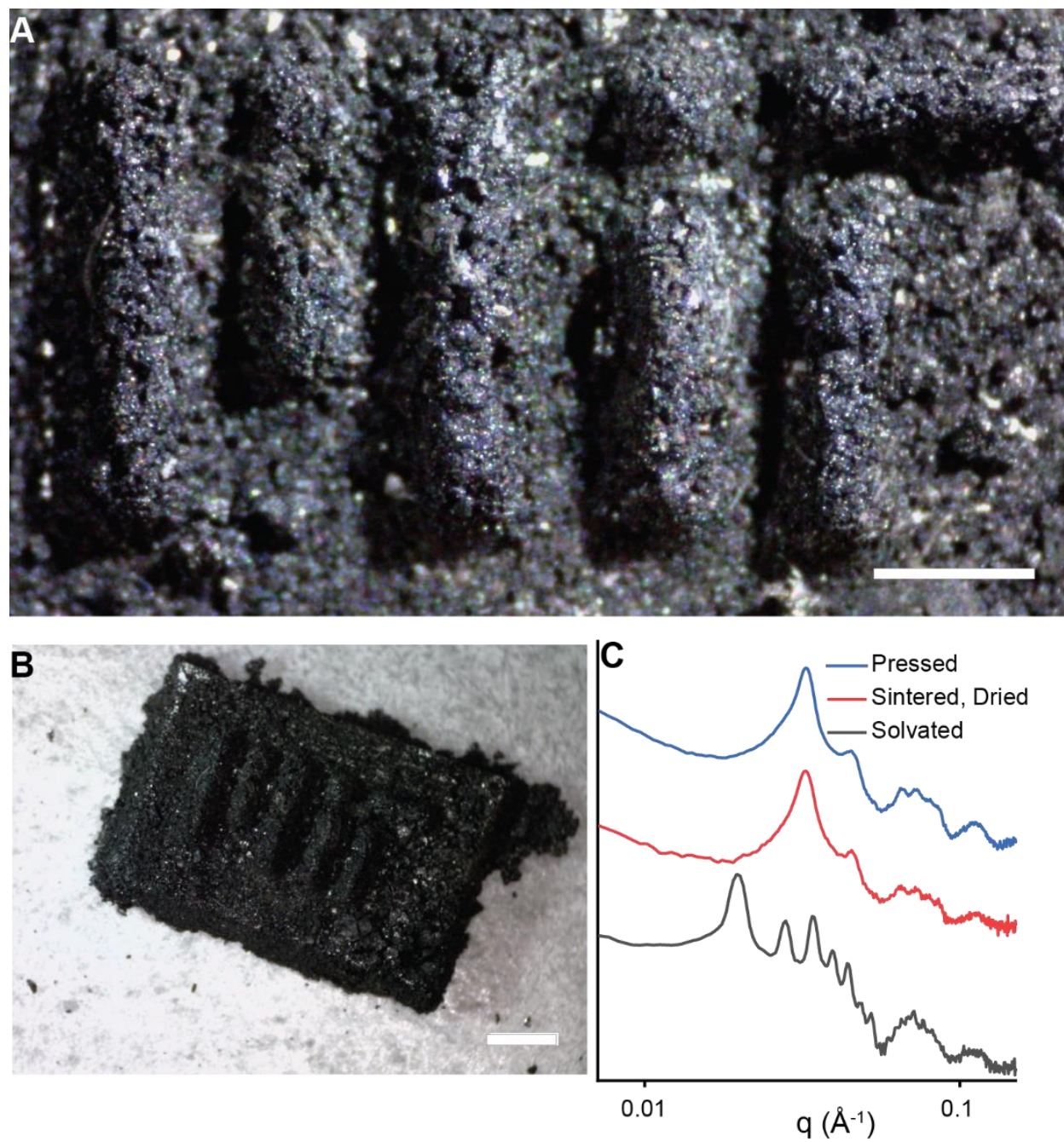
Figure D.47: Mechanically processed NCT solids can also be created from NCTs with 13 kDa polymers. (A and B) Optical images of the NCT solid. Scale bars are (A) 0.5 mm and (B) 1 mm. (C) SAXS demonstrating the material retains its crystallinity throughout its processing.

Appendix E. References

[1]   W. D. Callister, D. G. Rethwisch, *Materials Science and Engineering: An Introduction*, John Wiley & Sons, Hoboken, NJ, **2010**.

[2]   W. F. Smith, J. Hashemi, *Foundations of Materials Science and Engineering*, McGraw-Hill, **2011**.

[3]   R. T. Sanderson, *Chemical Periodicity*, Reinhold Pub. Corp., New York, **1960**.

[4]   W. M. Haynes, *CRC Handbook of Chemistry and Physics*, CRC Press, **2016**.

[5]   S. S. Zumdahl, D. J. DeCoste, *Chemical Principles*, Cengage Learning, **2012**.

[6]   L. Pauling, *J. Am. Chem. Soc.* **1929**, *51*, 1010.

[7]   J. W. Mullin, *Crystallization*, Elsevier, **2001**.

[8]   A. Lewis, M. Seckler, H. Kramer, G. van Rosmalen, *Industrial Crystallization: Fundamentals and Applications*, Cambridge University Press, **2015**.

[9]   A. G. Jones, *Crystallization Process Systems*, Elsevier, **2002**.

[10]   W. Caseri, *Macromol. Rapid Commun.* **2000**, *21*, 705.

[11]   A. Nasir, A. Kausar, A. Younus, *Polym.-Plast. Technol. Eng.* **2015**, *54*, 325.

[12]   A. N. Shipway, E. Katz, I. Willner, *ChemPhysChem* **2000**, *1*, 18.

[13]   S. H. Cole, E. A. Monroe, *J. Appl. Phys.* **1967**, *38*, 1872.

[14]   A. van Blaaderen, R. Ruel, P. Wiltzius, *Nature* **1997**, *385*, 321.

[15]   M. E. Leunissen, C. G. Christova, A.-P. Hynninen, C. P. Royall, A. I. Campbell, A. Imhof, M. Dijkstra, R. van Roij, A. van Blaaderen, *Nature* **2005**, *437*, 235.

[16]   E. V. Shevchenko, D. V. Talapin, N. A. Kotov, S. O'Brien, C. B. Murray, *Nature* **2006**, *439*, 55.

[17]   X. Ye, C. Zhu, P. Ercius, S. N. Raja, B. He, M. R. Jones, M. R. Hauwiller, Y. Liu, T. Xu, A. P. Alivisatos, *Nat. Commun.* **2015**, *6*, 10052.

[18]   A. M. Kalsin, M. Fialkowski, M. Paszewski, S. K. Smoukov, K. J. M. Bishop, B. A. Grzybowski, *Science* **2006**, *312*, 420.

[19]   K. Heo, C. Miesch, T. Emrick, R. C. Hayward, *Nano Lett.* **2013**, *13*, 5297.

[20]   C. A. Mirkin, R. L. Letsinger, R. C. Mucic, J. J. Storhoff, *Nature* **1996**, *382*, 607.

[21] J. Zhang, P. J. Santos, P. A. Gabrys, S. Lee, C. Liu, R. J. Macfarlane, *J. Am. Chem. Soc.* **2016**, *138*, 16228.

[22] R. Choudhury, D. R. Bowler, M. J. Gillan, *J. Phys. Condens. Matter* **2008**, *20*, 235227.

[23] D. G. Stroppa, R. D. Righetto, L. A. Montoro, L. Houben, J. Barthel, M. A. Cordeiro, E. R. Leite, W. Weng, C. J. Kiely, A. J. Ramirez, *Nanoscale Res. Lett.* **2013**, *8*, 475.

[24] N. K. Mahenderkar, Q. Chen, Y.-C. Liu, A. R. Duchild, S. Hofheins, E. Chason, J. A. Switzer, *Science* **2017**, *355*, 1203.

[25] C. Diaz-Egea, T. Ben, M. Herrera, J. Hernández, E. Pedrueza, J. L. Valdés, J. P. Martínez-Pastor, F. Attouchi, Z. Mafhoud, O. Stéphan, S. I. Molina, *Nanotechnology* **2015**, *26*, 405702.

[26] P. A. Gabrys, S. E. Seo, M. X. Wang, E. Oh, R. J. Macfarlane, C. A. Mirkin, *Nano Lett.* **2018**, *18*, 579.

[27] M. N. O'Brien, H.-X. Lin, M. Girard, M. Olvera de la Cruz, C. A. Mirkin, *J. Am. Chem. Soc.* **2016**, *138*, 14562.

[28] J. C. Ku, M. B. Ross, G. C. Schatz, C. A. Mirkin, *Adv. Mater.* **2015**, *27*, 3159.

[29] D. J. Park, J. C. Ku, L. Sun, C. M. Lethiec, N. P. Stern, G. C. Schatz, C. A. Mirkin, *Proc. Natl. Acad. Sci.* **2017**, *114*, 457.

[30] C. P. Collier, T. Vossmeyer, J. R. Heath, *Annu. Rev. Phys. Chem.* **1998**, *49*, 371.

[31] S. M. Ilett, A. Orrock, W. C. K. Poon, P. N. Pusey, *Phys. Rev. E* **1995**, *51*, 1344.

[32] M. Dijkstra, J. M. Brader, R. Evans, *J. Phys. Condens. Matter* **1999**, *11*, 10079.

[33] R. van Roij, J.-P. Hansen, *Phys. Rev. Lett.* **1997**, *79*, 3082.

[34] Y. Wang, Y. Wang, D. R. Breed, V. N. Manoharan, L. Feng, A. D. Hollingsworth, M. Weck, D. J. Pine, *Nature* **2012**, *491*, 51.

[35] G. Chen, K. J. Gibson, D. Liu, H. C. Rees, J.-H. Lee, W. Xia, R. Lin, H. L. Xin, O. Gang, Y. Weizmann, *Nat. Mater.* **2019**, *18*, 169.

[36] J. P. Rolland, B. W. Maynor, L. E. Euliss, A. E. Exner, G. M. Denison, J. M. DeSimone, *J. Am. Chem. Soc.* **2005**, *127*, 10096.

[37] S. E. A. Gratton, P. D. Pohlhaus, J. Lee, J. Guo, M. J. Cho, J. M. DeSimone, *J. Controlled Release* **2007**, *121*, 10.

[38] S. Sacanna, W. T. M. Irvine, P. M. Chaikin, D. J. Pine, *Nature* **2010**, *464*, 575.

[39] W. Lee, A. Chan, M. A. Bevan, J. A. Lewis, P. V. Braun, *Langmuir* **2004**, *20*, 5262.

[40] J. Zhuang, H. Wu, Y. Yang, Y. C. Cao, *J. Am. Chem. Soc.* **2007**, *129*, 14166.

[41] C. B. Murray, S. Sun, W. Gaschler, H. Doyle, T. A. Betley, C. R. Kagan, *IBM J. Res. Dev.* **2001**, *45*, 47.

[42] E. V. Shevchenko, D. V. Talapin, C. B. Murray, S. O'Brien, *J. Am. Chem. Soc.* **2006**, *128*, 3620.

[43] A. Dong, X. Ye, J. Chen, C. B. Murray, *Nano Lett.* **2011**, *11*, 1804.

[44] D. V. Talapin, E. V. Shevchenko, M. I. Bodnarchuk, X. Ye, J. Chen, C. B. Murray, *Nature* **2009**, *461*, 964.

[45] F. X. Redl, K.-S. Cho, C. B. Murray, S. O'Brien, *Nature* **2003**, *423*, 968.

[46] X. Ye, J. Chen, C. B. Murray, *J. Am. Chem. Soc.* **2011**, *133*, 2613.

[47] P. Bartlett, A. I. Campbell, *Phys. Rev. Lett.* **2005**, *95*, 128302.

[48] A. P. Alivisatos, K. P. Johnsson, X. Peng, T. E. Wilson, C. J. Loweth, M. P. Bruchez Jr., P. G. Schultz, *Nature* **1996**, *382*, 609.

[49] S. Y. Park, D. Stroud, *Phys. Rev. B* **2003**, *67*, 212202.

[50] L. M. Demers, C. A. Mirkin, R. C. Mucic, R. A. Reynolds, R. L. Letsinger, R. Elghanian, G. Viswanadham, *Anal. Chem.* **2000**, *72*, 5535.

[51] E.-Y. Kim, J. Stanton, R. A. Vega, K. J. Kunstman, C. A. Mirkin, S. M. Wolinsky, *Nucleic Acids Res.* **2006**, *34*, e54.

[52] S. J. Hurst, A. K. R. Lytton-Jean, C. A. Mirkin, *Anal. Chem.* **2006**, *78*, 8313.

[53] J. J. Storhoff, R. Elghanian, C. A. Mirkin, R. L. Letsinger, *Langmuir* **2002**, *18*, 6666.

[54] H. D. Hill, J. E. Millstone, M. J. Banholzer, C. A. Mirkin, *ACS Nano* **2009**, *3*, 418.

[55] J. J. Storhoff, R. Elghanian, R. C. Mucic, C. A. Mirkin, R. L. Letsinger, *J. Am. Chem. Soc.* **1998**, *120*, 1959.

[56] R. A. Reynolds, C. A. Mirkin, R. L. Letsinger, *J. Am. Chem. Soc.* **2000**, *122*, 3795.

[57] T. A. Taton, G. Lu, C. A. Mirkin, *J. Am. Chem. Soc.* **2001**, *123*, 5164.

[58] Y. C. Cao, R. Jin, C. A. Mirkin, *Science* **2002**, *297*, 1536.

[59] H. D. Hill, C. A. Mirkin, *Nat. Protoc.* **2006**, *1*, 324.

[60] D. G. Georganopoulou, L. Chang, J.-M. Nam, C. S. Thaxton, E. J. Mufson, W. L. Klein, C. A. Mirkin, *Proc. Natl. Acad. Sci.* **2005**, *102*, 2273.

[61] E. D. Goluch, J.-M. Nam, D. G. Georganopoulou, T. N. Chiesl, K. A. Shaikh, K. S. Ryu, A. E. Barron, C. A. Mirkin, C. Liu, *Lab. Chip* **2006**, *6*, 1293.

[62] R. Jin, G. Wu, Z. Li, C. A. Mirkin, G. C. Schatz, *J. Am. Chem. Soc.* **2003**, *125*, 1643.

[63] S.-J. Park, T. A. Taton, C. A. Mirkin, *Science* **2002**, *295*, 1503.

[64] J.-M. Nam, C. S. Thaxton, C. A. Mirkin, *Science* **2003**, *301*, 1884.

[65] D. A. Giljohann, D. S. Seferos, P. C. Patel, J. E. Millstone, N. L. Rosi, C. A. Mirkin, *Nano Lett.* **2007**, *7*, 3818.

[66] N. L. Rosi, D. A. Giljohann, C. S. Thaxton, A. K. R. Lytton-Jean, M. S. Han, C. A. Mirkin, *Science* **2006**, *312*, 1027.

[67] D. S. Seferos, D. A. Giljohann, H. D. Hill, A. E. Prigodich, C. A. Mirkin, *J. Am. Chem. Soc.* **2007**, *129*, 15477.

[68] J. I. Cutler, E. Auyeung, C. A. Mirkin, *J. Am. Chem. Soc.* **2012**, *134*, 1376.

[69] R. J. Macfarlane, B. Lee, M. R. Jones, N. Harris, G. C. Schatz, C. A. Mirkin, *Science* **2011**, *334*, 204.

[70] R. J. Macfarlane, M. N. O'Brien, S. H. Petrosko, C. A. Mirkin, *Angew. Chem. Int. Ed.* **2013**, *52*, 5688.

[71] J. J. Storhoff, A. A. Lazarides, R. C. Mucic, C. A. Mirkin, R. L. Letsinger, G. C. Schatz, *J. Am. Chem. Soc.* **2000**, *122*, 4640.

[72] T. A. Taton, R. C. Mucic, C. A. Mirkin, R. L. Letsinger, *J. Am. Chem. Soc.* **2000**, *122*, 6305.

[73] J.-S. Lee, S. I. Stoeva, C. A. Mirkin, *J. Am. Chem. Soc.* **2006**, *128*, 8899.

[74] S. Y. Park, D. Stroud, *Phys. Rev. B* **2003**, *68*, 224201.

[75] S. Y. Park, J.-S. Lee, D. Georganopoulou, C. A. Mirkin, G. C. Schatz, *J. Phys. Chem. B* **2006**, *110*, 12673.

[76] S.-J. Park, A. A. Lazarides, J. J. Storhoff, L. Pesce, C. A. Mirkin, *J. Phys. Chem. B* **2004**, *108*, 12375.

[77] A. J. Kim, P. L. Biancaniello, J. C. Crocker, *Langmuir* **2006**, *22*, 1991.

[78] S. Y. Park, A. K. R. Lytton-Jean, B. Lee, S. Weigand, G. C. Schatz, C. A. Mirkin, *Nature* **2008**, *451*, 553.

[79] D. Nykypanchuk, M. M. Maye, D. van der Lelie, O. Gang, *Nature* **2008**, *451*, 549.

[80] R. J. Macfarlane, R. V. Thaner, K. A. Brown, J. Zhang, B. Lee, S. T. Nguyen, C. A. Mirkin, *Proc. Natl. Acad. Sci.* **2014**, *111*, 14995.

[81] H. Xiong, D. van der Lelie, O. Gang, *J. Am. Chem. Soc.* **2008**, *130*, 2442.

[82] H. Xiong, D. van der Lelie, O. Gang, *Phys. Rev. Lett.* **2009**, *102*, 015504.

[83] C. Zhang, R. J. Macfarlane, K. L. Young, C. H. J. Choi, L. Hao, E. Auyeung, G. Liu, X. Zhou, C. A. Mirkin, *Nat. Mater.* **2013**, *12*, 741.

[84] Y. Zhang, F. Lu, K. G. Yager, D. van der Lelie, O. Gang, *Nat. Nanotechnol.* **2013**, *8*, 865.

[85] J.-S. Lee, A. K. R. Lytton-Jean, S. J. Hurst, C. A. Mirkin, *Nano Lett.* **2007**, *7*, 2112.

[86] Y. Cao, R. Jin, C. A. Mirkin, *J. Am. Chem. Soc.* **2001**, *123*, 7961.

[87] G. P. Mitchell, C. A. Mirkin, R. L. Letsinger, *J. Am. Chem. Soc.* **1999**, *121*, 8122.

[88] D. Sun, O. Gang, *J. Am. Chem. Soc.* **2011**, *133*, 5252.

[89] D. Sun, O. Gang, *Langmuir* **2013**, *29*, 7038.

[90] J. I. Cutler, D. Zheng, X. Xu, D. A. Giljohann, C. A. Mirkin, *Nano Lett.* **2010**, *10*, 1477.

[91] K. L. Young, A. W. Scott, L. Hao, S. E. Mirkin, G. Liu, C. A. Mirkin, *Nano Lett.* **2012**, *12*, 3867.

[92] Y. Wang, Y. Wang, X. Zheng, É. Ducrot, M.-G. Lee, G.-R. Yi, M. Weck, D. J. Pine, *J. Am. Chem. Soc.* **2015**, *137*, 10760.

[93] P. H. Rogers, E. Michel, C. A. Bauer, S. Vanderet, D. Hansen, B. K. Roberts, A. Calvez, J. B. Crews, K. O. Lau, A. Wood, D. J. Pine, P. V. Schwartz, *Langmuir* **2005**, *21*, 5562.

[94] S. Lee, J. H. Yoon, I.-S. Jo, J. S. Oh, D. J. Pine, T. S. Shim, G.-R. Yi, *Langmuir* **2018**, *34*, 11042.

[95] É. Ducrot, M. He, G.-R. Yi, D. J. Pine, *Nat. Mater.* **2017**, *16*, 652.

[96] W. Morris, W. E. Briley, E. Auyeung, M. D. Cabezas, C. A. Mirkin, *J. Am. Chem. Soc.* **2014**, *136*, 7261.

[97] E. Auyeung, J. I. Cutler, R. J. Macfarlane, M. R. Jones, J. Wu, G. Liu, K. Zhang, K. D. Osberg, C. A. Mirkin, *Nat. Nanotechnol.* **2012**, *7*, 24.

[98] M. R. Jones, R. J. Macfarlane, B. Lee, J. Zhang, K. L. Young, A. J. Senesi, C. A. Mirkin, *Nat. Mater.* **2010**, *9*, 913.

[99] M. N. O'Brien, M. R. Jones, B. Lee, C. A. Mirkin, *Nat. Mater.* **2015**, *14*, 833.

[100] V. N. Manoharan, M. T. Elsesser, D. J. Pine, *Science* **2003**, *301*, 483.

[101] O. G. Hayes, J. R. McMillan, B. Lee, C. A. Mirkin, *J. Am. Chem. Soc.* **2018**, *140*, 9269.

[102] W. Liu, M. Tagawa, H. L. Xin, T. Wang, H. Emamy, H. Li, K. G. Yager, F. W. Starr, A. V. Tkachenko, O. Gang, *Science* **2016**, *351*, 582.

[103] Y. Wang, I. C. Jenkins, J. T. McGinley, T. Sinno, J. C. Crocker, *Nat. Commun.* **2017**, *8*, 14173.

[104] Y. Wang, Y. Wang, X. Zheng, É. Ducrot, J. S. Yodh, M. Weck, D. J. Pine, *Nat. Commun.* **2015**, *6*, 7253.

[105] R. Dreyfus, M. E. Leunissen, R. Sha, A. V. Tkachenko, N. C. Seeman, D. J. Pine, P. M. Chaikin, *Phys. Rev. Lett.* **2009**, *102*, 048301.

[106] R. Dreyfus, M. E. Leunissen, R. Sha, A. Tkachenko, N. C. Seeman, D. J. Pine, P. M. Chaikin, *Phys. Rev. E* **2010**, *81*, 041404.

[107] R. J. Macfarlane, M. R. Jones, A. J. Senesi, K. L. Young, B. Lee, J. Wu, C. A. Mirkin, *Angew. Chem. Int. Ed.* **2010**, *49*, 4589.

[108] X. Xu, N. L. Rosi, Y. Wang, F. Huo, C. A. Mirkin, *J. Am. Chem. Soc.* **2006**, *128*, 9286.

[109] S.-J. Park, A. A. Lazarides, C. A. Mirkin, R. L. Letsinger, *Angew. Chem. Int. Ed.* **2001**, *40*, 2909.

[110] J. R. McMillan, J. D. Brodin, J. A. Millan, B. Lee, M. Olvera de la Cruz, C. A. Mirkin, *J. Am. Chem. Soc.* **2017**, *139*, 1754.

[111] J. R. McMillan, C. A. Mirkin, *J. Am. Chem. Soc.* **2018**, *140*, 6776.

[112] Y. Tian, Y. Zhang, T. Wang, H. L. Xin, H. Li, O. Gang, *Nat. Mater.* **2016**, *15*, 654.

[113] W. Liu, J. Halverson, Y. Tian, A. V. Tkachenko, O. Gang, *Nat. Chem.* **2016**, *8*, 867.

[114] M. R. Jones, R. J. Macfarlane, A. E. Prigodich, P. C. Patel, C. A. Mirkin, *J. Am. Chem. Soc.* **2011**, *133*, 18865.

[115] M. N. O'Brien, M. R. Jones, K. A. Brown, C. A. Mirkin, *J. Am. Chem. Soc.* **2014**, *136*, 7603.

[116] E. B. Mock, H. De Bruyn, B. S. Hawkett, R. G. Gilbert, C. F. Zukoski, *Langmuir* **2006**, *22*, 4037.

[117] J. S. DuChene, W. Niu, J. M. Abendroth, Q. Sun, W. Zhao, F. Huo, W. D. Wei, *Chem. Mater.* **2013**, *25*, 1392.

[118] B. D. Clark, C. R. Jacobson, M. Lou, J. Yang, L. Zhou, S. Gottheim, C. J. DeSantis, P. Nordlander, N. J. Halas, *Nano Lett.* **2018**, *18*, 1234.

[119] D. Lisjak, A. Mertelj, *Prog. Mater. Sci.* **2018**, *95*, 286.

[120] S. Vial, D. Nykypanchuk, K. G. Yager, A. V. Tkachenko, O. Gang, *ACS Nano* **2013**, *7*, 5437.

[121] F. Lu, K. G. Yager, Y. Zhang, H. Xin, O. Gang, *Nat. Commun.* **2015**, *6*, 6912.

[122] M. N. O'Brien, M. Girard, H.-X. Lin, J. A. Millan, M. Olvera de la Cruz, B. Lee, C. A. Mirkin, *Proc. Natl. Acad. Sci.* **2016**, *113*, 10485.

[123] H. D. Hill, R. J. Macfarlane, A. J. Senesi, B. Lee, S. Y. Park, C. A. Mirkin, *Nano Lett.* **2008**, *8*, 2341.

[124] S. E. Seo, M. X. Wang, C. M. Shade, J. L. Rouge, K. A. Brown, C. A. Mirkin, *ACS Nano* **2016**, *10*, 1771.

[125] S. Pal, Y. Zhang, S. K. Kumar, O. Gang, *J. Am. Chem. Soc.* **2015**, *137*, 4030.

[126] T. Oh, S. S. Park, C. A. Mirkin, *Adv. Mater.* **2019**, *31*, 1805480.

[127] A. J. Senesi, D. J. Eichelsdoerfer, K. A. Brown, B. Lee, E. Auyeung, C. H. J. Choi, R. J. Macfarlane, K. L. Young, C. A. Mirkin, *Adv. Mater.* **2014**, *26*, 7235.

[128] R. V. Thaner, Y. Kim, T. I. N. G. Li, R. J. Macfarlane, S. T. Nguyen, M. Olvera de la Cruz, C. A. Mirkin, *Nano Lett.* **2015**, *15*, 5545.

[129] G. L. Miessler, P. J. Fischer, D. A. Tarr, *Inorganic Chemistry*, Pearson, Boston, **2013**.

[130] J. E. Jones, *Proc R Soc Lond A* **1924**, *106*, 463.

[131] M. Mohebifar, E. R. Johnson, C. N. Rowley, *J. Chem. Theory Comput.* **2017**, *13*, 6146.

[132] S. E. Seo, T. Li, A. J. Senesi, C. A. Mirkin, B. Lee, *J. Am. Chem. Soc.* **2017**, *139*, 16528.

[133] H. Xiong, M. Y. Sfeir, O. Gang, *Nano Lett.* **2010**, *10*, 4456.

[134] J. A. Mason, C. R. Laramy, C.-T. Lai, M. N. O'Brien, Q.-Y. Lin, V. P. Dravid, G. C. Schatz, C. A. Mirkin, *J. Am. Chem. Soc.* **2016**, *138*, 8722.

[135] S. Srivastava, D. Nykypanchuk, M. M. Maye, A. V. Tkachenko, O. Gang, *Soft Matter* **2013**, *9*, 10452.

[136] J. Zhu, Y. Kim, H. Lin, S. Wang, C. A. Mirkin, *J. Am. Chem. Soc.* **2018**, *140*, 5061.

[137] G. Bonner, A. M. Klibanov, *Biotechnol. Bioeng.* **2000**, *68*, 339.

[138] A. Arcella, G. Portella, R. Collepardo-Guevara, D. Chakraborty, D. J. Wales, M. Orozco, *J. Phys. Chem. B* **2014**, *118*, 8540.

[139] J. Srinivasan, T. E. Cheatham, P. Cieplak, P. A. Kollman, D. A. Case, *J. Am. Chem. Soc.* **1998**, *120*, 9401.

[140] M. M. Maye, M. T. Kumara, D. Nykypanchuk, W. B. Sherman, O. Gang, *Nat. Nanotechnol.* **2010**, *5*, 116.

[141] Y. Kim, R. J. Macfarlane, C. A. Mirkin, *J. Am. Chem. Soc.* **2013**, *135*, 10342.

[142] Y. Kim, R. J. Macfarlane, M. R. Jones, C. A. Mirkin, *Science* **2016**, *351*, 579.

[143] B. Srinivasan, T. Vo, Y. Zhang, O. Gang, S. Kumar, V. Venkatasubramanian, *Proc. Natl. Acad. Sci.* **2013**, *110*, 18431.

[144] A. V. Tkachenko, *Phys. Rev. Lett.* **2002**, *89*, 148303.

[145] T. Vo, V. Venkatasubramanian, S. Kumar, B. Srinivasan, S. Pal, Y. Zhang, O. Gang, *Proc. Natl. Acad. Sci.* **2015**, *112*, 4982.

[146] R. J. Macfarlane, M. R. Jones, B. Lee, E. Auyeung, C. A. Mirkin, *Science* **2013**, *341*, 1222.

[147] M. X. Wang, S. E. Seo, P. A. Gabrys, D. Fleischman, B. Lee, Y. Kim, H. A. Atwater, R. J. Macfarlane, C. A. Mirkin, *ACS Nano* **2017**, *11*, 180.

[148] S. E. Seo, M. Girard, M. Olvera de la Cruz, C. A. Mirkin, *Nat. Commun.* **2018**, *9*, 4558.

[149] R. V. Thaner, I. Eryazici, R. J. Macfarlane, K. A. Brown, B. Lee, S. T. Nguyen, C. A. Mirkin, *J. Am. Chem. Soc.* **2016**, *138*, 6119.

[150] M. N. O'Brien, K. A. Brown, C. A. Mirkin, *ACS Nano* **2016**, *10*, 1363.

[151] Z. Jian, F. Chang, W. Ma, W. Yan, G. Yang, Y. Zhou, *Sci. China Ser. E Technol. Sci.* **2000**, *43*, 113.

[152] E. B. Moore, V. Molinero, *Nature* **2011**, *479*, 506.

[153] R. J. Macfarlane, B. Lee, H. D. Hill, A. J. Senesi, S. Seifert, C. A. Mirkin, *Proc. Natl. Acad. Sci.* **2009**, *106*, 10493.

[154] S. Dhakal, K. L. Kohlstedt, G. C. Schatz, C. A. Mirkin, M. Olvera de la Cruz, *ACS Nano* **2013**, *7*, 10948.

[155] E. Auyeung, T. I. N. G. Li, A. J. Senesi, A. L. Schmucker, B. C. Pals, M. Olvera de la Cruz, C. A. Mirkin, *Nature* **2014**, *505*, 73.

[156] G. Wulff, *Z. Für Krist. - Cryst. Mater.* **1901**, *34*, 449.

[157] T. Oh, J. C. Ku, J.-H. Lee, M. C. Hersam, C. A. Mirkin, *Nano Lett.* **2018**, *18*, 6022.

[158] M. N. O'Brien, B. Radha, K. A. Brown, M. R. Jones, C. A. Mirkin, *Angew. Chem.* **2014**, *126*, 9686.

[159] W. Zhou, Q.-Y. Lin, J. A. Mason, V. P. Dravid, C. A. Mirkin, *Small* **2018**, *14*, 1802742.

[160] Q.-Y. Lin, J. A. Mason, Z. Li, W. Zhou, M. N. O'Brien, K. A. Brown, M. R. Jones, S. Butun, B. Lee, V. P. Dravid, K. Aydin, C. A. Mirkin, *Science* **2018**, *359*, 669.

[161] D. J. Lewis, P. A. Gabrys, R. J. Macfarlane, *Langmuir* **2018**, *34*, 14842.

[162] B. D. Myers, Q.-Y. Lin, H. Wu, E. Luijten, C. A. Mirkin, V. P. Dravid, *ACS Nano* **2016**, *10*, 5679.

[163] A. J. Senesi, D. J. Eichelsdoerfer, R. J. Macfarlane, M. R. Jones, E. Auyeung, B. Lee, C. A. Mirkin, *Angew. Chem. Int. Ed.* **2013**, *52*, 6624.

[164] H. J. Frost, *Mater. Charact.* **1994**, *32*, 257.

[165] C. V. Thompson, H. J. Frost, F. Spaepen, *Acta Metall.* **1987**, *35*, 887.

[166] M. Ohring, *Materials Science of Thin Films: Deposition and Structure*, Academic Press, San Diego, CA, **2002**.

[167] S. L. Hellstrom, Y. Kim, J. S. Fakonas, A. J. Senesi, R. J. Macfarlane, C. A. Mirkin, H. A. Atwater, *Nano Lett.* **2013**, *13*, 6084.

[168] P. A. Gabrys, L. Z. Zornberg, R. J. Macfarlane, *Small* **2019**, *15*, 1805424.

[169] S. E. Seo, M. Girard, M. Olvera de la Cruz, C. A. Mirkin, *ACS Cent. Sci.* **2019**, *5*, 186.

[170] S. Kogikoski, L. T. Kubota, *Electrochem. Commun.* **2018**, *90*, 51.

[171] M. B. Ross, J. C. Ku, B. Lee, C. A. Mirkin, G. C. Schatz, *Adv. Mater.* **2016**, *28*, 2790.

[172] M. B. Ross, J. C. Ku, V. M. Vaccarezza, G. C. Schatz, C. A. Mirkin, *Nat. Nanotechnol.* **2015**, *10*, 453.

[173] C. V. Thompson, *Annu. Rev. Mater. Sci.* **1990**, *20*, 245.

[174] M. Shekhirev, E. Sutter, P. Sutter, *Adv. Funct. Mater.* **2019**, *29*, 1806924.

[175] E. Sutter, B. Zhang, S. Sutter, P. Sutter, *Nanoscale* **2019**, *11*, 34.

[176] E. Auyeung, R. J. Macfarlane, C. H. J. Choi, J. I. Cutler, C. A. Mirkin, *Adv. Mater.* **2012**, *24*, 5181.

[177] P. A. Gabrys, R. J. Macfarlane, *ACS Nano* **2019**, *13*, 8452.

[178] Z. Zhang, M. G. Lagally, *Science* **1997**, *276*, 377.

[179] M. C. Bartelt, J. W. Evans, *Phys. Rev. Lett.* **1995**, *75*, 4250.

[180] F. Hua, J. Shi, Y. Lvov, T. Cui, *Nano Lett.* **2002**, *2*, 1219.

[181] S. M. Rupich, F. C. Castro, W. T. M. Irvine, D. V. Talapin, *Nat. Commun.* **2014**, *5*, ncomms6045.

[182] A. Tao, F. Kim, C. Hess, J. Goldberger, R. He, Y. Sun, Y. Xia, P. Yang, *Nano Lett.* **2003**, *3*, 1229.

[183] N. A. Kotov, I. Dekany, J. H. Fendler, *J. Phys. Chem.* **1995**, *99*, 13065.

[184] C. H. Lalander, Y. Zheng, S. Dhuey, S. Cabrini, U. Bach, *ACS Nano* **2010**, *4*, 6153.

[185] J. D. Brodin, E. Auyeung, C. A. Mirkin, *Proc. Natl. Acad. Sci.* **2015**, *112*, 4564.

[186] D. D. Evanoff Jr., G. Chumanov, *ChemPhysChem* **2005**, *6*, 1221.

[187] K. L. Kelly, E. Coronado, L. L. Zhao, G. C. Schatz, *J. Phys. Chem. B* **2003**, *107*, 668.

[188] J.-H. Choi, H. Wang, S. J. Oh, T. Paik, P. Sung, J. Sung, X. Ye, T. Zhao, B. T. Diroll, C. B. Murray, C. R. Kagan, *Science* **2016**, *352*, 205.

[189] T. Li, A. J. Senesi, B. Lee, *Chem. Rev.* **2016**, *116*, 11128.

[190] S. T. Meyers, J. T. Anderson, C. M. Hung, J. Thompson, J. F. Wager, D. A. Keszler, *J. Am. Chem. Soc.* **2008**, *130*, 17603.

[191] C. M. Shade, R. D. Kennedy, J. L. Rouge, M. S. Rosen, M. X. Wang, S. E. Seo, D. J. Clingerman, C. A. Mirkin, *Chem. - Eur. J.* **2015**, *21*, 10983.

[192] E. Auyeung, R. J. Macfarlane, C. H. J. Choi, J. I. Cutler, C. A. Mirkin, *Adv. Mater.* **2012**, *24*, 5181.

[193] C. J. Palmstrom, *Annu. Rev. Mater. Sci.* **1995**, *25*, 389.

[194] J. E. Ayers, T. Kujofsa, P. Rago, J. Raphael, *Heteroepitaxy of Semiconductors: Theory, Growth, and Characterization, Second Edition*, CRC Press, **2016**.

[195] A. L. Fetter, J. D. Walecka, *Theoretical Mechanics of Particles and Continua*, Courier Corporation, **2003**.

[196] C. Kittel, *Am. J. Phys.* **1967**, *35*, 547.

[197] M. Born, K. Huang, *Am. J. Phys.* **1955**, *23*, 474.

[198] M. X. Wang, J. D. Brodin, J. A. Millan, S. E. Seo, M. Girard, M. Olvera de la Cruz, B. Lee, C. A. Mirkin, *Nano Lett.* **2017**, *17*, 5126.

[199] O.-S. Lee, V. Y. Cho, G. C. Schatz, *J. Phys. Chem. B* **2012**, *116*, 7000.

[200] M. M. Maye, D. Nykypanchuk, D. van der Lelie, O. Gang, *Small* **2007**, *3*, 1678.

[201] D. Nykypanchuk, M. M. Maye, D. van der Lelie, O. Gang, *Langmuir* **2007**, *23*, 6305.

[202] C. Bustamante, Z. Bryant, S. B. Smith, *Nature* **2003**, *421*, 423.

[203] M. Rief, H. Clausen-Schaumann, H. E. Gaub, *Nat. Struct. Mol. Biol.* **1999**, *6*, 346.

[204] J. F. Marko, S. Cocco, *Phys. World* **2003**, *16*, 37.

[205] C. Bustamante, S. B. Smith, J. Liphardt, D. Smith, *Curr. Opin. Struct. Biol.* **2000**, *10*, 279.

[206] K. M. Kosikov, A. A. Gorin, V. B. Zhurkin, W. K. Olson, *J. Mol. Biol.* **1999**, *289*, 1301.

[207] M. R. Begley, D. S. Gianola, T. R. Ray, *Science* **2019**, *364*, DOI 10.1126/science.aav4299.

[208] I. Levchenko, K. Bazaka, M. Keidar, S. Xu, J. Fang, *Adv. Mater.* **2018**, *30*, 1702226.

[209] S. Nayak, L. A. Lyon, *Angew. Chem. Int. Ed.* **2005**, *44*, 7686.

[210] Y. Xia, T. D. Nguyen, M. Yang, B. Lee, A. Santos, P. Podsiadlo, Z. Tang, S. C. Glotzer, N. A. Kotov, *Nat. Nanotechnol.* **2011**, *6*, 580.

[211] J. Kao, K. Thorkelsson, P. Bai, Z. Zhang, C. Sun, T. Xu, *Nat. Commun.* **2014**, *5*, 1.

[212] M. Grzelczak, L. M. Liz-Marzán, R. Klajn, *Chem. Soc. Rev.* **2019**, *48*, 1342.

[213] P. K. Kundu, D. Samanta, R. Leizrowice, B. Margulis, H. Zhao, M. Börner, T. Udayabhaskararao, D. Manna, R. Klajn, *Nat. Chem.* **2015**, *7*, 646.

[214] B. C. Steimle, J. L. Fenton, R. E. Schaak, *Science* **2020**, *367*, 418.

[215] W. Chen, D. Talreja, D. Eichfeld, P. Mahale, N. N. Nova, H. Y. Cheng, J. L. Russell, S.-Y. Yu, N. Poilvert, G. Mahan, S. E. Mohney, V. H. Crespi, T. E. Mallouk, J. V. Badding, B. Foley, V. Gopalan, I. Dabo, *ACS Nano* **2020**, DOI 10.1021/acsnano.9b09487.

[216] S. Nayak, N. Horst, H. Zhang, W. Wang, S. Mallapragada, A. Travesset, D. Vaknin, *J. Phys. Chem. C* **2019**, *123*, 836.

[217] J.-M. Ha, S.-H. Lim, J. Dey, S.-J. Lee, M.-J. Lee, S.-H. Kang, K. S. Jin, S.-M. Choi, *Nano Lett.* **2019**, *19*, 2313.

[218] A. Dreyer, A. Feld, A. Kornowski, E. D. Yilmaz, H. Noei, A. Meyer, T. Krekeler, C. Jiao, A. Stierle, V. Abetz, H. Weller, G. A. Schneider, *Nat. Mater.* **2016**, *15*, 522.

[219] Y. Nagaoka, H. Zhu, D. Eggert, O. Chen, *Science* **2018**, *362*, 1396.

[220] Y. Nagaoka, R. Tan, R. Li, H. Zhu, D. Eggert, Y. A. Wu, Y. Liu, Z. Wang, O. Chen, *Nature* **2018**, *561*, 378.

[221] X. Ye, J. Chen, M. E. Irrgang, M. Engel, A. Dong, S. C. Glotzer, C. B. Murray, *Nat. Mater.* **2017**, *16*, 214.

[222] H. Lin, S. Lee, L. Sun, M. Spellings, M. Engel, S. C. Glotzer, C. A. Mirkin, *Science* **2017**, *355*, 931.

[223] F. Lu, T. Vo, Y. Zhang, A. Frenkel, K. G. Yager, S. Kumar, O. Gang, *Sci. Adv.* **2019**, *5*, eaaw2399.

[224] Y. Jiao, D. Han, Y. Ding, X. Zhang, G. Guo, J. Hu, D. Yang, A. Dong, *Nat. Commun.* **2015**, *6*, 1.

[225] Z. Quan, H. Xu, C. Wang, X. Wen, Y. Wang, J. Zhu, R. Li, C. J. Sheehan, Z. Wang, D.-M. Smilgies, Z. Luo, J. Fang, *J. Am. Chem. Soc.* **2014**, *136*, 1352.

[226] A. Dong, J. Chen, P. M. Vora, J. M. Kikkawa, C. B. Murray, *Nature* **2010**, *466*, 474.

[227] E. Auyeung, T. I. N. G. Li, A. J. Senesi, A. L. Schmucker, B. C. Pals, M. O. de la Cruz, C. A. Mirkin, *Nature* **2014**, *505*, 73.

[228] Y. Kang, M. Li, Y. Cai, M. Cargnello, R. E. Diaz, T. R. Gordon, N. L. Wieder, R. R. Adzic, R. J. Gorte, E. A. Stach, C. B. Murray, *J. Am. Chem. Soc.* **2013**, *135*, 2741.

[229] D. J. Lewis, L. Z. Zornberg, D. J. D. Carter, R. J. Macfarlane, *Nat. Mater.* **2020**, 1.

[230] B. de Nijs, S. Dussi, F. Smallenburg, J. D. Meeldijk, D. J. Groenendijk, L. Filion, A. Imhof, A. van Blaaderen, M. Dijkstra, *Nat. Mater.* **2015**, *14*, 56.

[231] Y. Yang, B. Wang, X. Shen, L. Yao, L. Wang, X. Chen, S. Xie, T. Li, J. Hu, D. Yang, A. Dong, *J. Am. Chem. Soc.* **2018**, *140*, 15038.

[232] Y. Wang, P. J. Santos, J. M. Kubiak, X. Guo, M. S. Lee, R. J. Macfarlane, *J. Am. Chem. Soc.* **2019**, *141*, 13234.

[233] P. J. Santos, T. C. Cheung, R. J. Macfarlane, *Nano Lett.* **2019**, *19*, 5774.

[234] P. J. Santos, Z. Cao, J. Zhang, A. Alexander-Katz, R. J. Macfarlane, *J. Am. Chem. Soc.* **2019**, *141*, 14624.

[235] S. T. Milner, T. A. Witten, M. E. Cates, *Europhys. Lett. EPL* **1988**, *5*, 413.

[236] T. M. Birshtein, Y. V. Lyatskaya, *Macromolecules* **1994**, *27*, 1256.

[237] D. Samanta, A. Iscen, C. R. Laramy, S. B. Ebrahimi, K. E. Bujold, G. C. Schatz, C. A. Mirkin, *J. Am. Chem. Soc.* **2019**, *141*, 19973.

[238] S. Lee, C. Y. Zheng, K. E. Bujold, C. A. Mirkin, *J. Am. Chem. Soc.* **2019**, *141*, 11827.

[239] Y. Kang, M. Li, Y. Cai, M. Cargnello, R. E. Diaz, T. R. Gordon, N. L. Wieder, R. R. Adzic, R. J. Gorte, E. A. Stach, C. B. Murray, *J. Am. Chem. Soc.* **2013**, *135*, 2741.

[240] J. J. De Yoreo, P. U. P. A. Gilbert, N. A. J. M. Sommerdijk, R. L. Penn, S. Whitelam, D. Joester, H. Zhang, J. D. Rimer, A. Navrotsky, J. F. Banfield, A. F. Wallace, F. M. Michel, F. C. Meldrum, H. Cölfen, P. M. Dove, *Science* **2015**, *349*, aaa6760.

[241] R. Chaim, M. Levin, A. Shlayer, C. Estournes, *Adv. Appl. Ceram.* **2008**, *107*, 159.

[242] G. S. Jayaraman, J. F. Wallace, P. H. Geil, E. Baer, *Polym. Eng. Sci.* **1976**, *16*, 529.

[243] Z. Z. Fang, H. Wang, *Int. Mater. Rev.* **2008**, *53*, 326.

[244] P. J. Santos, R. J. Macfarlane, *J. Am. Chem. Soc.* **2020**, *142*, 1170.

[245] W. L. Bragg, J. F. Nye, *Proc. R. Soc. Lond. Ser. Math. Phys. Sci.* **1947**, *190*, 474.

[246] A. S. Argon, H. Y. Kuo, *Mater. Sci. Eng.* **1979**, *39*, 101.

[247] J. W. Matthews, *J. Vac. Sci. Technol.* **1975**, *12*, 126.

[248] J. Kim, Z. Ou, M. R. Jones, X. Song, Q. Chen, *Nat. Commun.* **2017**, *8*, 761.

[249] J. Kim, M. R. Jones, Z. Ou, Q. Chen, *ACS Nano* **2016**, *10*, 9801.

[250] G. Antczak, G. Ehrlich, *Surf. Sci. Rep.* **2007**, *62*, 39.

[251] G. Antczak, G. Ehrlich, *Surface Diffusion: Metals, Metal Atoms, and Clusters*, Cambridge University Press, **2010**.

[252] A. Danescu, *Int. J. Solids Struct.* **2001**, *38*, 4671.

[253] P. Politi, G. Grenet, A. Marty, A. Ponchet, J. Villain, *Phys. Rep.* **2000**, *324*, 271.

[254] K. Iwata, S. Yamazaki, P. Mutombo, P. Hapala, M. Ondráček, P. Jelínek, Y. Sugimoto, *Nat. Commun.* **2015**, *6*, 7766.

[255] N. de Jonge, F. M. Ross, *Nat. Nanotechnol.* **2011**, *6*, 695.

[256] B. R. Pauw, *J. Phys. Condens. Matter* **2013**, *25*, 383201.

[257] J. Kotakoski, C. Mangler, J. C. Meyer, *Nat. Commun.* **2014**, *5*, 3991.

[258] B. S. Swartzentruber, *Phys. Rev. Lett.* **1996**, *76*, 459.

[259] L. Zhong, F. Sansoz, Y. He, C. Wang, Z. Zhang, S. X. Mao, *Nat. Mater.* **2017**, *16*, 439.

[260] K. Fujiwara, R. Maeda, K. Maeda, H. Morito, *Scr. Mater.* **2017**, *133*, 65.

[261] S. Tokita, H. Kokawa, Y. S. Sato, H. T. Fujii, *Mater. Charact.* **2017**, *131*, 31.

[262] D. J. Park, C. Zhang, J. C. Ku, Y. Zhou, G. C. Schatz, C. A. Mirkin, *Proc. Natl. Acad. Sci.* **2015**, *112*, 977.

[263] L. Sun, H. Lin, D. J. Park, M. R. Bourgeois, M. B. Ross, J. C. Ku, G. C. Schatz, C. A. Mirkin, *Nano Lett.* **2017**, *17*, 2313.

[264] H. Alaeian, J. A. Dionne, *Opt. Express* **2012**, *20*, 15781.

[265] M. B. Ross, M. G. Blaber, G. C. Schatz, *Nat. Commun.* **2014**, *5*, 4090.

[266] A. Myerson, *Handbook of Industrial Crystallization*, Butterworth-Heinemann, **2002**.

[267] W. L. Winterbottom, *Acta Metall.* **1967**, *15*, 303.

[268] W. Bao, W. Jiang, D. Srolovitz, Y. Wang, *SIAM J. Appl. Math.* **2017**, *77*, 2093.

[269] R. K. P. Zia, J. E. Avron, J. E. Taylor, *J. Stat. Phys.* **1988**, *50*, 727.

[270] B. Bhushan, D. Luo, S. R. Schricker, W. Sigmund, S. Zauscher, *Handbook of Nanomaterials Properties*, Springer Science & Business Media, **2014**.

[271] F. A. Cotton, G. Wilkinson, C. A. Murillo, M. Bochmann, *Advanced Inorganic Chemistry*, Wiley-Interscience, New York, **1999**.

[272] G. Bastard, *Wave Mechanics Applied to Semiconductor Heterostructures*, Les Éditions De Physique, **1988**.

[273] D. V. Morgan, K. Board, *An Introduction to Semiconductor Microtechnology*, J. Wiley, Chichester; New York, **1990**.

[274] R. C. Mucic, J. J. Storhoff, C. A. Mirkin, R. L. Letsinger, *J. Am. Chem. Soc.* **1998**, *120*, 12674.

[275] J. B. Lassiter, H. Sobhani, J. A. Fan, J. Kundu, F. Capasso, P. Nordlander, N. J. Halas, *Nano Lett.* **2010**, *10*, 3184.

[276] S. Strauf, *Nat. Photonics* **2011**, *5*, 72.

[277] A. D. Lantada, A. de B. Romero, M. Schwentenwein, C. Jellinek, J. Homa, *Smart Mater. Struct.* **2016**, *25*, 054015.

[278] A. Fernández-Pacheco, R. Streubel, O. Fruchart, R. Hertel, P. Fischer, R. P. Cowburn, *Nat. Commun.* **2017**, *8*, 15756.

[279] T. Lee, J. Jang, H. Jeong, J. Rho, *Nano Converg.* **2018**, *5*, 1.

[280] U. S. Inan, A. Inan, *Electromagnetic Waves*, Prentice Hall, Upper Saddle River, N.J, **1999**.

[281] S. R. Cherry, J. A. Sorenson, M. E. Phelps, *Physics in Nuclear Medicine*, Elsevier Health Sciences, **2012**.

[282] R. C. Schroden, M. Al-Daous, C. F. Blanford, A. Stein, *Chem. Mater.* **2002**, *14*, 3305.

[283] S. Peng, R. Zhang, V. H. Chen, E. T. Khabiboulline, P. Braun, H. A. Atwater, *ACS Photonics* **2016**, *3*, 1131.

[284] M. K. Bhuyan, A. Soleilhac, M. Somayaji, T. E. Itina, R. Antoine, R. Stoian, *Sci. Rep.* **2018**, *8*, 9665.

[285] A. Dinwiddie, R. Null, M. Pizzano, L. Chuong, A. Leigh Krup, H. Ee Tan, N. H. Patel, *Dev. Biol.* **2014**, *392*, 404.

[286] Z.-Z. Gu, H. Uetsuka, K. Takahashi, R. Nakajima, H. Onishi, A. Fujishima, O. Sato, *Angew. Chem. Int. Ed.* **2003**, *42*, 894.

[287] Y. Zhao, Z. Xie, H. Gu, C. Zhu, Z. Gu, *Chem. Soc. Rev.* **2012**, *41*, 3297.

[288] L. Sun, H. Lin, K. L. Kohlstedt, G. C. Schatz, C. A. Mirkin, *Proc. Natl. Acad. Sci.* **2018**, *115*, 7242.

[289] N. W. Ashcroft, N. D. Mermin, *Solid State Physics*, Cengage Learning, New York, **1976**.

[290] W. Cai, V. Shalaev, *Optical Metamaterials: Fundamentals and Applications*, Springer Science & Business Media, **2009**.

[291] S. J. Barrow, X. Wei, J. S. Baldauf, A. M. Funston, P. Mulvaney, *Nat. Commun.* **2012**, *3*, 1275.

[292] S. J. Barrow, A. M. Funston, X. Wei, P. Mulvaney, *Nano Today* **2013**, *8*, 138.

[293] R. H. Tarkanyan, D. G. Niarchos, *Opt. Express* **2006**, *14*, 5433.

[294] T. Ito, S. Okazaki, *Nature* **2000**, *406*, 1027.

[295] V. R. Manfrinato, L. Zhang, D. Su, H. Duan, R. G. Hobbs, E. A. Stach, K. K. Berggren, *Nano Lett.* **2013**, *13*, 1555.

[296] P. Hajiyev, C. Cong, C. Qiu, T. Yu, *Sci. Rep.* **2013**, *3*, 2593.

[297] W. Cheng, M. J. Campolongo, J. J. Cha, S. J. Tan, C. C. Umbach, D. A. Muller, D. Luo, *Nat. Mater.* **2009**, *8*, 519.

[298] D. Zhao, D. Schneider, G. Fytas, S. K. Kumar, *ACS Nano* **2014**, *8*, 8163.

[299] W. Kim, J. Zide, A. Gossard, D. Klenov, S. Stemmer, A. Shakouri, A. Majumdar, *Phys. Rev. Lett.* **2006**, *96*, 045901.

[300] X. C. Tong, *Functional Metamaterials and Metadevices*, Springer, **2017**.

[301] L. Jiang, B. Gu, H. Hu, *Compos. Struct.* **2016**, *135*, 23.

[302] Z. Wang, A. Zulifqar, H. Hu, in *Adv. Compos. Mater. Aerosp. Eng.* (Eds: S. Rana, R. Fangueiro), Woodhead Publishing, **2016**, pp. 213–240.

[303] Z. Zhang, S. C. Glotzer, *Nano Lett.* **2004**, *4*, 1407.

[304] E. Maciá, *Rep. Prog. Phys.* **2006**, *69*, 397.

[305] D. Mousanezhad, B. Haghpanah, R. Ghosh, A. M. Hamouda, H. Nayeb-Hashemi, A. Vaziri, *Theor. Appl. Mech. Lett.* **2016**, *6*, 81.

[306] M. C. Gao, J.-W. Yeh, P. K. Liaw, Y. Zhang, *High-Entropy Alloys: Fundamentals and Applications*, Springer, **2016**.

[307] N. G. Bastús, J. Comenge, V. Puntes, *Langmuir* **2011**, *27*, 11098.

[308] H. Schnablegger, Y. Singh, *The SAXS Guide*, Anton Paar GmbH, Austria, **2013**.

[309] P. Pincus, *Macromolecules* **1991**, *24*, 2912.

[310] K. Matyjaszewski, *Macromolecules* **2012**, *45*, 4015.

[311] J. Park, K. An, Y. Hwang, J.-G. Park, H.-J. Noh, J.-Y. Kim, J.-H. Park, N.-M. Hwang, T. Hyeon, *Nat. Mater.* **2004**, *3*, 891.

[312] J.-H. Huh, J. Lee, S. Lee, *Nano Lett.* **2020**, DOI 10.1021/acs.nanolett.0c00422.

[313] S. A. Majetich, T. Wen, R. A. Booth, *ACS Nano* **2011**, *5*, 6081.

[314] K. Lord, *Grad. Theses Diss.* **2013**, DOI https://doi.org/10.31274/etd-180810-3172.